UNIVERSITY OF CALIFORNIA, SAN DIEGO

Transitions Out of High-Confinement Mode to Lower Confinement Regimes in Tokamaks

A dissertation submitted in partial satisfaction of the
requirements for the degree
Doctor of Philosophy

in

Physics

by

David Eldon

Committee in charge:

George Tynan, Chair
Patrick Diamond, Co-Chair
Farhat Beg
Jose Boedo
David Kleinfeld
Clifford Surko

2015

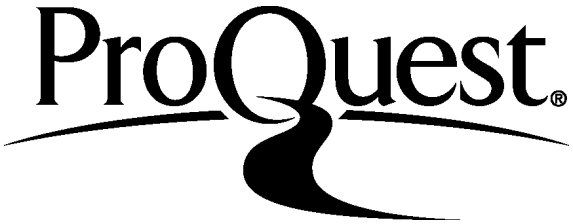

The dissertation of David Eldon is approved, and it is acceptable in quality and form for publication on microfilm and electronically:

_____

_____

_____

_____

_____
Co-Chair

_____
Chair

University of California, San Diego

2015

DEDICATION

To my son, Henry. The idea of having children has inspired me to work for a better future since long before he was born.

TABLE OF CONTENTS

Signature Page . . . iii

Dedication . . . iv

Table of Contents . . . v

List of Figures . . . viii

List of Tables . . . xii

Acknowledgements . . . xiii

Vita . . . xvi

Abstract of the Dissertation . . . xix

1 Introduction . . . 1
- 1.1 Nuclear Fusion for Energy Production . . . 1
- 1.2 Magnetic Confinement . . . 2
- 1.3 Tokamaks . . . 3
  - 1.3.1 Coordinate System . . . 6
  - 1.3.2 High Confinment Mode . . . 12
  - 1.3.3 Edge Localized Modes . . . 12
- 1.4 Transition Physics . . . 14
  - 1.4.1 Hahm-Burrell Shearing . . . 19
- 1.5 H-mode Termination . . . 19
  - 1.5.1 Phenomenology of the H-L Transition Sequence . . . 20
- 1.6 Hypotheses . . . 22
- 1.7 Organization . . . 24

2 High Resolution Thomson Scattering Diagnostic Upgrade at DIII-D . . . 26
- 2.1 Introduction . . . 26
- 2.2 Background . . . 28
  - 2.2.1 Thomson scattering . . . 28
  - 2.2.2 Diagnostic Implementation . . . 30
- 2.3 DIII-D High Resolution Thomson Scattering Upgrade . . . 40
  - 2.3.1 Upgrade requirements . . . 40
  - 2.3.2 Upgrade implementation . . . 44
  - 2.3.3 New analysis software . . . 51
- 2.4 Results . . . 53
  - 2.4.1 Upgrade performance . . . 53
  - 2.4.2 Systematic errors revealed and corrected . . . 54

2.5 Special Techniques . . . 57
2.5.1 Bunch Mode . . . 57
2.6 Analysis Techniques . . . 59
2.6.1 Variable Radius Gaussian Blur with Uncertainty Weighting . 60
2.6.2 Weighted Average of Offset Profiles Interpolated to Common Position Base . . . 63
2.6.3 Edge Detection . . . 65
2.7 Physics Usage of the High Resolution Thomson Scattering Diagnostic 66
2.7.1 EPED Validation . . . 67
2.7.2 Scrape Off Layer Physics . . . 68
2.7.3 Profile Changes During Applied Resonant Magnetic Perturbations . . . 68
2.8 Other Diagnostics . . . 74
2.8.1 Charge Exchange Recombination Spectroscopy . . . 75
2.8.2 Beam Emission Spectroscopy . . . 77
2.8.3 Magnetics . . . 79
2.9 Thomson Scattering Conclusion . . . 80
2.10 Acknowledgments . . . 81

3 Background: Theory and Numerical Calculations . . . 82
3.1 MHD and Equilibrium . . . 82
3.1.1 Linear Ideal Stability Calculations . . . 85
3.1.2 Diamagnetic Stabilization . . . 92
3.1.3 Ballooning . . . 93
3.1.4 Peeling . . . 95
3.1.5 Coupled Peeling-Ballooning . . . 98
3.1.6 Physical Origin of the Bootstrap Current . . . 99
3.2 Equilibrium and Stability Analysis . . . 101
3.2.1 Preparation of Kinetic Equilibrium Reconstructions as Inputs 101
3.2.2 Ideal Linear Stability of Peeling-Ballooning Modes (ELITE) . 106
3.2.3 Resonance and Edge q in Numerical Models . . . 109
3.3 Acknowledgements . . . 111

4 Ideal MHD Stability Analysis of H-L Back Transitions with ELITE . . . 112
4.1 Experiment Setup . . . 113
4.2 Stability Analysis . . . 119
4.3 Other Tests . . . 128
4.3.1 Triangularity Scan . . . 128
4.3.2 Radial Structure of Pedestal Collapse . . . 132
4.4 Discussion . . . 135
4.5 Acknowledgements . . . 138

5 Evolution of E×B Shear and Coherent Fluctuations Prior to H-L Transitions in DIII-D and Contol Strategies for H-L Transitions 140
5.1 Introduction 140
5.2 Experiment 142
5.3 Evolution of E×B Shear Prior to H-L Sequence 147
5.4 Characterization of the Modulating Pedestal Mode 156
5.4.1 Fluctuation Spectra Evolution Prior to the H-L Back Transition 156
5.4.2 Amplitude and Propagation Velocity Modulations Prior to the H-L Back Transition 158
5.4.3 Evolution of Dispersion Relation Leading up to the H-L Back Transition 160
5.4.4 Spatial Localization of the MPM Leading up to the H-L Back Transition 162
5.4.5 Transport Effects of the MPM 166
5.5 Conditions for Soft H-L Transitions 171
5.6 Discussion 181
5.7 Conclusion 186
5.8 Acknowledgments 186

6 Conclusion 187
6.1 High Resolution Thomson Scattering Upgrade 187
6.2 Ideal MHD Stability Analysis 187
6.3 Evolution of E×B Shear and Comparison to Turbulence Decorrelation Rate 188
6.4 Investigation of the Modulating Pedestal Mode 188
6.5 Conditions for a "Soft Landing" 189
6.6 Summary 190

A Notes on Calculations and Programming 191
A.1 Method of Determining Dominant MPM Parameters: k, f, and v_p 191
A.2 Local Wavenumber Anaysis to Determine the Dispersion Relation of the MPM 193
A.3 Correction to `IDL`'s Native Time Delayed Cross Correlation Function 193
A.4 Modification to `IDL`'s 2D Histogram to Better Handle Floating Point Numbers 195
A.5 Using the Distribution of χ^2 Values to Detect Calibration Errors . . 196

B Corrections to Account for Diagnostic Alignment Errors 198
B.1 Alignment Issues When Comparing Thomson scattering to BES . . 198

Bibliography 199

LIST OF FIGURES

Figure 1.1: Magnetic confinement. 3
Figure 1.2: Cutaway view of the DIII-D vacuum vessel 4
Figure 1.3: Illustration of drifts due to magnetic field gradients and electric fields. 6
Figure 1.4: Illustration of the combined effects of the gradient drift and the resulting $E \times B$ drift 7
Figure 1.5: Tokamak magnetic configuration. 8
Figure 1.6: DIII-D[1] with standard coordinate system labels. 9
Figure 1.7: Contours of normalized poloidal flux ψ_N for an example DIII-D shot. 10
Figure 1.8: Comparison of T_e and n_e between L-mode (light blue) and H-mode (red). 13
Figure 1.9: Periodic spikes in D_α emission and drops in pedestal pressure and stored energy during Type-I ELMing H-mode. 14
Figure 1.10: The Pedestal: profile of electron pressure 15
Figure 1.11: E_r before and after an L-H transition and later in H-mode. . . 18
Figure 1.12: Phenomenology of the H-mode termination phase 22

Figure 2.1: A pre-upgrade, under-resolved profile of electron density 28
Figure 2.2: Simple diagram of Thomson scattering. 29
Figure 2.3: Example spectral density function S 30
Figure 2.4: TS laser paths and viewchord center lines. 31
Figure 2.5: Model of a set of collection optics for Thomson scattering. . . . 32
Figure 2.6: Polychromator physical layout. 33
Figure 2.7: Example filter set. 34
Figure 2.8: Schematic of the TS hardware subtraction circuit. 35
Figure 2.9: Look-up table values for an example polychromator 36
Figure 2.10: Variation of the scattered spectral density vs. $1 - \lambda/\lambda_0$ 37
Figure 2.11: Diagram showing the instrument function of a typical scattering volume. 42
Figure 2.12: Diminishing returns for scattering length reduction. 43
Figure 2.13: Placement of a possible TS system at the midplane 45
Figure 2.14: Model showing terminators of fiber optic bundles 46
Figure 2.15: Example TS filter sets. 47
Figure 2.16: Variation in temperature accuracy with temperature 49
Figure 2.17: Post-upgrade example profile of electron temperature 54
Figure 2.18: Post-upgrade example profile of electron density 55
Figure 2.19: Cartoon explaining bunch mode 58
Figure 2.20: Sequential profiles of T_e and n_e during a disruption. 59
Figure 2.21: Demonstration of the weighted average of profiles interpolated to a common base technique 64

Figure 2.22: Difference of Gaussian edge detection scheme. 66
Figure 2.23: Contour of TS electron temperature during RMP ELM suppression 71
Figure 2.24: Comparison of RMP ELM suppressed and non-suppressed profiles. 73
Figure 2.25: Plan view of neutral beam injection locations on DIII-D. 76
Figure 2.26: Positions of the centers of imaging volumes for CER chords . . 77
Figure 2.27: Example of a square BES configuration 78
Figure 2.28: Arrangement of probes for measuring changes in magnetic field 80

Figure 3.1: Schematic of an interchange instability. 91
Figure 3.2: Schematic of a ballooning mode. 95
Figure 3.3: Helical kink displacement in a periodic plasma column. 97
Figure 3.4: Illustration of the destabilizing effect of the dJ_ϕ/dr 98
Figure 3.5: Example structure of an $n = 5$ P-B mode. 100
Figure 3.6: P-B Stability diagram in $p' - J$ space. 101

Figure 4.1: `EFIT` equilibrium reconstruction of shot 154749 at 4400 ms. . . 115
Figure 4.2: Evolution of a plasma leading up to an H-L back transition. . . 117
Figure 4.3: Relaxation of the pedestal as a result of the candidate event at the beginning of the back transition sequence. 118
Figure 4.4: Time trace of D_α emission at the outer strike point shaded to show the data selection windows for a set of `ELITE` runs. 122
Figure 4.5: Stability diagram for the plasma in ELM-free operation shortly after the completion of the L-H transition sequence. 123
Figure 4.6: Stability diagram for 80-99% of the ELM cycle 124
Figure 4.7: Pre-H-L back transition stability diagram. 125
Figure 4.8: Pre-H-L back transition stability diagram, showing the distribution of test points in the $p' - J$ perturbation scan. 126
Figure 4.9: Overlay of the boundaries and operating points from figures 4.5-4.7. 127
Figure 4.10: Overlay of the boundaries of several mode numbers 128
Figure 4.11: Variation of upper triangularity. 129
Figure 4.12: Setup of a typical shot 130
Figure 4.13: Pressure gradients vs. upper triangularity. 132
Figure 4.14: Changes in electron temperature profile from Thomson scattering before and after a typical type-I ELM (left) and a back transition transient (right) 134

Figure 5.1: Neutral beam injected torque vs. time for producing two classes of back transitions. 143
Figure 5.2: History of H-mode from the conclusion of the L-H transition sequence until the beginning of the H-L sequence. 145
Figure 5.3: History of H-mode for a shot with low-power steady NBI providing BES measurements. 146

Figure 5.4: E_r and shear profiles. 150
Figure 5.5: Method of calculating decorrelation rate ω_T from BES data. . . 151
Figure 5.6: $\omega_{E\times B}$ and ω_T comparison for the termination phase of an H-mode with a hard H-L transition. 153
Figure 5.7: $\omega_{E\times B}$ and ω_T comparison for the termination phase of an H-mode with a soft H-L transition. 154
Figure 5.8: (a) Electron pressure gradient, (b) radial electric field, and (c) $E \times B$ shear evolution up to and during H-L transition sequence. 155
Figure 5.9: Spectrograms of a BES chord aimed at the steep gradient region, measuring fast density fluctuations 157
Figure 5.10: 1 MS/s, AC coupled BES signal measuring short timescale density fluctuations 158
Figure 5.11: Contours of BES $\tilde{I}/I \propto \tilde{n}/n$ 159
Figure 5.12: Time histories of (a) amplitude ($\tilde{n}/n$), (b) frequency, (c) wavenumber, (d) propagation velocity, and (e) D_α 161
Figure 5.13: Phase relationship between (a) MPM amplitude and (b) propagation velocity. 162
Figure 5.14: Dispersion plot: histograms of k, f 163
Figure 5.15: Comparison of spatial localization of (a) density fluctuations with $40 \leq f \leq 80$ kHz measured by BES to (b) electron temperature, (c) density, and (d) pressure gradient measured by Thomson scattering 165
Figure 5.16: Spectrograms of line averaged density measurements by the CO_2 interferometer. 166
Figure 5.17: Localization to the low field side by using the interferometer. . 167
Figure 5.18: Effect of the MPM on transport. 168
Figure 5.19: Analysis shown in figure 5.18 repeated for a column of chords closer to the separatrix. 169
Figure 5.20: Demonstration that the lag in propagation velocity on outboard chords relative to the location of peak amplitude is consistent with the delay in D_α emission. 170
Figure 5.21: Comparison of H-L back transitions out of ECH and NBI powered H-modes. 173
Figure 5.22: H-L Back transition sequences following NBI powered H-modes were "soft" if a correctly timed increase in upper triangularity was added 174
Figure 5.23: Change in boundary from 2500 ms (red) to 2900 ms (blue) . . . 175
Figure 5.24: Control of the transient associated with H-L transition sequences by varying torque injection 176
Figure 5.25: Electron profiles from Thomson scattering before the first v_p locking events 177
Figure 5.26: Carbon ion rotation profiles from CER with BES fluctuation power for reference 179

Figure 5.27: Effects of the intial event of H-L sequences vs. edge toroidal rotation. 180
Figure 5.28: Evolution of density fluctuation amplitude and resistivity prior to the start of an H-L transition. 183

Figure A.1: Time delayed cross correlation functions 192
Figure A.2: Correction of the time delay cross correlation function. 195

LIST OF TABLES

Table 4.1: Typical shot parameters 114

ACKNOWLEDGEMENTS

I would like to thank my advisor, Professor George Tynan, for connecting me to an opportunity to work in fusion, for providing sound scientific advice, and for consistently finding clear and elegant prose for expressing complicated concepts. His guidance has been very valuable. I am also extremely grateful for support and inspiration from my mentors at DIII-D, Dr. Réjean Boivin and Dr. Richard Groebner. Dr. Boivin provided excellent direction, especially with respect to my diagnostic work. Dr. Groebner was always available with constructive feedback, encouragement, and extremely clear explanations on a wide range of topics.

Dr. Lothar Schmitz worked closely with me in planning and executing my experiments, offered clear explanations of plasma turbulence and microwave diagnostics, and contributed to several papers and presentations. I am very thankful for his support.

I am very grateful to Professor Egemen Kolemen and Dr. Raffi Nazikian for their support and encouragement.

I am grateful to Drs. Phil Snyder and Alan Turnbull for their guidance with running MHD stability calculations and for providing clear explanations of MHD theory in general.

Specialized analysis software written or maintained by Drs. George McKee, Tom Osborne, Terry Rhodes, Phil Snyder, Professor Howard Wilson, Mr. David Kaplan and Mrs. Caizhen Liu was essential to this work and I am thankful to have been able to use it (often with instruction from the authors).

Input from Drs. Kieth Burrell, Punit Gohil, Schmitz, Snyder, and Professor Tynan was key to planning aspects of the experiments such as parameter scans.

Drs. Bruce Bray, Burrell, Colin Chrystal, Groebner, McKee, Adam McLean, Rhodes, and Zheng Yan operated key diagnostics during my experiments, helped interpret their output, and contributed to the planning process by explaining diagnostic abilities and limitations. Drs. Josh King and Morgan Shafer also helped by explaining abilities and limitations of important diagnostics.

Thanks to UCSD physics graduate coordinator Mrs. Hilari Ford and Mrs. Lupe Cerda at GA for all their help, and to the GA publications department,

especially Mrs. Woodie Jarrett and Mrs. Karla Bakos.

Drs. Bray, Boivin, Groebner, Tony Leonard, Tom Carlstrom, Osborne, and Snyder helped develop requirements for and plan the high resolution Thomson scattering upgrade. Mr. James Kulchar and Mr. David Ayala provided indispensable help in upgrading and maintaining hardware for the Thomson scattering diagnostic (and several other DIII-D systems). A much needed overhaul of the Thomson scattering calibration procedures was made possible by the efforts of Drs. Carlstrom and McLean with support from Mr. Matt Watkins and Mrs. Liu.

These experiments were supported by the DIII-D operations group, including many hardworking and talented scientists, engineers, and technicians. In particular, Dr. Tim Scoville and Joe Rauch helped plan neutral beam power changes, Dr. Mirela Cengher helped plan electron cyclotron heating usage, and chief operators Dr. Peter Taylor, Dr. Rick Lee, and Chris Chrobak and physics operators Dr. Robert La Haye, Dr. Osborne, and Dr. Robert Pinkser helped direct operations.

Thanks to Dr. Chrystal for sharing his experience with preparing and formatting the dissertation.

Finally, I am very grateful for support from my family.

Chapter 2 contains material from Review of Scientific Instruments vol. 83. Eldon, David; Bray, Bruce D.; Deterly, Timothy M.; Liu, Caizhen; Watkins, Matthias; Groebner, Richard J.; Leonard, Anthony W.; Osborne, Thomas H.; Snyder, Philip B.; Boivin, Réjean L.; Tynan, George R., American Institute of Physics, 2012. The dissertation author was the primary investigator and author of this paper.

Chapter 2 contains material which has been submitted for publication in Physics of Plasmas. Eldon, David; Boivin, Réjean L.; Chrystal, Colin ; Groebner, Richard J.; McKee, George R. ; Schmitz, Lothar; Tynan, George R. ; Yan, Zheng ; Boedo, Jose A.; Burrell, Keith H.; King, Josh D. ; Kolemen, Egemen; Muscatello, Chris ; Osborne, Thomas H. ; Snyder, Philip B., American Institute of Physics, 2015. The disseration author was the primary investigator and author of this paper.

Chapter 3 contains material from Physics of Plasmas vol. 22. Eldon, David; Boivin, Réjean L.; Groebner, Richard J.; Osborne, Thomas H.; Snyder, Philip B.; Turnbull, Alan D.; Tynan, George R.; Boedo, Jose A.; Burrell, Keith H.; Kolemen, Egemen; Schmitz, Lothar; Wilson, Howard R., American Institute of Physics, 2015. The disseration author was the primary investigator and author of this paper.

Chapter 4 contains material from Physics of Plasmas vol. 22. Eldon, David; Boivin, Réjean L.; Groebner, Richard J.; Osborne, Thomas H.; Snyder, Philip B.; Turnbull, Alan D.; Tynan, George R.; Boedo, Jose A.; Burrell, Keith H.; Kolemen, Egemen; Schmitz, Lothar; Wilson, Howard R., American Institute of Physics, 2015. The disseration author was the primary investigator and author of this paper.

Chapter 5 contains material which has been submitted for publication in Physics of Plasmas. Eldon, David; Boivin, Réjean L.; Chrystal, Colin ; Groebner, Richard J.; McKee, George R. ; Schmitz, Lothar; Tynan, George R. ; Yan, Zheng ; Boedo, Jose A.; Burrell, Keith H.; King, Josh D. ; Kolemen, Egemen; Muscatello, Chris ; Osborne, Thomas H. ; Snyder, Philip B., American Institute of Physics, 2015. The disseration author was the primary investigator and author of this paper.

This material is based upon work supported in part by the U.S. Department of Energy, Office of Science, Office of Fusion Energy Sciences, using the DIII-D National Fusion Facility, a DOE Office of Science user facility, under Award Nos. DE-FC02-04ER54698, DE-FG02-07ER54917, DE-AC02-09CH11466, and DE-FG02-08ER54984

VITA

2007	B.S. in Physics *cum laude*, University of California, San Diego
2007-2009	Teaching Assistant, University of California, San Diego
2009	M.S. in Physics, University of California, San Diego
2009-2014	Graduate Student Research Assistant, Based at DIII-D at General Atomics
2013	C.Phil in Physics, University of California, San Diego
2015-2015	Senior Research Assistant, Princeton University, based at DIII-D
2015	Ph.D. in Physics, University of California, San Diego
2015-	Postdoctoral Research Assistant, Princeton University, based at DIII-D

PUBLICATIONS

D. Eldon, R.L. Boivin, C. Chrystal, R.J Groebner, G.R. McKee, L. Schmitz, G.R. Tynan, Z. Yan, J.A. Boedo, K.H. Burrell, J.D. King, E. Kolemen, C. Muscatello, T.H. Osborne, and P.B. Snyder, "Evolution of E×B shear and coherent fluctuations prior to H-L transitions in DIII-D and control strategies for H-L transitions", manuscript **submitted** to Phys. Plasmas (2015)

D. Eldon, R.L. Boivin, R.J Groebner, T.H. Osborne, P.B. Snyder, A.D. Turnbull, G.R. Tynan, J.A. Boedo, K.H. Burrell, E. Kolemen, L. Schmitz, and H.R. Wilson, "Investigation of peeling-ballooning stability prior to transient outbursts accompanying transitions out of H-mode in DIII-D", Phys. Plasmas **22**, 052109 (2015)

D. Eldon, B. D. Bray, T. M. Deterly, C. Liu, M. Watkins, R. J. Groebner, A. W. Leonard, T. H. Osborne, P. B. Snyder, R. L. Boivin, and G. R. Tynan, "Initial results of the high resolution edge Thomson scattering upgrade at DIII-D", Rev. Sci. Instrum. **83**, 10E343 (2012).

D. Eldon, A. G. McLean, T. N. Carlstrom, C. Liu, M. Watkins, B. D. Bray, E. Kolemen, R. J. Groebner, T. H. Osborne, P. B. Snyder, R. L. Boivin, and G. R. Tynan. "Maintaining, upgrading, and expanding the role of Thomson scattering at DIII-D", **Invited talk** presented at the 16th international symposium on Laser-Aided Plasma Diagnostics in Madison, WI (2013).

R. Nazikian, C. Paz-Soldan, J. deGrassie, **D. Eldon**, T. E. Evans, N. M. Ferraro, B. A. Grierson, R. J. Groebner, S. Haskey, J. D. King, N. Logan, G. R. McKee, R. A. Moyer, M. Okabayashi, D. M. Orlov, T. H. Osborne, J.-K. Park, T. L. Rhodes, M. W. Shaefer, S. P. Smith, P. B. Snyder, E. J. Strait, and M. R. Wade, "Pedestal bifurcations and resonant field penetration near the threshold of ELM suppression in the DIII-D tokamak", Phys. Rev. Lett. **114**, 105002 (2015)

P. C. Stangeby, J. M. Canik, J. D. Elder, C. J. Lasnier, A. W. Leonard, **D. Eldon**, M. A. Makowski, T. H. Osborne, B. A. Grierson, "Identifying the location of the OMP Separatrix in DIII-D using power accounting", Nucl. Fusion **55**, 093014 (2015)

A. M. Garofalo, K. H. Burrell, **D. Eldon**, B. A. Grierson, J. M. Hanson, C. Holland, G. T. A. Huijsmans, F. Liu, A. Loarte, O. Meneghini, T. H. Osborne, C. Paz-Soldan, S. P. Smith, P. B. Snyder, W. M. Solomon, A. D. Turnbull, L. Zeng, "The quiescent H-mode regime for high performance edge localized mode-stable operation in future burning plasmas", Phys. Plasmas **22**, 056116 (2015)

A. G. McLean, A. W. Leonard, M. A. Makowski, M. Groth, S. L. Allen, J. A. Boedo, B. D. Bray, A. R. Briesmeister, T. N. Carlstrom, **D. Eldon**, M. E. Fenstermacher, D. N. Hill, C. J. Lasnier, C. Liu, T. H. Osborne, T. W. Petrie, V. A. Soukhanovskii, P. C. Stangeby, C. Tsui, E. A. Unterberg, J. G. Watkins, "Electron pressure balance in the SOL through the transition to detachment", J. Nucl. Mater. **463**, 533 (2015)

D. M. Orlov, R. A. Moyer, T. E. Evans, A. Wingen, R. J. Buttery, N. M. Ferraro, B. A. Grierson, **D. Eldon**, J. G. Watkins, and R. Nazikian, "Comparison of the numerical modelling and experimental measurements of DIII-D separatrix displacements during H-modes with resomant magnetic perturbations", Nucl. Fusion **54**, 093008 (2014)

R. J. Groebner, C. S. Chang, J. W. Hughes, R. Maingi, P. B. Snyder, X. Q. Xu, J. A. Boedo, D. P. Boyle, J. D. Callen, J. M. Canik, I. Cziegler, E. M. Davis, A. Diallo, P. H. Diamond, J. D. Elder, **D. P. Eldon**, D. R. Ernst, D. P. Fulton, M. Landerman, A. W. Leonard, J. D. Lore, T. H. Osborne, A. Y. Pankin, S. E. Parker, T. L. Rhodes, S. P. Smith, A. C. Sontag, W. M. Stacey, J. Walk, W. Wan, E. H.-J. Wang, J. G. Watkins, A. E. White, D. G. Whyte, Z. Yan, E. A. Belli, B. D. Bray, J. Candy, R. M. Churchill, T. M. Deterly, E. J. Doyle, M. E. Fenstermacher, N. M. Ferraro, A. E. Hubbard, I. Joseph, J. E. Kinsey, B. LaBombard, C. J. Lasnier, Z. Lin, B. L. Lipshultz, C. Liu, Y. Ma, G. R. McKee, D. M. Ponce, J. C. Rost, L. Schmitz, G. M. Staebler, L. E. Sugiyama, J. L. Terry, M. V. Umansky, R. E. Waltz, S. M. Wolfe, L. Zeng, and S. J. Zweben, "Improved understanding of physics process in pedestal structure, leading to improved predictive capability for ITER", Nucl. Fusion **53**, 093024 (2013).

S. P. Smith, J. D. Callen, R. J. Groebner, T. H. Osborne, A. W. Leonard, **D. Eldon**, B. D. Bray, and the DIII-D Team, "Comparisons of paleoclassical based pedestal model predictions of electron quantities to measured DIII-D H-mode profiles", Nucl. Fusion **52**, 114016 (2012).

D. M. Ponce-Marquez, B. D. Bray, T. M. Deterly, C. Liu, and **D. Eldon**, "Thomson scattering diagnostic upgrade on DIII-D", Rev. Sci. Instrum. **81**, 10D525 (2010).

ABSTRACT OF THE DISSERTATION

Transitions Out of High-Confinement Mode to Lower Confinement Regimes in Tokamaks

by

David Eldon

Doctor of Philosophy in Physics

University of California, San Diego, 2015

George Tynan, Chair
Patrick Diamond, Co-Chair

A high-resolution edge Thomson Scattering (TS) system was developed and installed on the DIII-D tokamak, and was then used to study the back transition from High Confinement (H-mode) to Low Confinement (L-mode) in DIII-D. The transient event seen to initiate some back transition sequences is superficially similar to a large type-I ELM, which is described by the linear ideal MHD theory of peeling-ballooning modes. Detailed edge pedestal profile evolution studies during the back transition show that the plasma does not exceed this linear stability limit during the back transition, indicating that the transient is not a type-I ELM event. The $E \times B$ shearing rate $\omega_{E\times B}$ and turbulence decorrelation rate ω_T were

then compared before the H-L sequence. The results show that the back transition sequence begins while $\omega_{E\times B}$ is still well above ω_T, indicating that the sequences observed in these experiments are not triggered by the collapse of the $E \times B$ shear layer. Further investigation is made to characterize a coherent density fluctuation whose behavior is linked to back transition sequences. Strategies for avoiding the transient are tested and a reliable method for producing a "soft" back transition is identified. Such cases are compared to the class of "hard" transitions in which the pedestal pressure gradient rapidly relaxes.

1 Introduction

1.1 Nuclear Fusion for Energy Production

Nuclear fusion has the potential to provide a clean, safe, and abundant source of energy. No smog, CO_2 or long-lived radioactive waste is produced. Fusion is passively safe; no meltdowns or runaway reactions can escape the reactor. The deuterium-tritium fuel cycle relies on two isotopes of hydrogen, one of which is inexhaustible and the other may be produced from lithium, which is abundant. Fusion reactors do not depend on availability of geographic features and could be built anywhere. The energy density of the fuel is much higher than for any other technology, which would make fuel distribution easy and support the ability to place a fusion power plant anywhere in the world. For these reasons, nuclear fusion is extremely attractive as a potential source of energy. Research is ongoing all over the world.

Facilitating a nuclear fusion reaction requires imparting enough kinetic energy to atomic nuclei in the fuel such that they can overcome the coulomb barrier and fuse, and confining the fuel so that other nuclei are available to fuse with. There are three known ways to accomplish this: gravitational confinement, inertial confinement, and magnetic confinement. In gravitational confinement, the mass of a star creates enough pressure to confine a plasma so that fusion may take place, and heat is provided initially by gravitational collapse and later by ongoing fusion. This strategy is obviously unavailable for terrestrial power production. The goal of inertial confinement is for fusion to take place before a sample of fuel can expand and dilute as it is pushed outward by internal pressure; the source of "confinement" is that the fuel can't run away fast enough. This can be accomplished

by blasting a fuel pellet with extremely high powered lasers, which heat the fuel and induce fusion as the pellet explodes. Magnetic confinement uses a magnetic field to confine plasma and will be described in more detail below.

The primary fuel cycle currently being developed by both inertial and magnetic confinement strategies combines deuterium and tritium to produce helium and a neutron: ${}_1\mathrm{D}^2 +_1 \mathrm{T}^3 \rightarrow_2 \mathrm{He}^4 +_0 \mathrm{n}^1$. The cross section for this reaction peaks near 100 keV, or about 10^9 K.[2] Other fuel cycles have the disadvantage that they peak at higher temperatures and have lower cross sections, but these may be worth exploring once economical D-T fusion is achieved. The products of the ${}_1\mathrm{D}^2 +_2 \mathrm{He}^3 \rightarrow_2 \mathrm{He}^4 +_1 \mathrm{H}^1$ reaction, for example, are all charged particles which can be controlled by the magnetic field, rather than escaping like the neutron in D-T fusion.

1.2 Magnetic Confinement

The pressure exerted by a magnetic field B is $B^2/2\mu_0$, which is many times atmospheric pressure for typical field strengths in modern tokamaks, which are on the order of a few Tesla. This magnetic pressure acts like a "bottle" for the plasma, keeping it confined, pressurized, and away from the physical walls of the device. Large scale contact between the plasma and solid components of the reactor is deleterious as the plasma will be rapidly cooled and thus unable to fuse and the solid walls are prone to ablation, melting, or other wear and damage.

The charged particles which make up the plasma are deflected by magnetic fields according to the Lorentz force: $F = q\vec{v} \times \vec{B}$, where q is the particle's charge and $\vec{v}$ its velocity. The trajectory of a charged particle under the influence of a magnetic field is shown in figure 1.1. To lowest order, the particle is constrained to make close spirals around the field line. Its average position moves along the field like a bead on a wire. This average position through the center of the spiral is called the guiding center.

Several types of magnetic confinement devices have been invented. For example, a mirror machine consists of a long cylindrical plasma (somewhat similar

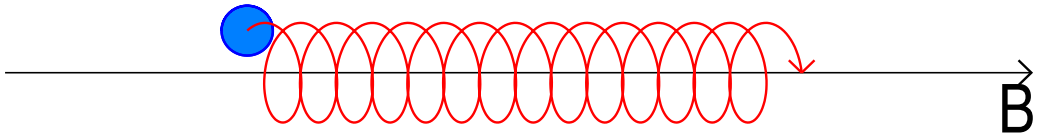

Figure 1.1: Magnetic confinement. A charged particle (blue) follows a spiral orbit (red) around a magnetic field line (black). The average position of the particle over time traces a path through the center of the spiral.

to figure 1.1 but with many particles) capped at both ends by magnetic "mirrors": regions of higher field strength which reflect trapped particles back towards the center of the cylinder. Other examples include the tokamak and the stellarator.

In all of these configurations, energy enters the plasma by ohmic heating, auxiliary heating such as neutral beam injection, or nuclear fusion reactions. However, magnetic confinement is not perfect and energy and particles flow out of the field by various drifts, collisional diffusion, or turbulence. As energy escapes from confinement, it flows to the solid walls of the machine. Higher outflow of energy requires higher input energy to maintain temperature and also the solid walls of the reactor must be able to tolerate the heat load.

1.3 Tokamaks

A tokamak[3] is a magnetic confinement device (Figs. 1.2-1.7). In a tokamak, a primary toroidal field around the central axis is produced by external coils, and a poloidal field is produced by plasma current around the axis. The combined field counteracts many plasma drifts, but leakage still occurs due to diffusion and turbulence. Any given field line within the tokamak either intersects a solid wall within the device (open field line) or loops around the central pillar continuously (closed field line). Plasma pressure is generally much higher on the closed field lines than on the open ones, so the boundary between open and closed lines is taken to be the edge of the plasma.

Mirror machines,[4] as mentioned earlier, are simple and confine plasma well in two directions. A mirror machine is simply a long, cylindrical solenoid with a

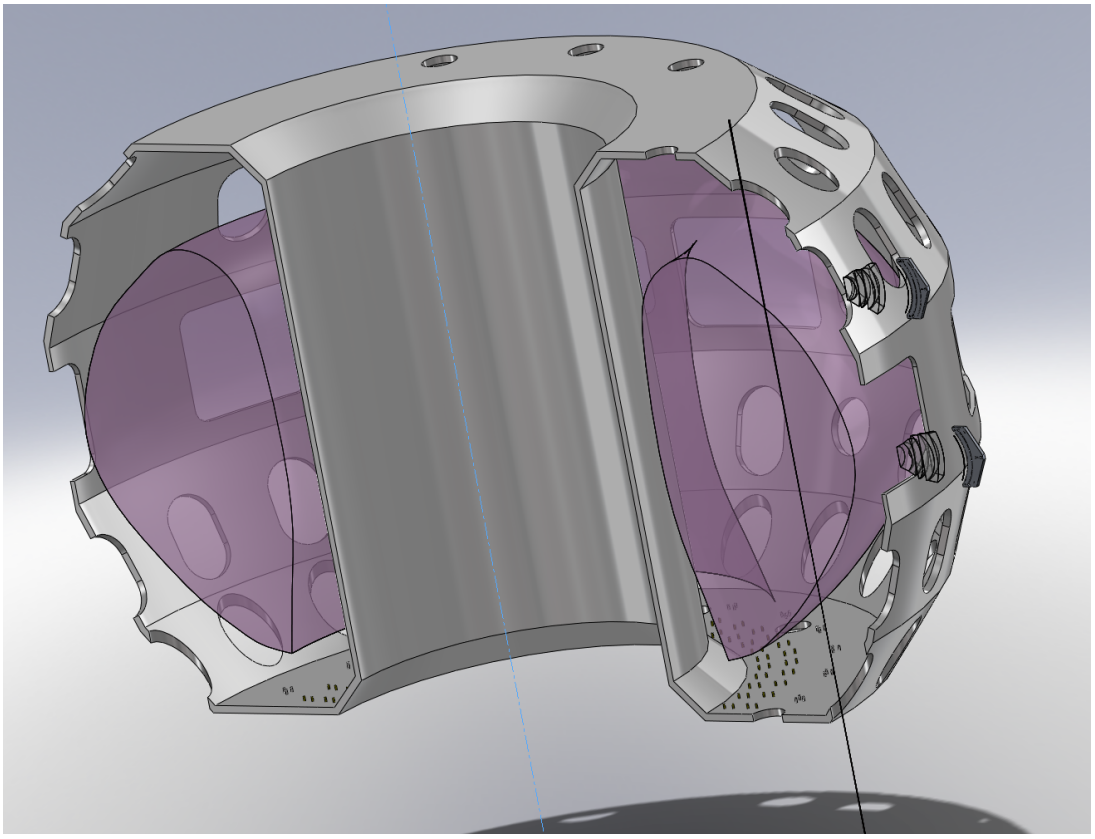

Figure 1.2: Cutaway view of the DIII-D vacuum vessel and an example plasma. Heating, diagnostic, and other equipment is installed in the ports, which are shown open. Carbon tiles (not shown) are mounted inside the vessel. Hardware related to the Thomson scattering diagnostic (relevant to later chapters) is visible outside the vessel on the right side. The black line near this equipment is the path taken by the lasers used by Thomson scattering.

magnetic field running along its axis. The axial field prevents plasma from escaping outward from the axis. Capping the ends, however, is quite challenging. To avoid this challenge, the cylinder may be bent around into a ring or torus. Doing so, however, introduces a gradient in the magnetic field, which is stronger toward the center of the torus. As the radius of gyration of charged particles in a magnetic field depends on the field strength, the orbits become wider on one side than the other, and so the center of the orbit drifts over time as seen in the left side of figure 1.3. If the field were somehow constructed to curve with no radial variation in magnitude, there would still be a drift due to the centrifugal force experienced

by a particle following the curved field line. Drifts are easily computed from the equation of motion for a single particle:

$$m\frac{d\vec{v}}{dt} = q(\vec{E} + \vec{v} \times \vec{B}) \tag{1.1}$$

where m is mass and $\vec{E}$ is electric field. A gradient in magnetic field strength (with no change in field direction and no electric field) causes the guiding center of the particle's orbit to drift with constant velocity $\vec{v}_{\nabla B}$ given by

$$\vec{v}_{\nabla B} = \frac{1}{2}\frac{mv_{\perp}^2}{qB}\frac{\vec{B} \times \vec{\nabla} B}{B^2} \tag{1.2}$$

and the drift velocity in a curved magnetic field in a vacuum where gradients in the field are purely due to curvature (that is, including drifts due to both centrifugal force and variation in field strength) is given by

$$\vec{v}_{curved} = \frac{m}{q}\left(v_{\parallel}^2 + \frac{1}{2}v_{\perp}^2\right)\frac{\vec{R}_c \times \vec{B}}{R_c^2 B^2} \tag{1.3}$$

where the $\parallel$ and $\perp$ subscripts refer to velocity components parallel and perpendicular to the local magnetic field B and $\vec{R}_c$ is the radius of curvature, directed out from the center of curvature (in this case the axis of the machine).

It can be seen in equation 1.3 that ions and electrons experience gradient drifts in opposite directions. The separation of charges results in an electric field. This electric field drift carries plasma to larger radius and out of the confinement system. The drift velocity produced by uniform E and B fields is

$$\vec{v}_E = \vec{E} \times \vec{B}/B^2 \tag{1.4}$$

The v_E and $v_{\nabla B}$ drifts are explained in figure 1.3. Figure 1.4 shows how they conspire to allow the plasma to escape a simple toroidal confinement scheme.

To correct for the drifts associated with curving the magnetic field, a stellarator[5] twists the torus around its axis so that the gradient drift changes direction and averages out to zero as a particle travels around the device. Early stellarator designs were in the shape of a figure 8: two half toroids connected with straight sections. In a tokamak, current is driven through the ring of plasma. The component of magnetic field generated by this current adds a twist to the total field,

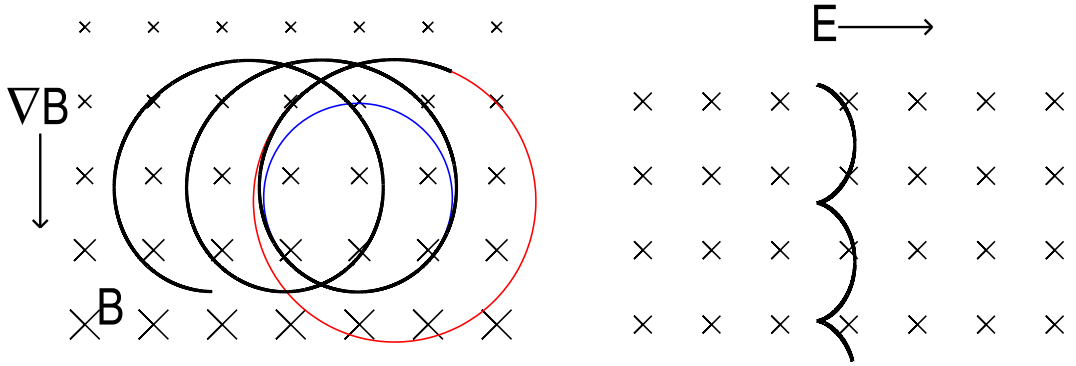

Figure 1.3: Illustration of drifts due to magnetic field gradients and electric fields. Left: A magnetic field B is directed into the page with varying strength as shown by the size of the "X"s (gradient in field strength points down). As a particle following the black curve moves into the region of higher field, its orbit contracts to the radius of the blue circle. As the particle travels back out into the region of lower field, its radius of gyration increases until it reaches the radius shown by the large red circle. Thus, when moving to one side, the radius is small, and the radius large when moving to the other side, and so the particle drifts perpendicular to the gradient of the field. Right: a particle is attracted by the electric field E and gains velocity perpendicular to B. The $v \times B$ force deflects the particle such that it follows a cycloid curve (thick black line).

as seen in figure 1.5. Particles experience drifts in different directions as they follow the twisted field: a particle experiencing an upward gradient drift would move away from the magnetic axis while at the top of the plasma, but would drift back toward the axis when it came to the bottom of the plasma as it followed the field. The poloidal components of the magnetic field also short out the electric field which would arise from charge separation. Particles can easily travel parallel to the magnetic field and the addition of a poloidal component to the field creates a parallel path for a return current (called the Pfirsch Sclüter current), preventing charge accumulation due to the ∇B drifts.[6]

1.3.1 Coordinate System

As tokamaks are nominally figures of rotation, cylindrical coordinates are useful for describing them (R, ϕ, Z), especially when dealing with hardware. It is also useful to consider a toroidal system of (r, θ, ϕ), where r is the minor radius,

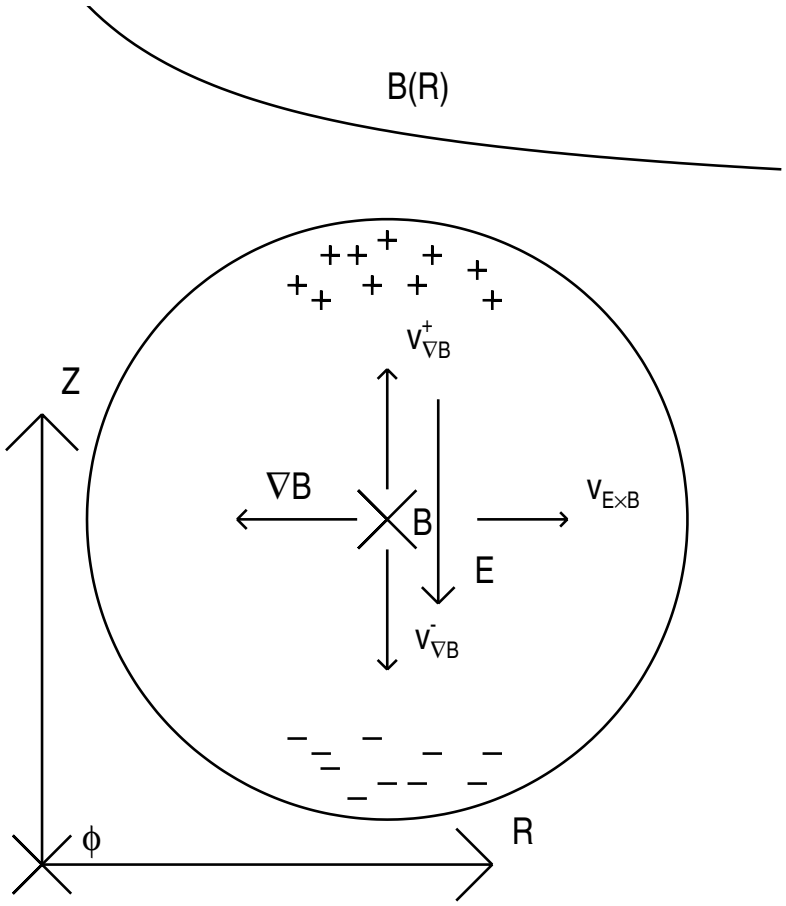

Figure 1.4: Illustration of the combined effects of the gradient drift and the resulting $E \times B$ drift which arise when a linear confinement system is bent into a ring. The cross section of the plasma ring is shown, with the center of curvature to the left. The magnetic field B is directed into the page with strength proportional to $1/R$, the gradient points radially inward, so the gradient drift for positive charges is directed upward, and the drift for negative charges is down. Charge separation produces a vertical electric field E, which causes an $E \times B$ drift outward. Reversing the magnetic field also reverses the electric field and the $E \times B$ drift is still outward.

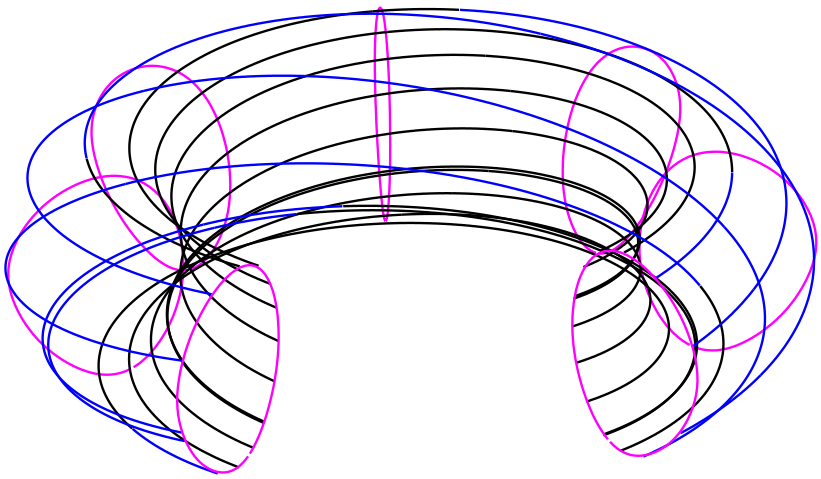

Figure 1.5: Tokamak magnetic configuration. A field line is traced through space for several toroidal orbits. The line is drawn in blue when it is outside of the magnetic axis and in black when it is inside the magnetic axis. As the line pierces the R-Z plane on each successive orbit, the intersection points form a flux surface (magenta).

which is zero at the magnetic axis in the center of the plasma, θ is the poloidal angle, and ϕ is the toroidal angle (See figure 1.6). Note that a left handed toroidal angle is used for labeling hardware in DIII-D:[1,7] it increases going clockwise when viewed from above, with zero at geographic north. The toroidal angle ϕ used for physics is right handed (this definition is shown in figure 1.6). Any use of the left handed toroidal angle when discussing hardware will be clearly marked.

The equilibrium magnetic configuration of a tokamak consists primarily of a toroidal field and a poloidal field. The poloidal component causes the field to twist around the magnetic axis helically as seen in figure 1.5. In this example, a small radial component (in minor radius, r, as distinct from major radius, R)

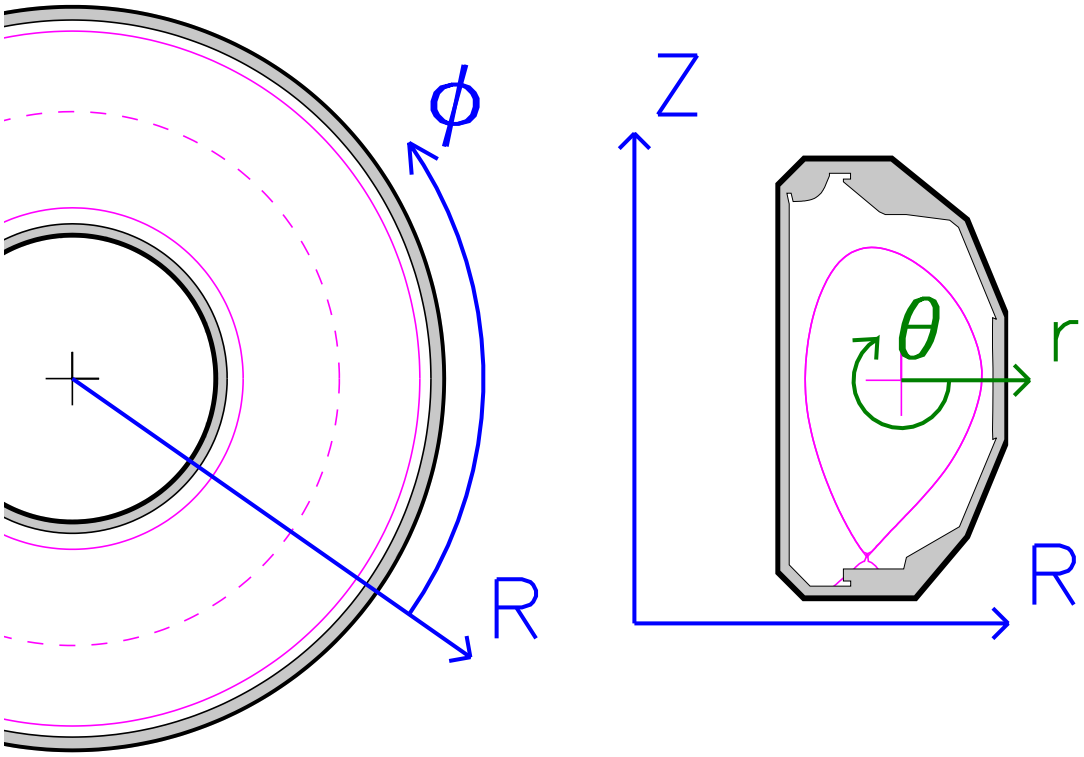

Figure 1.6: DIII-D[1] with standard coordinate system labels. The vacuum vessel is represented by a thick black line, inside of which carbon tiles block off the area shaded in gray. An example plasma boundary curve is drawn in magenta. Useful for hardware description is the cylindrical coordinate system, (R, ϕ, Z). For physics, (r, θ, ϕ) (minor radius, poloidal angle, toroidal angle) is often more convenient. The magnetic axis, where the poloidal field is zero, is marked with a dashed line in the overhead view and a plus in the side cross section view. The drawings are scaled to each other.

alters the boundary shape, which would otherwise be approximately circular at large enough aspect ratio. Figure 1.5 also illustrates the concept of flux surfaces. The magenta curves are on the same flux surface at different toroidal angles. The magnetic configuration of a tokamak consists of nested flux surfaces. As particles are essentially free to move along the magnetic field lines (the sound speed is typically high $\sim 10^5 - 10^6$ m/s),[2] many key parameters are constant on each surface. This allows the minor radius to be replaced with a coordinate which labels flux surfaces. Such a system is the most convenient way to describe the physics. ψ, the poloidal magnetic flux per radian in ϕ is a popular label for flux surfaces. The magnetic field in $R - Z$ is related to ψ by $B_R = -\frac{1}{R}\frac{\partial \psi}{\partial Z}$, $B_Z = \frac{1}{R}\frac{\partial \psi}{\partial R}$.

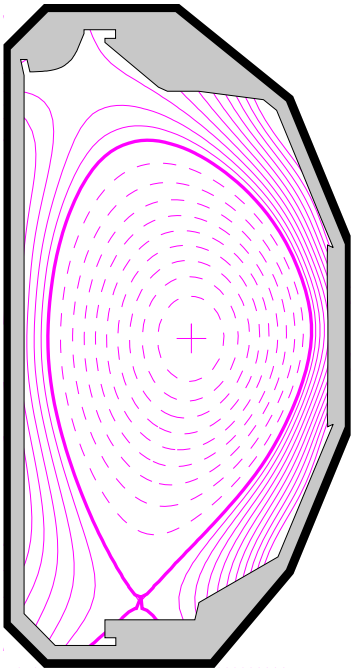

Figure 1.7: Contours of normalized poloidal flux ψ_N for an example DIII-D shot. The magnetic axis ($\psi_N = 0$) is marked with a plus. The separatrix ($\psi_N = 1$) is marked with a thick magenta curve. Closed surfaces within the separatrix are marked with dashed lines at intervals of 0.1 in ψ_N. Open surfaces, which intersect the walls, are marked with solid lines at intervals of 0.05 in ψ_N.

ψ is often normalized such that ψ_N is 0 at the magnetic axis and 1 at the boundary or last closed flux surface (LCFS). An example map of ψ_N contours is shown in figure 1.7. In a diverted plasma as is shown in the example figures, the LCFS is a separatrix. In a limited plasma, it would be the surface tangent to the wall.

DIII-D

DIII-D[1] is a rebuild of the original Doublet 3 tokamak (DIII), using the same toroidal field coils but with a new vacuum vessel. Doublet 3 was designed to generate plasma cross sections with two lobes, one above the other (doublets). In DIII-D, the nominal plasma shape is a "Dee", as reflected by the shape of the new vacuum vessel (Fig. 1.2). The final "D" comes from the shape of the new vacuum vessel and was added to the tokamak's name after the modification. The outer and inner radii of the vacuum vessel interior are 2.43 m and 0.96 m. Typical plasmas

have a major radius (position of magnetic axis) of 1.7 m and minor radius of 0.5 m (DIII-D measurements and data are used in the production of all tokamak figures where appropriate; See figures 1.2, 1.5, 1.6 and 1.7). Toroidal field at 1.67 m can be up to 2.17 T. The magnetic system was originally designed for a maximum plasma current of 5 MA, although operation near 1 MA is typical. DIII-D has immense flexibility for producing plasmas with different shapes, which aids in comparison to other tokamaks.

Heating is accomplished through ohmic heating, neutral beam injection, or electron cyclotron resonance heating. Fueling is by gas puffing, neutral beam injection, or pellet injection. Numerous ports are cut in the vacuum vessel to serve heating, fueling, and diagnostic needs (see Fig. 1.2). The interior of the vessel is lined with graphite tiles, behind which are arrays of magnetic probes[8] which are critical for diagnosis of the magnetic configuration and detection and control of some instabilities. Graphite is chosen because of its resilience to high temperatures and because it is inevitable that some material from the wall will make it into the plasma. Materials with low atomic number like carbon are less problematic as impurities in the plasma than are materials such as iron or nickel.

Neutral beams ionize a fueling gas using an arc discharge in a plasma generating chamber, accelerate the ions electrostatically, neutralize them, and remove any remaining ions magnetically. The remaining stream of neutral particles is directed at the plasma, carrying with it the energy gained through the accelerating voltage. Being neutral, the particles in the beam are unaffected by the magnetic field and cross into the plasma easily. The gas used in the beam is normally the same as the gas being used in the experiment (deuterium into deuterium, for example). Under typical operation, the accelerating voltages are about 75 kV and injected power is about 2 MW from each of eight beam sources. Some sources are conditioned to allow higher power operation up to 93 kV or 3.6 MW. Neutral beam sources may be easily down tuned to 50 kV (lower is possible but there are complications) to produce less than 1 MW, which is useful for operating beam dependent diagnostics with low auxiliary power application.[1]

1.3.2 High Confinment Mode

When the heat flux across the edge of the plasma becomes great enough, a surprising thing happens: confinement suddenly improves.[9] Turbulent transport of particles and heat is suppressed in the edge region and steep gradients in temperature and density form there. The slopes of the temperature and density profiles deeper in the core of the plasma are largely unchanged from the lower confinement regime, so the average pressure essentially increases by the value at the edge. This is called high confinement mode or H-mode, as distinct from low confinement mode or L-mode. Example profiles of electron density and temperature are shown in figure 1.8.

A popular figure of merit for fusion power production is the Lawson criterion: density times temperature times confinement time ($n \times T \times \tau_E$). All of these terms are increased in H-mode, making it a very attractive mode of operation for a fusion reactor. H-mode has been observed in mirror machines, stellarators, and tokamaks.[10]

1.3.3 Edge Localized Modes

There are complications to operation in H-mode. The steep pressure gradient and associated edge current provide a source of free energy to ballooning and peeling modes, respectively.[11–14] In fact, these modes can join together as the coupled peeling-ballooning mode.[14,15] These modes are localized to the edge of the plasma where the steep gradient exists, hence the designation Edge Localized Mode (ELM). When ELMs go unstable, they cause a rapid relaxation of the edge pressure gradient, temporarily reducing temperature and density there. Figure 1.9 shows the results of a series of ELMs: the instability ejects material from the plasma which causes a flash of light at the deuterium Balmer alpha (D_α) line[16] at 656.1 nm [1.9(a)] and reduces the pedestal pressure and total stored energy. Recovery is often swift (in the example in figure 1.9, the period is about 50 ms, but this varies), and ELMs can have the beneficial effect of controlling impurity density. However, the rapid expulsion of heated plasma (could be a few percent of the total stored energy in the plasma, in figure 1.9 the loss is $\approx$ 50 kJ per

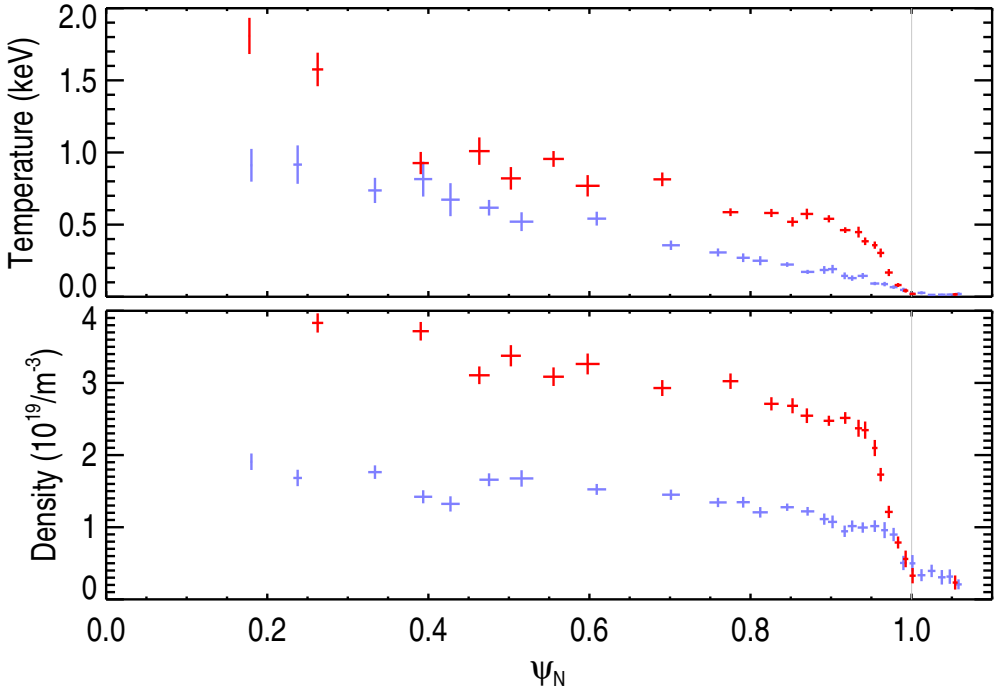

Figure 1.8: Comparison of T_e and n_e between L-mode (light blue) and H-mode (red).

ELM compared to $\approx$ 600 kJ total stored energy) caused by an ELM is a potential problem for future devices. As magnetic confinement configurations get larger, the amount of energy expelled by ELMs is predicted to increase. In a reactor, this would have undesirable effects on the lifetime of plasma facing components.[17–20]

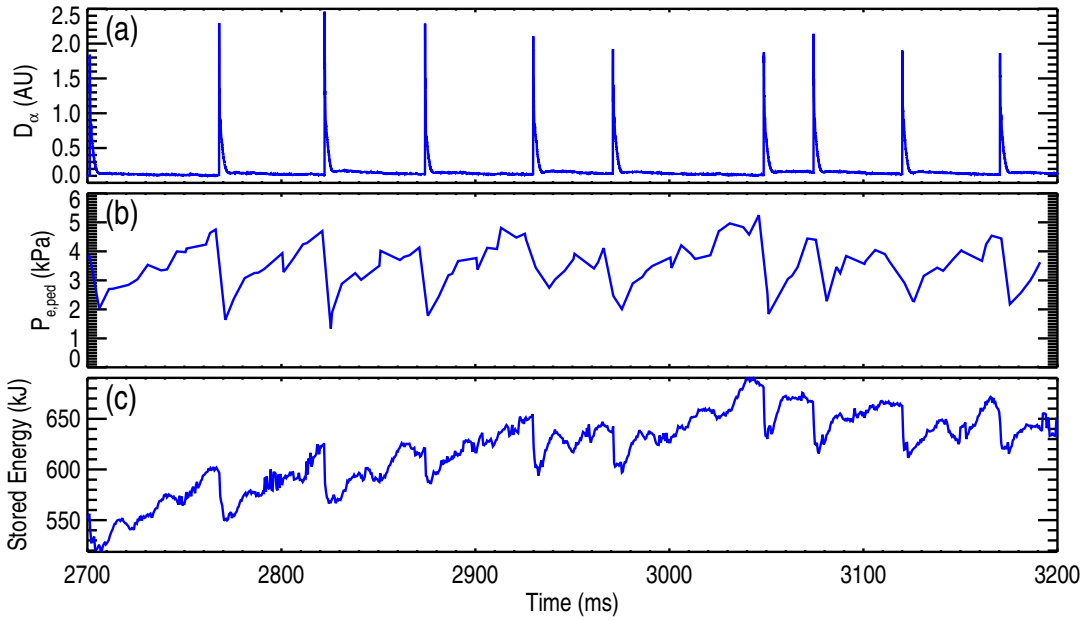

Figure 1.9: Periodic spikes in D_α emission and drops in pedestal pressure and stored energy during Type-I ELMing H-mode. (a) D_α light measured by a photodiode behind a narrow optical bandpass filter aimed at the outer strike point (point of contact between outer separatrix leg and solid limiting surface). (b) electron pressure at the top of the pedestal (usually near $\psi_N \approx 0.95$). (c) Energy stored in the plasma. When an ELM is triggered, material is released from the edge of the plasma, lowering pedestal pressure and stored energy. The escaping material emits D_α light as it escapes and cools.

1.4 Transition Physics

Accessing and sustaining H-mode is important for reactor operation as the increases in average density, temperature, and confinement time are quite significant.[10,21,22] The defining feature of H-mode is a transport barrier at the edge of the plasma, wherein the spatial gradients of temperature and density are much higher than elsewhere, where gradients may be similar to L-mode. The swift increase in these quantities at the edge of the plasma is called the pedestal: the core profile, largely unchanged from L-mode, looks as if it has been lifted up atop a pedestal (see figure 1.10). Models[23] explaining limitations on pedestal height (the value at the top of the pedestal or inner edge of the steep gradient region) are essential for predicting performance of future devices and a portion of this work will describe

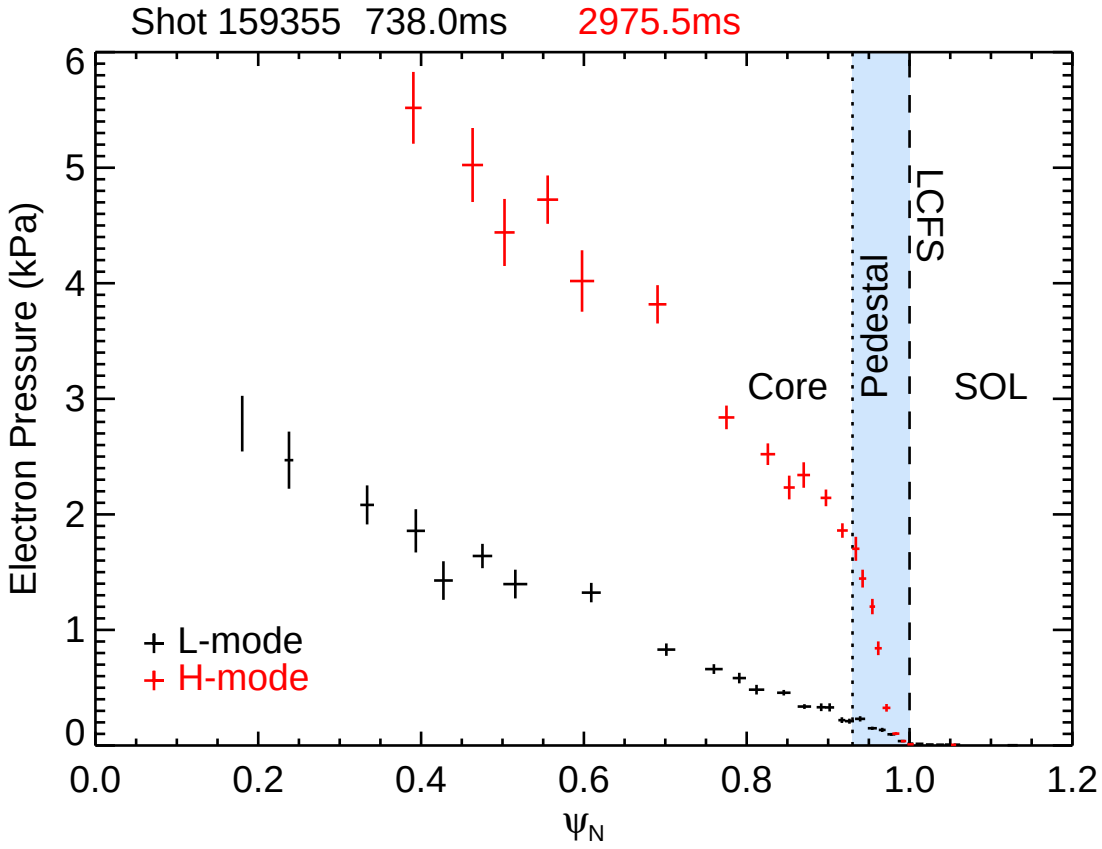

Figure 1.10: The Pedestal: profile of electron pressure vs. radius for L-mode (black) and H-mode (red). The sharp increase in pressure at the edge is called the pedestal. This region is shaded in blue and bounded by dotted and dashed lines. The dashed line is the last closed flux surface (LCFS). It can be seen that for H-mode relative to L-mode, the average pressure inside the plasma is increased roughly by the pedestal amount. Inside of the pedestal is the core plasma and outside is the scrape-off layer (SOL).

diagnostic advances to support such models. The problem of accessing H-mode and the transition from L to H modes is of some interest as it relates to the transition out of H-mode which must occur when a plasma discharge is terminated.

In general, transport of heat and particles is governed in large part by turbulence. The turbulent contribution to total transport keeps pressure gradients throughout most of the plasma well below what would be predicted from neoclassical theory.[24] In the transport barrier, turbulence is suppressed and transport is reduced. This allows for a much steeper than usual pressure gradient, which

contributes to a radial electric field, as seen in the following equations:

$$0 = neZ(\vec{E} + \vec{v} \times \vec{B}) - \vec{\nabla} p \tag{1.5}$$

Equation 1.5 describes an equilibrium where the Lorentz force balances with the pressure gradient, where n is number density, e is the elementary charge, Z is charge state (-1 for electrons), E and B are the electric and magnetic fields, v is velocity, and p is pressure. Equation 1.5 is a single fluid equation and the temperature, density, and mean flow velocity should all be for the same species (electrons, main ions, or a particular species of impurity ions). It may be used for any species as long as n, T, and $\vec{v}$ for that species are known. In practice, these quantities are measured for fully stripped ($Z = +6$ charge state) carbon impurities by CER[25] (diagnostics will be described in chapter 2). Solving equation 1.5 for $\vec{E}$ and taking the radial component[26] gives

$$E_r = \frac{1}{neZ}\frac{\partial p}{\partial r} - v_\theta B_\phi + v_\phi B_\theta \tag{1.6}$$

The electric field causes an $E \times B$ drift:

$$\vec{v}_{E\times B} = \frac{\vec{E} \times \vec{B}}{B^2} \tag{1.7}$$

$$\vec{v}_{E\times B} = \frac{\vec{\nabla} p \times \vec{B}}{neZB^2} + \vec{v}_\perp \tag{1.8}$$

Note that equation 1.8 is equivalent to stating that flow perpendicular to the magnetic field is due to the $E \times B$ drift and the diamagnetic drift $\vec{v}_D$:

$$\begin{aligned} \vec{v}_\perp &= \vec{v}_D + \vec{v}_{E\times B} \\ \vec{v}_D &= -\vec{\nabla} p \times \vec{B}/(neZB^2) \end{aligned} \tag{1.9}$$

As the field is mostly toroidal, the poloidal component of $v_{E\times B}$ is strongest,

$$v_{E\times B,\theta} = -\frac{\partial p}{\partial r}\frac{B_\phi}{neZB^2} + v_\theta \frac{B_\phi^2}{B^2} - v_\phi \frac{B_\theta B_\phi}{B^2} \tag{1.10}$$

And this may be approximated as

$$v_{E\times B,\theta} \approx -\frac{\partial p}{\partial r}\frac{1}{neZB_\phi} + v_\theta - v_\phi \frac{B_\theta}{B_\phi} \tag{1.11}$$

Assuming $B_\phi \gg B_\theta$ and $|B| \simeq |B_\phi|$. Note that the v_ϕ term has been retained despite the presence of the small B_θ/B_ϕ factor as v_ϕ is typically larger than v_θ. B_ϕ is used instead of B as the sign of this factor is important.

If the overall perpendicular flow remains low, which for ions it often does, then increases in the pressure gradient tend to be balanced by an electric field directed radially inward and an associated $E \times B$ drift. It is important to consider the $E \times B$ drift because it is the same for all particles. Electrons may have different flow velocities than ions and different ion species may differ from each other, but all species experience the same contribution to their velocities from $v_{E\times B}$ and there is a tendency for perturbations to be dragged along at this velocity.[27] As the steep pressure gradient is localized to the edge, so is the diamagnetic contribution to the $E \times B$ drift, as seen in the E_r profile shown in figure 1.11. This localization leads to flow shear. Turbulence suppression by radial flow shear is identified as the mechanism for the H-mode transport barrier.[10,26,28–32] One explanation is that the shear decorrelates radially extended features, such as turbulent eddies. Eddies whose radial extent allowed them to transport particles outward are stretched and broken up.[26] This reduces radial turbulent transport and allows a pressure gradient to form. In another interpretation,[33,34] energy is transferred from turbulence into benign fluctuations which do not cause radial transport. Both pictures agree that radial flow shear leads to turbulence suppression.

Clearly, the mechanism thus far described is self-reinforcing. To arrive at this condition, one might attempt to simply dump an enormous amount of power into the plasma, forcing the inventory of particles to accumulate faster than it could leak out, raising the gradient, and initiating the transport barrier. Fortunately, this is unnecessary. The predator prey model[35–38] describes a mechanism by which azimuthally symmetric, radially localized "zonal flows" (ZFs), generated by the turbulence through Reynolds stress,[39,40] act as an intermediary and supply some of the flow shear necessary to achieve turbulence suppression and allow the transport barrier to form at lower input power than would be required by brute force. Recent work[33,34,41–43] has shown this model to be consistent with experiment. This is a very important model as it could support physics based predictions of power

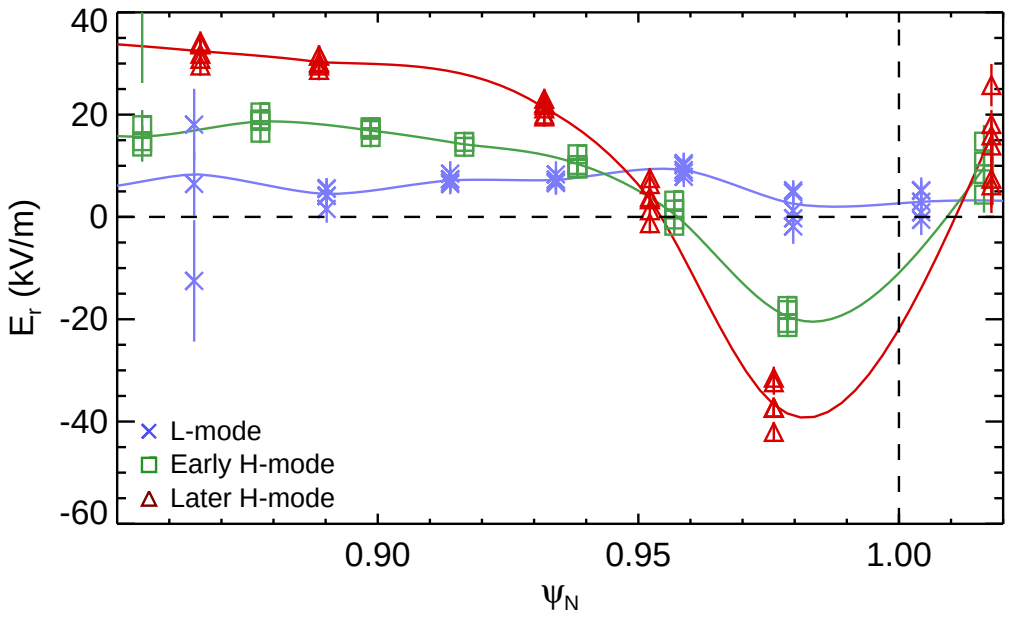

Figure 1.11: E_r before and after an L-H transition and later in H-mode. Calculated with equation 1.6. Blue Xs: L-mode just before the start of a dithering L-H transition sequence. Green squares: H-mode just after the end of the L-H transition. Red triangles: H-mode just before the first type-I ELM. Note the difference in gradient around $\psi_N = 0.97$.

thresholds for transitions into and out of H-mode.

If surplus power flux across the edge is low enough, a period of limit cycle oscillations (LCO) may occur during the transition sequence from L-mode to H-mode. During the LCO, the ZFs rise in amplitude, rob the turbulence of energy and also suppress it through flow shear. With their energy source depleted, the zonal flows decay and turbulence recovers to drive ZFs once again. This cycle will repeat until the equilibrium pressure gradient grows large enough to take over suppression. The time required depends on the amount of power flux across the edge and can be very short, to the point that there is no LCO but only a burst of zonal flows, or so long that H-mode is not reached before the end of the discharge.[37]

1.4.1 Hahm-Burrell Shearing

Hahm and Burrell[10, 26, 29–31] derive a condition for shear suppression, which will be described in more detail in chapter 5, where turbulent transport is significantly reduced when the $E \times B$ shearing rate $\omega_{E\times B}$ is greater than the turbulence decorrelation rate ω_T. Activation of the suppression mechanism is not all-or-nothing and stronger shear tends to result in weaker turbulence. The L-H and H-L transitions should be expected when $\omega_{E\times B} \approx \omega_T$.

$$\omega_{E\times B} = \frac{(RB_\theta)^2}{B}\frac{\partial}{\partial\psi}\left(\frac{E_r}{RB_\theta}\right) \tag{1.12}$$

Turbulence decorrelation in the plasma frame is an estimator for the turbulence growth rate.[28] This is measurable through methods which will be detailed later. So $\omega_{E\times B} > \omega_T$ can be interpreted as a statement that the $E \times B$ shearing rate exceeds the estimated turbulence growth rate and eddies are being torn apart faster than they can grow.

1.5 H-mode Termination

Placing a power source within a confinement system obviously leads to a buildup of stored energy. Should the confinement quality decrease suddenly, the transient power outflow would be quite large; the breaking of a dam comes to mind. Studies of the formation of the H-mode transport barrier indicate that the increase in confinement can be rapid. If the barrier dissipates as quickly as it forms, then plasma facing components in large future tokamaks will be faced with high heat loads which could shorten their lifetime significantly. Observations of transitions from H back to L-mode reveal that there is commonly a sudden drop in pedestal height, so it is indeed the case that part of the barrier can collapse quickly.

In a back transition, total heating power is reduced and the amount of energy stored in the plasma begins to decrease. The outflow of energy from the plasma core maintains heat flux across the edge for a time, preventing an immediate back transition. If no other process intervened, one might expect the shear flow suppression mechanism to weaken (because of decreasing pressure) until tur-

bulence recovered, ushering a return to L-mode. During this time, the recovering turbulence could drive zonal flows and start a LCO during the back transition sequence. This much is observed in practice:[42] after the beginning of back transition activity, a period of LCO is observed when conditions permit (expression of the LCO seems to be sensitive to the shape of the plasma boundary, as it is in the forward L-H transitions).

There are two main classes of H-L back transition sequences which are relevant to this work. "Hard" H-L sequences begin with with a sudden decrease in pedestal height and plasma stored energy which is reminiscent of a large type-I ELM. The transient event which rapidly reduces the pedestal height is fairly easy to spot as a large D_α spike which, in a dithering transition, is followed by smaller D_α spikes. "Soft" H-L sequences lack this initial transient and begin with the smaller D_α spikes and there is no obvious discontinuity in traces of pedestal height and stored energy. Where a hard back transition begins with an obvious step down in energy followed by decay, soft transitions have only a decay phase with no step down.

1.5.1 Phenomenology of the H-L Transition Sequence

The H-mode termination phase has been observed to include the following elements which are shown in figure 1.12, beginning in type-I ELMing H-mode with the reduction of heating power to below the H-L threshold: cessation of ELMs; a potentially long lasting (hundreds of milliseconds) period of ELM-free operation, during which the Modulating Pedestal Mode (MPM, to be examined in section 5.4) typically appears in our scenario; a rapid relaxation of the pedestal similar to a type-I ELM;[42,44] a period of small repetitive D_α bursts or "dithering", which is composed of bursts of two distinct characters; and finally L-mode. The first phase of the dithering transition is made up of type-III ELMs, which is a broad label for small, frequent (compared to type-I ELMs) D_α bursts which are not completely explained by ideal peeling-ballooning theory and may be a resistive or other non-ideal instability.[14,45,46] The dithering then changes character and becomes consistent with a predator prey limit cycle oscillation, as shown by analysis

of $E \times B$ flows by Schmitz *et al.* in a series of DIII-D experiments carried out with the same setup as ours.[41,42] Periods of LCO are more easily distinguished from type-III ELMs by their higher ($\approx$ 2 kHz), very regular frequency, clear inverse relationship between freqeuncy and density, and absence of the MPM between D_α bursts. By contrast, type-III ELMs repeat at $<$ 1 kHz with a less regular period and intensity, and each is synchronous with modulations of the MPM, which reappears between type-III ELMs. Similar distinctions between type-III ELMs and LCOs or dithering L-H transitions have been made before.[47,48] In particular, see figure 18 of Xu *et al.*,[48] where a $\approx$ 70 kHz precursor oscillation with spectral sidebands (compare to the MPM in sections 5.4) is used to define the first few D_α spikes as type-III ELMs, in contrast to the later LCO. Except for the first large relaxation of the pedestal (similar to a type-I ELM), the sequence of events in a back transition is the mirror image of a forward L-H transition.[42,48]

From the spectrogram in figure 1.12(a), it can be seen that the period between D_α bursts in the dithering H-L transition sequence (starting around 2020 ms) is initially irregular. These are type-III ELMs. As time progresses, fluctuation power concentrates into a sharply defined fundamental frequency around 2100 ms and then the frequency increases. This is the LCO. Note the lack of a clear cutoff between the two phases. Even the MPM fades out gradually.

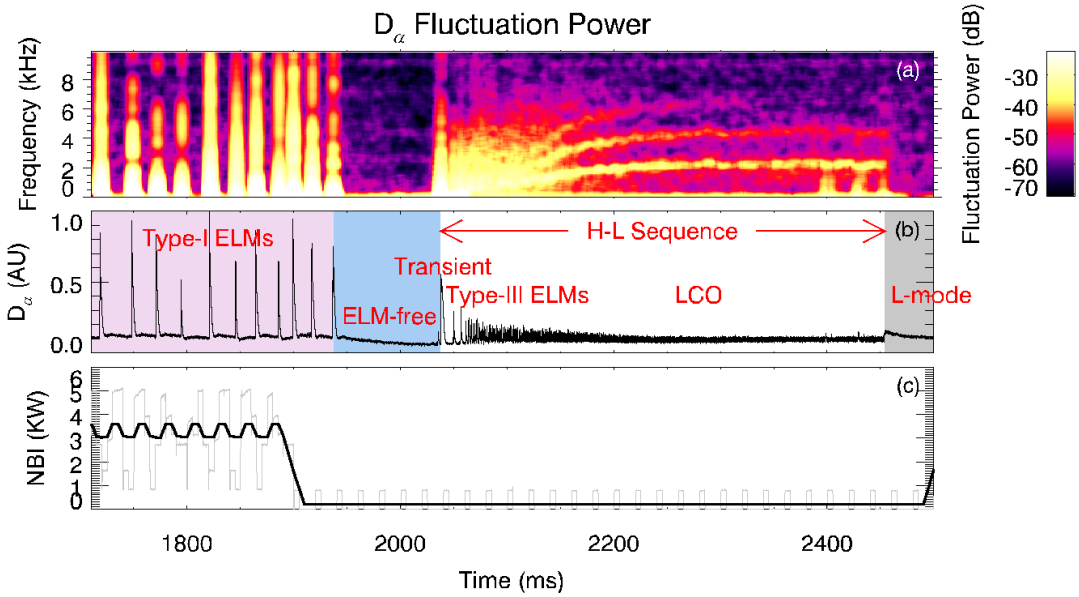

Figure 1.12: Phenomenology of the H-mode termination phase and H-L transition sequence. (a) spectrogram of D_α emission. (b) history of D_α emission from the outer strike point. H-mode is shaded in pale pink (ELMing) and blue (ELM-free), the H-L sequence is unshaded, and L-mode is shaded in gray. (c) Neutral beam injected power, raw (gray) and smoothed (black). The time range begins during type-I ELMing H-mode. The type-I ELMs stop following the input power reduction (to minimal diagnostic levels, below the H-L threshold). The H-L sequence begins with the transient, followed by "dithering" which changes character from type-III ELMs to LCOs at around 2100 ms.

1.6 Hypotheses

It is important to manage heat flux out of the plasma during H-L back transitions and to prevent unintentional H-L transitions. Therefore, mechanisms involved in triggering back transitions must be understood. The obvious starting point is to identify the trigger for the large initial transient in "hard" back transitions.

As the initial transient appears to be similar to a type-I ELM and has been referred to as one in published literature,[42,44] it is useful to test whether these events are triggered the same way. Conditions before large type-I ELMs are consistent with ideal peeling-ballooning modes of intermediate toroidal mode number n as the triggering mechanism.[14] Chapter 4 uses the `ELITE` code[14,49] as

well as secondary experiments to test the hypothesis that the transients at the start of hard back transition sequences are type-I ELMs triggered by ideal peeling-ballooning modes of intermediate n. Stability analysis with `ELITE` indicates that the transients are not triggered by ideal peeling-ballooning with $n \geq 5$. Further arguments are made against low $n < 5$ ideal peeling-ballooning instability as the trigger, but it is not ruled out completely. Regardless, typical ELMs are triggered by intermediate n peeling-ballooning, so the transient is distinct. These conclusions are supported by the secondary experiments described in chapter 4.

Another reasonable hypothesis is that $E \times B$ shear decays after auxiliary power is reduced and the back transition sequences begin when the shear suppression mechanism becomes too weak to maintain turbulence suppression ($\omega_{E\times B} \approx \omega_T$). The transient in hard back transitions would then be explained by a rapid feedback loop as recovering turbulence reduced the pressure gradient and further weakened the suppression mechanism. Soft transitions would also begin when $\omega_{E\times B} \approx \omega_T$ and the lack of a large initial transient might be explained by differences in the rotational contributions to the E_r well as explained below:

The pressure gradient provides free energy for driving turbulence as well as powering the turbulence suppression mechanism. The rotation terms in Eqn. 1.6 could affect the balance between these effects and select for hard or soft back transitions, with soft transitions losing suppression at a lower value of $\partial p/\partial r$ when less energy is available to drive turbulence. For a given value of E_r, $\partial p/\partial r$ will increase with increasing toroidal rotation v_ϕ. The magnitude of E_r at the bottom of the well correlates with $\omega_{E\times B}$, so plasmas with low toroidal rotation at the edge should then be able to achieve turbulence suppression at a lower value of $\partial p/\partial r$ in the pedestal, thus weakening turbulence drive relative to damping. As will be seen in chapter 5, there is a clear correlation between low v_ϕ at the edge of the plasma and soft H-L transitions.

So, the $E \times B$ shear decay hypothesis is that $\omega_{E\times B}$ decays significantly leading up to the back transition, that $\omega_{E\times B} \approx \omega_T$ when the back transition sequence begins, and that hard and soft back transitions begin with similar values of E_r and $\omega_{E\times B}$ but different pressure gradients. However, it is found that the peak

value of $\omega_{E\times B}$ changes very little during the evolution before the back transition, that $\omega_{E\times B} > \omega_T$ when D_α bursts associated with the H-L transition sequence begin, and that the profiles of most parameters, other than v_ϕ, and including E_r and $\omega_{E\times B}$, at the edge are very similar: this hypothesis is falsified.

With the beginning of the H-L sequence unexplained by P-B instability and spontaneous failure of the shear suppression mechanism, the next logical hypothesis is that conditions in the ELM-free period prior to the back transition allow the growth of some other instability and that this instability is responsible for the start of the H-L sequence. A coherent mode (the MPM) does appear in the pedestal during the pre-H-L ELM-free period and its amplitude grows as the pedestal evolves. A detailed characterization of fluctuations is performed and reported in chapter 5.

1.7 Organization

The purpose of this work is to examine the phenomenology of the H-L back transition. Relevant plasma diagnostics will be described in chapter 2, with special emphasis on the recently upgraded Thomson scattering system throughout most of the chapter followed by discussion of other diagnostics in section 2.8. Data from Thomson scattering play a key role in chapter 4, where conditions in the plasma are tested against the peeling-ballooning model (described in chapter 3), which successfully describes type-I ELMs. It is found that the transient event before the back transition is not linearly unstable to ideal peeling-ballooning modes and thus is not a type-I ELM. In chapter 5, $\omega_{E\times B}$ is measured and compared to the decorrelation rate of turbulence ω_T. It is found that $\omega_{E\times B}$ does not decay dramatically prior to the H-L back transition and in many cases is nearly constant at a value significantly greater than the turbulence decorrelation rate. This is followed by characterization of fluctuations in the pedestal leading up to the back transition and a comparison of hard and soft back transitions, also in chapter 5. Of particular interest is the modulating pedestal mode (MPM), a coherent, intermediate wavelength ($\lambda_\theta \sim 20$ cm) density fluctuation which appears consistently in the last ~ 100 ms of ELM-free H-mode in our experiments. A robust method of producing

soft back transitions by controlling torque inputs to the plasma is documented along with other potential control schemes. Chapter 6 summarizes the results.

2 High Resolution Thomson Scattering Diagnostic Upgrade at DIII-D

2.1 Introduction

In order to accurately predict the performance of future tokamaks, it is necessary to validate models for the height of the H-mode pedestal. Theory work by Snyder *et al.*[50] (the `EPED` model) describes constraints on the width and height of the pressure pedestal due to Kinetic Ballooning Modes and coupled Peeling Ballooning Modes. The `EPED` model predicts a path of pedestal evolution through height-width space. The path is initially controlled by KBM induced transport but terminates in a PBM triggered, type-I edge localized mode (ELM). Validation of this model requires accurate, high resolution measurements of the pressure profile to determine pedestal width and height. Thomson scattering is a key diagnostic for testing this and other models because it simultaneously measures electron temperature and density at many spatial locations, its performance and availability are independent of other systems, it is non-perturbative, and analysis of the raw data is relatively simple and quick: experimenters need not make special requests for analysis for most applications. In order to support theory work including `EPED`, the DIII-D Thomson scattering diagnostic was upgraded in 2010 to enhance its spatial resolution.[51–56] Separately managed, concurrent upgrades decreased random measurement errors by improving the detection electronics[57] and increased tem-

poral resolution by adding more lasers.[58] Subsequent work developed a powerful tool for regularly and systematically checking data quality. This led to significant improvements in calibration and maintenance procedures over pre-upgrade standards, resulting in higher quality data with reduced systematic errors (systematic T_e errors of $\approx 1 - 30\%$ were eliminated).

The edge/pedestal section of the original multi-pulse DIII-D Thomson scattering diagnostic[59] was aimed at the top of the machine to take advantage of the variable packing of the flux surfaces (flux expansion) to effectively increase spatial resolution (by $\approx 2\times$) relative to diagnostics aimed at the machine midplane[60] (note the spacing of flux surfaces in Fig. 1.7 and the placement of TS in Fig. 2.4). However, it was still possible for the pedestal to be so narrow that fewer than two Thomson points were located in the steep gradient region as shown in figure 2.1. Only an upper bound on the pedestal width could be calculated in such cases. There is a technique for effectively increasing resolution by combining several profiles with slightly different flux maps. That is, the edge of the plasma can be moved slightly relative to the fixed chords to change the relative positions of the measurements. Even a single chord could produce arbitrary resolution in this way. However, the finite extent of the measurement volume necessarily introduces some blurring and this will unavoidably set a lower limit on measurable pedestal width. In other words, the diagnostic's spot size or instrument function smears the measured profiles spatially and prevents resolution of narrow pedestals regardless of the effective chord-chord spacing. Thus, reduction of spot size was a key goal of the upgrade.

As part of this dissertation, the High Resolution Thomson Scattering (HRTS) upgrade was performed to reduce the measurement spot size and increase the number of chords across a region spanning the typical range of edge positions. As reductions in scattering length (spot size) necessarily result in loss of Signal to Noise Ratio (SNR), the upgrade was essentially a trade off between temperature accuracy and spatial resolving power, and careful planning and simulation were required to ensure that the final result would be acceptable. The concurrent upgrade[57] to the amplifier electronics mitigated the loss of SNR.

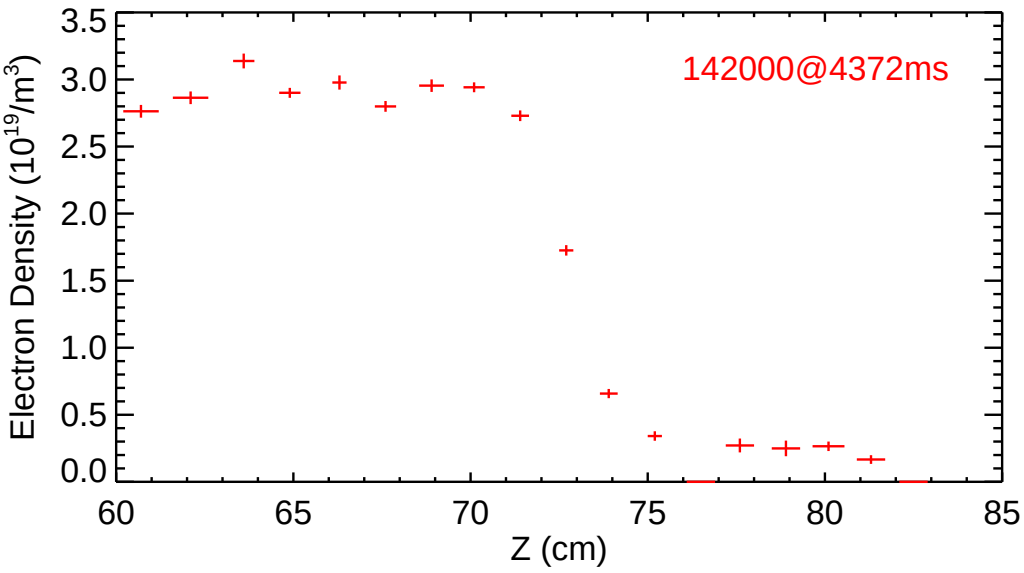

Figure 2.1: A pre-upgrade, under-resolved profile of electron density vs. Z, position along the vertical laser (see Fig. 2.4), as measured by Thomson scattering in 2010. There are too few points in the steep gradient region to determine the pedestal width confidently. Two points (in the scrape off layer, to the right, outside of the region of steep gradient) were rejected due to poor SNR.

2.2 Background

2.2.1 Thomson scattering

Thomson scattering is the elastic scattering of light from free charged particles, as shown in figure 2.2. In this case, the charged particles are electrons and the light is generated by a pulsed Nd:YAG laser. The DIII-D Thomson diagnostic is built on the assumption of Maxwellian electron velocity distribution with mean velocity neglected compared to thermal motions: $f \propto \mathrm{Exp}\,(-mv^2/2T_e)$.

The cross section for Thomson scattering from a Maxwellian electron distribution depends on the incident and scattered wavelengths λ_i and λ_s, described by the normalized wavelength shift $\epsilon = (\lambda_s - \lambda_i)/\lambda_i$, the scattering angle θ (not to be confused with the poloidal angle, which does not appear in equations in this chapter), and the electron thermal energy T_e, which is included in the following equations through $2\alpha = m_e c^2/T_e$ (m_e and c are the electron mass and speed of

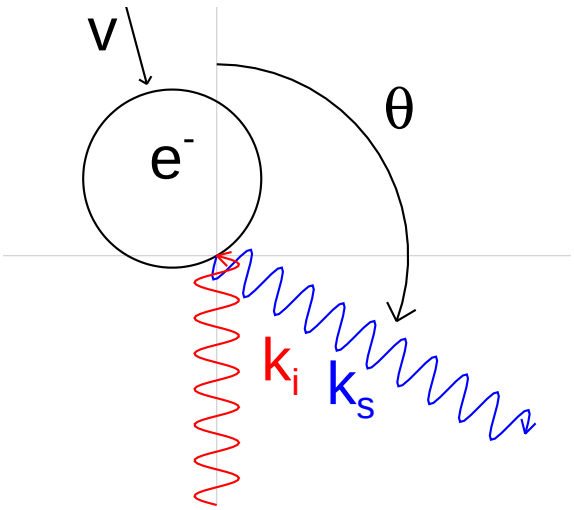

Figure 2.2: Simple diagram of Thomson scattering. Incident photon k_i (red) collides with free electron e^-, resulting in scattered photon k_s (blue) traveling at angle θ with respect to k_i. Thermal motion v of the electron causes a doppler shift in the scattered light.

light, respectively). Scattered power per unit solid angle per normalized wavlength shift is given by Equations 2.1-2.4:

$$\frac{d^2P}{d\Omega_s d\epsilon} = r_e^2 \int d^3\vec{r}\langle S_i\rangle S(\epsilon,\theta,2\alpha) \tag{2.1}$$

$$S(\epsilon,\theta,2\alpha) = S_Z(\epsilon,\theta,2\alpha)q(\epsilon,\theta,2\alpha) \tag{2.2}$$

where r_e is the classical electron radius, $\langle S_i\rangle$ is the mean Poynting vector, S_Z is Zhuravlev's[61] expression for the spectral density function S, which neglects relativistic depolarization, and $q(\epsilon,\theta,2\alpha)$ is the relativistic depolarization correction derived by Naito *et al.*[62] or alternatively by Selden[63] or Sheffield.[64] The depolarization correction is used in calculations to obtain the final measurements and to generate the following plots, but it is fairly minor at or below typical plasma temperatures of about 1 keV and the properties of the scattered spectra can be understood qualitatively by examining Zhuravlev's expression only:

$$S_Z(\epsilon,\theta,2\alpha) = \frac{\mathrm{Exp}(-2\alpha x)}{2\mathrm{K}_2(2\alpha)(1+\epsilon)^3}[2(1-\cos(\theta))(1+\epsilon)+\epsilon^2]^{-1/2} \tag{2.3}$$

$$x = \sqrt{1+\frac{\epsilon^2}{2(1-\cos\theta)(1+\epsilon)}} \tag{2.4}$$

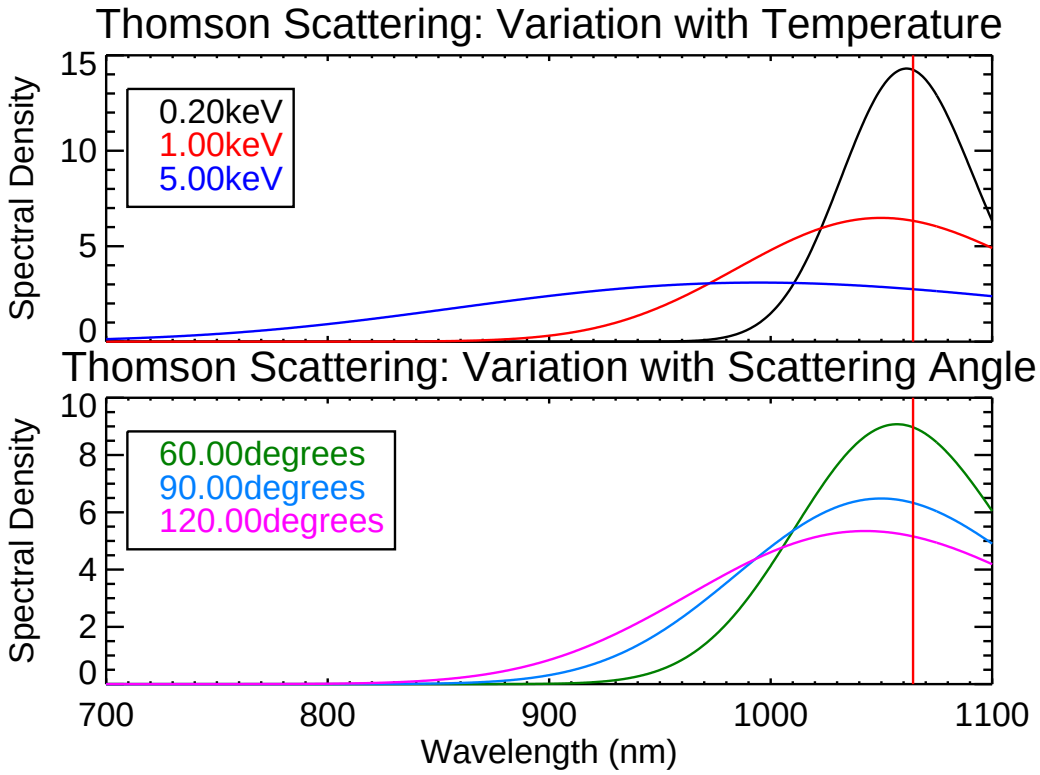

Figure 2.3: Example spectral density function S at selected temperatures and scattering angles. Top: 90° scattering at selected temperatures. Bottom: scattering at various angles from a 1 keV plasma. The incident wavelength is 1064.3 nm, as is output by the Nd:YAG lasers used in the diagnostic implementation at DIII-D. At higher temperatures and more obtuse scattering angles, the spectrum broadens and experiences greater relativistic blue-shift.

where $K_2()$ is a modified Bessel function of the second kind with index 2. Note that the volume integral of equation 2.1 may be reasonably replaced by the assumption of negligible variation over the small scattering volume, making the scattered power proportional to S.

Examples of scattered spectra at selected temperatures and scattering angles are shown in figure 2.3.

2.2.2 Diagnostic Implementation

The DIII-D Thomson scattering diagnostic is composed of three laser groups or subsystems on three paths through the plasma (see Fig. 2.4). Scattered light is

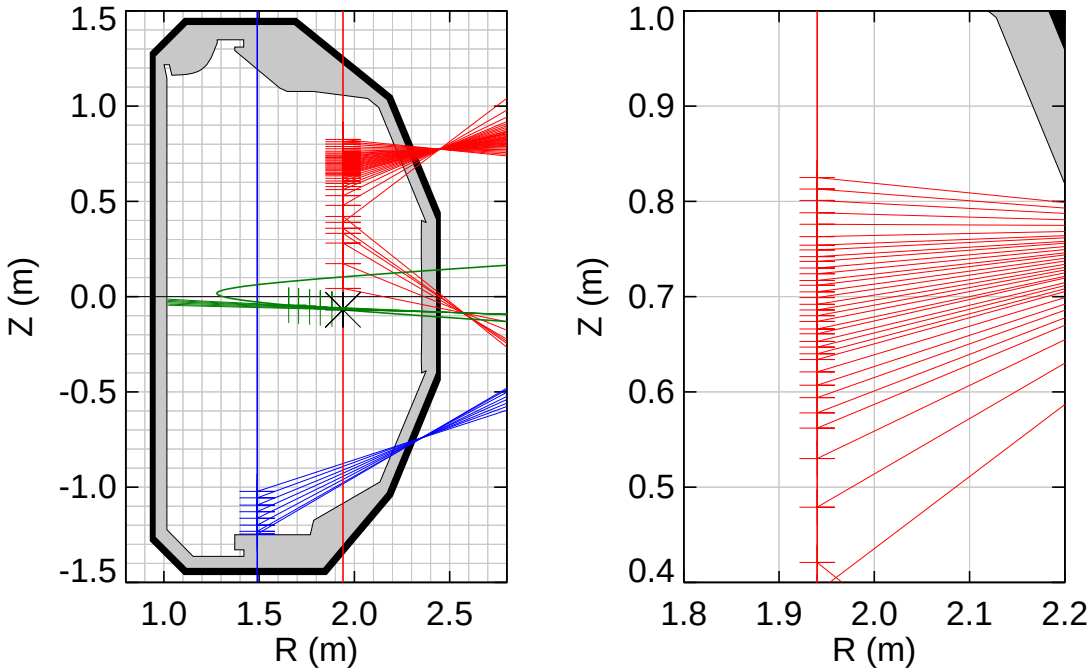

Figure 2.4: TS laser paths and viewchord center lines. The core (red) and divertor (blue) subsystems are co-planar at left-handed hardware toroidal angle of 120 degrees and enter the machine through the V2 and V1 ports at 1.94 and 1.49 m respectively. The tangential laser path is the green curve which enters the plot from the right, makes closest approach to the center-post at $\approx$ 1.3 m, and exits the plot area again to the right. The tangential viewchords, also green, end on the center-post.

collected through three port windows. Behind each window is a set of collection optics (see Fig. 2.5) that focuses the scattered light onto a set of fiber bundles. The bundles are about 30 m long and they run from the machine pit to the Thomson lab where they terminate in detection apparatus.[65]

The most suitable type of laser for this application is Nd:YAG (neodymium-doped yttrium aluminum garnet)[66] operating at 1064.3 nm, which puts critical parts of the scattered spectrum outside of the optimal wavelength range for image intensified CCD cameras. Therefore, polychromators are used instead of spectrometers.[67] Each polychromator consists of a set of optical band pass filters which accept a carefully chosen wavelength range and reflect the rest to the next

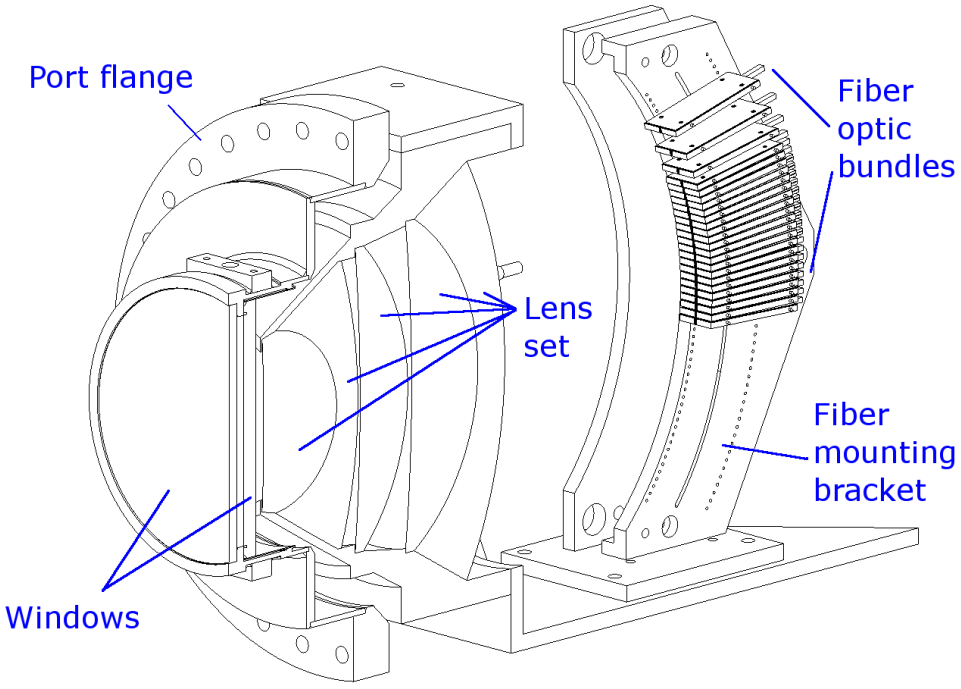

Figure 2.5: Model of a set of collection optics for Thomson scattering. The port flange assembly at the left mates with the vacuum vessel. The lens set and fiber mount are mechanically isolated from the vessel.

filter. A diagram of a polychromator is shown in figure 2.6 and spectral response functions for the filter set in an example polychromator unit are shown in figure 2.7.

Behind each filter is an Avalanche Photo Diode (APD) based detector unit containing an APD and an amplifier circuit.[57,68] The detectors measure the scattered light level as well as the background light, which is used to determine uncertainty in the individual signals so that the fits used to obtain temperature and density may be properly weighted. Correct measurement of the background light is necessary for obtaining the final fit parameters and their uncertainties. Background signal is subtracted in hardware with a 30 ns delay line. The nominal output of the subtraction circuit is 0 until a positive pulse comes, followed by its negative echo 30 ns later (see figure 2.8). A 25 ns integration gate is tuned to capture the positive pulse. The laser pulse is nominally 8 ns long, but the waveform

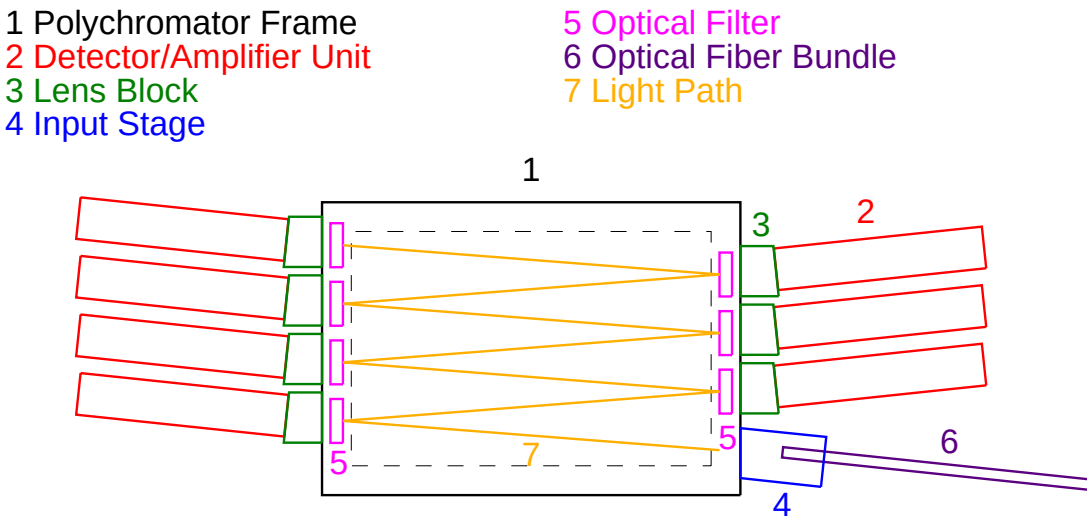

Figure 2.6: Polychromator physical layout. Scattered light is carried by an optical fiber bundle (6) to the input stage (4) containing a collimating lens. When light reaches the first of the optical bandpass filters (5), most of it is reflected down the line (7) from filter to filter. There are additional lenses (not shown) in front of each filter to maintain collimation. The fraction of light which is transmitted through a filter is focused by a lens in the lens block (3) onto an APD at the front of the detector/amplifier unit (2). The detector modules are connected to a data acquisition system.

is not square, requiring a ≈ 20 ns window to capture all of the power. Padding the window allows for some margin of error in the timing but increases background noise. Minor imperfections in the subtraction circuit are calibrated out. Major imperfections require re-tuning (through variable capacitor and potentiometers) or replacement of the amplifier circuit. The signal from each set of detectors is fit to a model for relativistic Thomson scattering[62,63] (see section 2.2.1) to produce the final electron temperature and density measurements. Random uncertainty in the measurement comes from photon statistics and from detector dark noise. The detector dark noise is measured before every shot before the lasers begin to fire. The level of noise in the scattered signal as a result of background light can be more than $\sqrt{n_{ph}}$, the statistical value expected from an ideal detector where n_{ph} is the photon count; a calibration is performed to measure the signal noise enhancement factor.

The expected signal is proportional to electron density, laser energy, a

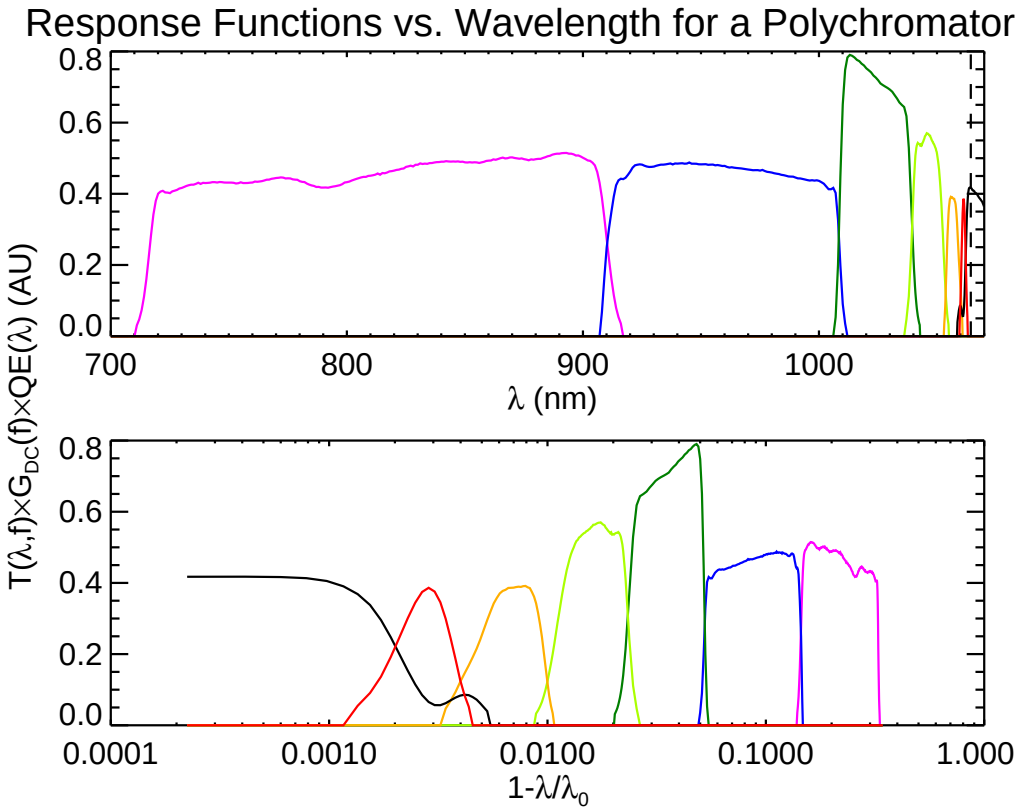

Figure 2.7: Example filter set. Spectral response vs. wavelength (top) and vs. $1-\lambda/\lambda_0$ (bottom) for the detection hardware in one polychromator. The spectral response is the convolution of the filter transmission function with the detector quantum efficiency and the amplifier gain on the DC channel, which is used for background light measurements and calibrations.

Rayleigh scattering calibration factor, and a factor which depends on the temperature, scattering angle, and the combined detector+filter spectral response function.

$$Signal(f,\theta,T_e,n_e,E_{laser}) = n_e \times E_{laser} \times Rayleigh \times LUT(f,\theta,T_e) \qquad (2.5)$$

The temperature dependent factor is pre-calculated for values on a logarithmic grid and stored with the calibration set, and is referred to as the Look Up Table or LUT:

$$LUT(f,\theta,T_e) = \frac{\left(\frac{G_{PL}(f)}{G_{DC}(f)}\right)}{\left(\frac{G_{PL}(f_0)}{G_{DC}(f_0)}\right)} \int_{all\lambda} S(\lambda,\theta,T_e) \frac{Response(f,\lambda)}{Response(f_0,\lambda_0)} \frac{E_{photon}(\lambda_0)}{E_{photon}(\lambda)} \frac{d\lambda}{\lambda_0} \qquad (2.6)$$

where f refers to one of a set of optical bandpass filters in the polychromators, f_0

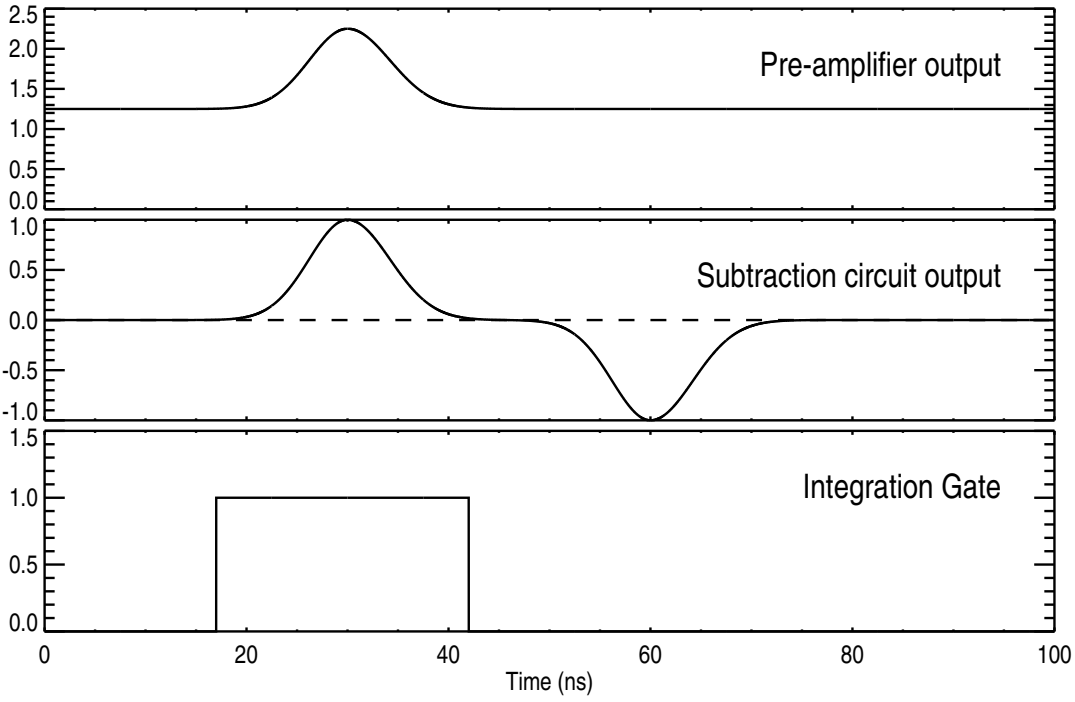

Figure 2.8: Schematic of the TS hardware subtraction circuit. Output from the pre-amplifier (top) spikes when scattered light from a laser pulse is received. This signal is the sum of background and scattered light. The subtraction circuit output (middle) is the sum of the "live" pre-amp signal and the inverted delayed signal, which removes variation with a long timescale, such as background light. The integration gate (bottom) is timed to capture the real pulse from the subtraction circuit without catching the negative echo.

refers to the filter which passes the laser wavelength, G_{PL} and G_{DC} are the gains for the pulsed (scattered light) and DC (background light) channels of the individual detectors, $Response(f, \lambda)$ is the number of digitizer counts returned on the DC channel per incident photon energy for filter+detector pair f, $E_{photon}(\lambda) = \frac{hc}{\lambda}$ is the photon energy and λ_0 refers to the laser or incident wavelength, which is 1064.3 nm in this case. $Response(f, \lambda)$, G_{PL} and G_{DC} are measured directly during calibrations. *Response* is determined using a scanning monochromatic light source and includes variation in gain with wavelength due to quantum efficiency of the APD as well as the transmission of the filter. G_{PL} and G_{DC} are measured at a single wavelength with a pulsed and a CW laser.

An example of the LUT for all of the usable channels in one polychromator is

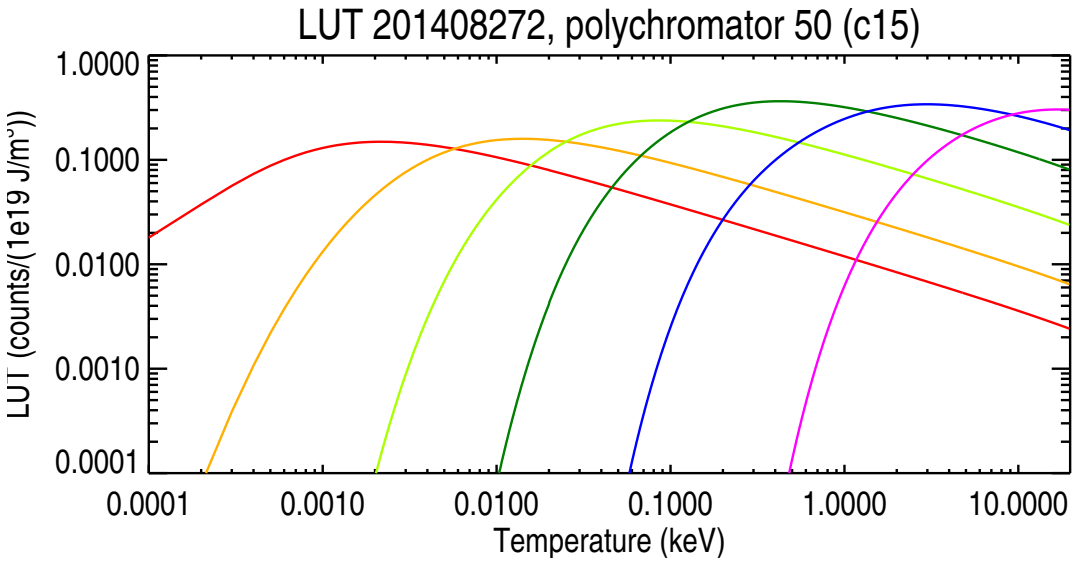

Figure 2.9: Look-up table values for an example polychromator corresponding to the filter set shown in figure 2.7. This is the temperature dependent factor in the determination of signal levels, given by equation 2.6. As temperature increases, the scattered spectrum broadens and blue shifts, activating the higher temperature filters: the ones centered at shorter wavelengths and with greater bandwidth. The scattering angle for this unit is 82.14 degrees. The curve for f_0, the filter admitting 1064.3 nm, is not used in the fit and is not shown here.

plotted in figure 2.9. During the fitting process, expected values are interpolated from the LUT and multiplied by density and other appropriate factors, as seen in equation 2.5, to get the expected signal. The final estimates for temperature and density are converged upon using the Levenberg-Marquardt algorithm.[69] For reference, figure 2.10 reproduces the scattered spectral density calculation shown in figure 2.3 on a log plot with new temperatures selected which roughly correspond to the peaks in signal for each detector in the example hardware. To successfully fit a temperature, it is necessary to have two or more reasonably strong signals to compare. Since the ratio of the top two signals tends to dominate the fit, it is useful to arrange the filter set such that there will also be two strong signals with opposite (or at least significantly different) slopes vs. temperature at any given temperature within the range of interest.

The filter sets are designed so that there are evenly spaced (logarithmically in temperature) peaks in expected signal. When the system is working properly

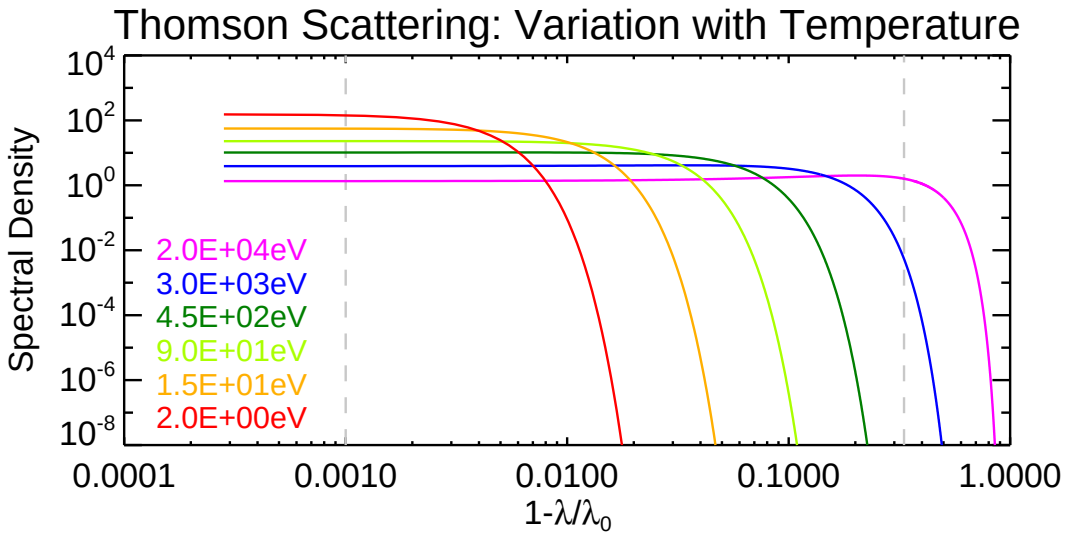

Figure 2.10: Variation of the scattered spectral density vs. $1 - \lambda/\lambda_0$ for several temperatures in the relevant range with $\theta = 82.14\,^\circ$. The vertical dashed gray lines show the range of wavelengths accepted by the polychromators.

and density is sufficient, there are always two clear signals with opposite slope between ∼2 eV and ∼20 keV. In practice, low temperatures tend to occur at low density, where it can be seen that signal, being proportional to density, will be low (eqn. 2.5). Background light comes mainly from bremsstrahlung, which is proportional to n_e^2,[70] making background noise proportional to n_e. Dark noise, however, is constant. At low enough density, dark noise dominates the total noise and SNR is proportional to density. At high density, bremsstrahlung dominates the total noise and SNR is independent of density. However, the detectors will eventually saturate, producing an upper limit on density. Amplifiers which are expected to be exposed to higher signal (such as the wide filters in polychromators aimed at the center of the machine where the plasma core usually is) can be tuned to lower gain to compensate. Thus, the limiting factor for measuring low density is signal level and the limit for high density is dynamic range of the system (this limit is higher than typical DIII-D densities). The lower limit on temperature results from failure to resolve very narrow spectra which occur at low temperatures because of the minimum bandwidth of the optical filters. The upper limit on temperature could be extended by adding more filter channels to sample shorter

wavelengths, although background light becomes brighter below 700 nm and the D_α line at 656 nm must be avoided.

The measured signals obviously depend on the solid angle of light collected by the optics. This is accounted for in the Rayleigh scattering calibration rather than integrating the lens collection efficiency over the solid angle it subtends for each chord, which would be difficult to measure accurately. During a Rayleigh calibration, the vacuum vessel is filled with a small amount of argon gas (typically 3 torr). The lasers are fired through the gas and the Rayleigh scattered light is collected through the so-called "laser" filter, the only one which admits 1064.3 nm light. The laser filter is shown in black on figure 2.7 and is not used to calculate the reported temperature and density because of issues with stray laser light. It exists only to allow the Rayleigh calibration. Stray light is accounted for in this calibration by scanning the amount of gas in the vessel and taking the slope of signal vs. pressure. Furthermore, Rayleigh scattering is performed with the magnets off, so the vacuum vessel is not deflected as it is during a plasma shot. This results in reduced stray light during Rayleigh calibrations compared to plasma shots. The deflection of the vessel while the magnets are on may be partly responsible for stray laser light during plasma shots, as the entry windows and baffle tubes are mechanically connected to the vacuum vessel and shake with the machine. The rest of the laser beam line and the collection optics are mechanically isolated. The other filters which are used for plasma measurements must have good rejection (OD4) of 1064.3 nm light or else their signals will be polluted with stray laser light.

The laser group labeled "core" (red in Fig. 2.4) is imaged where it intersects the top of the plasma and it is this subsystem which provides the useful pedestal measurements. This laser path has the capacity to include eight individual lasers and it runs vertically at a radius of 1.94 m from the machine axis. Typically the plasma magnetic axis is located at $R \approx 1.6 - 1.7$ m, and the Last Closed Flux Surface (LCFS) extends to $R \approx 2.3$ m at the midplane. The core group does not typically provide measurements close ($\psi_N < 0.2$) to the magnetic axis; these are obtained via the tangential subsystem (green in Fig. 2.4). The toroidal location

of the core path and collection hardware is 120 degrees in DIII-D's left handed machine pit hardware labeling system (0 degrees = north). Previously, there were four 20 Hz Nd:YAG lasers assigned to this group for an overall repetition rate of 80 Hz. This was upgraded to 230 Hz at the same time the spatial resolution upgrade was being performed by adding three 50 Hz Nd:YAG lasers. The tangential laser path intersects the core laser at $R = 1.94$ m, $Z = -0.069$ m.

Nominally, each standard (pre-upgrade) chord has a bundle of 104 silica fibers with a core diameter of 200 μm. The original bundles are 3.0 mm high in the direction parallel to the laser, and 1.5 mm wide across the laser. The image of the laser should be about 1 mm wide; extra width is necessary to provide alignment tolerance (in the plasma, each bundle sees a volume ≈ 4.3 mm wide, compared to a ≈ 3 mm diameter laser). The centers of the measurement volumes were 12 mm apart at the closest, and the minimum scattering length was about 9 mm. The lens magnification is not constant and chords passing through farther from the axis of the lens system are longer and farther apart. Fortunately, the axis of the lens is aimed close to the typical intersection of laser with the LCFS. An equilibrium reconstruction from `EFIT`[71] may be used to map Thomson chord positions and sizes to the outboard midplane, where most profile diagnostics are located on DIII-D. The mapped chord spacing was 7 mm center-center and the radial extent of the measurement volumes was about 5 mm prior to the upgrade.

Note that the alignment tolerance of the laser is less than 1 mm at the end of the 30 m beam-line. An automatic feedback alignment system has not been implemented. The Thomson operator monitors alignment with a system of dedicated fibers interleaved with the measurement fiber bundles and with cameras viewing a small fraction of the beam energy. Constant, low power (compared to the measurement lasers) HeNe guide lasers are launched along the three paths taken by the YAG lasers so that the steering mirrors can be adjusted without firing the YAGs. The YAGs can be fired and matched to the HeNe guide lasers as a second order alignment.

For a standard sized scattering volume at a typical DIII-D density, roughly one photon out of every 10^{14} photons fired into the vessel will hit the lens. Con-

sidering properties of the hardware such as transmission efficiencies and typical input energy, the number of photons counted per pulse per detector in typical measurable scenarios ranges from $\mathcal{O}10^2 - 10^4$.

2.3 DIII-D High Resolution Thomson Scattering Upgrade

2.3.1 Upgrade requirements

The old system was sometimes capable of resolving the steep gradient region, and so it was suspected that chord spacing was nearly adequate. Because the composite profile or conditional averaging technique is popular as a means of increasing effective resolution, the top priority goal was to decrease the spot size or extent of the scattering volume across the flux surfaces: even a sparsely populated system with small scattering volumes might be capable of producing a good profile measurement if the edge of the plasma were scanned across the diagnostic slightly.

A decrease in spot size by a factor of two was determined to be enough to allow significantly improved tests of some key models. Decreasing spot size and packing more chords into the same fiber mount necessarily means decreasing scattering length and therefore reducing signal levels: uncertainty in position is being decreased at the cost of higher uncertainty in temperature and density. Finding the optimal balance for this trade was an important part of the design process. The key accuracy requirement was that temperature uncertainty should be maintained below 10% under typical operating conditions in spite of the reduced signal. It was also required that the upgrade be capable of this level of accuracy with electron density as low as $2 \times 10^{19}/\mathrm{m}^3$. Finally, the region of enhanced resolution had to be broad enough to encompass the typical range of pedestal locations.

It is important to localize the scattering volumes as tightly as possible in flux space. The widths of the lasers set a lower limit on the extent of the chords in ψ_N, meaning that there are diminishing returns for reductions of the scattering length (viewchord height). Analyzing this scattering volume geometry

is important for correctly optimizing the system. For an example viewchord, figure 2.11 shows the intersection of the line of sight from the optics with the laser in a plane perpendicular to both. In figure 2.11(a), filled contours of laser power are shown, with the darker area in the center representing more laser power density. Dashed vertical red lines give landmarks for the edges of the laser at 2σ (the power distribution is assumed to be Gaussian). These dashed red lines have the same meaning in figures 2.11(b) and 2.11(c). The dashed dotted red lines show the top and bottom of the viewchord. The angle between these and the vertical is the scattering angle θ_{scat}. The black and blue solid lines are parallel to the flux surfaces, making angle θ_{flux} with the vertical. The blue lines show the full width half maximum of the final spot [Fig. 2.11(d)]. It can be seen that even if the scattering length (vertical height of the spot) were greatly reduced, the width of the laser would still stretch across several flux surfaces. This sets a limit on resolving power and complicates the trade off between accuracy (long scattering length) and resolution (short scattering length). Figure 2.11 details the analysis which translates scattering length into the chords' span across flux surfaces, which is meaningful for studying physics.

Figure 2.11(c) is a reproduction of 2.11(a), but rotated such that the new X axis is a coordinate parallel to the flux surfaces, and the new Y axis goes across the flux surfaces. 2.11(b) is the integration of 2.11(a) along the vertical axis so as to collapse it to a function of the coordinate x; this is essentially laser beam power across the beam cross section. 2.11(d) is the integration of 2.11(c) over the coordinate q [x-axis of 2.11(d)] so as to collapse power collected into a function of the coordinate r, which is perpendicular to the flux surfaces and is the physics relevant coordinate. This is the instrument function: the relative amount of signal from each flux surface. Instead of r, the instrument function can just as easily be calculated as a function of ψ_N. This r is like the minor radius, but is not exactly the same.

The instrument function is computed for several values of scattering length for a chord near the lens axis and the results are plotted in figure 2.12. It can be seen that there is a clear disadvantage in terms of resolving power gained vs.

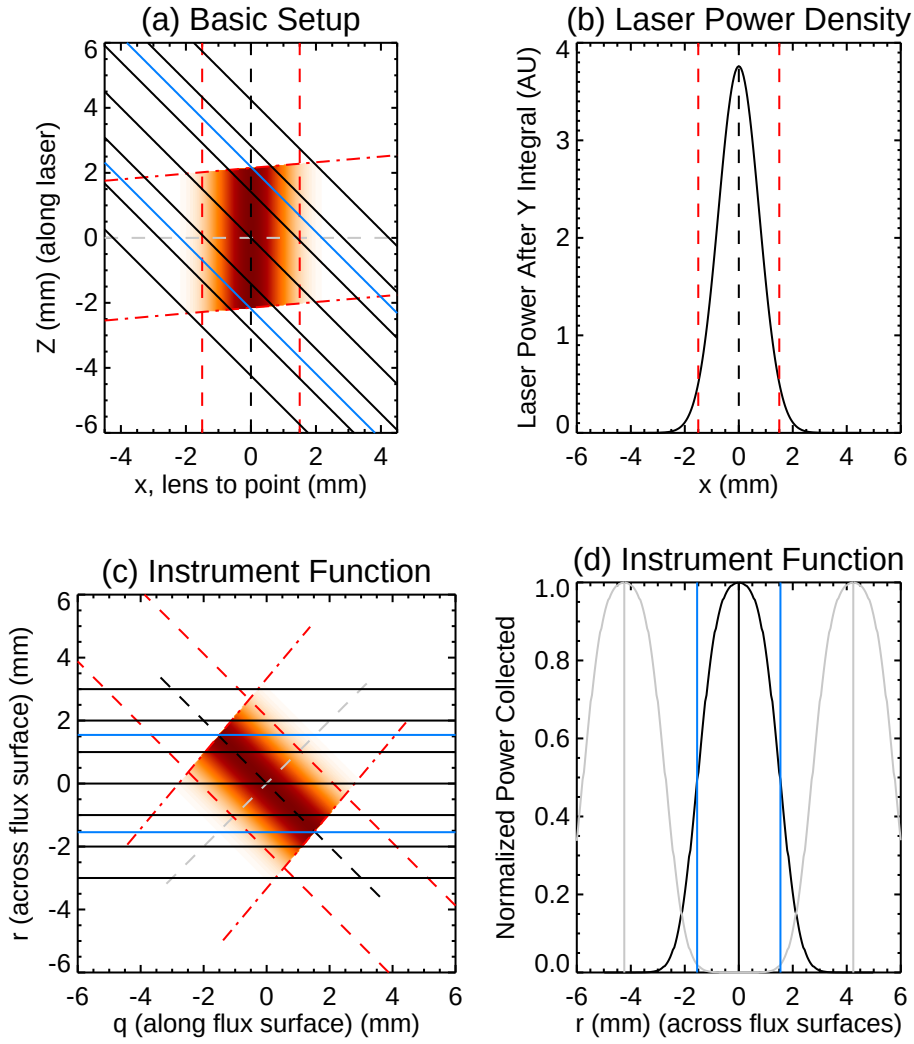

Figure 2.11: Diagram showing the instrument function of a typical scattering volume. Filled contours: laser power density. Red dashed lines: nominal laser edges. Dashed-dotted lines: top and bottom of viewchord. Solid lines: flux surfaces. Dashed gray and black lines: horizontal and vertical reference. (a) chord geometry. (b) 1D power laser power density vs. horizontal coordinate. (c) chord geometry, rotated to coordinate system aligned to flux surfaces. (d) 1D power density vs. coordinate perpendicular to the flux surfaces [(d) is the integral of (c) along q].

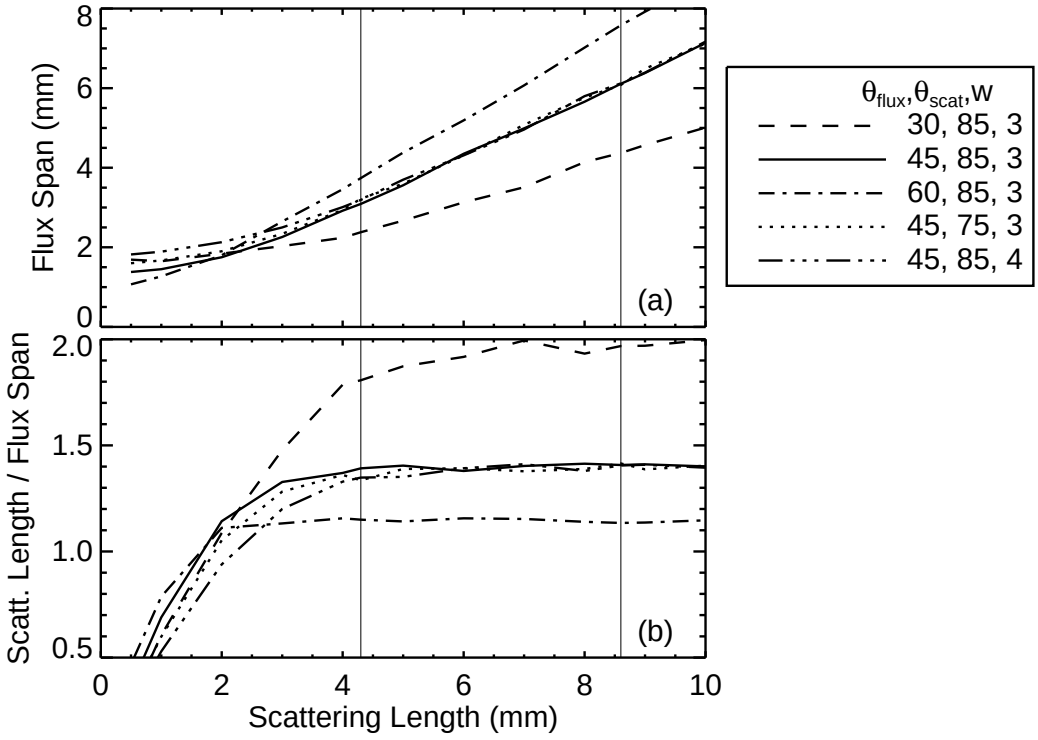

Figure 2.12: Diminishing returns for scattering length reduction. (a) FWHM span of a scattering volume across flux surfaces [see Fig. 2.11(d)]. (b) Product of scattering length (improves accuracy) with the reciprocal of flux span (improves resolving power). The analysis is performed for various combinations of the angle between the flux surfaces and the vertical θ_{flux}, scattering angle θ_{scat}, and w, the 2σ Gaussian laser width. It can be seen that the product of accuracy with resolving power (b) decreases as scattering length is reduced below 2-4 mm, but is approximately constant when scattering length is long enough. Vertical lines mark the scattering lengths of the original system (8.6 mm) and the upgrade (4.3 mm).

measurement accuracy sacrificed for reducing the scattering length below 3 mm, and some cases will suffer with scattering lengths below 4 mm. That is, the efficiency of the trade off is constant if the scattering length is long enough, but short scattering lengths result in inefficient conversion of accuracy to resolution. The chosen value of 4.3 mm is the minimum value which achieves fully efficient conversion of accuracy into resolving power and the maximum value which meets the physics requirements.

2.3.2 Upgrade implementation

Placement

The original system measured the pedestal region along the core laser path and so the upgrade could be implemented by replacing existing fiber bundles with twice as many bundles of a smaller size. Although this was the solution which was finally selected, there was an attractive alternative which received some analysis.

The tangential beam crosses the edge of the plasma within view of one of the ports, and this intersection is very close to the machine midplane. Most diagnostics produce measurements at the midplane and although it is possible to relate profiles from different poloidal locations through the equilibrium reconstruction, the mapping is not perfect (see Sec. 2.8). It would be very useful to have electron and ion profiles taken from the same poloidal angle to reduce uncertainty in the total pressure gradient and the main ion density. Furthermore, tangential/midplane placement of the upgrade would have made it an addition to the top of the machine profiles and would have allowed interesting comparisons. The proposed location of the edge midplane TS system is shown in figure 2.13.

However, the flux surfaces are more tightly packed at the midplane than at the top of the machine. In order to achieve the same effective resolution, chords at the midplane would have to use smaller fiber bundles and thus experience lower signal to noise ratios. Even worse, these chords would be close to the extreme limit of the midplane lens's field of view even after reasonable modifications. Simulations showed that not enough signal could be collected to meet both the design accuracy and resolution requirements without completely replacing the collection optics, port flange, and mounting hardware. Even then, the top of pedestal view would have superior performance.

A HRTS implementation at the midplane would have been less accurate, more expensive, more difficult to implement, impractical to reverse in case of serious problems, and harder to predict. Therefore, it was decided that chords would be replaced in the original top of machine view of the pedestal.

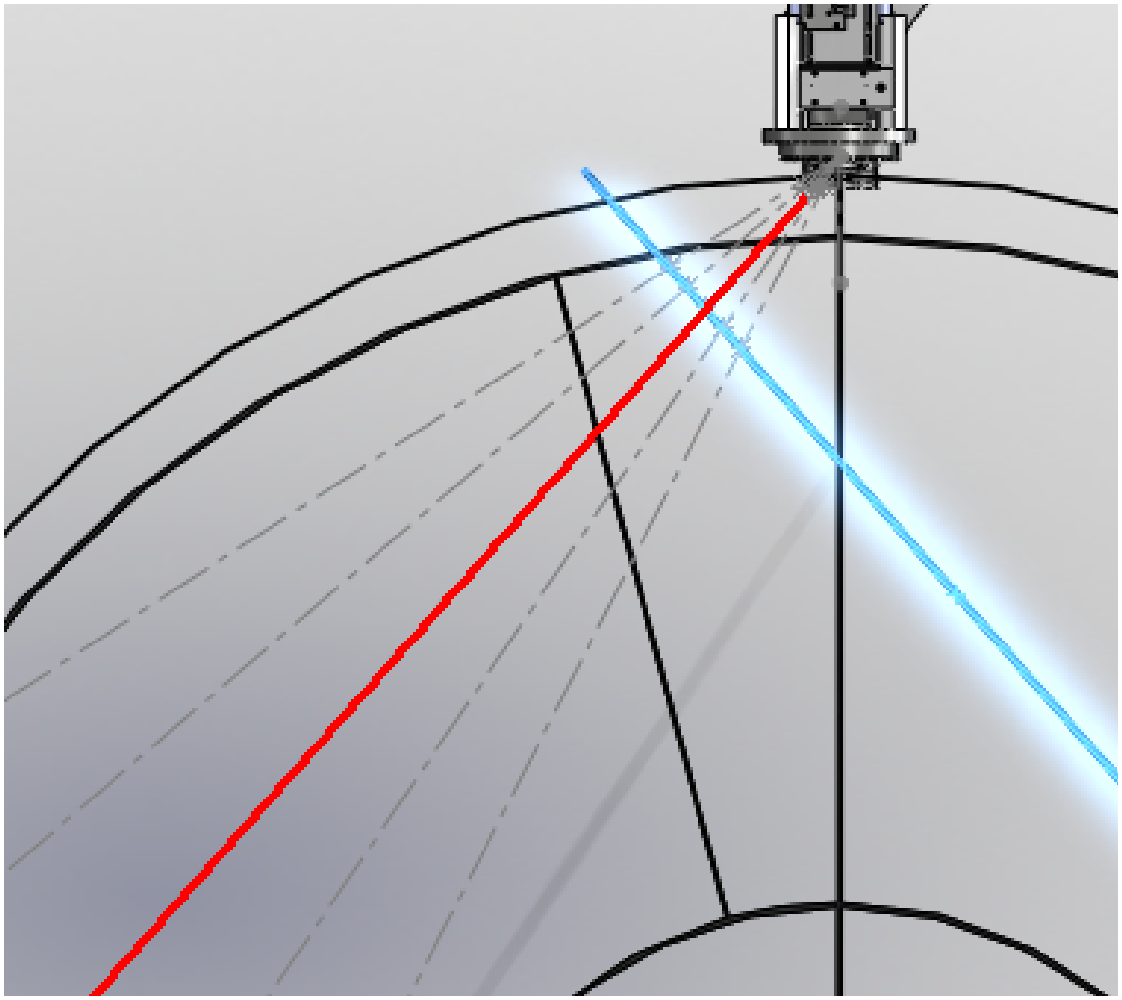

Figure 2.13: Placement of a possible TS system at the midplane of DIII-D. Concentric rings (black) are placed at the radius of the front of the first lens, the inner wall of the vacuum vessel at the outboard side, and the inner wall of the vessel at the center-post. The tangential laser path is shown with a glowing blue line. A chord aimed at R =2.29 m (intersection of chord with laser) is shown in red. Other chords (gray broken dashed lines) fan from R =2.20 to 2.35 m. A black line from the machine axis to the lenses is at machine angle of 120 degrees. Another radial black line between the vessel walls marks 105 degrees, which is the nominal entry point of the tangential laser.

Collection Fiber Bundle Design

The final design was to pack two 1.5×1.5 mm fiber bundles into a terminator of the same dimensions as the original fiber bundle ends. This allows the high resolution chords to be seamlessly integrated into the existing system and to be repositioned by swapping with the original bundles within the fiber mount. Both types of terminators are shown together in the final configuration in figure 2.14. The fibers are of the same silica/silica construction as the originals with 200 μm diameter cores, but with an additional anti-reflective coating applied to the terminals. Other terminator designs were considered, but were abandoned in favor of the simple solution described here as a factor of two reduction in bundle height was found to be optimal.

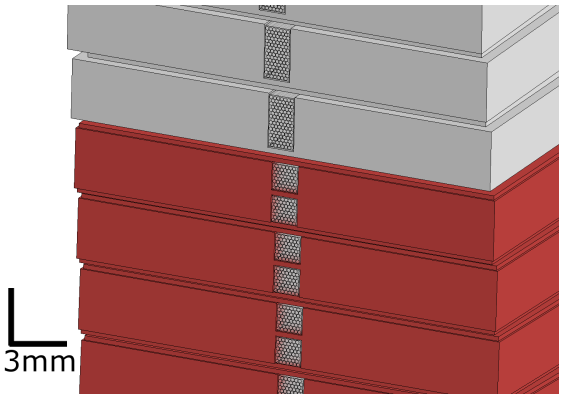

Figure 2.14: Model showing terminators of fiber optic bundles for Thomson measurements. Terminators of the original type are visible at the top of the image in gray. New terminators are at the bottom in red. The new terminators house two fiber bundles each in a package with the same external dimensions as the original, allowing them to be installed in the existing mounts. They are fully interchangeable with the old terminators.

Additional Detection Hardware

The original collection optics, fiber mount, and polychromator design were retained, although additional polychromators had to be constructed to serve the new view-chords. Ten standard chords were replaced with twenty high resolution chords occupying ten slots in the fiber mount. Ten new polychromators were built

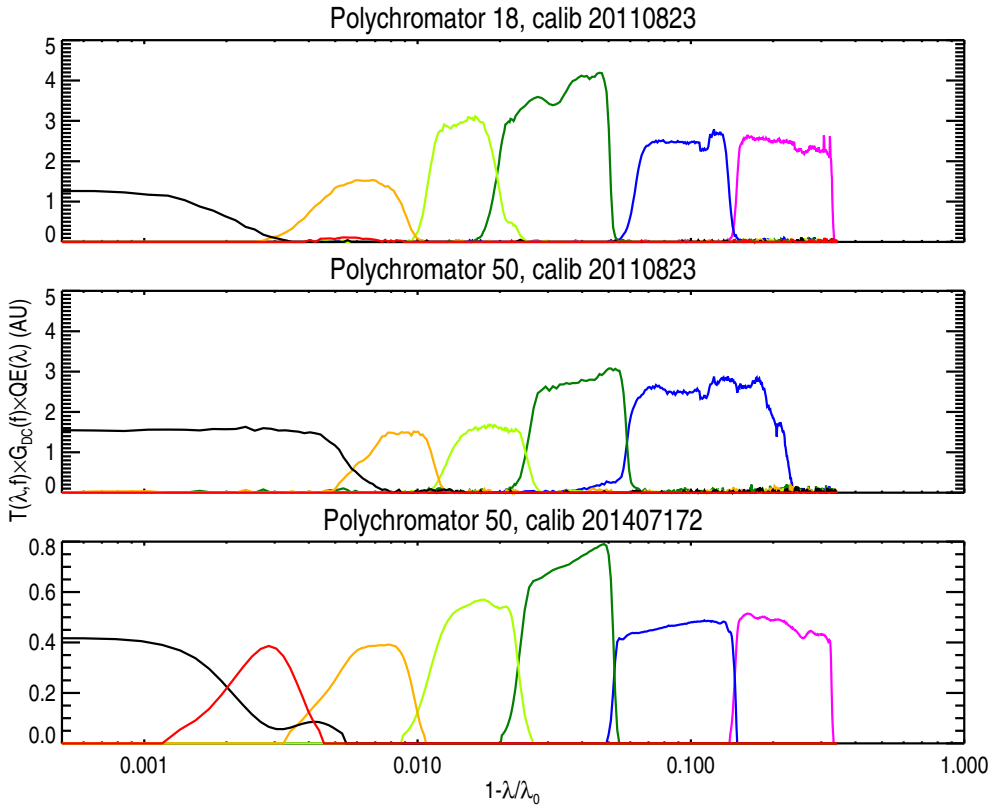

Figure 2.15: Example TS filter sets. Standard (top), new (middle) and final (bottom). The unit convention for the transmission profile is different for the bottom plot, which is reproduced from 2.7. The convention has no bearing on the final measurement (see eqn. 2.6) as long as it is consistently applied within each calibration set.

and originally used a reduced filter set, as simulations indicated that the shortest wavelength filter was unnecessary for the temperatures expected in the pedestal region (see Fig. 2.15).

Compared to the traditional filter set, the new filter set shown in figure 2.15, which was in use immediately after the upgrade, narrowed the gaps between some filters (blue and dark green), expanded the laser filter (black), deleted the shortest wavelength filter (magenta) and greatly expanded the next shortest filter (blue) into its place. Finally, although it is difficult to see, the traditional set for polychromators near the edge includes the extreme low temperature filter, plotted in red. In the example hardware shown above, this filter is performing so badly

that it barely shows up (there is a slight bump under the orange filter), although it is physically installed. The new filter set omitted this filter as it rarely made a difference, partly because it was not working properly and partly because the expected temperatures were too high for it to be relevant.

The final temperature accuracy of these polychromators is not constant, but experiences ripples due to the finite number of bins as seen in figure 2.16. Some temperature ranges are less favorable. When any given detector is producing peak signal, reports from its neighbors are needed to fix the temperature. If the temperatures where its neighbors peak are farther away because the spectral profiles of the filters have gaps, then uncertainty in temperature will be increased. So, the new filters were set up so that the shoulders would overlap a little.

Considering the example shown in figure 2.16, there are four filters in the set, making three unique pairings of nearest neighbors, and there are three minima in the temperature uncertainty corresponding to where expected signals from the dominant pair have opposite derivatives with respect to temperature. In this filter set, the "blue" filter (see middle row of Fig. 2.15) has been widened and the magenta filter has been deleted. The shift of the center wavelength of the blue filter to shorter wavelength moves the minimum associated with the blue-dark green pair out to higher temperature. However, the maximum associated with the peak of the dark green filter has increased because the blue filter has gotten farther away. When the green filter has very little variation of signal with respect to temperature because it is close to peak output, the light green and blue filters are needed to make the measurement.

It is important that the transmission probability of laser light through the "1064 nm" filter (black in Fig. 2.15) be known accurately, as it is used to relate the Rayleigh scattering calibration to the actual measurements. In the existing filter set, the transmission function is not constant with respect to wavelength around the laser wavelength (this varies between polychromators and the example shown at the top of figure 2.15 is not the worst offender). This translates even slight errors in the calibration of the wavelength of the scanning monochromatic light source (monochromator) into significant systematic errors in density. The

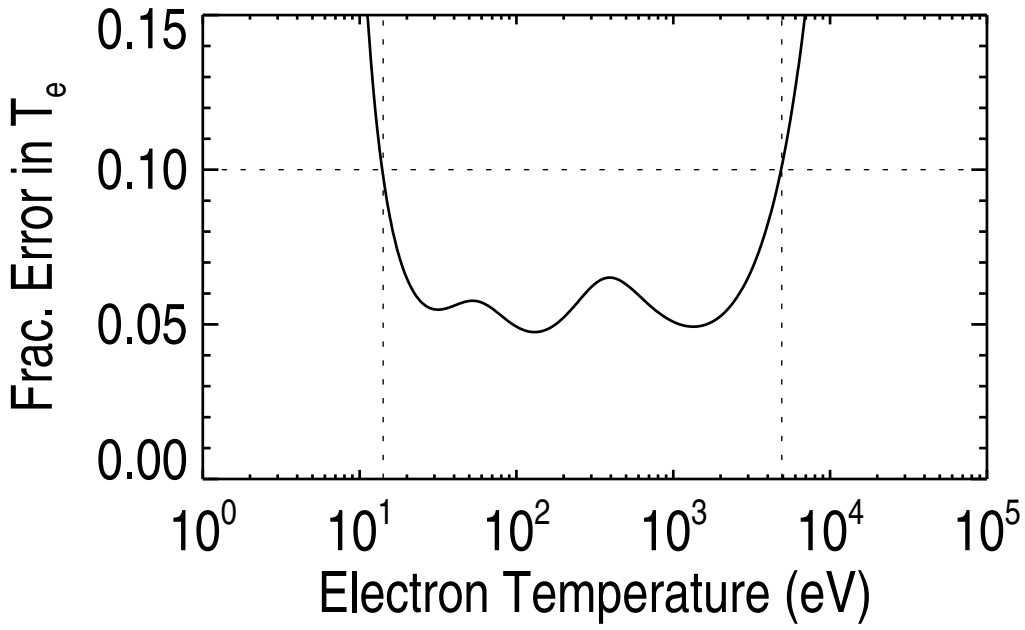

Figure 2.16: Variation in temperature accuracy with temperature for a polychromator using the reduced filter set shown in the middle row of figure 2.15.

new laser filters feature constant transmission around the laser line, which tends to reduce systematic density errors. Following the upgrade, the 1064 nm filters in the rest of the system were inspected and replaced with new filters with similarly flat transmission around the laser line. Furthermore, a low power CW YAG laser was introduced to the spectral calibration procedure to allow calibration of the monochromator wavelength by providing a landmark: The YAG is mounted near monochromator's white light source, behind the slits which select for output wavelength. Thus, YAG light escapes the monochromator only when the true output is 1064.3 nm. When the nominal output wavelength is close to 1064.3 nm, measurements are repeated with the YAG on and off at each wavelength increment. The series of measurements with the YAG on reveals a sharp peak at 1064.3 nm and allows the nominal wavelengths to be corrected.

The new filter set performed as expected and satisfied the design requirements while reducing the cost and complexity of the initial upgrade compared to producing new hardware with the traditional filter set. However, it was found

that it was easier to maintain a system of identical hardware and that the high temperature filter's contribution was sometimes useful. It is also convenient (e.g. for experimenters planning plasma shapes) for as many of the the polychromators as possible to have the same temperature ranges and performance. Therefore, the filter sets were eventually modified to converge on a common standard.

The following changes, made by the Thomson scattering group, standardized the filter set: the shortest wavelength filter (magenta, high temperature relevant) was added to the new polychromators and the next filter (blue) was reverted to the original specification (rather than the extra wide version). As mentioned above, the laser filter (black) was altered as needed (in older hardware) to acheive flatter transmission around the laser line. It can also be seen in figure 2.15 that the lowest temperature filter (red) has been added. Most of the standard chords which were located in the spatial resolution upgrade region did not originally have this filter, but the success of the upgrade generated interest in further improvements and so the red filter was added to some of the new hardware, and was replaced in old hardware where it was found to be under-performing.

Electronics and Lasers

A concurrent upgrade to the amplifier electronics decreased the length of the integration gate from 65 ns to 25 ns and reduced the delay time in the background subtraction circuit from 100 ns to 30 ns.[57] Other improvements to the electronics included reducing dark noise from 40 to 30 photo-electrons per pulse and an upgrade to a modern D-TACQ digitizer system, which can serve more chords with a shorter time between acquisitions and is also more reliable than the old CAMAC digitizer. The net result on signal to noise was improvement by a factor of 2.5 to 6, depending on conditions. This offset the loss of signal due to shortening of the scattering length. Another concurrent upgrade increased temporal resolution by adding more lasers, resulting in seven operational lasers on the core path with a total repetition rate of 230 Hz.[58]

2.3.3 New analysis software

The Thomson scattering diagnostic is managed by an operator in the control room to ensure data quality is acceptable. This entails examining analyzed data and taking corrective action as needed, such as replacing failed detectors, resetting and aligning lasers, warning the session leader of non-optimal positioning of the plasma for TS measurements, or flagging problem chords for recalibration. Previously, the operator would use standard physics analysis software to inspect Thomson data in a painfully slow process that allowed spot checks of profiles or time traces of measurements from a few chords at a time. The Thomson Scattering Data Viewer (`TSDV`) was developed to allow fast, complete inspection of the fitted and raw data and convenient access to statistical tools. This software has improved data quality by making the Thomson operator more effective at managing the diagnostic in the control room.

The tedium of data inspection was reduced dramatically, which resulted in faster and better identification of problems. Subtle, long standing calibration errors became obvious and quantifiable and were subsequently corrected by the Thomson group. Although this new ability to quickly and easily view data motivated several improvements to hardware and calibration procedures, systematic errors continue to exist. This is due to uncertainty in the calibration measurements themselves and drift in gains and spectral transmission functions over time. The statistical tools included in this software package allow a trained operator to distinguish between small ($\sim$1%) systematic errors and small scale physical features. This allows Thomson scattering measurements to go beyond being used to merely determine the height and width of the pedestal and be used, for example, as a tool for detecting subtle changes in gradients which can then be compared to theories about formation of islands or stochastic regions, or localized changes in transport.

The centerpiece of `TSDV` is a trio of plots which can be quickly and easily customized and repeated and which have persistent settings selected from a common control panel, ensuring that the different plots correspond to each other perfectly. The three centerpiece plots are a contour of a chosen parameter (e.g. electron temperature) vs. time and position, a profile of a parameter vs. position,

and a time trace of a parameter.

The contour plot is especially useful, not least because it is (surprisingly) unavailable from the previous tool-set (technically it is possible to obtain contours, but they are mapped incorrectly and they can not be customized and correlated to profiles and traces quickly or easily). The contour plot gives the best overview of a shot and displays all of the data for one parameter at once, rather than slicing it. Data are correctly mapped to real space along the laser, to flux space (ψ_N or ρ_N), or mapped to the midplane using a flux map. A flux map is computed for each time-slice separately (automatic JT `EFIT` loaded by default as EFIT03).[71] Systematic errors stand out as straight lines that follow the fixed locations of the individual chords in real space and break unnaturally from the contours of the plasma in flux space. The contour plot is especially helpful because chords can transition from being systematically low to systematically high in different temperature ranges, which can defeat attempts to compare time averaged values to neighboring chords and can be confusing when stepping through time-sliced profiles. From a well configured set of contour plots, a trained operator can identify several different pathologies at a glance. `TSDV` provides extremely fast and convenient access to this functionality.

The parameter options obviously include temperature and density, but also include background signal level and signal to noise level, which are useful in discriminating between background saturation events and more serious problems. A great strength of this program is the speed with which the user can switch between an overview of a shot on a contour and one of the more specific plots, such as a profile. The profile can in turn be averaged over the same time range as was selected and displayed in the contour, allowing the same data set to be viewed from different perspectives within the same tool.

The data set can easily be filtered based on the main plots and then fed into a suite of calibration checks including a comparison of the measured signals with expected signals based on the calibration and measured laser energy, and statistical tests (see appendix A.5). The ability to select and visualize the same data set as is being supplied to the calibration and statistical checks is very useful and allows

the operator to quickly understand what is happening. Errors in calibration can be identified minutes after a shot completes and traced to specific temperature ranges where specific filters are active, allowing maintenance efforts to be precisely targeted.

2.4 Results

2.4.1 Upgrade performance

The upgraded Thomson system came online for the 2011 experimental campaign.[51,53,54,56] The achieved resolution was half of the previous value at 6 mm between chord centers along the laser, or 3.5 mm when mapped the outer midplane with a typical flux map (previously: 12 mm and 6.8 mm respectively). The mapped extent of the scattering volume across the flux surfaces at the midplane is 2.5 mm for a typical discharge, compared to 4.9 mm previously. Examples of profiles from single laser pulses from the upgraded HRTS are shown in figures 2.17 and 2.18. If lower random errors are required, profiles from several profiles may be averaged together.

Transmission through the new fiber bundles was surprisingly high: the new fibers transmitted roughly 50% more efficiently than the old ones after controlling for individual broken fibers within the old bundles (usually from 0 to 2 per bundle of 104). The cause is thought to be a combination of radiation darkening of the old fibers and the anti-reflective coating on the new fibers, which is expected to provide a $\sim 5\%$ improvement. The silica fibers being used are fairly tolerant of radiation, but they have been in place for decades. So although the new bundles are half the size of the old ones, they transmit nearly as much light. The new system would've met its temperature accuracy and minimum density requirements even without this bonus, but because of it, random errors in measurements from the high resolution chords are comparable to random errors from the standard chords, as seen in figures 2.17 and 2.18. All chords benefited equally from the electronics upgrade.

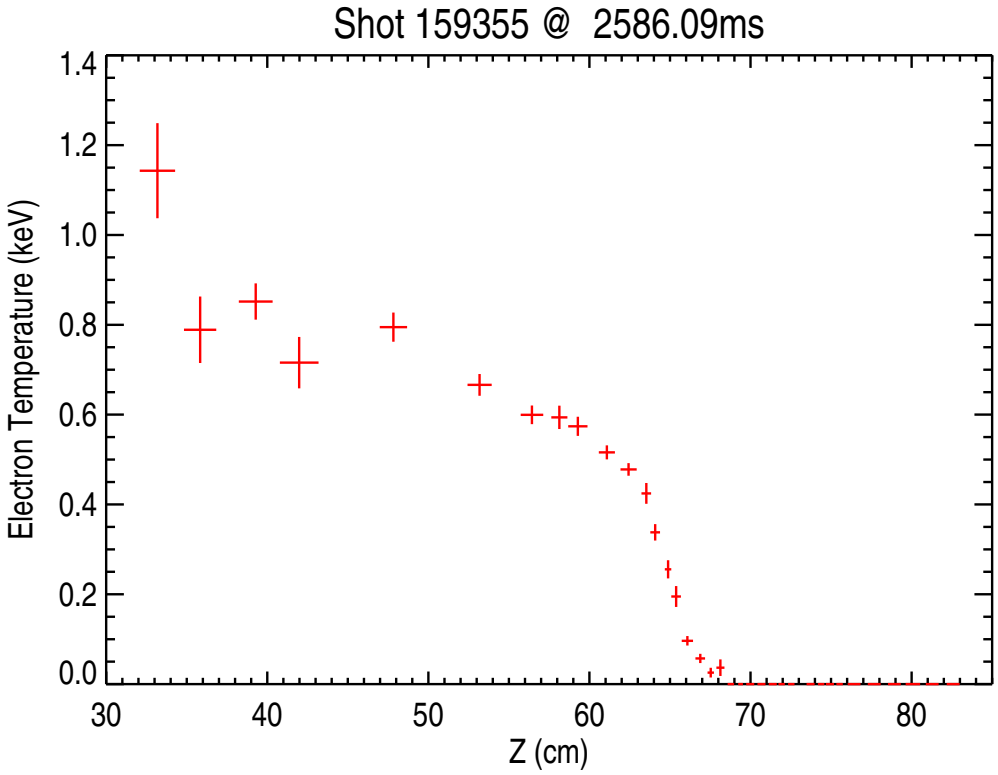

Figure 2.17: Post-upgrade example profile of electron temperature vs. Z along the core laser path (see Fig. 2.4). The vertical error bars represent 1 sigma random uncertainty in the reported temperature, calculated from photon statistics and detector dark noise. The horizontal error bars represent the empirically measured scattering lengths. The high resolution band starts at the knee of the pedestal in this shot (63.5 cm).

2.4.2 Systematic errors revealed and corrected

Because of improved spatial resolution in some parts of the system, improved accuracy (electronics upgrade) and temporal resolution everywhere, and innovations in the way data were checked in and out of the control room, any systematic errors in the final measurements are now very obvious.[56] When the upgrade came online, it was evident that the calibration set was flawed and systematic errors were present in the reported temperature and density data. In general, repeating the calibration procedure did not correct the apparent errors. The factors which contributed to the observed systematic errors were pre-existing and were only made more obvious by the upgrade, due to higher spatio-temporal

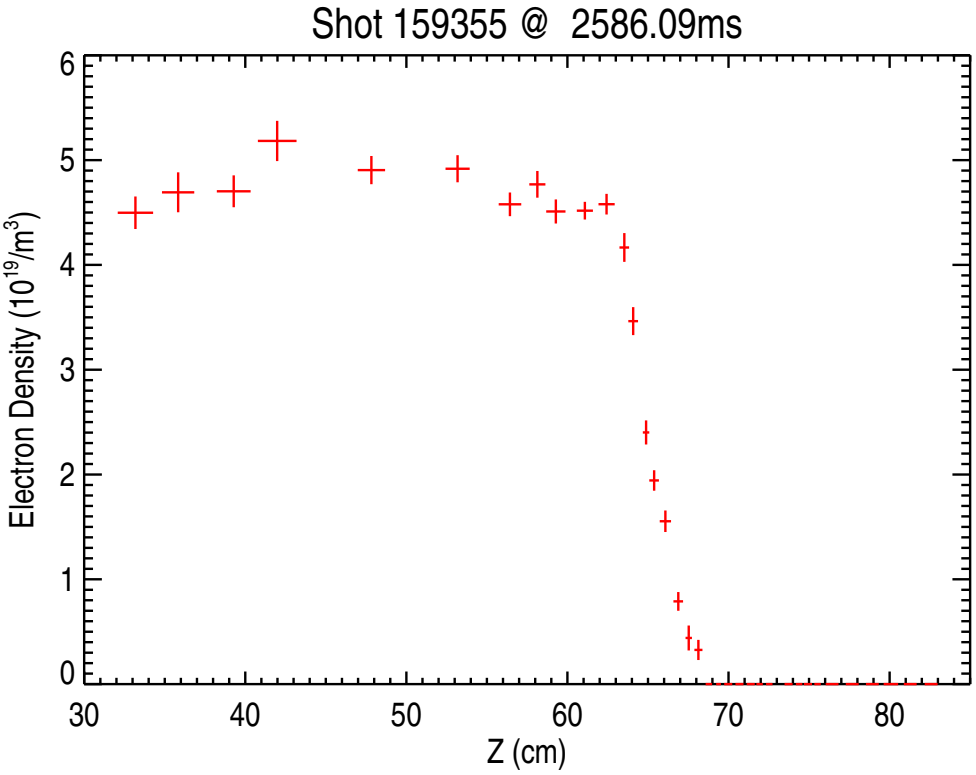

Figure 2.18: Post-upgrade example profile of electron density vs. Z; corresponds to figure 2.17.

resolution, smaller random errors, and better tools.

The dominant factor was that details in the calibration which may have been negligible with new hardware when the system was built in 1990 had become significant as the system aged or as a result of modifications or upgrades. For example, the glass in the lenses was darkened by radiation. The standing assumption prior to analysis related to the HRTS upgrade had been that the darkening did not have significant spectral dependence and would be taken care of by the Rayleigh scattering calibration which is carried out at the laser wavelength only. It turned out that the lenses had browned significantly and transmission was much lower at shorter wavelengths than at the laser wavelength. This resulted in systematic temperature errors as large as about 30% in the most extreme cases (high temperature, large scattering angle), but on the order of 1% in the pedestal. These errors were similar for most neighboring chords, which made them harder to detect. It

is now understood that all of the collection optics must be spectrally calibrated at regular intervals.

Another serious problem was that the gain of the detectors is sensitive to the temperature of the APD and the detectors must be maintained at the same temperature as the temperature at which they were calibrated. Temperature is measured via a thermistor mounted in the copper block which houses the APD. More serious still is that the ratio of gains between the pulsed (scattered light) and DC (background light) channels seems to depend on temperature, for unknown reasons. Additionally, there is hysteresis in gain as temperature varies, preventing a simple calibration from overcoming the effect. These issues may or may not be features of the new amplifier design. It is also possible that the improved signal to noise ratio of the new amplifier circuits means that errors of this nature are now more apparent compared to uncertainty due to photon statistics. Temperature stabilization is accomplished through a water cooling system. However, the new amplifier design changed the physical dimensions of the detector/amplifier unit and this may have increased its thermal coupling with the air in the room. The air conditioning unit in the lab cycles on and off periodically and is only capable of stabilizing the room temperature to within 1 °C, which results in unacceptable variation in gain and gain ratios. An insulating enclosure was erected around the detection hardware and the water chiller was upgraded, stabilizing temperatures to within 0.1 °C and solving the problem.

Laser alignment monitoring was improved following the high resolution upgrade. The area imaged by the collection fibers is 4.6 mm wide, whereas the lasers are about 3 mm wide. As the amount of energy emitted in each pulse is measured before the laser enters the vacuum vessel and this information is required for a correct density measurement, it is important that the laser stays within the imaging area. The original system was equipped with alignment monitoring fibers mounted behind the collection optics[60] and with cameras placed along the beam-line. The fibers were arranged in groups of 5 and interleaved with the fiber bundles used to take data such that in the case of optimal alignment, all of the imaged laser light would fall on three of the five alignment fibers, with the other two at the edges of

the group and receiving almost no scattered light (they will see a little due to the beam halo).[65] However, this system had fallen into disuse and the cameras alone were relied upon for controlling alignment during operations. This proved to be insufficient, as systematic differences in density between measurements made by the same detectors but using different lasers were observed. The fiber based alignment monitoring system was repaired and it was confirmed that nominal alignment to the reticules on the cameras did not result in ideal alignment as measured by the fiber system. Changes to the alignment procedures improved systematic agreement in density measurements by different lasers.

2.5 Special Techniques

2.5.1 Bunch Mode

In systems using pulsed lasers, data are gathered over a short window ($\sim$ 10 ns in this case) and temporal resolution is as fast as the laser(s) can repeat. In general, the short averaging time allows pulses from the same phase of a periodic behavior to be combined into a composite profile, even if the cycle is faster than the system's temporal resolution, because any given profile is practically instantaneous compared to the timescale of most plasma processes. In systems that use a group of co-linear lasers, such as at DIII-D, "bunching" the pulses together in time can provide brief periods of elevated temporal resolution to examine rapid evolution during or after a short-timescale event or process such as a disruption, pellet injection, ELM, L-H transition or limit cycle oscillation.

Activating bunch mode is simply a matter of adjusting the phase shifts of the different lasers, which each repeat at their own preset frequency of either 20 or 50 Hz (see figure 2.19). Arbitrary phase shifts are allowed as long as the time between pulses is long enough for the data acquisition system to finish a measurement before the next pulse arrives. The time required for data acquisition is nominally 100 μs, although measurements with 80 μs spacing have been successful. If the spacing is too short, the second pulse may not be recorded. The phase shifts are pre-programmed and fixed before a shot.

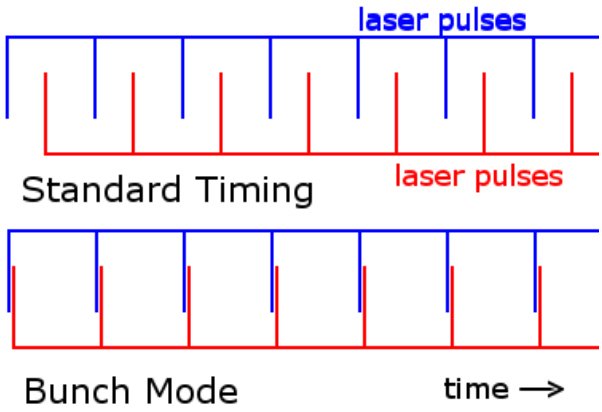

Figure 2.19: Cartoon explaining bunch mode for two colinear pulsed lasers. The phase shifts are adjusted so that the pulses occur in rapid succession, rather than being evenly spaced. This is obviously generalizable to arbitrary laser count.

If all of the pulses are arranged into a single bunch, the main bunch will repeat at 10 Hz (set by the least common multiple of the 20 ms and 50 ms periods), and there will be smaller bunches interspersed at 20 and 50 Hz between the main bunches. The cost of bunch mode is increased maximum time interval between pulses, although the average pulse frequency is constant.

Figure 2.20 shows an example use of bunch mode to observe fast shutdown triggered by Massive Gas Injection (MGI). MGI is a disruption mitigation technique which is being tested in preparation for use in ITER.[72] In this case, the injected gas is neon, which effective at dissipating large amounts of energy through radiation, which reduces the heat load on the divertor. MGI also increases density in an attempt to suppress runaway electrons[73] through enhanced collisional damping. Thomson scattering in bunch mode has been used to observe a cold front propagating inward, as seen in the figure: density increases dramatically while temperature falls below 100 eV. In the last two frames, background light is very high and most Thomson chords fail to return useful data, but the few survivors indicate very cold dense plasma, consistent with the trend in the earlier frames.

Bunch mode might also be used as a means of trading temporal resolution for accuracy. That is, run bunch mode in a low SNR environment with the intent to average each bunch into a single profile. Physics analysis is often done with data taken over the shortest time range that provides adequate accuracy through

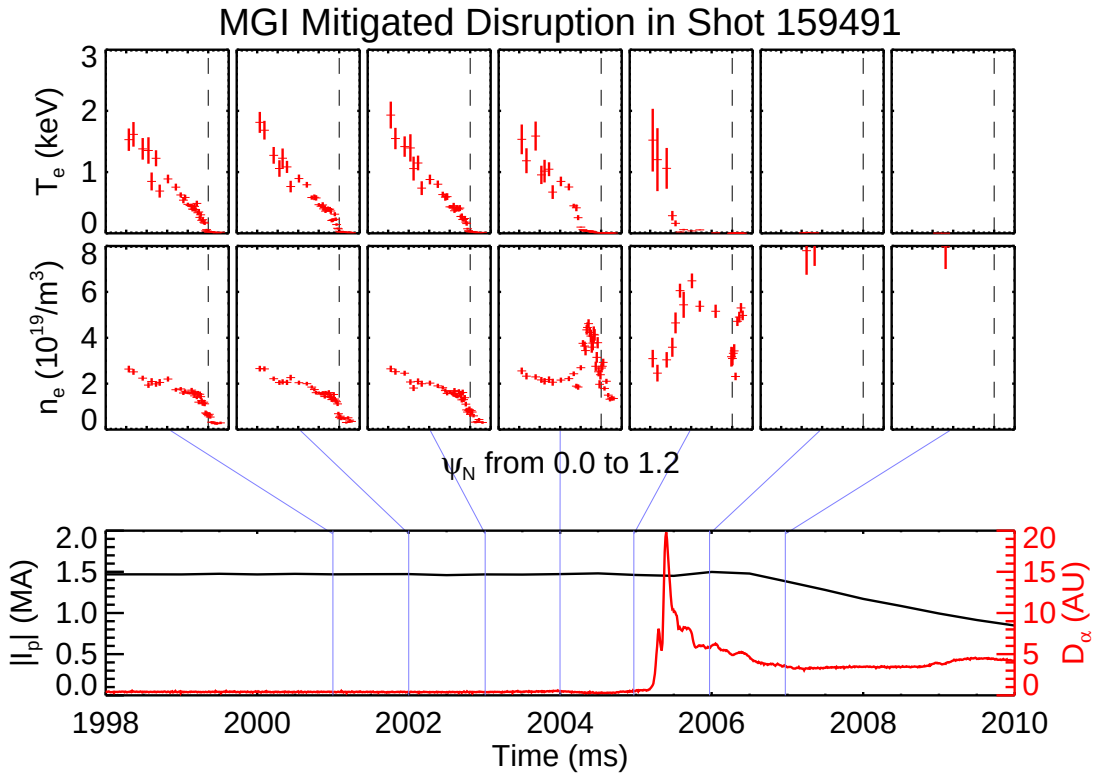

Figure 2.20: Sequential profiles of T_e and n_e during a disruption. Top: T_e profile series. Middle: n_e profiles. Bottom: plasma current I_p and D_α line emission. Bunch mode is used to obtain data at 1 ms intervals for 7 pulses.

averaging several pulses at different times. If the number of slices required to achieve a good profile is less than or equal to the number of lasers (seven lasers are available on the core path), bunch mode would allow an accurate profile to be constructed from a much narrower time range (< 1 ms instead of ~ 30 ms). However, this technique has not achieved popularity.

2.6 Analysis Techniques

In the past, the modified hyperbolic tangent fit has been a reliable means of obtaining smooth curves describing the electron temperature, density, or pressure profiles[74] which remains useful for most cases today. However, this fit is purely empirical: it looks right, but there is no underlying physics model to justify it.

Furthermore, the high resolution Thomson scattering system is capable of measuring detail beyond what the tanh fit is capable of describing and decidedly non-tanh profiles have been observed, especially in the presence of 3D magnetic perturbations. Spline fits are an option for dealing with non-tanh features, but common methods rely on a human operator to choose the number or placement of knots for each fit which is bad for speed and reproducibility. Therefore, new methods are explored for quickly and consistently producing smooth curves describing the electron profiles measured by HRTS.

Profiles produced by the following techniques have shown very good agreement with tanh fits in many cases, which supports continued use of the tanh fit in profile analysis. For the cases examined in chapter 4, there is no significant difference in the results of tanh fits and the alternatives presented here, and so standard tanh fits are used for consistency with previous results. However, there are cases (see Sec. 2.7.3) where the tanh fit is clearly inadequate and so alternatives are used. Even for profiles where a tanh fit appears to be fairly successful, fine structure may be overlooked and detailed comparison of profiles in chapter 5 takes advantage of the new techniques discussed here. These methods have also been adapted to analyze profiles from other diagnostics in chapter 5.

2.6.1 Variable Radius Gaussian Blur with Uncertainty Weighting

Inspired by a common smoothing method for treating images such as photographs, the VAriable RAdius Gaussian blur with Uncertainty weighting (VARAG-U)[55] computes the value at an arbitrary location as the weighted average of points in the neighborhood, with the weighting function given by a Gaussian modified by a factor to account for uncertainty:

$$W = \mathrm{Exp}\left(-\frac{\Delta x^2}{2\lambda^2}\right)\mathrm{Exp}\left(-\frac{\Delta t^2}{2\tau^2}\right)\frac{1}{\sigma^2} \tag{2.7}$$

where Δx and Δt are the differences in position and time between the calculation point and the measured data, λ is the spatial blur radius, τ is the temporal blur radius, and σ is the measurement uncertainty. In recognition that the diagnostic

inherently blurs its own measurement (finite instrument function, see figure 2.11), λ is set to be proportional to the local instrument function: $\lambda = f\delta x$ where δx is the extent of the measurement volume across the coordinate of interest. For example, the half width half maximum of the instrument function in ψ_N is a good choice of definition for δx. VARAG-U may be operated with more output points than input points, resulting in up-sampling to a smooth curve rather than a jagged linear interpolation. The dependence of the value y and uncertainty σ of output point i on neighborhood points j is given by

$$y_i = \sum_j y_j p_{ij} \tag{2.8}$$

$$\sigma_i = \sqrt{\sum_j \sigma_j^2 p_{ij}^2} \tag{2.9}$$

where p_{ij} is the normalized weight:

$$p_{ij} = \frac{\frac{1}{\sigma_j^2}\mathrm{Exp}\left(-\frac{(x_i-x_j)^2}{2(f\delta x)^2}\right)\mathrm{Exp}\left(-\frac{(t_i-t_j)^2}{2\tau^2}\right)}{\sum_j \frac{1}{\sigma_j^2}\mathrm{Exp}\left(-\frac{(x_i-x_j)^2}{2(f\delta x)^2}\right)\mathrm{Exp}\left(-\frac{(t_i-t_j)^2}{2\tau^2}\right)} \tag{2.10}$$

and it has been assumed that random errors in neighboring points are uncorrelated, as they must be for Thomson measurements.

If it is assumed that systematic errors are randomly oriented and that there are enough chords available that a subset of half the chords could capture meaningful structure if working ideally, then the blur factor f can be increased until variation on the scale of the chord spacing begins to be suppressed. This will confer some protection from systematic errors while still producing a reproducible smooth curve which operates on the data using only one control parameter per dimension (f for space and τ for time).

VARAG-U differs from typical Gaussian blur techniques in common usage in that it recognizes that its source data are not from evenly spaced identical pixels but from uniquely shaped scattering volumes with varying degrees of accuracy.

The technique can be extended even further to use missing data (recorded as 0 ± 0; successful fits and uncertainties cannot be 0) as information by making reasonable assumptions about the behavior of the TS diagnostic. Data will

be missing because (1) random errors in the raw signals happened to defeat an individual fit to temperature and density, (2) the chord malfunctioned or one of its detectors saturated and its measurements were automatically suppressed, (3) the density and/or temperature were out of range of the filter set. (1) typically causes individual missing points surrounded (in time and space) by good data. (2) typically causes "lines" of missing data surrounded in space by mostly good data. (3) typically causes large groups of missing data with a few scattered successful measurements. So, if a missing datum has neighbors which are mostly good, then it is just a bad point and should be ignored. But if a missing datum has neighbors which are also missing, then the local density and temperature are probably low (this could in principle happen because of out of range high temperature or density, but this has not been observed in the pedestal region). This information can be used to improve the behavior of profiles returned by VARAG-U by readmitting the bad (0 ± 0) data which occur in large groups and assigning them large uncertainty (at least double the measured error in nearby good chords). This gives a soft constraint which pulls the profile down toward zero smoothly at the edge of the profile. Otherwise, if all of the low valued SOL points fail to return fits, then the profile will extend a shelf out at the minimum measured value and then truncate abruptly when Δx becomes large enough to cause a floating underflow in $\mathrm{Exp}(-\Delta x^2/2f^2\delta x^2)$. The version which uses the 0s agrees better with slices where points in the SOL do return valid measurements, produces cleaner gradients, and makes more physical sense.

Of course, the best option is to cut off the part of the SOL which is returning 0 ± 0, but this can be difficult if the plasma moves relative to the selected position coordinate or if data are processed in bulk with minimal human supervision. The treatment of missing data described here will give results containing relatively benign artifacts which won't confuse edge detection schemes, rather than unnatural "shelves" which will produce huge spikes in gradients.

2.6.2 Weighted Average of Offset Profiles Interpolated to Common Position Base

A simple technique for obtaining a profile with minimal random error is to average the values returned from each chord during a specified time window. However, this method is defeated if the equilibrium shifts by more than roughly the chord size during the time window. The time averaging technique can be extended to instead embrace equilibrium shifts by first interpolating the data to a common position base and then averaging. This works surprisingly well, especially if the uncertainties are also interpolated and used in a weighted average. The result is a smooth curve with arbitrary up-sampling which gives a good representation of the source data and has no user controls other than the data ranges in time and space. The Weighted Average of Interpolations to a Common base (WAIC) technique is demonstrated in figure 2.21.

Given a set of data y_{in} as a function of position x_{in} with uncertainty σ_{in}, where all three quantities can vary with time and space (they are 2D), and a desired output position array x_{out}, which is 1D, y_{out} is a simple linear interpolation from x_{in} to x_{out} for each timeslice and y_f is the weighted time average of the slices y_{out} with weighting function $w = 1/\sigma_{out}^2$ and normalized weighting function $p = w/\sum w$ where the sum is over time.

To enhance rejection of bad chords, the uncertainties are not interpolated directly but instead $\sigma_{out} = \sqrt{\text{interpol}(\sigma_{in}^2)}$ where interpol is a function which interpolates from x_{in} to x_{out}. The difference is shown in the middle plot in figure 2.21 where the black curve represents the formula given above and the dashed red curve results from $\sigma_{out} = \text{interpol}(\sigma_{in})$. It can be seen that data in the neighborhood of a high uncertainty point are given less weight (more rejection) by the black curve. Bad data (e.g. $y_{in} = 0 \pm 0$ or a chord with a serious calibration problem) should be removed prior to interpolation. It is furthermore useful to enforce a minimum error level, to prevent extrapolation to 0 or negative uncertainty at the edges of the data set (assuming the data end in the SOL where SNR is low and many measurements fail, providing sparse data). The final uncertainty σ_f can be calculated as the standard deviation or the error in the mean (eqn. 2.9). The weighted standard

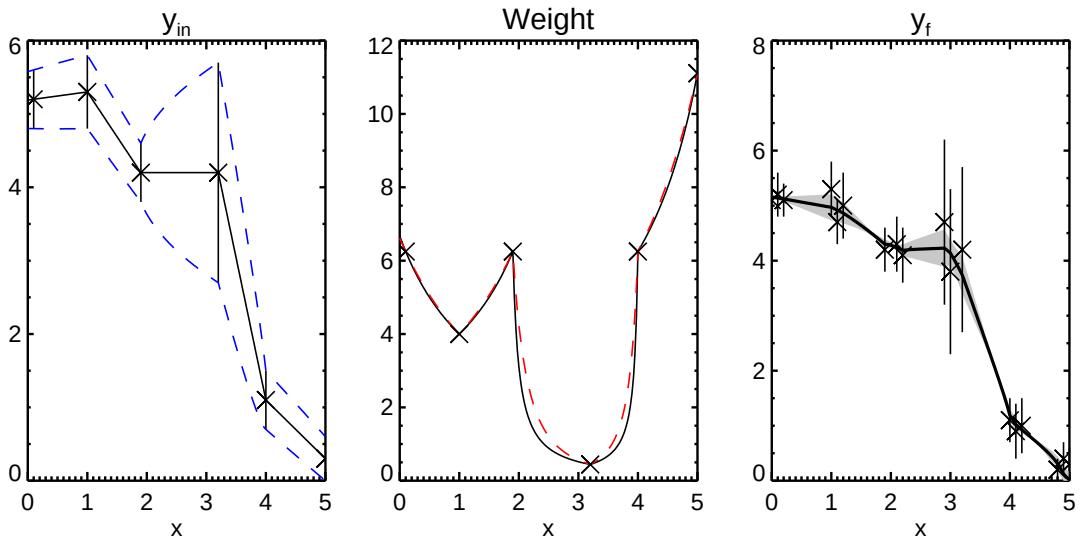

Figure 2.21: Demonstration of the weighted average of profiles interpolated to a common base technique for producing smooth representations of experimental data. Left: a single time slice of data (Xs) and the interpolation (black line). Middle: the weighting function (black) compared to a simpler weighting function (red dashes). Right: a set of data (Xs with error bars) and the resulting smoothed curve (thick black line) and uncertainty (shaded gray area).

deviation is $\sigma_f = \sqrt{\sum p(y_{out} - y_f)^2}$ and this quantity has been represented by the gray area in figure 2.21.

If this technique is employed in a data set where the positions shift over time, then minor chord-chord systematic errors can be defeated if the shift is greater than the chord spacing. Positions might shift over time if the the spatial coordinate is flux based such as ψ_N and the equilibrium reconstruction changes during the time window. Each timeslice should then be given its own equilibrium mapping. The final profile represents the data as they are measured: systematic errors are not removed unless neighboring chords have uncorrelated systematic errors and the position sweep is long enough to smear these together. The WAIC technique is available as an option in TSDV (see section 2.3.3).

A surprising feature of this technique is that it produces smooth curves if the chord positions vary even slightly over time. While a linear interpolation to a single slice returns a jagged set of line segments, WAIC operated on a handful of slices returns a more natural curve which is useful for physics analysis. It is

also computationally cheap and has been used in chapter 5 and in some example applications of the Thomson upgrade listed later in this chapter.

2.6.3 Edge Detection

An advantage of the tanh fit is that it provides parameters for the pedestal height and width. To reproduce this feature, should it be required, using the smoothed curves obtained by VARAG-U or WAIC, an edge detection scheme may be used.[55] Either of these methods can simultaneously provide arbitrary up-sampling and enough smoothing to support several derivatives. The positive and negative peaks in the second derivative can be used to define edges of the steep gradient region. From there, assigning height and width is trivial.

Another strategy is to take the difference of two levels of smoothing of the first derivative in a difference of Gaussian scheme (see figure 2.22): blur the gradient (reusing VARAG-U would be a good choice) and save it as SG_1, blur the gradient again with stronger smoothing ($5-6\times$ larger Gaussian radius is typical) and save it as SG_2, take the difference $DG = SG_1 - SG_2$. There will be a root in DG on each side of the maximum gradient. These are the edges of the steep gradient region, from which can be found the pedestal height and width. They may need to be scaled for compatibility with tanh fits in cases where the shape conforms to the tanh function.

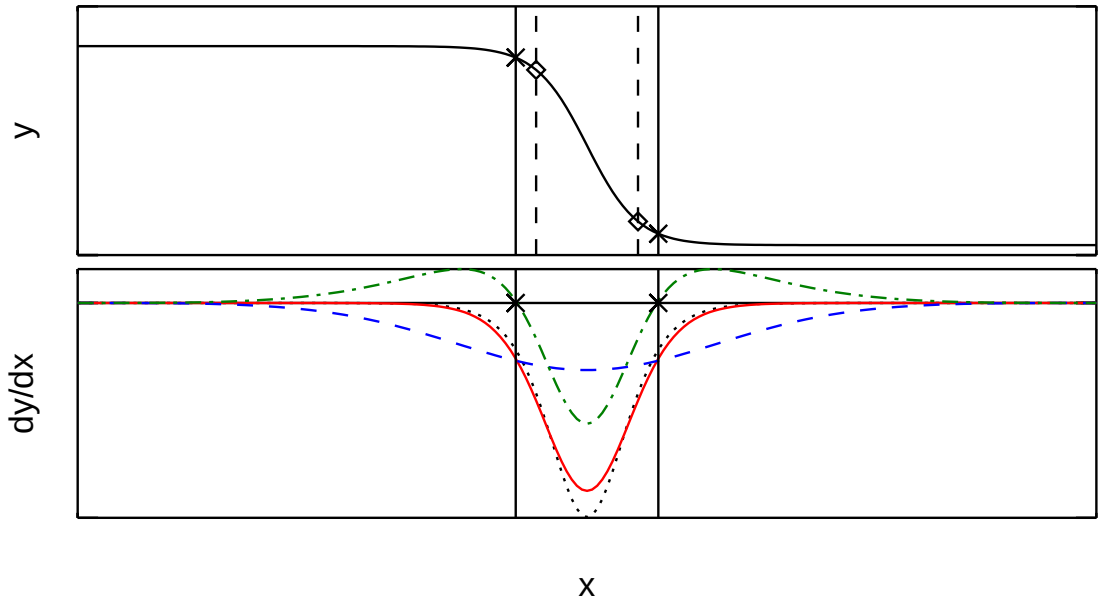

Figure 2.22: Difference of Gaussian edge detection scheme. Top: $y(x)$. Bottom: dy/dx (black dotted line), mild smooth SG_1 (red solid), aggressive smooth SG_2 (blue dashed), difference DG (green dashed dotted line). The zeros of DG closest to the peak in dy/dx are the edges of the steep gradient region, marked with solid vertical lines and Xs. The edges of the tanh function are shown with dashed vertical lines and diamonds.

2.7 Physics Usage of the High Resolution Thomson Scattering Diagnostic

Thomson scattering is a key diagnostic which provides electron temperature and density profiles to every experiment. As the resolution upgrade was built seamlessly into the existing TS system, HRTS data are available for virtually every DIII-D shot since the upgrade was commissioned in 2010. Aside from making routine analysis for general cases more convenient, HRTS has proven to be an extremely useful cutting edge scientific instrument which has been essential to several recent physics advances, including improved validation of the `EPED` model for pedestal height and width, studies of the heat flux width in the scrape off layer, identification of local flattening of electron temperature profiles during application of resonant magnetic perturbations, and the stability analysis in chapter 4 of this

dissertation. Thomson data were also useful in chapter 5.

While convenient access to analyzed Thomson temperature and density measurements is provided through standard software at DIII-D and this is sufficient for a broad range of applications, some of the research listed below required more detailed analysis and careful inspection of the Thomson data, which was accomplished using TSDV (see Sec. 2.3.3).

2.7.1 EPED Validation

The significant improvement in pedestal width and gradient measurements following the high resolution Thomson scattering upgrade has allowed validation tests of the EPED model over a broader range of parameters than was previously possible. The EPED model predicts evolution of the pedestal height and width using models for Kinetic Ballooning Modes (KBMs) and ideal Peeling-Ballooning (P-B) modes[50] and is an important tool for understanding pedestal physics.[75]

The KBM is a short wavelength instability driven by pressure gradients. KBMs regulate pressure gradients by driving enhanced transport when the gradient is near the critical level. The KBM constraint in EPED is cast as a limit on pressure pedestal height as a function of pressure pedestal width. After transitioning to H-mode or after recovering from a large ELM, the pedestal height will quickly develop until it reaches the KBM limit. Then, further increases in height must come with increases in pedestal width. The plasma evolves along a trajectory in height-width space set by the KBM.[50]

Ideal P-B modes also set a limit on pedestal pressure height vs. width, but unlike the gentle KBM, the pedestal pressure gradient rapidly relaxes, expelling material into the scrape off layer to be transported to the divertor targets. The P-B limit on pedestal height is also cast as a function of pedestal width, but it has a different slope than the KBM limit such that typical evolution involves the pedestal height and width increasing along the KBM line until the intersection with the P-B constraint, at which point a P-B instability drives an ELM and rapidly reduces the pedestal height. The cycle will repeat as long as power is available to drive it. An example of this cycle is shown in figure 6 of Snyder *et al.*[50]

Both the KBM and P-B constraints vary with parameters such as plasma current. When current is varied, the trajectories and intersection points (where ELMs are triggered) change. Higher currents result in narrower pedestals.

The TS upgrade has supported validation work by Snyder and others[50,75] and has allowed `EPED` to be tested with greater accuracy. HRTS is especially important for the narrow pedestal / high current cases. `EPED` has now been validated on three machines including DIII-D with pressure varying by a factor of 20, thanks in part to high resolution Thomson diagnostics on those machines.[75]

2.7.2 Scrape Off Layer Physics

Heat flux from the plasma to material surfaces is a very important topic for next step devices like ITER and DEMO. In particular, it is important to be able to predict the width of the heat flux profile onto the divertor targets. Good measurements of the temperature and density scale lengths at the foot of the pedestal and in the scrape off layer are required for testing models for heat flux width and these measurements are now available as a result of the upgrades to the Thomson scattering system at DIII-D.[76]

Makowski *et al.*[76,77] use Thomson data to test models for heat flux width, finding evidence to support a model where microinstability of ballooning character (they propose a kinetic ballooning mode) sets a critical pressure gradient. In this model, the heat flux width is set by the pressure gradient scale length at the separatrix. High resolution is essential to resolving gradient scale lengths.

2.7.3 Profile Changes During Applied Resonant Magnetic Perturbations

Resonant Magnetic Perturbations (RMPs) are applied using sets of internal and external coils. On DIII-D, the internal coils are arranged in two rows of six, above and below the midplane and between the vacuum vessel and the carbon tiles. RMPs are of interest because they have been shown to suppress type-I ELMs in H-mode under the right circumstances.[78]

A suspected mechanism for ELM suppression by RMP is that formation of a magnetic island or stochastic region near the top of the pedestal provides a limit to pedestal growth.[50] That is, a localized increase in transport resulting from stochasticity or an island forces a shallow pressure gradient at some location inside of the pedestal. An island is a closed magnetic flux tube which is bounded by its own separatrix and forms by reconnection of magnetic field lines. As the pedestal develops, the inner edge of the steep gradient region cannot expand past the RMP induced gradient reduction. The outer edge obviously cannot expand past the separatrix and into the open field lines. This sets an upper limit on pedestal width. The pedestal height is limited by the kinetic ballooning mode at any given width. The effect of RMPs then is to place an upper limit on pedestal height and width. If this limit is below the threshold for triggering type-I ELMs, then ELM-suppressed H-mode results. The location of the RMP induced "wall" against pedestal expansion is determined by the q profile and the mode number of the RMP. Islands or stochasticity should form around a flux surface which is resonant with the RMP. The physics basis of RMP ELM suppression is still a subject of active research and there are unresolved issues. For example, stochasticity might be expected to reduce temperatures while having minimal effect on density, yet it is observed that density decreases significantly when RMPs is applied while temperature changes relatively little.

High resolution Thomson scattering can be used to test for localized reductions in the gradients of temperature, density, or pressure which would be expected to result if magnetic reconnection of the field lines formed an island. Islands are predicted to reduce the temperature gradient the most. As the islands are expected to be small, it is necessary that every chord in the relevant region agree systematically with the trend set by its neighbors. A single bad chord can easily give the appearance of an island. The HRTS upgrade and associated calibration improvements (Sec. 2.4.2), software tools for checking calibration and data quality (Sec. 2.3.3), and new profile analysis tools (Sec. 2.6) allow detection of local flattening of the profiles while clearly distinguishing it from diagnostic errors. This level of confidence has never before been possible and is a result of the data in-

spection tool-set discussed in section 2.3.3; both directly through using the tool-set for analysis and indirectly in that precise characterization of diagnostic problems was necessary for motivating long overdue, critical refurbishments and updates to maintenance procedures.

Validation of the chords around the pedestal was accomplished by first checking the density and temperature contours and time averaged profiles for anomalies in the absence of RMP and in different temperature ranges, as systematic errors in TS data can be temperature dependent. Then, statistical tools were used to check for bad χ^2 distributions and each polychromator's raw data were compared to the model. Again, variation with temperature must be considered here. A few problem chords were identified and removed from the data set. With one exception, the "problem" chords here were suffering from small ($< 5\%$) systematic errors which would go unnoticed in typical pedestal analysis (data are plentiful enough that one bad chord cannot defeat a tanh fit, nor can a set of small, randomly oriented systematic errors).

An example of reduction in temperature gradient near the top of the pedestal is shown in figure 2.23. In this case, RMP is applied and marginal ELM suppression is achieved part of the time. That is, windows of suppression are broken by ELMs. The period just before and between the two ELMs near 2080 ms represents an unsuppressed temperature profile. Notice that the contour centered around the $\psi_N \approx 0.9$ flux surface at the start of the time range is relatively narrow. After the ELM at 2087 ms, this contour widens significantly (this is not seen during typical ELM cycles). There is some variation of the width of this contour during the suppression window. Before the next ELM at 2073 ms, the contour narrows, the pedestal steepens, and the lower temperature surfaces contract. The contraction is seen in real space as well as flux space. Some mild time smoothing has been done to improve the appearance of the plot, but the fact that the contraction precedes the ELM is not an artifact of any processing. Variation in the low temperature contours with respect to the magnetic separatrix may be an indication of kinking in response to the RMP. The RMP is a fundamentally 3D field (toroidal asymmetry) and the 2D `EFIT` is incapable of describing it properly.

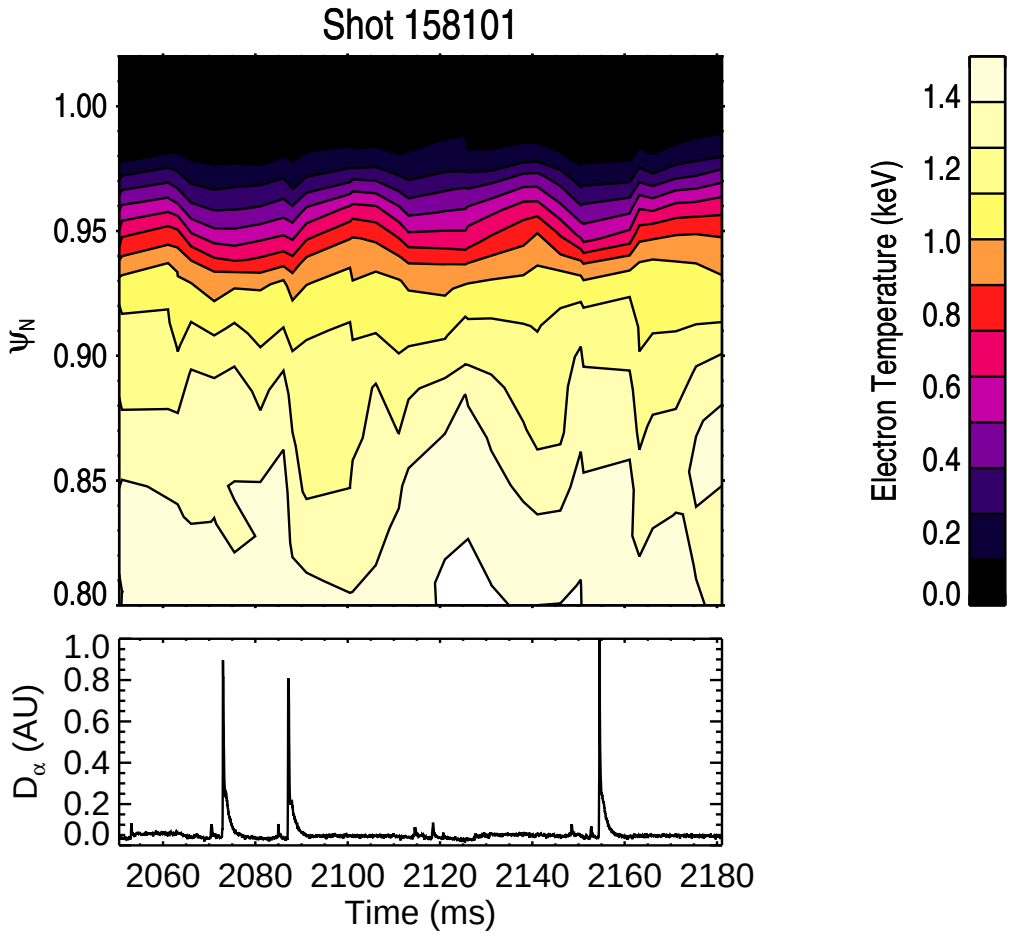

Figure 2.23: Contour of TS electron temperature during RMP ELM suppression plotted vs. time (x) and ψ_N (y). The top of the temperature scale is 1.5 keV and mild smoothing has been done. Below: trace of D_α showing spikes in emission corresponding to ELMs. The upper knee of the pedestal is near $\psi_N \approx 0.93$, corresponding to the 1-1.1 keV contour.

Profiles corresponding to windows of suppression and ELMs are shown in figure 2.24. The blue curve (lower everywhere inside of the pedestal, slightly steeper in pedestal) is from windows interpreted to be RMP ELM suppressed based on the interval between ELMs, changes apparent in the temperature contours (see Fig. 2.23), and activity in the magnetic and rotation data (not shown here; see Fig. 2 of Nazikian *et al.*[79]). The data which make up the red curve are taken between closely-spaced ELMs and at the ends of suppression windows, just before ELMs, when profiles and magnetic indicators suggest failure of suppression. It is

of some interest that signs of suppression failure are detected some milliseconds before ELMs occur. The composite profiles have been constructed from sets of individual slices using the WAIC method described in section 2.6.2.

In figure 2.24 it can be seen that the gradient just inside of the pedestal is lower in the suppressed case. The difference in gradient at the top of the pedestal is greater than the propagated error bars (which represent the error in the mean). The feature is small enough in spatial extent that systematic error in one of the Thomson chords should be ruled out as causing the feature. Each of the relevant chords is suppressed in turn and the feature remains statistically significant in each case, demonstrating that it is indeed likely a real feature. Further examples of this analysis may be found in Fig. 3 of Nazikian *et al.*[79] and Fig. 6 of King *et al.*[80]

Due to 3D field mapping issues, the nominal separatrix given by `EFIT` does not appear to correspond to the separatrix position which would be inferred from the temperature profile and also the foot of the profile moves considerably with respect to the nominal separatrix (at least $0.01\psi_N$). Therefore, the position where temperature has some selected value (70 eV in this case) is subtracted from the position bases of both profiles to align them to each others. The shift is calculated for each individual time slice separately, before the slices are combined. This accounts for any motion of the separatrix during the time windows examined.

In addition to expected flattening in the T_e profile at the top of the pedestal, RMPs have been observed to deform the density profile in the pedestal significantly. The features in question involve small scale radial variations which the HRTS upgrade helps to diagnose.

Work on RMP related islands or stochastic regions is reported on in more detail by Nazikian *et al.*,[79] including comparison to changes in 3D magnetic response and to rotation at the transitions into and out of suppression. These effects are linked to changes in the profiles measured by TS.

HRTS measurements have also supported tests done by Orlov *et al.*[81] of models for displacement of the plasma boundary in response to RMPs. While the standard `EFIT` reconstruction is limited in its utility in the presence of non-axisymmetric fields, fully 3D reconstructions are computationally intensive and this

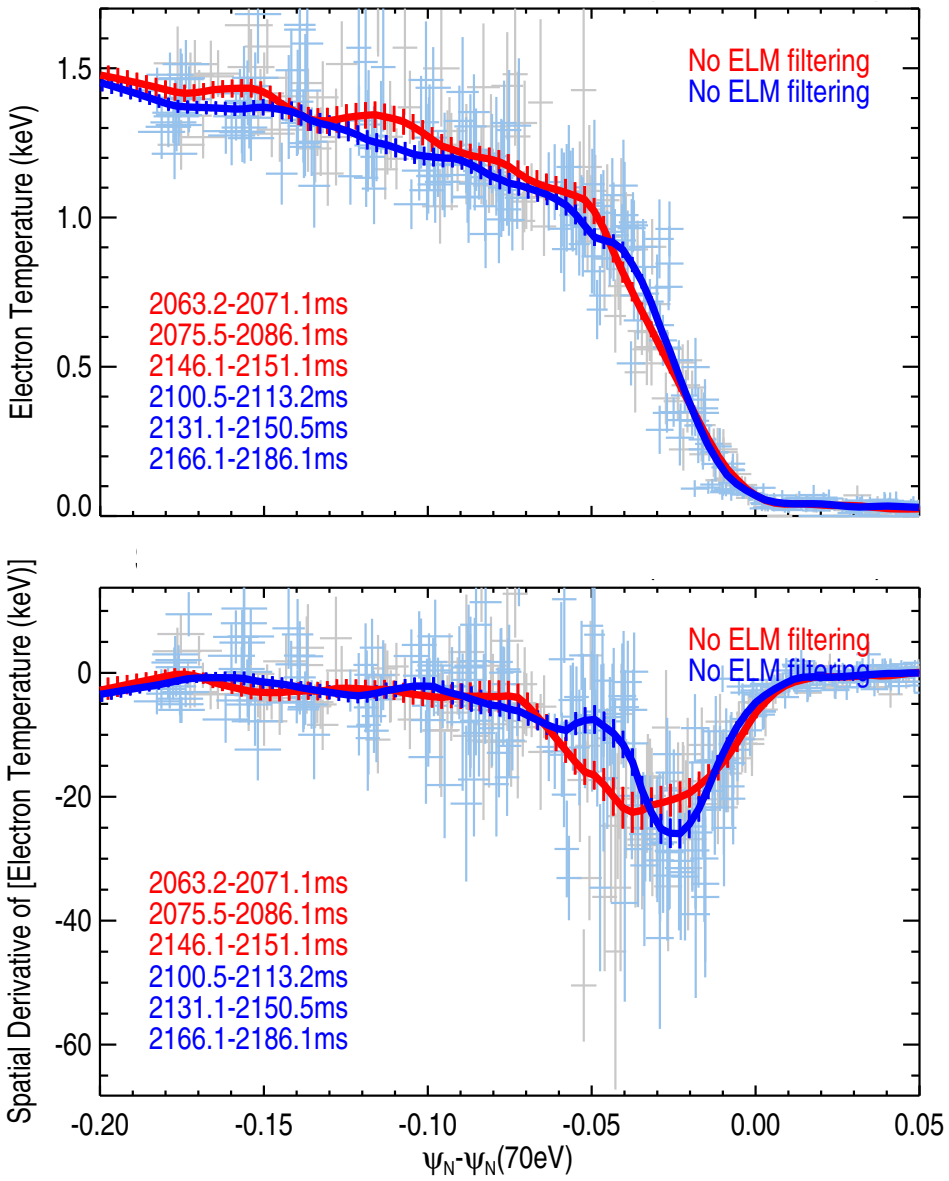

Figure 2.24: Comparison of RMP ELM suppressed and non-suppressed profiles. Top: Composite temperature profiles of times when ELM suppression appears to be active (blue) and inactive (red). The source data are shown in the background in gray (ELMing) and pale blue (suppressed). Windows exclude the ELMs themselves; no additional filtering is needed. The smoothed curves are weighted averages of linear interpolations of the individual slices with uncertainty given by propagating errors through the average. Bottom: spatial derivative of the data shown in the top plot.

limits the amount of analysis which can be done. One solution is to compute a 2D equilibrium and add the 3D perturbations from each coil to it while neglecting the

plasma response to the 3D perturbations. Clearly, the lack of a plasma response model is a limitation of these vacuum codes. Orlov[81] explores the ability of vacuum models to predict the location and movement of the plasma boundary when it is displaced by 3D magnetic field effects, using TS profiles to measure motion of the separatrix.

2.8 Other Diagnostics

This section discusses critical diagnostics which were used in the analysis reported in chapters 4 and 5 with the exception of Thomson scattering, which is described in detail in the earlier sections of chapter 2.

Profile alignment

Many of the diagnostics on DIII-D take measurements at or near the machine midplane ($Z = 0$). However, Thomson Scattering (TS) takes measurements along a vertical laser beam which crosses the separatrix closer to $Z = 70$ cm for typical plasmas. In order to compare diagnostics at different locations, a map of the flux surfaces must be used, such as the one shown in figure 1.7. Such a map allows profiles from different diagnostics to be aligned and stretched to correspond to each other. However, the standard equilibrium reconstruction code, `EFIT`, only produces 2D flux maps in $R - Z$; toroidal variation is not accounted for. Toroidal variation exists because of imperfections in the symmetry of DIII-D and can also be introduced intentionally by application of resonant magnetic perturbations.

An example of one of the more severe 3D field errors (at least from the perspective of Thomson scattering) is that one of the poloidal field shaping coils (F-coils) at the top of the machine is out of round and is slightly off center. This can introduce significant toroidal asymmetry to the equilibrium flux surfaces which is ignored by `EFIT`, causing problems when aligning diagnostic measurements from different locations. The problem is usually worst when aligning edge Thomson to edge CER, which are on opposite sides of the machine toroidally. Furthermore, CER measures near the midplane while Thomson measures above the midplane

near the flawed F-coil. The result is that the alignment between the TS and CER pedestal measurements can be off by as much as 1 cm. Standard practice is to assume that CER is properly aligned to the `EFIT` reconstruction and adjust TS profiles by one of two methods: define the separatrix temperature using a model for scrape off layer physics (typically ~ 70 eV) and shift the TS profile until it matches, or define the separatrix as the foot of a tanh fit to the temperature profile.

For this work, Thomson data were shifted to match the tanh fit to the `EFIT` separatrix when calculating the total pressure profiles used to constrain magnetic equilibrium reconstructions which were then used for stability analysis in chapter 4. Also note that while the machine midplane is thought to be less vulnerable to mapping errors than the top, the BES and edge CER systems are on roughly opposite sides of the midplane and could be mis-mapped to each other. A misalignment of up to 5 mm is possible.[82] This will be relevant when comparing data in chapter 5. Specific issues and corrections for BES vs. CER misalignment are discussed in more detail in appendix B.1.

Neutral Beams

Two key diagnostics, CER and BES, described in the following sections, rely on active neutral beam injection to make their measurements. Chapter 5 uses beams injecting torque in opposite directions to control toroidal rotation. There are four beam groups, each with two sources. The positions of the beam centerlines are shown in figure 2.25.

2.8.1 Charge Exchange Recombination Spectroscopy

Charge Exchange Recombination spectroscopy (CER, also known as CHERS)[25,83,84] measures the temperature, flow velocity, and density of ions in the plasma. Charge exchange refers to the transfer from an electron from an incoming neutral atom injected by the neutral beams to an ion in the plasma. The captured electron is originally in an excited orbit around its new ion, and emits a photon when it relaxes. The target ion species of CER is designated by the ion charge state before charge exchange takes place.

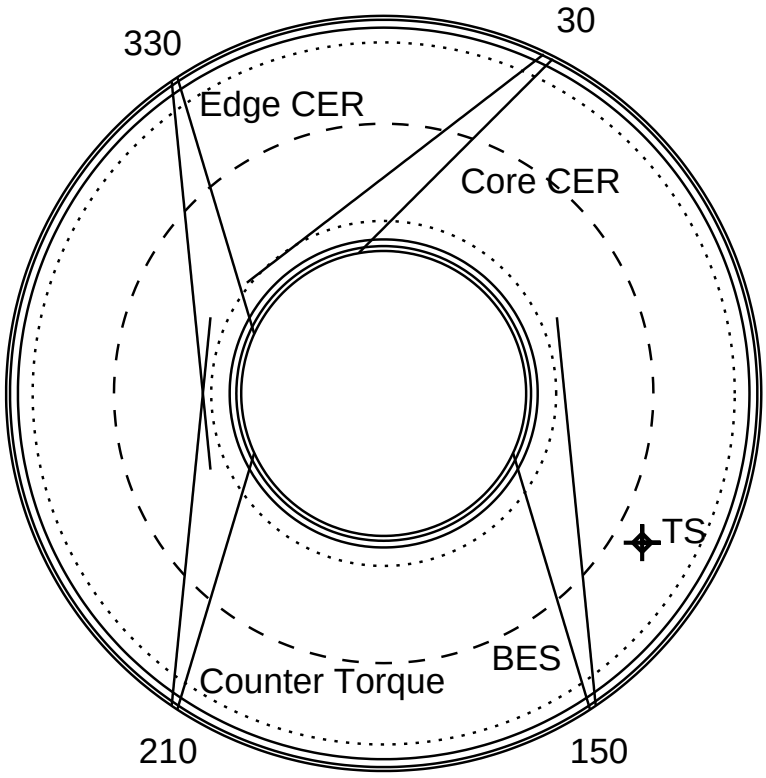

Figure 2.25: Plan view of neutral beam injection locations on DIII-D. Solid curves: cross section at the midplane of the vacuum vessel and limiting surfaces. Dashed and dotted curves: magnetic axis and LCFS at the midplane for a typical shot. Straight lines: center-lines of injection paths for the eight beam sources, labeled with their usage in this work. Also marked is the position of the core Thomson scattering (TS) laser path.

Thermal motions of ions in the plasma cause Doppler broadening of the emission line. Bulk motion (rotation) of the plasma causes the center wavelength of the emission spectrum to shift. The total amount of light emitted is proportional to the density of the target ion species and the density of the beam. Beam attenuation must be accounted for to get an accurate density measurement.

Spectrometers are used to resolve the emission spectra onto CCD detectors. The DIII-D CER system uses vertically oriented viewchords to capture ion temperature, density, and poloidal rotation velocity and tangential cords to measure temperature, density, and toroidal rotation. The system can be targeted at dif-

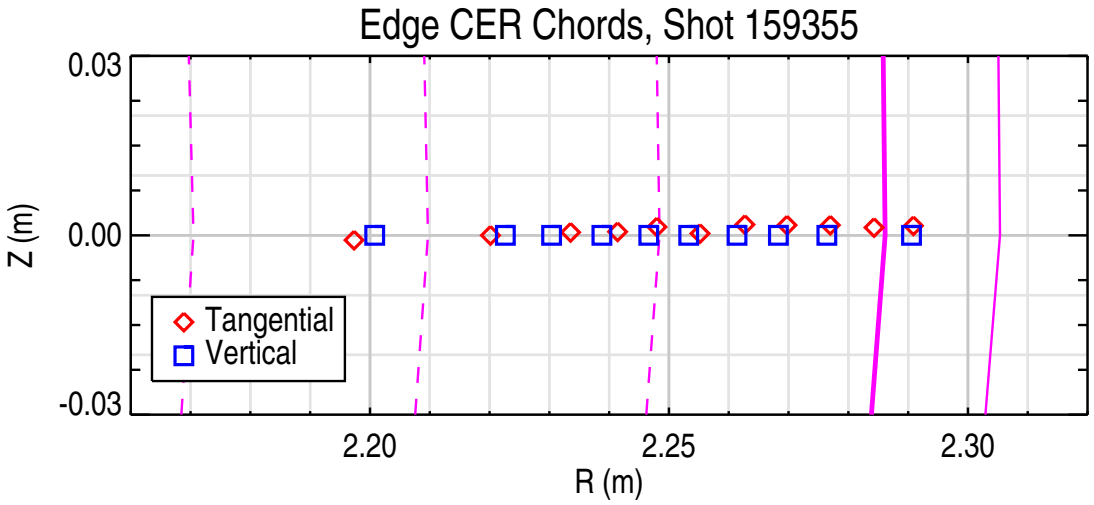

Figure 2.26: Positions of the centers of imaging volumes for CER chords aimed at the 330R neutral beam line.

ferent impurity ions. Some chords are optimized to measure main ions (normally deuterium). Measurements on fully stripped carbon impurity ions are standard (that is, an electron is transferred to a carbon ion that was in the plasma with a $Z = +6$ charge state). A set of closely spaced chords is aimed at the edge of the plasma to capture the pedestal, as seen in figure 2.26.

As information about the magnetic field is usually readily available, data from CER can complete equation 1.8 and provide a measurement of E_r. The radial variation of this quantity is important for turbulence suppression by shear flows, as discussed in section 1.4 and thus CER is essential for the analysis in section 5.3. The ion pressure measurements are also essential for completing the total pressure profile and constraining the grad-shafranov equation, which is essential for the stability analysis in chapter 4.

2.8.2 Beam Emission Spectroscopy

Beam Emission Spectroscopy (BES)[27,85–88] measures collisionally excited emission from particles injected by neutral beams. The emission of the beam particles is Doppler shifted according to the beam injection velocity, allowing isolation

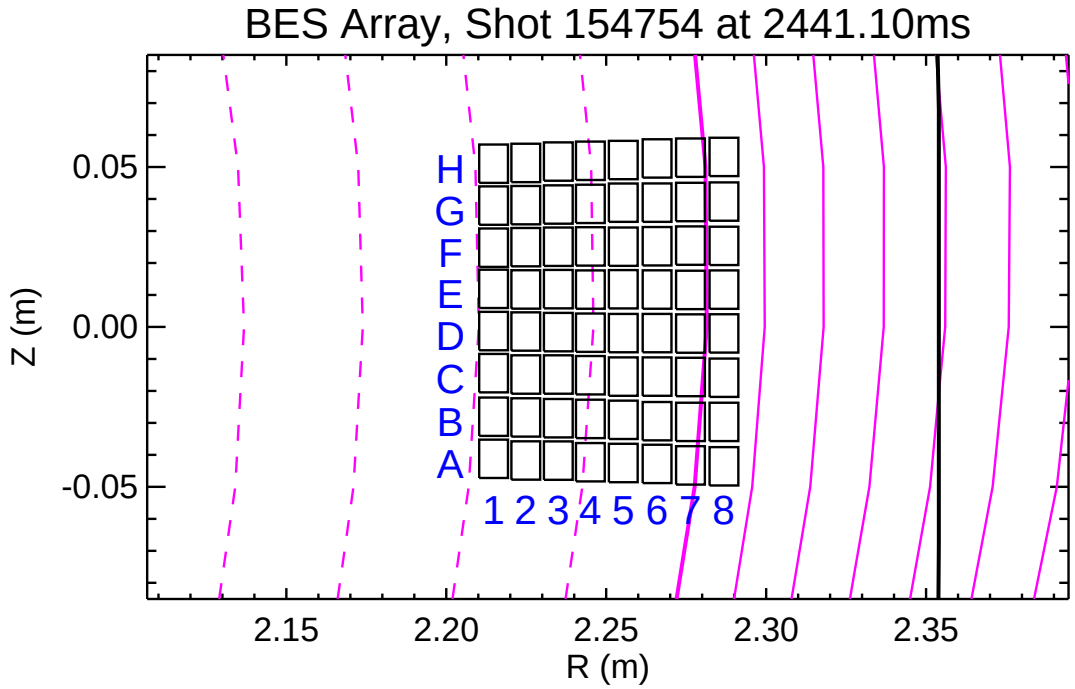

Figure 2.27: Example of a square BES configuration with flux surfaces (see Fig. 1.7) from shot 154754. Each chord is represented by a black rectangle. The limiting surface is visible at the right of the plot (black line). The separatrix (thick magenta curve) separates the last column of chords from the rest of the array. This configuration (or very similar, including relation to flux surfaces) is used in all experiments to be discussed in later chapters. The rows and columns are labeled A-H and 1-8, with the nominal separatrix position between columns 7 and 8.

from emission of the same line from the plasma. The fluctuations in the measured signal intensity I are related to density fluctuations in the plasma by $\tilde{n}/n \propto \tilde{I}/I$.

In DIII-D, the BES system is tuned to measure the D_α line at 656.1 nm, but with a blue shift on the order of nanometers due to injection velocity. The viewchords are packed in a modifiable (between experiments) 2D (Fig. 2.27) array which can be scanned remotely (between shots) to cover different areas of the plasma. The volume imaged by each chord is about 1 cm wide radially and poloidally, and much longer toroidally (beam FWHM=13 cm). Turbulent eddies are expected to be extended along the field lines, however, so the large toroidal extent of the measurement is acceptable.

The BES viewchords are nominally aligned to the magnetic field with a 5 degree tilt from the horizontal. The pitch angle of the field lines in a typical discharge relevant to the following work is about 10 degrees. This causes blurring in the poloidal dimension resulting in a ∼30% increase in the poloidal FWHM spot size, as seen in figure 4c of Shafer *et al.*[87]

The excited state typically lasts for up to 3-4 ns, allowing travel of ≈ 1 cm along the beam before emission. This means that some of the signal is due to a source which is farther out in R than the nominal center of the viewchord, leading to radial smearing of the spot size, as seen in fibure 4b of Shafer *et al.*[87]

The ≈1 cm spot size means the diagnostic picks up wavenumbers $k \lesssim 3\,\mathrm{cm}^{-1}$, and is fully sensitive to $k_\theta < 1\,\mathrm{cm}^{-1}$. See Shafer *et al.*[87] for a detailed analysis of the spatial transfer function. As the MPM discussed in section 5.4 has $k_\theta < 1\ \mathrm{cm}^{-1}$, no corrections based on the spatial transfer function are required.

Fiber optics carry captured light to optical interference filters, which reject the un-shifted D_α line at $\lambda = 656.1$ nm. Photoconductive photodiodes are used as detectors, which are are digitized at 1 MS/s and are cooled with liquid nitrogen to reduce noise.

This work uses data gathered by BES in chapter 5 to characterize a particular coherent fluctuation and to measure the decorrelation rate of the background turbulence at frequencies away from this mode.

2.8.3 Magnetics

DIII-D is equipped with many magnetic sensors mounted between the inside of the vacuum vessel and the carbon tiles.[8] These are essential for calculating the equilibrium reconstructions with `EFIT`[71] and they also provide some information about instabilities in the plasma. Recent upgrades to the magnetics have improved their ability to diagnose modes in the plasma, including extending the range of resolvable toroidal mode numbers to $n = 4$.[89] The distribution of pickup coils for measuring fast changes in magnetic field ($\dot{B}$) is shown in figure 2.28.

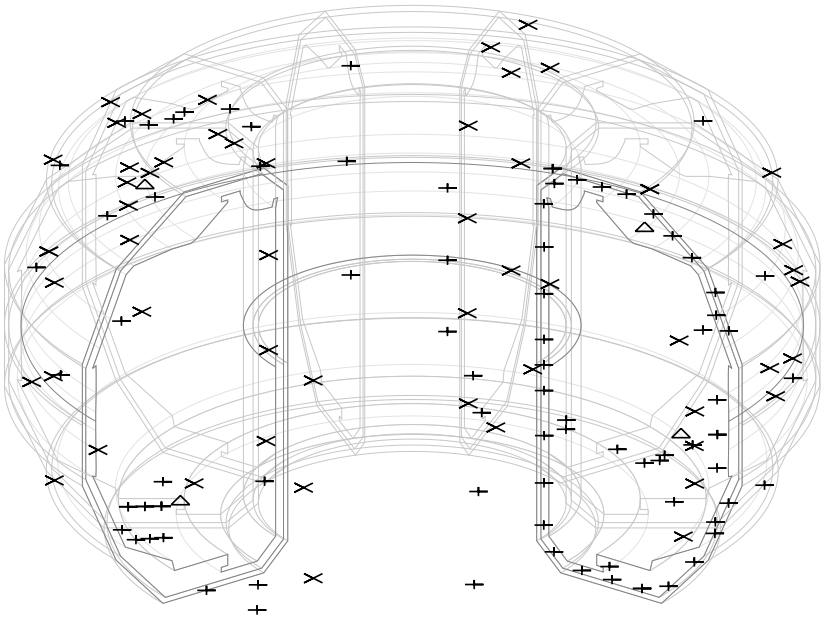

Figure 2.28: Arrangement of probes for measuring changes in magnetic field components: +: poloidal, X: radial, Δ: toroidal, overlaid on a wire-frame of the DIII-D vacuum vessel and limiting surfaces.

2.9 Thomson Scattering Conclusion

The high spatial resolution upgrade to the DIII-D Thomson scattering diagnostic was successful in providing meaningful improvements in the ability to resolve the steep gradient region in the pedestal. The new capability has supported high priority physics research, including more extensive validation of the EPED model.[50,75] Availability of higher resolution data with smaller random errors, coupled with innovations in data viewing software, made long standing systematic errors painfully obvious and those errors were then corrected by the Thomson group. The transformative ability of the new data inspection software to identify and quantify systematic errors in the final data, coupled with a suite of creative visualization options built into the same software, have allowed Thomson data to support searches for subtle changes in temperature gradients such as those which are predicted as a result of magnetic island formation. The spatial resolution upgrade and associated work have dramatically improved the utility of the Thom-

son scattering diagnostic at DIII-D. The improved Thomson data were used in chapters 4 and 5 of this dissertation.

2.10 Acknowledgments

Chapter 2 contains material from Review of Scientific Instruments vol. 83. Eldon, David; Bray, Bruce D.; Deterly, Timothy M.; Liu, Caizhen; Watkins, Matthias; Groebner, Richard J.; Leonard, Anthony W.; Osborne, Thomas H.; Snyder, Philip B.; Boivin, Réjean L.; Tynan, George R., American Institute of Physics, 2012. The dissertation author was the primary investigator and author of this paper.

Chapter 2 contains material which has been submitted for publication in Physics of Plasmas. Eldon, David; Boivin, Réjean L.; Chrystal, Colin ; Groebner, Richard J.; McKee, George R. ; Schmitz, Lothar; Tynan, George R. ; Yan, Zheng ; Boedo, Jose A.; Burrell, Keith H.; King, Josh D. ; Kolemen, Egemen; Muscatello, Chris ; Osborne, Thomas H. ; Snyder, Philip B., American Institute of Physics, 2015. The disseration author was the primary investigator and author of this paper.

3 Background: Theory and Numerical Calculations

This chapter discusses the theory behind the hypothesis introduced in section 1.6 that the initial transient in hard back transitions is a large type-I ELM. This is followed by information about the calculations in section 3.2

3.1 MHD and Equilibrium

An equilibrium plasma configuration is unstable with respect to a perturbation if the amplitude of that perturbation grows with time, and stable if the amplitude is oscillatory or damped. The two-fluid model of a plasma is given by:[90]

$$\frac{\partial n_j}{\partial t} + \vec{\nabla} \cdot (n_j \vec{v_j}) = 0 \tag{3.1}$$

$$m_j n_j \left(\frac{\partial \vec{v_j}}{\partial t} + \left(\vec{v_j} \cdot \vec{\nabla} \right) \vec{v_j} \right) = -\vec{\nabla} p_j + n_j e Z_j \left(\vec{E} + \vec{v_j} \times \vec{B} \right) + \vec{P}_{jj'} + \vec{f}_{ext} \tag{3.2}$$

$$\frac{\partial}{\partial t} \left(\frac{p_j}{n_j^\gamma} \right) + \vec{v_j} \cdot \vec{\nabla} \left(\frac{p_j}{n_j^\gamma} \right) = 0 \tag{3.3}$$

$$\vec{\nabla} \cdot \vec{E} = \frac{e Z_i n_i - e n_e}{\epsilon_0} \tag{3.4}$$

$$\vec{\nabla} \cdot \vec{B} = 0 \tag{3.5}$$

$$\vec{\nabla} \times \vec{E} = -\frac{\partial}{\partial t} \vec{B} \tag{3.6}$$

$$\vec{\nabla} \times \vec{B} = \mu_0 \epsilon_0 \frac{\partial}{\partial t} \vec{E} + \mu_0 e \left(Z_i n_i \vec{v_i} - n_e \vec{v_e} \right) \tag{3.7}$$

where the subscript j denotes species, subscript i denotes an ion species (if more than one, include additional terms, one per ion species), and subscript e denotes electrons. Equations 3.1-3.3 may be used once per species. Here, n is number density, v is mean flow speed for the species, p is pressure, Z is charge state (-1 for electrons), E and B are the electric and magnetic fields, $P_{jj'}$ is the rate of collisional momentum transfer from species j' to j, f_{ext} is the external force density, and γ is the adiabatic index (adiabatic compression: $\gamma = (2+N)/N$, isothermal: $\gamma = 1$, N is degrees of freedom).

Let it be assumed that collisions within each species (electron-electron, ion-ion) are frequent enough to ensure that the velocity distributions are Maxwellian. This is equivalent to saying that the mean free path between collisions is short compared to the scale of variation in the plasma.[90] The velocity $\vec{v}$ above is the average of the Maxwellian distribution.

By writing $\vec{\nabla}p$, it has been assumed that pressure is isotropic on a flux surface (which would be the case in part because of collisions) and viscosity is negligible. In the general case, the pressure term is given by the divergence of a tensor, i.e. by $\vec{\nabla}\cdot \overleftrightarrow{P}$. The off diagonal terms are associated with viscosity in a normal fluid. In a magnetized plasma, they can arise from collisions and finite Larmor radius effects. It is sometimes convenient to split the pressure tensor into separate pressure and viscosity: $\vec{\nabla} \cdot \overleftrightarrow{P} = \vec{\nabla}p + \vec{\nabla} \cdot \overleftrightarrow{\pi}$. Although collisions will be assumed to be strong enough to relax the velocity distributions to be Maxwellian, viscosity and later resistivity, which are contributed to by collisions, will be neglected.

Equations 3.1-3.7 describe two (or more, if terms for additional ion species are included) interpenetrating fluids. An appropriate linear combination of these equations can give a description of the plasma as a single fluid. Defining mass density $\rho = n_i m_i + n_e m_e$, mass velocity $\vec{v} = \frac{1}{\rho}(n_i m_i \vec{v_i} + n_e m_e \vec{v_e})$, and current density $\vec{J} = e(Z_i n_i \vec{v_i} - n_e \vec{v_e})$ and combining the multi-fluid equations gives:[90–93]

$$\frac{\partial \rho}{\partial t} + \vec{\nabla} \cdot (\rho \vec{v}) = 0 \tag{3.8}$$

$$\frac{\partial \sigma}{\partial t} + \vec{\nabla} \cdot \vec{J} = 0 \tag{3.9}$$

$$\rho\left(\frac{\partial\vec{v}}{\partial t}+\left(\vec{v}\cdot\vec{\nabla}\right)\vec{v}\right)=-\vec{\nabla}p+\vec{J}\times\vec{B}+\vec{f}_{ext} \tag{3.10}$$

$$\frac{\partial}{\partial t}\left(\frac{p}{\rho^{\gamma}}\right)+\vec{v}\cdot\vec{\nabla}\left(\frac{p}{\rho^{\gamma}}\right)=0 \tag{3.11}$$

$$\vec{\nabla}\cdot\vec{E}=\frac{\sigma}{\epsilon_0} \tag{3.12}$$

$$\vec{\nabla}\cdot\vec{B}=0 \tag{3.13}$$

$$\vec{\nabla}\times\vec{E}=-\frac{\partial}{\partial t}\vec{B} \tag{3.14}$$

$$\vec{\nabla}\times\vec{B}=\mu_0\epsilon_0\frac{\partial}{\partial t}\vec{E}+\mu_0\vec{J} \tag{3.15}$$

For simplicity, assume quasi-neutrality ($n_i \approx n_e \approx n$). Using $\vec{P}_{ei}=\eta en\vec{J}$:[90]

$$\vec{E}+\vec{v}\times\vec{B}-\eta\vec{J}=\frac{1}{e\rho}\left[\frac{m_i m_e n}{e}\frac{\partial}{\partial t}\left(\frac{\vec{J}}{n}\right)+(m_i-m_e)\vec{J}\times\vec{B}+m_e\vec{\nabla}p_i-m_i\vec{\nabla}p_e\right] \tag{3.16}$$

$\sigma = e(Z_i n_i - n_e)$ is the charge density and $p = p_i + p_e$ is the total kinetic pressure ($p_e = n_e T_e$). Equation 3.16 is often taken in the limit of $m_e/m_i \to 0$ and slow motions (compared to the cyclotron frequency), which simplifies the right side:

$$\vec{E}+\vec{v}\times\vec{B}-\eta\vec{J}=\frac{1}{en}\left(\vec{J}\times\vec{B}-\vec{\nabla}p_e\right) \tag{3.17}$$

The right side of 3.17 contains the Hall term and the electron pressure gradient, and may be neglected in many cases. If the resistivity is also ignored:

$$\vec{E}+\vec{v}\times\vec{B}=0 \tag{3.18}$$

Equations 3.8 through 3.15 and 3.18 make up the set of ideal magnetohydrodynamic (MHD) equations.

The energy of the system is given by equation 3.19:[91,94]

$$\mathbb{E}=\frac{1}{2}\iiint_V \mathrm{d}\vec{x}\left(\rho v^2\right)+\iiint_V \mathrm{d}\vec{x}\left(\frac{p}{\gamma-1}+\frac{B^2}{2\mu_0}+\rho\phi\right) \tag{3.19}$$

where V indicates integration over the volume of the system, ϕ is the potential due to a gravitational acceleration $\vec{g}$ (easily replaced by another form of potential energy if needed: let ϕ be another potential and ρ be the "charge" density associated with the relevant force. For gravity, this is mass density).

3.1.1 Linear Ideal Stability Calculations

The problem of determining stability may be simplified by making a few assumptions. First, that the perturbation is small, such that only terms which are lowest order in ξ need be considered and higher order terms may be neglected. Next, that the velocity distributions are ideal Maxwellians, and there is no resistance ($\eta = 0$).

Eventually a perturbation which is linearly unstable may grow until it is stabilized by nonlienar terms.[2] That is, the perturbation can experience nonlinear saturation. Nonlinear instability is also possible for a perturbation which is linearly stable. In that case, a large enough initial kick might set off the instabililty.[90] These effects will not be considered here.

As an example, consider a static equilibrium with $v = 0$ and neglible Hall effects (right side of Ohm's law, equation. 3.16). The equilibrium will then satisfy:[91,95]

$$\vec{J_0} \times \vec{B_0} = \vec{\nabla} p_0 \tag{3.20}$$

$$\vec{\nabla} \times \vec{B_0} = \mu_0 \vec{J_0} \tag{3.21}$$

$$\vec{\nabla} \cdot \vec{B_0} = 0 \tag{3.22}$$

where the subscript 0 indicates an unperturbed quantity and these are now independent of time. The assumption of $v = 0$, $\eta = 0$ with no Hall terms results in trivial solutions to the other equations.

The importance of resistivity is given by the magnetic Reynolds number $R_m = \mu_0 v L/\eta$, where v here is a typical velocity scale for the system and L is a typical length scale. When R_m is large, the resistivity term is small and can probably be ignored. If the Alfvén speed[96] ($v_A = B/\sqrt{\mu_0 \rho}$) is used as the velocity scale, the number is called the Lundquist number S. Assuming a scale size of 1 m and typical tokamak values for the relevant parameters ($B = 2$ T,$T = 1$ keV,$n = 5 \times 10^{19}/\mathrm{m}^3$) gives $S \approx 10^8$. So, resistivity may be neglected for many tokamak relevant situations.[91]

This equilibrium is not possible for an arbitrary magnetic configuration. $\vec{\nabla} \times \vec{\nabla} p$ must be 0, but $\vec{\nabla} \times (\vec{J} \times \vec{B})$ is not necessarily zero:[97] $\vec{\nabla} p$ cannot balance arbitrary $\vec{J} \times \vec{B}$.

Now consider a small motion ξ away from equilibrium such that $\vec{x} = \vec{x_0} + \vec{\xi}(\vec{x_0}, t)$. The quantities will then take the form $\rho(\vec{x}, t) = \rho_0(\vec{x_0}) + \rho_1(\vec{x}, t)$, for example. Since a perturbation due to a small displacement is being considered, ρ_1 may be given in terms of ξ: $\rho_1 = -\vec{\nabla} \cdot (\rho_0 \vec{\xi})$. The other quantities will also be the sum of equilibrium and perturbed parts. For quantities G and H, the perturbed parts (subscript 1) will be assumed to be small such that $G_1 H_1 \simeq 0$. The resulting equations are linear in the perturbed quantities.

Forces on the plasma will change as a result of the initial perturbation. It must now be determined if the perturbed force induces further growth in ξ, which will result in instability. Procedures for accomplishing this include use of the energy principle and normal mode analysis.

The Energy Principle

Determination of stability using the energy principle requires calculating the change in energy resulting from some perturbation. If the change in energy is positive (see eqn. 3.19), work would have to be done to generate the perturbation, and the plasma is stable to that perturbation. If the change in energy is negative, the instability, once formed, will gain energy from the plasma and is unstable.[98] It is sometimes possible to find a sufficient condition for stability using the energy principle, but it is more common to use a trial displacement and calculate the resulting change in energy. A separate test is then needed for each type of instability, making it difficult to conclude that a configuration is stable. The energy principle is best used when a particular class of instability with a known form of ξ is suspected.[91]

The change in energy resulting from a displacement ξ is[2,91,93]

$$\delta W = -\frac{1}{2} \iiint_V \mathrm{d}\vec{x} \left(\vec{\xi} \cdot \vec{F} \right) \tag{3.23}$$

where F is the force density resulting from the displacement, given by 3.10 as

$$\vec{F} = (\vec{J}_0 + \vec{J}_1) \times (\vec{B}_0 + \vec{B}_1) - \vec{\nabla} p_0 - \vec{\nabla} p_1 \tag{3.24}$$

The first order perturbed force is given as:[2]

$$\vec{F} = \vec{J}_0 \times \vec{B}_1 + \vec{J}_1 \times \vec{B}_0 - \vec{\nabla} p_1 \tag{3.25}$$

Combining Faraday's law (eqn. 3.14) and Ohm's law (eqn. 3.18 gives:

$$\frac{\partial}{\partial t}\vec{B} = \vec{\nabla} \times \left(\frac{\partial \vec{\xi}}{\partial t} \times \vec{B} \right) \tag{3.26}$$

which, after linearization and integration in time results in:[2]

$$\vec{B}_1 = \vec{\nabla} \times \left(\vec{\xi} \times \vec{B}_0 \right) \tag{3.27}$$

The equations of state (Eqn. 3.11) and mass continuity (Eqn. 3.8) are combined to give an expression for perturbed pressure:[2]

$$p_1 = -\vec{\xi} \cdot \vec{\nabla} p_0 - \gamma p_0 \vec{\nabla} \cdot \vec{\xi} \tag{3.28}$$

The perturbed current is obtained from equation 3.15:

$$\vec{J}_1 = \frac{1}{\mu_0} \vec{\nabla} \times \vec{B}_1 \tag{3.29}$$

Use of equations 3.28 and 3.29 allows δW (eqn. 3.23) to be written in terms of equilibrium quantities and ξ:[2]

$$\begin{aligned} \delta W = -\frac{1}{2} \iiint_V \mathrm{d}\vec{x} \Bigg[\frac{1}{\mu_0} \vec{\xi} \cdot \Big(\Big(\vec{\nabla} \times \vec{B}_0 \Big) \times \vec{B}_1 + \Big(\vec{\nabla} \times \vec{B}_1 \Big) \times \vec{B}_0 \Big) \\ + \vec{\xi} \cdot \vec{\nabla} \Big(\gamma p_0 \vec{\nabla} \cdot \vec{\xi} + \vec{\xi} \cdot \vec{\nabla} p_0 \Big) \Bigg] \end{aligned} \tag{3.30}$$

with B_1 given by equation 3.27.

Solving equation 3.30 for the change in energy as a result of a trial perturbation is sufficient for determination of stability of that perturbation. If growth rates are required, then introduce the perturbed kinetic energy:

$$K = \frac{1}{2} \iiint_V \mathrm{d}\vec{x}\, \rho(\vec{x}) \left(\frac{\partial}{\partial t} \xi(\vec{x_0}, t) \right)^2 = \frac{1}{2} \iiint_V \mathrm{d}\vec{x}\, \rho \omega^2 \xi^2 \tag{3.31}$$

The eigenfrequency is then given by

$$\omega^2 = \frac{\delta W}{\frac{1}{2}\iiint_V \mathrm{d}\vec{x}\,\rho\xi^2} \tag{3.32}$$

and the system is unstable if $\omega^2 < 0$. This is equivalent to solving the full set of linearized MHD equations.[2,94,95]

Normal Modes

An alternative to the energy principle is to solve the MHD equations directly. For example, take equation 3.2 for a cold plasma ($T \sim 0$) for $Z = 1$ ions, neglecting collisions:[90]

$$Mn\left(\frac{\partial\vec{v}}{\partial t} + \left(\vec{v}\cdot\vec{\nabla}\right)\vec{v}\right) = ne\vec{E} + ne\,\vec{v}\times\vec{B} + n\vec{F}_{ext} \tag{3.33}$$

Consider an equilibrium density gradient $n_0 = n_{00} - \vec{n}_0'\cdot\vec{x}$ perpendicular to the equilibrium field $\vec{B}_0$. Consider a uniform external force $\vec{F}_{ext}$, causing a drift in the equilibrium velocity $\vec{v}_F = \vec{F}_{ext}\times\vec{B}_0/eB_0^2$ (this is the ion drift. Electrons drift in the opposite direction).

Substituting $n = n_0 + n_1$, etc. into equation 3.33 gives the first order perturbed momentum equation for the ions:[90]

$$Mn_0\left(\frac{\partial\vec{v}_1}{\partial t} + \left(\vec{v}_0\cdot\vec{\nabla}\right)\vec{v}_1\right) = n_0 e\left(\vec{E}_1 + \vec{v}_0\times\vec{B}_1 + \vec{v}_1\times\vec{B}_0\right) \tag{3.34}$$

F_{ext} remains relevant because of the equilibrium drift velocity it causes (v_0). The $(\vec{v}_1\cdot\vec{\nabla})\vec{v}_0$ term was dropped because v_0 is assumed to result purely from drifts associated with a uniform F_{ext}.[90]

If the perturbations are proportional to $\exp\left[i(\vec{k}\cdot\vec{x} - \omega t)\right]$,[90] then

$$\left(\omega - \vec{v}_0\cdot\vec{k}\right)\vec{v}_1 = \frac{ie}{M}\left(\vec{E}_1 + \vec{v}_0\times\vec{B}_1 + \vec{v}_1\times\vec{B}_0\right) \tag{3.35}$$

B_1 is given by equation 3.27, which becomes $\vec{B}_1 = i(\vec{B}_0\cdot\vec{k})\vec{\xi} - i\vec{B}_0(\vec{k}\cdot\vec{\xi})$ if B_0 is assumed to be uniform. For a transverse wave ($\vec{k}\cdot\vec{\xi} = 0$) propagating across the equilibrium field ($\vec{k}\cdot\vec{B}_0 = 0$), it can be seen that $B_1 = 0$.

Setting $\vec{B}_0 = \hat{z}B_0$ and splitting $\vec{v}_1$ into components v_x and v_y gives

$$v_x = i\frac{eB_0/M}{\left(\omega - \vec{v}_0 \cdot \vec{k}\right)}\left(E_x/B_0 + v_y\right) \tag{3.36}$$

$$v_y = i\frac{eB_0/M}{\left(\omega - \vec{v}_0 \cdot \vec{k}\right)}\left(E_y/B_0 - v_x\right) \tag{3.37}$$

The z component along the field does not enter into the equations for the other two and will be ignored. Solving equations 3.36 and 3.37 gives

$$v_{x,i} = \frac{E_y}{B} \tag{3.38}$$

$$v_{y,i} = -i\frac{\left(\omega - \vec{v}_{0,i} \cdot \vec{k}\right)}{\Omega_c}\frac{E_y}{B} \tag{3.39}$$

where $\Omega_c = eB/M$ is the ion cyclotron frequency. It was assumed that $\left(\omega - k_y v_0\right)^2 \ll \Omega_c^2$ (essentially that $\omega_{lab}^2 \ll \Omega_c^2$, where typically $\Omega_c \approx 10^8$ Rad/s in DIII-D) and the external force was assigned to the $+\hat{x}$ direction.

The same solution applies to the electrons, but $v_{y,e}$ is neglected because $m \ll M$. The electron velocities are:

$$v_{x,e} = \frac{E_y}{B} \tag{3.40}$$

$$v_{y,e} = 0 \tag{3.41}$$

It has already been assumed that a transverse wave is being considered and the equilibrium drift v_0 has been defined to be in the y direction, so k_y is the relevant component of k and $\vec{\xi} = \hat{x}\xi$.

The continuity equation (Eqn. 3.1) is linearized as

$$0 = -i\omega n_1 + n_0' v_{x,i} + i n_0 k_y v_{y,i} + i k_y n_1 v_{0,i} \tag{3.42}$$

$$0 = -i\omega n_1 + n_0' v_{x,e} + i k_y n_1 v_{0,e} \tag{3.43}$$

The electrons are solved by substituting in velocities from equations 3.40 and 3.41 into equation 3.43:

$$\frac{E_y}{B} = i\frac{n_1}{n_0'}\left(\omega - k_y v_{0,e}\right) \tag{3.44}$$

And then the ions can be solved by combining equations 3.38, 3.39, 3.42, and 3.44:

$$(\omega - kv_{0,i})(\omega - kv_{0,e}) = -\frac{n_0'}{n_0}\Omega_c (v_{0,i} - v_{0,e}) \tag{3.45}$$

Now, v_0 is the drift resulting from F_{ext}, given by $v_{0,y} = -F_{ext,x}/eB_z$. If the electrons and ions experience F_{ext} equally, then $v_{0,e} = -v_{0,i}$ and ω is given by

$$\omega = \sqrt{k^2 v_{0,i}^2 + 2\frac{n_0'}{n_0}\frac{F_{ext}}{M_i}} \tag{3.46}$$

and the system is unstable if ω is imaginary. Instability is only possible if F_{ext} and n_0' have opposite sign; that is if the force is directed down the density gradient.

In the more likely case that an external force will be proportional to mass, the electron drift will be much smaller than the ion drift and may be neglected. This is true in the cases of gravity ($\vec{F}_{ext} = m\vec{g}$) and centrifugal force in a curved magnetic field, such as may be found in a tokamak: $\vec{F}_{ext} = m\left(v_\parallel^2 + \frac{1}{2}v_\perp^2\right)\vec{R}_c/R_c^2$. $\left\langle v_\parallel^2 \right\rangle = \langle v_\perp^2/2 \rangle = T/m$ so the acceleration $g = 2T/(m\,R_c)$ for centrifugal force.[99] For a force proportional to mass with acceleration g in $\hat{x}$ and neglecting the electron mass, equation 3.45 becomes

$$\omega^2 - \omega k v_{0,i} = -\frac{n_0'}{n_0}\Omega_c v_{0,i} \tag{3.47}$$

$$\omega^2 - \omega k v_0 = \frac{n_0'}{n_0} g \tag{3.48}$$

$$\omega = \frac{kv_0}{2} \pm \sqrt{\frac{1}{4}k^2 v_0^2 + \frac{n_0'}{n_0}g} \tag{3.49}$$

Instability is only possible if g and n_0' have opposite sign. Again, the force must be down the density gradient. The growth rate is the imaginary part of ω, which for long wavelengths is

$$\gamma = Im(\omega) \simeq \sqrt{-\frac{n_0'}{n_0}g} \tag{3.50}$$

This instability is of the interchange type. A dense fluid (the plasma) is being supported by a lightweight fluid (the magnetic field). The field is capable of producing enough pressure to support the plasma against the external force. However, if a ripple develops at the surface (see figure 3.1), the drifts due to the

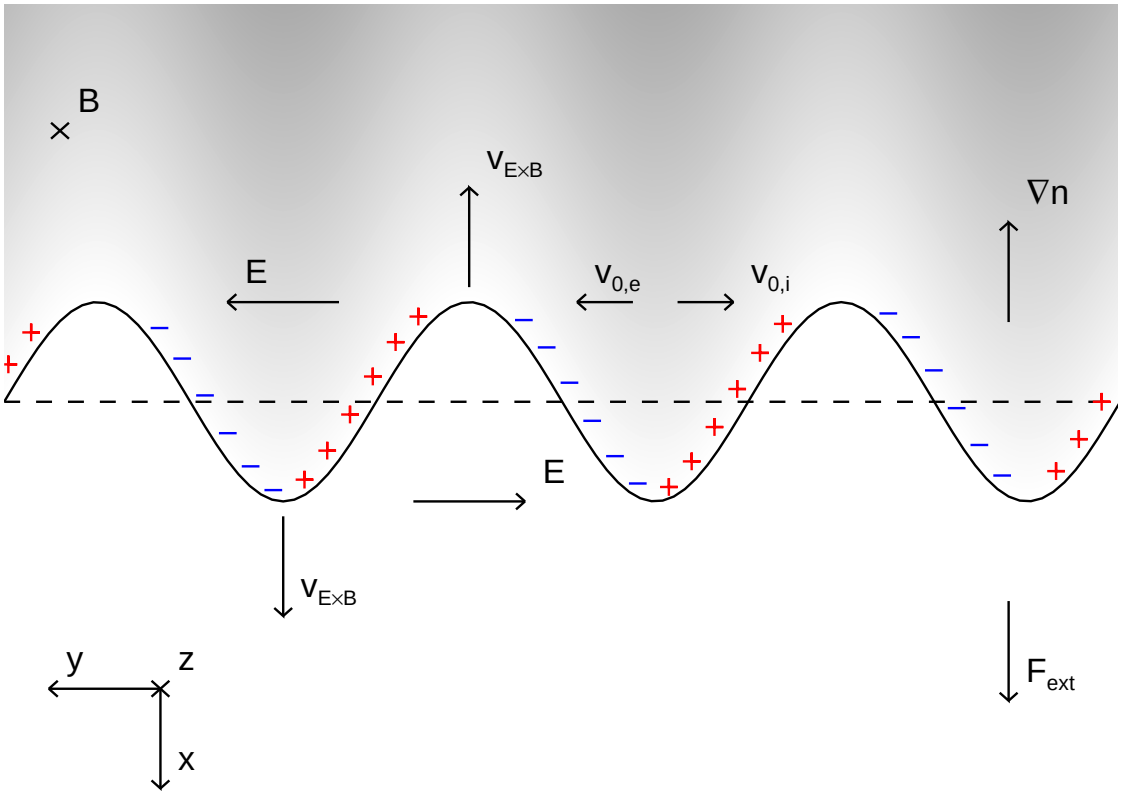

Figure 3.1: Schematic of an interchange instability. The top of the figure is occupied by plasma with density gradient ∇n. Below it is a region of vacuum. An external force F_{ext} in $\hat{x}$ causes a drift v_0 in $\mp\hat{y}$ for $\pm$ charges. If a ripple develops, positive and negative charges separate and set up an electric field. The resulting $E \times B$ drift amplifies the original displacement.

external force will move the electrons and ions to opposite sides of the peaks in the ripple. For every peak, there will be a concentration of positive charge on one edge and negative charge on the other. The resulting electric field drift will tend to move material outward to enhance the perturbation. For a trough, the electric field is in the opposite direction and material is pushed inward, also enhancing the ripple.[2,90,95]

If the external force were in fact electric, then the drifts would be equal and in the same direction, and the right side of equation 3.45 would vanish, giving the result $\omega = kv_0$, which describes a family of purely oscillatory modes which propagate harmlessly along the edge (there is no way to obtain an imaginary ω).

3.1.2 Diamagnetic Stabilization

Finite gyration radius $r_L = mv_\perp/ZeB$ has a stabilizing effect on the interchange instability.[14,95,100] This enters through inclusion of a sort of viscosity in the equation of motion[100] (eqn. 3.10):

$$\rho\left(\frac{\partial\vec{v}}{\partial t} + \left(\vec{v}\cdot\vec{\nabla}\right)\vec{v}\right) = \vec{J}\times\vec{B} - \vec{\nabla}p - \vec{\nabla}\cdot\overleftrightarrow{\pi} + \vec{f}_{ext} \tag{3.51}$$

where $p + \overleftrightarrow{\pi}$ is the full pressure tensor which has been split into p and π and the relevant components of $\overleftrightarrow{\pi}$ are, assuming $\vec{B} = \hat{z}B$:[100]

$$\begin{aligned}
\pi_{xx} &= -\rho\nu\left(\frac{\partial v_y}{\partial x} + \frac{\partial v_x}{\partial y}\right)\\
\pi_{yy} &= +\rho\nu\left(\frac{\partial v_y}{\partial x} + \frac{\partial v_x}{\partial y}\right)\\
\pi_{xy} &= +\rho\nu\left(\frac{\partial v_x}{\partial x} - \frac{\partial v_y}{\partial y}\right)
\end{aligned} \tag{3.52}$$

and the "viscosity" $\nu = r_L^2\Omega_c/4$. Roberts and Taylor[100] solve the MHD equations with $\overleftrightarrow{\pi}$ included to obtain the dispersion relation:

$$\omega^2 - 2\nu L_n^{-1}k\omega = gL_n^{-1} \tag{3.53}$$

where L_n^{-1} is the inverse density gradient scale length, k is the wavenumber, and g is the acceleration due to an external force such as gravity.[100] Identifying the right side with the growth rate calculated in the simple example (eqn. 3.50) $\gamma_{MHD}^2 = -L_n^{-1}g$ and using the definition of the diamagnetic frequency $\omega_{*i} = kT_iL_n^{-1}/(ZeB)$, equation 3.53 becomes

$$\omega\left(\omega - \omega_{*i}\right) = -\gamma_{MHD}^2 \tag{3.54}$$

From equation 3.54 it can be seen that ω will be imaginary if $\gamma_{MHD} > \omega_{*i}/2$ and thus instability will result. That is, the threshold for actual instability is not when the ideal growth rate γ_{MHD} becomes positive, but when it surpasses $\omega_{*i}/2$. The physical picture of an interchange instability is that charge separation occurs due to the opposite motions of ions and electrons in response to the acceleration $\vec{g}$ and a ripple in density. However, the ions can experience a different average electric field than the electrons if their Larmor radius is large enough. This difference in

effective electric field also has a charge separation effect, which will tend to cancel the charge separation caused by $\vec{g}$ and thus stabilize the interchange mode.[95] Ideal interchange growth rates computed from the above physics should be compared against the ion diamagnetic stabilization term to determine if instability will likely exist.

3.1.3 Ballooning

Ballooning modes are a type of interchange instability, driven by pressure gradients and unfavorable curvature. The drive is essentially similar to the Rayleigh-Taylor instability, with centrifugal force taking the place of the external or gravitational force.[90] That is, the physical picture is similar to the interpretation of the simple example instability in section 3.1.1 and figure 3.1 with the result given in equation 3.50. The magnetic field acts as a lightweight fluid supporting the denser plasma against centrifugal force. The rotation here might come from bulk mass flows, but is also contributed to by thermal motions (which are obviously incompatible with the simple example where it was assumed that $T = 0$. Regardless, the simplification is useful for understanding the basic mechanism). Clearly, the drive only exists on the low field side of the plasma and the curvature is stabilizing on the high field side (see Fig. 3.2), with the perturbed potential energy as a result of the mode being roughly $\delta W \sim \frac{dp/dr}{R_c}\xi^2$ in the local high-n limit.[2] Interchange can be stabilized in a tokamak by connecting the favorable and unfavorable regions, as shown by the thick green magnetic field line in figure 3.2. When ballooning modes become unstable, they must overcome the stabilizing influence of the high field side by bending the magnetic field lines such that their amplitude may be greater in the region of destabilizing curvature and lower in the region of stabilizing curvature (see red cross section curve of Fig. 3.2).[95,99] Energy is expended in the bending of magnetic field lines and details of the magnetic configuration affect the stability of this mode. The energy cost of field line bending[2] is $\delta W \sim k_{\parallel}^2(B_\phi^2/\mu_0)\xi^2$. Instability results when the pressure gradient becomes large

enough to overcome the energy cost of field line bending:[2]

$$\frac{dp}{dr}\frac{1}{R}\xi^2 \sim \frac{B^2}{\mu_0}k_\parallel^2\xi^2 \tag{3.55}$$

where $k_\parallel$ can be found by assuming that the poloidal variation must give high amplitude on the low field side and low amplitude on the high field side, so the wavelength for a circular cross section must be

$$\begin{aligned}\lambda_\theta = \Delta\theta r &= 2\pi r \\ \frac{2\pi}{k_\theta} &= 2\pi r\end{aligned} \tag{3.56}$$

the relationship between ϕ and θ is found by

$$q = \frac{d\phi}{d\theta}\Big|_{along\ field\ lines} \sim \frac{\Delta\phi}{\Delta\theta} \tag{3.57}$$

$$\Delta\phi = q\Delta\theta = 2\pi q \tag{3.58}$$

$$2\pi/k_\parallel \approx 2\pi/k_\phi = \lambda_\phi = R\Delta\phi = 2\pi Rq \tag{3.59}$$

$$k_\parallel = \frac{1}{Rq} \tag{3.60}$$

Using this expression for $k_\parallel$:

$$-\frac{dp}{dr} \sim \frac{1}{Rq^2}\frac{B^2}{\mu_0} \tag{3.61}$$

$$-\frac{d\beta}{dr} \sim \frac{1}{Rq^2} \tag{3.62}$$

$$\beta \sim \frac{r}{Rq^2} = \frac{\epsilon}{q^2} \tag{3.63}$$

using $\beta = 2\mu_0 p/B^2$.

Equation 3.63 estimates the critical β required to trigger a ballooning instability, but it does not consider the concentration of pressure gradient at the edge of the plasma in H-mode. A critical value for edge beta could be had by replacing r with the pedestal width and p with the pressure pedestal height, which could give a lower limit by about an order of magnitude under typical DIII-D H-mode conditions. This is why ballooning instability often occurs at the edge of tokamaks in H-mode and contributes to driving Edge Localized Modes (ELMs). With non-local (finite n) effects, the width of the steep gradient region is also important for quantitative evaluation of stability.[14,23]

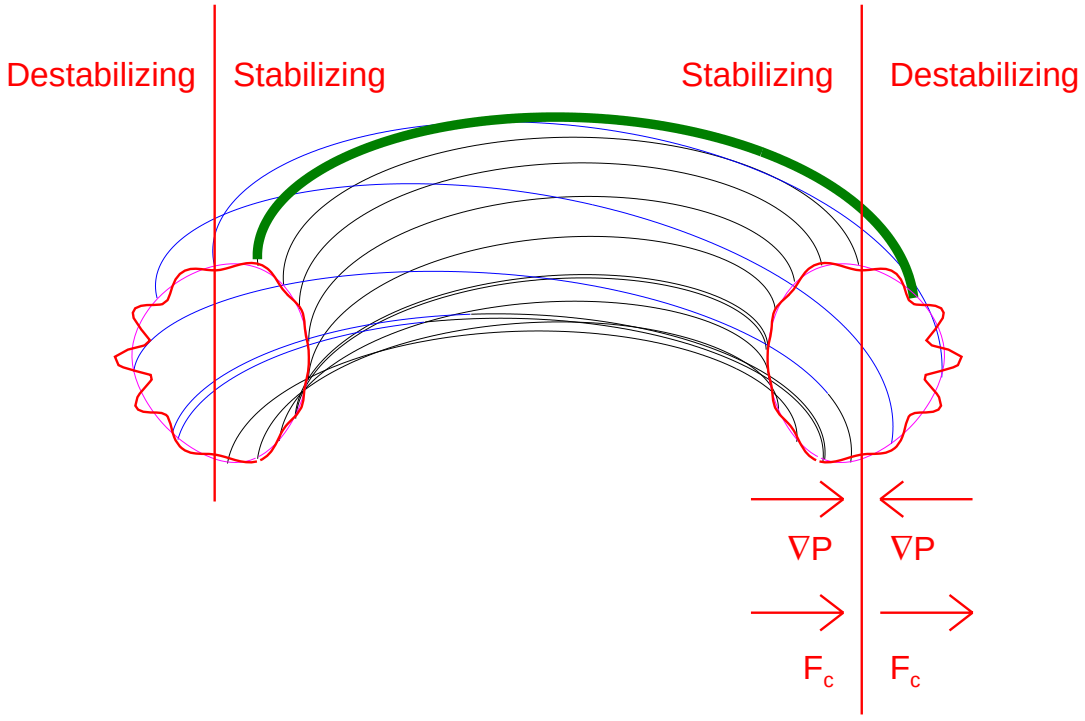

Figure 3.2: Schematic of a ballooning mode. Field lines are traced in blue and black on a flux surface as in figure 1.5. Red cross section curves show a hypothetical displacement away from a flux surface. Interchange modes tend to be excited when the pressure gradient ∇P and external force (here, that is centrifugal force F_c) are in opposite directions, and are stabilized by $\nabla P \parallel F_c$.[95] Thus, the mode is localized to the region of unfavorable curvature. The thick green curve shows a field line connecting the stabilizing inner region to the destabilizing outer region. Exciting the mode only on the outside requires bending of this line.

3.1.4 Peeling

Peeling or external kink modes are driven by edge current and are most unstable when a resonant surface is in the vacuum just outside the plasma.[11,49,93,101] Example kink displacements are shown in figure 3.3. For a tokamak with circular cross section and in the large aspect ratio limit, energy available for a kink displacement ξ is $\sim (B_\theta/m)(m-nq)(-dJ_\phi/dr)\xi^2$, where dJ_ϕ/dr is generally negative, so $m > nq$ is required for instability. Kinking is stabilized by the energy penalty for bending or compressing magnetic fields $\sim B_1^2$, where $\vec{B}_1 = \vec{\nabla} \times (\vec{\xi} \times \vec{B}_0)$ is the

perturbed magnetic field and its r component gives the energy cost of bending B along its length: $B_{1r}^2 \sim (B_0^2/R^2q^2)(nq-m)^2\xi^2 \sim \xi^2 B_0^2 k_\parallel^2$. So we estimate that kink drive can overcome the energy cost of field line bending when

$$-J'_\phi \sim (m-nq)\frac{mB_\theta}{\mu_0 r^2} \tag{3.64}$$

although the drive and field bending terms must both be integrated across the minor radius as seen in Eqn. 10 of Wesson.[93] In H-mode, there is a peak in current in the pedestal due to the bootstrap effect (see section 3.1.6), the magnitude of which is related to the pedestal height. Between this peak and the nearby vacuum, there is a large gradient in current density, which drives the peeling mode. The amount of current needed to trigger a kink can be seen to increase with mode number m, and also with poloidal field, which is generated by current throughout the plasma. The factor $(m-nq)$ will be smallest (lowest threshold) at the edge of the plasma, and for a mode with a rational surface close to the edge of the plasma: the penalty for field line bending vanishes when the mode is perfectly aligned with the field. However, in this limit, the energy cost of field compression may no longer be neglected and the rough estimate given by equation 3.64 breaks down. For a surface inside the plasma, the $(m-nq)$ factor in the drive term changes sign and the J' term becomes stabilizing instead of destabilizing for a typical scenario where current decreases with minor radius.

Physically, the drive arises from a torque provided by the perturbed $\vec{J}\times\vec{B}_1$ force on a flux tube, as seen in figure 3.4. For a flux tube in a region of negative current gradient, J_ϕ will be larger on the inner edge (smaller r) than on the outside, so the poloidal force $J_\phi B_{1r}$ is larger on the inside and the tube tends to be rotated in the $r-\theta$ plane. This force acts to enhance ripples if $m > nq$.[93] Only B_1 is considered because B_0 is balanced by ∇p.

In the limit where the resonant surface approaches the plasma, the perturbation ξ becomes increasingly localized near the surface:[93]

$$\xi = \xi_a(m-nq_a)/(m-nq) \tag{3.65}$$

where the subscript a denotes quantities at the plasma surface. Higher m modes tend to be more localized near the surface. This can be seen in the expression

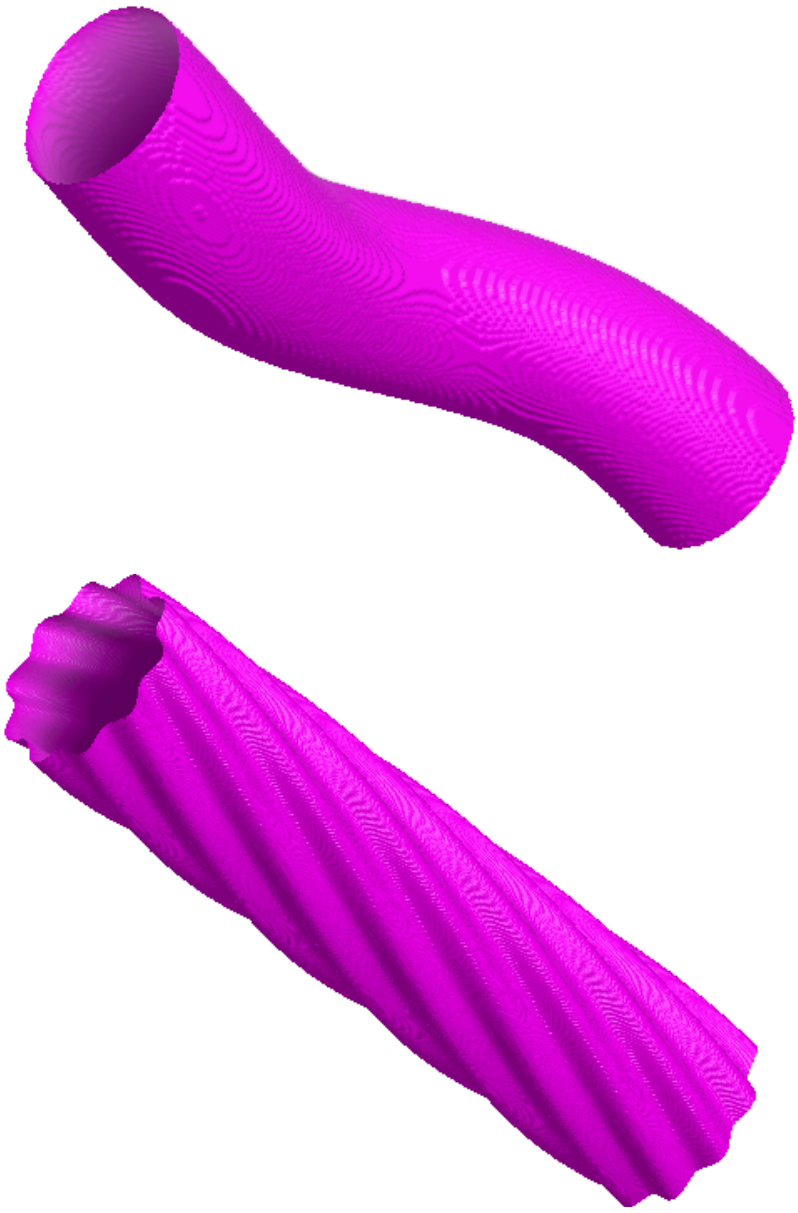

Figure 3.3: Helical kink displacement in a periodic plasma column. The radial displacement is $\xi_r = \xi_0 \cos(m\,\theta - n\,\phi)$ where θ is the angle around the axis, ϕ is along the axis ranging from 0 to 2π (this would loop around as the toroidal angle in a tokamak), and the mode numbers shown in this example are $m, n = 1, 1$ and $10, 5$.

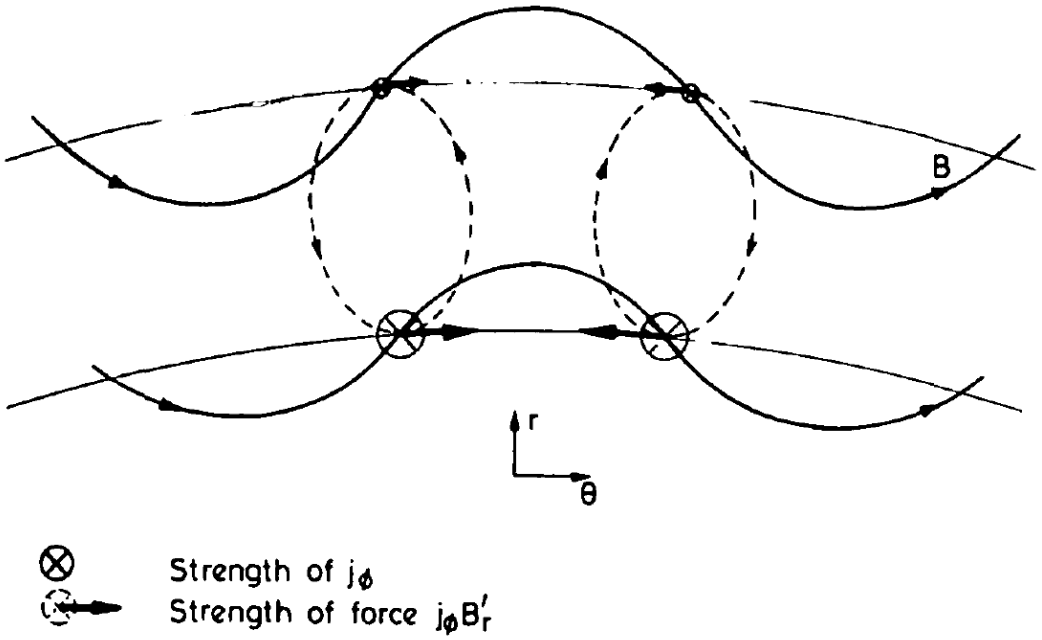

Figure 3.4: Illustration of the destabilizing effect of the dJ_ϕ/dr for $nq < m$. Current crosses the radial component of the perturbed field B_{1r}, resulting in a poloidal force $J_\phi B_{1r}$. Torque results from the difference in values of J_ϕ at different r. The torque around the dotted line tends to enhance the original displacement. Reproduced from figure 4 of Wesson.[93]

(Eqn. 3.65) for localization if it is assumed that $dq/dr > 0$: for a given q_a, destabilizing higher m modes requires higher n, and then the slope of nq will be higher, so the negative term in the denominator shrinks more quickly going into the plasma. Such localization gives the peeling mode its name: the edge layer "peels" away. Peeling dominated modes often drive smaller ELMs as their radial penetration depth is typically short, and they tend to occur at lower density where the bootstrap current is higher.[14]

3.1.5 Coupled Peeling-Ballooning

Tokamak geometry and common shaping effects break the symmetry that would be found in a cylinder, resulting in coupling of Fourier harmonics with the same toroidal mode number (m couples to $m + b$, where b is some integer).

The ballooning mode can couple to modes associated with rational surfaces in the vacuum and thus draw energy from sources associated with the peeling mode, and the peeling mode can couple to sideband harmonics in the plasma and take on a ballooning character.[15] Coupling of the ballooning and peeling modes has the effect of reducing overall stability as the coupled mode can be unstable when ideal ballooning and peeling would be independently stable.[14,102] The mode structure of an example case (the same case as will be used in chapter 4) is shown in figure 3.5. Coupling tends to be strongest at intermediate toroidal mode number n close to 20, and is affected by boundary shape and aspect ratio.[14] In particular, increases in upper triangularity for a diverted plasma with a dominant X-point at the bottom tend to reduce coupling and increase the stable area in $p' - J$ space. Figure 3.6, adapted from figure 5 of Snyder *et al.*,[14] shows a schematic of the typical effect of increasing upper triangularity in a lower single null discharge: the original stable area at low triangularity (in dark blue) expands until the light blue area is also stable. Higher n modes tend to be stabilized by magnetic shear or finite Larmor radius effects.

Steeper pressure gradients have a stabilizing effect on peeling modes, and edge current tends to stabilize ballooning modes and hence the purely peeling and purely ballooning branch boundaries have the slopes shown in the figure. Edge current is generated by the bootstrap current.[12,13] While temperature and density cooperate to form the pressure gradient, they have competing effects on collisionality $\nu_* \sim n/T^2$, which is significant for determination of the bootstrap current.[12] So, separate dependence on temperature and density must be considered.[14] Otherwise, the problem of P-B stability could be reduced to a function of one variable: the current profile could be completely determined by the pressure profile with no need for representation on its own axis.

3.1.6 Physical Origin of the Bootstrap Current

The strong pressure gradient in the pedestal leads to the formation of a bootstrap current, which is also localized to the pedestal and contributes to P-B instability. The bootstrap current is caused by trapped electrons in the presence of

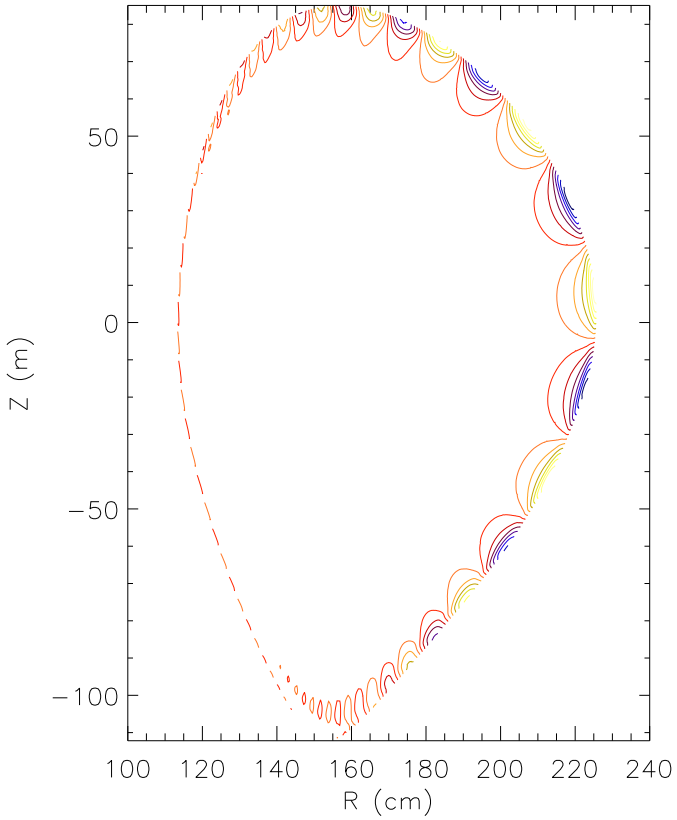

Figure 3.5: Example structure of an $n = 5$ P-B mode. Contours show magnitude of radial displacement as calculated by `ELITE` for shot 154749 before ELMs. m_0, the poloidal mode number of the rational surface just outside of the calculation mesh, is 31.

a density gradient. The banana orbits of the trapped electrons result in a parallel current analogous to the diamagnetic current which results from finite gyro orbits in the presence of a density gradient. The net motion of trapped particles in a region with a density gradient can entrain untrapped electrons through collisions or trapped electrons can become untrapped through collisions with ions. The resulting untrapped electrons (from both processes) carry a parallel current.[2,103] In the limit of low collisionality ($\nu_* < 1$, banana regime, where ν_* is the ratio of collision frequency to bounce frequency for trapped particles), the resulting bootstrap current is $J_{BS} = -A\frac{\sqrt{\epsilon}}{B_\theta}\frac{dp}{dr}$.[104] Trapped electrons must be able to complete banana orbits in order to produce a strong bootstrap current. If collisionality $\nu_* \gg 1$ (Pfirsch-Schlüter regime), then the bootstrap current is insignificant.[105]

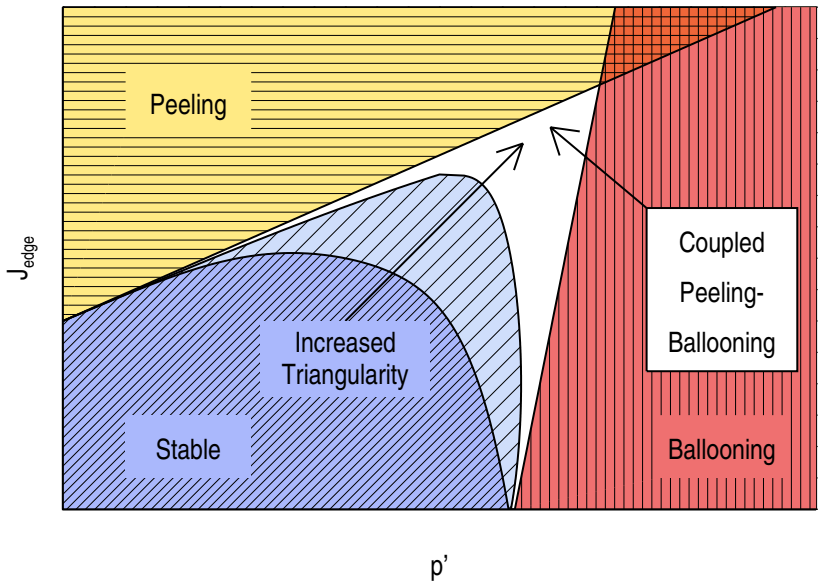

Figure 3.6: P-B Stability diagram in $p' - J$ space. Ballooning modes (red, vertical hash) are excited by high pressure gradients. Peeling modes (yellow, horizontal hash) are excited by edge current. Coupled peeling-ballooning modes (white, no hash) can be excited under conditions to which peeling and ballooning are independently stable. Increasing triangularity helps stabilize the coupled modes (pale blue, coarsely spaced diagonal hash). Some parameter ranges are stable without strong shaping (darker blue, finely spaced diagonal hash). Based on figure 5 of Snyder *et al.*[14]

3.2 Equilibrium and Stability Analysis

3.2.1 Preparation of Kinetic Equilibrium Reconstructions as Inputs

In this work, stability analysis is done using equilibria produced by the `EFIT` code[71] as inputs. The equilibria are based on measurements from magnetic probes[8,89] and the experimental pressure profile as measured by Thomson scattering[51] and Charge Exchange Recombination spectroscopy (CER).[25,106] These data are used to constrain solutions to the Grad-Shafranov equation and find a self-consistent solution for the magnetic field, current and pressure everywhere. The additional pressure and current constraints define a *kinetic* equilibrium reconstruc-

tion, whereas a general reconstruction might use only data from external magnetic sensors. Because the parallel current is not directly measured in the edge barrier region, calculated bootstrap current,[12] together with Ohmic current, is used to reconstruct the current profile in this region, as is standard practice in edge stability analysis (*e.g.* Snyder *et al.*[23]) The calculated Ohmic + bootstrap current profile is provided to `EFIT`, which attempts to find a solution which is consistent with both the calculated profile and the data from magnetic probes. Hyperbolic tangent and spline fits are used to prepare temperature and density measurements to form the pressure constraints used in the reconstruction.

It is common practice when performing edge stability analysis to vary the experimental pressure and current profiles and to find equilibrium solutions for many ($\sim 10^2$) points in perturbed $p' - J$ space. The stability of each hypothetical equilibrium is then calculated and a map of the stable region of $p' - J$ space may be constructed.

Constructing the Total Pressure Profile

Electron temperature and density are fit to modified hyperbolic tangent functions in the manner described by Groebner, *et al.*,[74] with ψ_N as the position basis. Ion temperature is fit with a cubic spline. The treatment is similar to the description given by Osborne *et al.*,[107] but with complications due to sparser CER data: as total injected power for these discharges had to be kept low, only the beams which supply CER measurements in the pedestal region were active during some time windows. In these cases, core T_i was constrained by assuming $T_i = T_e$ at $\psi_N = 0$, which is a reasonable assumption based on observations when core T_i measurements were available, and edge stability analysis should not be sensitive to the error introduced by this assumption about the core plasma. Fast ion density and pressure (due to neutral beams) are obtained from calculations with the `ONETWO` transport code,[108] and contributions to total pressure due to rotation are also considered. The fast ion and rotational pressure terms are generally small at the edge,[107] and the fast ion term is even smaller than usual due to the low beam power injected by de-rated and modulated beams. These terms are still included

in the calculation, despite being insignificant in this experiment.

As the total current is known and the core current profile depends on the resistivity profile, bad assumptions about, or measurements of, temperature and density in one region can affect the fitted current profile elsewhere. However, the current fit is constrained to a calculation including J_{BS}[12] near the edge at several points, so the critical part of the current profile which affects peeling stability should not be sensitive to errors in the deep core current profile, which can be made up elsewhere inside of the pedestal to maintain the correct value of total current. So again, the stability of the edge should be insensitive to gaps in ion data in the core.

CER measures the intensity of emission from fully stripped carbon atoms that capture an electron during a collision with a fast beam atom. Deuterium density is determined by assuming quasi-neutrality: $n_e = n_D + 6n_C + n_{fast}$ (n_{fast} should be small in the pedestal). The carbon density n_C is often determined by a fit to carbon fraction rather than fitting carbon density directly. Assuming $T_D = T_C = T_i$, the fits are combined to form a total pressure profile.

As discussed in section 2.8, there is some difficulty in mapping the electron profiles from TS to the ion profiles from CER. In the following analysis, the CER data were assumed to be correctly mapped to ψ_N and TS data were shifted such that the foot of the tanh fit to T_e aligned with the separatrix, which is the commonly accepted procedure.

Grad-Shafranov Equation

The pressure gradient is related to the currents and fields in a stationary equilibrium with no external forces by

$$\vec{J} \times \vec{B} = \vec{\nabla} p \tag{3.66}$$

using equation 3.10. The poloidal components of the field and current can be written using the definition of the magnetic flux function ψ given in section 1.3.1 and introducing the current flux function f:

$$\vec{B}_p = \frac{\vec{\nabla}\psi \times \hat{\phi}}{R} \tag{3.67}$$

$$\vec{J}_p = \frac{\vec{\nabla} f \times \hat{\phi}}{R} \tag{3.68}$$

With these definitions, equation 3.66 becomes

$$\vec{\nabla} p = \frac{\vec{\nabla} f \times \hat{\phi}}{R} \times \hat{\phi} B_\phi + \hat{\phi} J_\phi \times \frac{\vec{\nabla} \psi \times \hat{\phi}}{R} \tag{3.69}$$

and with the axisymmetry of the problem, $\hat{\phi} \cdot \vec{\nabla} \psi = \hat{\phi} \cdot \vec{\nabla} f = 0$, so

$$\vec{\nabla} p = -\frac{\vec{\nabla} f}{R} B_\phi + J_\phi \frac{\vec{\nabla} \psi}{R} \tag{3.70}$$

Using the chain rule:

$$\frac{dp}{d\psi} \vec{\nabla} \psi = -\frac{df}{d\psi} \vec{\nabla} \psi \frac{B_\phi}{R} + \frac{J_\phi}{R} \vec{\nabla} \psi \tag{3.71}$$

$$R \frac{dp}{d\psi} + \frac{df}{d\psi} B_\phi = J_\phi \tag{3.72}$$

Comparing Ampére's law (Eqn. 3.15) to the definition for f, which is $J_R = -\frac{1}{R}\frac{\partial f}{\partial Z}$, $J_Z = \frac{1}{R}\frac{\partial f}{\partial R}$, it is seen that $f = RB_\phi/\mu_0$. Substituting $B_R = -\frac{1}{R}\frac{\partial \psi}{\partial Z}$, $B_Z = \frac{1}{R}\frac{\partial \psi}{\partial R}$ into Ampére's law gives:

$$\mu_0 J_\phi = \frac{\partial}{\partial Z} B_R - \frac{\partial}{\partial R} B_Z \tag{3.73}$$

$$\mu_0 J_\phi = -\frac{\partial}{\partial Z}\left(\frac{1}{R}\frac{\partial \psi}{\partial Z}\right) - \frac{\partial}{\partial R}\left(\frac{1}{R}\frac{\partial \psi}{\partial R}\right) \tag{3.74}$$

$$J_\phi = -\frac{1}{\mu_0 R}\frac{\partial^2 \psi}{\partial Z^2} - \frac{1}{\mu_0}\frac{\partial}{\partial R}\left(\frac{1}{R}\frac{\partial \psi}{\partial R}\right) \tag{3.75}$$

Substituting $B_\phi = f\mu_0/R$ and equation 3.75 into equation 3.72:

$$R\frac{dp}{d\psi} + \frac{f\mu_0}{R}\frac{df}{d\psi} = -\frac{1}{\mu_0 R}\frac{\partial^2 \psi}{\partial Z^2} - \frac{1}{\mu_0}\frac{\partial}{\partial R}\left(\frac{1}{R}\frac{\partial \psi}{\partial R}\right) \tag{3.76}$$

$$R\frac{\partial}{\partial R}\left(\frac{1}{R}\frac{\partial \psi}{\partial R}\right) + \frac{\partial^2 \psi}{\partial Z^2} = -\mu_0 R^2 \frac{dp}{d\psi} - \mu_0^2 f \frac{df}{d\psi} \tag{3.77}$$

which can be written as

$$\Delta^* \psi = -\mu_0 R^2 p' - F F' \tag{3.78}$$

where Δ^* is the elliptic operator (given by the left hand side of Eqn. 3.77), $a' = da/d\psi$, and $F = \mu_0 f$.

Equation 3.77 is the Grad-Shafranov equation.[2,109] It is clear where the pressure profile from TS and CER enters in the second term on the right. Additional constraints come from magnetic measurements and assumptions about the current profile.[12]

External magnetic sensors allow determination of the total plasma current I_p through the integral form of Ampére's law. The internal inductance l_i is a measure of how peaked the current profile is and can also be determined by measurements of the magnetic field on an external surface surrounding the plasma,[71,110] although it can only be separated from β_p for sufficient elongation. The externally applied loop voltage is known, as is the resistivity profile from the temperature and density fits, allowing an estimate of the current profile from Ohm's law. The final piece of information about the current profile is a calculation[12] of the diamagnetic and bootstrap currents, which are significant in the pedestal. The external magnetic sensors also give information about the local behavior of ψ and allow determination of the poloidal beta $\beta_p = 2\mu_0 p/B_p^2$.[110]

In general, information about the current profile in the core is available from the Motional Stark Effect (MSE) diagnostic.[111] However, this requires use of a high voltage/high power neutral beam in addition to the beam needed for the edge CER measurements, which is incompatible with the goal of diagnosing back transitions and as a result, MSE is unavailable for most of the reconstructions used here. As mentioned before, edge stability is insensitive to the details of the core current profile and omission of MSE data is acceptable for this analysis.

The final kinetic `EFIT` uses experimental information about p, J, and the external B to construct a self consistent solution for ψ, f, and p which gives the correct I_p, l_i, and β_p. This process is then repeated for an array of perturbed pressure and current profiles to produce a set of equilibria covering a region of $p' - J$ space around the unperturbed experimental profile, and stability analysis is performed on each equilibrium solution. Obviously, exact agreement between the `EFIT` p and J and the measured and calculated p and J is not expected due to uncertainties in the measurements.

Another source of current is the Pfirsch-Schlüter current, J_{PS}, which is

a parallel return current that maintains divergence free current density in the case of poloidally asymmetric poloidal currents, such as those would arise from the magnetic gradient drift.[6,112] The flux surface average of this current is zero and so it does not provide free energy to kinking. However, the average of the Pfirsch-Schlüter current weighted to the localization of a ballooning mode, which is localized to the low field side, is not zero, so it may have a small effect. The equilibrium reconstruction will contain J_{PS}, regardless of whether or not it has a significant effect on peeling-ballooning stability.[112]

Finally, note that many of the fits performed in the process of constructing a kinetic `EFIT` from the temperature, etc. measurements require some human intervention. Different preferences when manually adjusting knots, as is sometimes required, or different interpretations of what profiles should look like (for example, the impurity fraction in the pedestal is believed by some to be constant) can lead to different results. The discrepancy in `EFIT`s produced by different experienced users has been studied and can dominate experimental uncertainty. Estimated uncertainties in the edge current and pressure gradient due to these fitting uncertainties are used as the error bars displayed on the $p' - J$ space stability maps shown later.

3.2.2 Ideal Linear Stability of Peeling-Ballooning Modes (`ELITE`)

In order to efficiently study the discharges found in DIII-D, including realistic geometry and non-local effects, the `ELITE` code was used.[14,49,113] `ELITE` solves an expansion of the ideal MHD equations to the accuracy required to study peeling-ballooning mode thresholds, and to calculate growth rates for experimental or hypothetical equilibria. `ELITE` employs an analytical expansion and numerical methods which allow it to very efficiently study intermediate to high n modes which are thought to cause type-I ELMs. The MHD energy equations are expanded in $1/n$ to second order and the resulting set of Cauchy-Euler equations for Fourier mode amplitudes are then solved numerically. The Fourier modes here are trial solutions with the form $\exp[i(m\theta - n\phi - \omega t)]$. `ELITE` is further optimized to improve

efficiency by noting that Fourier modes will be concentrated around their rational ($m = nq$) surfaces, so only a subset of poloidal harmonics, determined by the q profile and the toroidal harmonic being considered, are significant at any given point and the rest can be neglected. An analytic expansion of the Grad-Shafranov equation (eqn. 3.77) is performed to allow more precise calculation of local (same flux surface) quantities and their derivatives. Finally, the grid for evaluating the finely varying Fourier modes is separated from the grid for the equilibrium, which can be much coarser. The expansion in $1/n$ means that `ELITE` is appropriate for n values of at least 4 or 5, and typical type-I ELMs have $n \sim 5 - 30$.

It can be seen from equations 9, A4, and A5 of Wilson *et al.*[49] that the eigenvalue γ^2_{MHD} depends on mass density as $\gamma^2_{MHD} \sim 1/\rho$, making it convenient to normalize growth rates to the Alfvén[96] frequency $\omega_A = v_A/R$, where $v_A = B/\sqrt{\mu_0 \rho}$, and results are given in terms of γ/ω_A in many of the papers on the subject. This also allows ideal codes to be run with a simplified setup that only uses the information contained in the equilibrium reconstruction and not the experimental density and still provide γ_{MHD}/ω_A.

The ideal model does not account for stabilization by finite Larmor radius and diamagnetic effects, and it is common practice to compare the calculated growth rates to $\omega_{*i}/2$, where $\omega_{*i} = kT_i n_i'/(ZeBn_i)$ is the ion diamagnetic drift frequency, $k = 2\pi/\lambda$, is the wavenumber, n_i and T_i are the ion density and temperature, Z is the charge state, and e is the elementary charge. Ion temperature gradients are typically much shallower than density gradients at the edge of a tokamak. With this diamagnetic threshold ($\gamma_{MHD} > \omega_{*i}/2$,[100] see section 3.1.2), `ELITE` does successfully predict ELM onset in most regimes, including large type-I ELMs.[14] An exception is high density type-III ELMs, which may involve kinetic or resistive effects.[14] In fact, ω_{*i} is subject to variation over the width of the pedestal. The simplest approach is to use the peak value of ω_{*i}, but this can be improved by using an effective value ω_{*eff} which accounts for variation across the pedestal. ω_{*eff} may be obtained from a two-fluid calculation with the `BOUT++` code;[114] the condition for instability is then $\gamma_{MHD} > \omega_{*eff}/2$.[115] That is, `BOUT++` is used to calculate P-B ballooning stability with self consistent treatment of the rapid spatial

variation of the diamagnetic frequency included, and comparison with a calculation which does not directly include kinetic effects (such as ELITE) gives ω_{*eff}. This can be used to check the results of the faster, ideal calculations against more computationally expensive, two-fluid calculations, or ω_{*eff} can be fit to two-fluid results and used as an improved threshold in future ideal calculations.[115] Details of ω_* are more important for higher n and changes in the ballooning limit on p' will be greater than changes in the peeling limit on J, where the growth rate increases rapidly as a function of current and reasonable error in ω_{*i} should not move the boundary significantly: ω_{*eff} calculations are most valuable for high n ballooning dominated modes and least important for low n peeling dominated modes. As will be seen, the plasma discharges considered in this work are closer to going peeling unstable ($(J_{limit} - J)/\sigma_J < (p'_{limit} - p')/\sigma_{p'}$) and the most unstable modes are low $n \sim 5$, so the advanced treatment of ω_{*eff} is neglected and constant ω_{*i}, evaluated at its peak value in the pedestal, is used. The quality of this approximation can be understood from figure 4 of Snyder *et al.*,[115] while remembering that errors in growth rates translate into small errors in the position of the stability boundary in $p' - J$ space.

ELITE has been successfully benchmarked against GATO[116] for $4 \leq n \leq 10$, the MISHKA compressionless MHD code[117] for $5 \leq n \leq 20$, MARG2D for $5 \leq n \leq 100$,[118] M3D-C^1 for $5 \leq n \leq 40$,[119] NIMROD for $5 \leq n \leq 20$,[120] and BOUT++ for $5 \leq n \leq 45$.[121] Further evidence of ELITE's validity for computing pedestal stability comes from the success of the EPED model, which combines ELITE calculations on sets of model equilibria with a model for kinetic ballooning modes constraints to predict the pedestal height and width.[23,75,115] EPED is described in more detail in section 2.7.1.

When ELITE runs are badly set up or the inputs poorly resolved, ELITE will attempt to calculate growth rates anyway and will flag potentially bad runs. ELITE is also computationally cheap to the point that many perturbation points in $p' - J$ may be tested and thus bad runs which escape ELITE's automatic error identification are apparent as they break unnaturally from the trends set by neighboring points (assuming enough of the neighbors are valid to form a clear trend).

It is easy to assess the quality of results.

In the analysis reported here, ELITE has consistently returned reasonable stability maps. Furthermore, ELITE runs prior to back transitions are grouped with ELITE runs on the ELMing and early (shortly after the L-H transition) phases of the same H-modes, which always identify stability or instability consistent with the observed absence or presence of type-I ELMs. This establishes that ELITE is valid for the shape and other conditions being tested and is being operated correctly.

3.2.3 Resonance and Edge q in Numerical Models

An additional consideration for ideal stability analysis near the edge of the plasma is the value of the safety factor at the edge of the model, q_a. The model in ELITE includes an ideal plasma and an ideal vacuum with a sharp transition between them. In reality, the high temperature and highly conductive (Spitzer resistivity $\eta \sim T^{-1.5}$) core plasma connects to the insulating vacuum through a boundary layer where temperatures are much lower. The layer where neither the ideal plasma nor the ideal vacuum approximation may be applied is generally thin enough[a] that treating it as an abrupt transition generally provides a reasonable approximation. These models place the plasma-vacuum transition slightly inside of the nominal separatrix to avoid an ideal plasma calculation at the X-point, where q diverges, where length scales become smaller than the gyro radius such that ideal MHD is no longer a good approximation, where models based on Fourier expansion in the poloidal direction break down, and where 3D effects (such as small errors in the applied magnetic field) are important such that the 2D equilibrium approximation breaks down.[122] That is, the ideal edge of the plasma is placed slightly inside the nominal 2D separatrix. But since q increases rapidly at the edge, small differences in the cutoff condition result in large differences in edge q. This makes the status of the resonance condition, $m = nq_a$, very uncertain.

[a] Resistivity in the pedestal has not been measured directly. Length scale of exponential fit to Spitzer resistivity $\approx 2\%\psi_N \approx 0.7$ cm in H-mode; Lundquist number[91] S with 3 cm (∼pedestal width) length scale drops to $\sim 10^4$ at $\psi_N \approx 0.99 \approx 0.3$ cm inside the separatrix, compared to $> 10^6$ inside of the pedestal. In fact, the region of small S is too thin to measure with Thomson scattering beyond an upper bound.

While this has little bearing on the limiting pressure and current (the position of the stability boundary in $p' - J$ space is insensitive to variation in the exact cutoff location within the typical range of values), matching cutoff settings can be important when comparing results from different codes or when making precise comparisons between results from the same code at different mode numbers. This is relevant to this work as we would like to understand how stability limits vary with mode number.

ELITE is able make small adjustments to the equilibrium f (see eqn. 3.77) to control the value of $\Delta = (m - nq_a)$. For small values of Δ, peeling drive is larger than for higher values. When a finite diamagnetic threshold is included, variation in Δ and cutoff location (when beyond $\psi_N \approx 0.994$) are generally small effects (compared to measurement uncertainty) on the calculated stability threshold.[23] Nonetheless, consistency in treatment of these effects is required if one wishes a code benchmark to precisely reproduce calculated growth rates across different codes.

If constant Δ is not used, then variation in stability with respect to mode number n can be masked by variation in response to changing Δ (recall that the current profile is modified to produce the variational equilibrium set and stability map; this alters q). At high n, there may be many n values with similar behavior and averaging these can remove fluctuations due to changing Δ. But at low n, every step can have large effect and no averaging to remove Δ dependence is possible. In order to precisely compare stability between $n = 5$ and $n = 10$, for example, as a function of mode number, the Δ dependence must be treated consistently. ELITE can make a negligible change to the toroidal field, modifying $f^2 = (RB_\phi)^2$, in order to accommodate specified values for both cutoff location and Δ. This changes q_a slightly, but the change is well within the uncertainty. Because n is fairly large, the change in q_a needed to fix Δ is quite modest (*e.g.* for $n = 15$, changing Δ by 0.5 requires a change in q_a of $0.5/15 = 0.03$). The specified value of Δ was 0.2 for this work, which is consistent with past results and gives a value which is typical of the average growth rate averaged over possible values of Δ.

3.3 Acknowledgements

Chapter 3 contains material from Physics of Plasmas vol. 22. Eldon, David; Boivin, Réjean L.; Groebner, Richard J.; Osborne, Thomas H.; Snyder, Philip B.; Turnbull, Alan D.; Tynan, George R.; Boedo, Jose A.; Burrell, Keith H.; Kolemen, Egemen; Schmitz, Lothar; Wilson, Howard R., American Institute of Physics, 2015. The disseration author was the primary investigator and author of this paper.

4 Ideal MHD Stability Analysis of H-L Back Transitions with ELITE

High confinement or H-mode is an attractive regime of tokamak operation as it allows operation at higher temperature and density than L-mode or Ohmic operation.[9,10] In H-mode, additional stored energy builds up behind a transport barrier which is present in the last $\sim 5\%$ of closed flux surfaces. This inventory of heat and particles must necessarily be released during the termination of a plasma discharge. The transport barrier typically forms rapidly and it can also dissipate abruptly. The resulting outflow of plasma may have deleterious effects on the plasma facing components of ITER or a reactor and must be better understood and possibly mitigated. Understanding what physical processes are involved in or before H-L back transitions is necessary in order to predict heat loads and to plan mitigation techniques.

This chapter tests whether the H-L back transitions in a given scenario begin with peeling-ballooning instabilities. The large, sudden pedestal relaxations observed at the start of back transition sequences have been referred to as type-I ELMs in previous publications.[42,44] Type-I ELMs are understood to be triggered by ideal peeling-ballooning modes,[14] and there is much research available for predicting heat loads and guiding mitigation or suppression[50,78–80] strategies of these modes. So, identification of an ideal peeling-ballooning mode as an important component of the H-L sequence would lead to useful understanding and ability to control H-L transitions. However, the transient event in question is shown in this

chapter to be distinct from the ideal P-B driven type-I ELMs. So, work done on type-I ELMs cannot be applied. Fortunately, chapter 5 will present a promising strategy for controlling energy released by the transient.

4.1 Experiment Setup

The goal of these experiments was to test whether an ideal peeling-ballooning instability is triggering the initial "transient", which in this chapter will refer to the large D_α spike and sudden reduction in pedestal height at the start of the H-L back transition sequence.

The case of a simple, spontaneous transition out of H-mode was isolated by establishing ELMing H-mode with NBI; during this period, type-I ELMs set the limit on pedestal height, which in turn sets the boundary conditions for core physics. The toroidal field and plasma current are held steady while the beam heating power is reduced to minimal levels needed for diagnostics, and a back transition then occurs. The back transitions examined here are furthermore distinct from cases where an actively heated H-mode plasma experiences a large type-I ELM which dissipates enough edge pressure that the plasma temporarily transitions back to L-mode before recovering into H-mode. Here, the power is low and the H-L transients are well separated in time from the periodic type-I ELMs. Typical shot parameters are listed in table 4.1 and a typical boundary shape in relation to key diagnostics is shown in figure 4.1.

The conditions of this experiment were arranged to make the transition sequence as long as possible to facilitate diagnosis of important phenomena and because of interest in identifying conditions for a "soft landing", which is a transition that avoids the rapid collapse of the edge pedestal and instead provides a longer, more gradual reduction in edge pressure gradient. To this end, a shape which has produced long "dithering" H-L transition sequences in previous experiments was chosen. Dithering periods during L-H or H-L transitions are characterized by small, rapid D_α bursts and confinement times between L- and H-mode values: the dithering phase is an intermediate step in the transition. Although

Table 4.1: Typical shot parameters

Symbol	Value	Name
B_t	-2.15 T	Toroidal field, vacuum, at magnetic axis
I_p	1.0 MA	Plasma current
β_N	1.0-2.0	Normalized beta during ELMing H-mode
q_{95}	4.6-4.9	Safety factor at 95% flux surface
κ	1.75	Elongation
δ_{up}	0.11-0.38	Upper triangularity
δ_{low}	0.3	Lower triangularity
a	0.58 m	Minor radius
R_m	1.74-1.77 m	R: Major radius, magnetic axis
Z_m	-0.02-0.00 m	Z: Height above machine midplane, magnetic axis
R_{xpt}	1.53 m	R, dominant X point
Z_{xpt}	-1.17 m	Z, dominant X-point
$R_{gap,out}$	8.3 cm	Outer gap
P_{inj}	3300 kW (heating) 160 kW (diagnostics)	Average neutral beam power injected
V_{ac}	50, 75, 81 kV	Beam accelerating voltage for various heating and diagnostic purposes
$\bar{n}_e$	$1.7 \times 10^{19}/\,\mathrm{m}^3$	Line average density before L-H transition

long dithering phases are present in the transition sequences examined, the start of the sequence is still associated with a large, ELM-like transient which rapidly relaxes the pedestal height (figure 4.2 at 4402 ms and figure 4.3). In this chapter, it is only the first spike in D_α (or rather, conditions immediately preceding it and the rapid pedestal collapse) which is being tested against P-B calculations.

In these discharges, the type-I ELMs driven during the heated phase are separated from the start of the back transition sequence by a long ELM-free period lasting up to hundreds of milliseconds (about 170 ms in the example of figure 4.2).

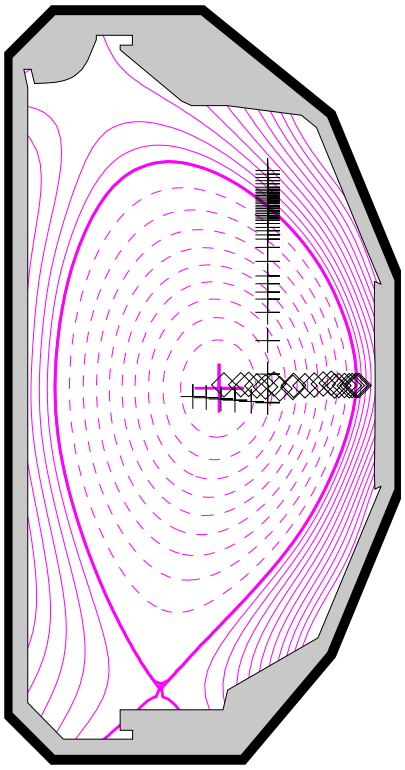

Figure 4.1: `EFIT` equilibrium reconstruction of shot 154749 at 4400 ms. CER chords with tangential views are marked with black diamonds. Thomson scattering chords on the core and tangential subsystems are marked with black plus signs. The separatrix is a thick magenta line. The vacuum vessel is a thick black line around the outside, and the gray area within it is taken up by equipment and carbon wall tiles.

During this time, low powered neutral beams are used to enable measurements of carbon ion impurity temperature, density, and rotation with CER. The ion profiles were combined with electron profiles and used to reconstruct equilibria with the `EFIT` code.[71]

H- to L-mode back transitions have been observed to be accompanied by a sudden drop in stored energy and pedestal height, as shown in figure 4.2 by time traces of these and other parameters, and in figure 4.3 by profiles before and after the intial D_α spike (4402 ms, figure 4.2) associated with the H-L transition sequence. Depending on how the energy released by the transient scales

with machine size, this event could pose a problem for next step devices such as ITER. The transient is superficially similar to a large type-I Edge Localized Mode (ELM). Although benign in present-day tokamaks, models of peeling-ballooning driven type-I ELMs indicate that these events will cause high levels of wall erosion in ITER and must be controlled.[17–20] The onset of many varieties of ELMs, including large type-I ELMs have been shown to be consistent with ideal peeling-ballooning modes[a].[14,49,123,124] If the transient is a peeling-ballooning unstable type-I ELM,[14,46] then existing ELM models may be applicable and could provide estimates of heat loads or guide mitigation strategies. Here we provide a detailed MHD stability analysis of the edge pedestal immediately preceding the H-L back transition transient. The results indicate that the H-L transient is not driven by ideal peeling-ballooning modes.

In the representative example shown in figure 4.2, neutral beam injection (NBI) is turned on at the start of the plot range and soon triggers the L-H transition, ending in ELM-free H-mode at 3540 ms. The H-mode develops until ELMs are driven starting at 3770 ms. Beams are reduced to diagnostic levels at 4200 ms, and ELMs stop at 4230 ms. An ELM free period persists until 4402 ms, when the back transition sequence begins with the large transient in D_α emission [figure 4.2(a)]. Figure 4.3 shows the relaxation of the pedestal as a result of the transient at 4402 ms: the height of the pedestal (especially in density) is greatly reduced between the slices at 4401 and 4411 ms.

[a] The ideal peeling-ballooning model provides explanations for large and small type-I ELMs, type-II ELMs, and low density type-III ELMs.

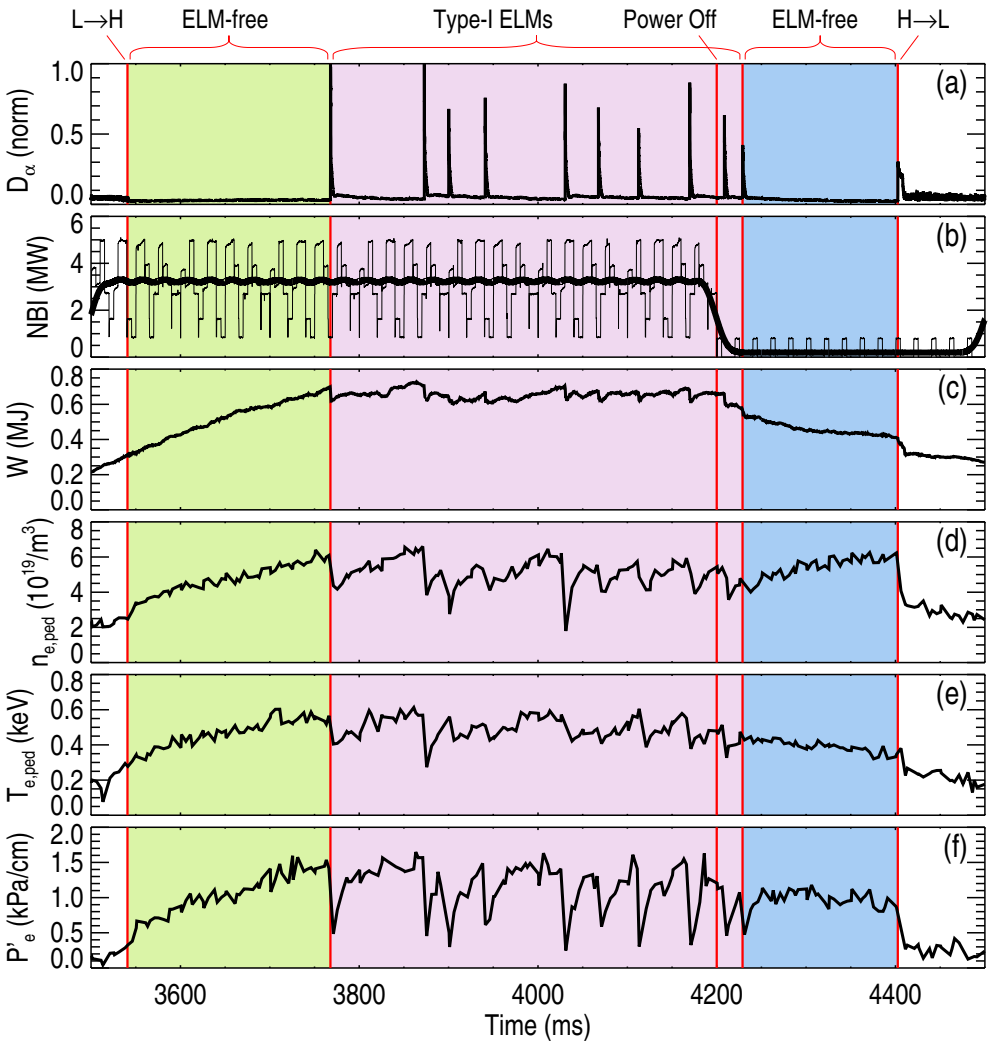

Figure 4.2: Evolution of a plasma leading up to an H-L back transition. Critical times are marked with vertical red lines. (a) D_α emission measured on a chord ending on the outer strike point on the divertor shelf, (b) NBI average power; several beams are modulated for diagnostic reasons. Smoothed power is plotted in bold, (c) plasma stored enrgy from MHD calculation, (d) pedestal electron density from tanh fit to Thomson scattering data, (e) corresponding pedestal electron temperature. (f) pedestal pressure gradient from tanh fit.

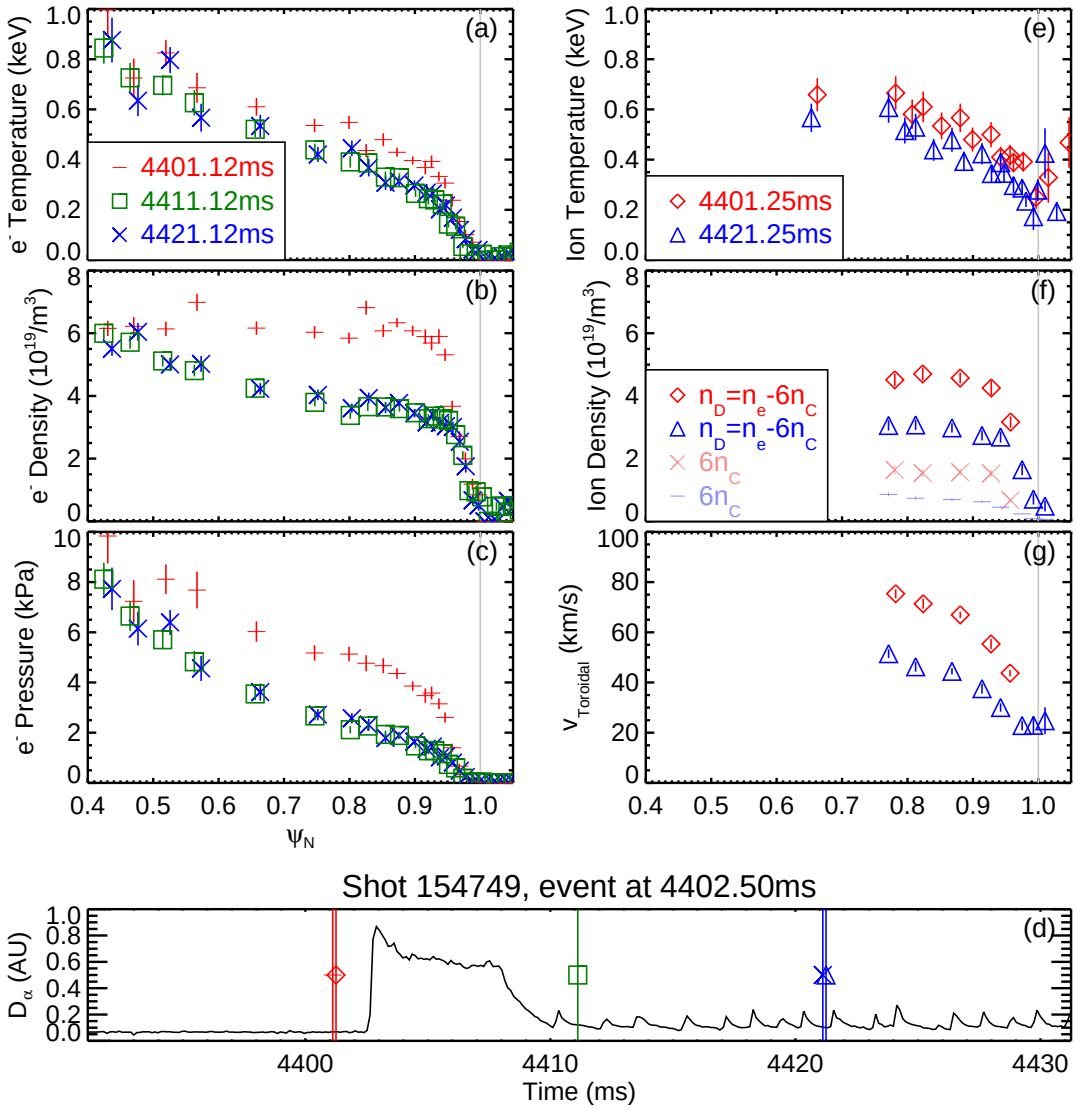

Figure 4.3: Relaxation of the pedestal as a result of the candidate event at the beginning of the back transition sequence. A time slice immediately before the event is shown with red dashes (Thomson scattering) and diamonds (CER), 10 ms later (after the event) with green squares (Thomson scattering), and 20 ms after the first slice with blue Xs (Thomson scattering) and triangles (CER). (a-c) Electron temperature, density, and pressure, (d) D_α from the outer strike point on the divertor shelf with vertical lines marking the times in the profiles above, (e) ion temperature, (f) fully stripped carbon density from CER (faded dashes and Xs) and calculated deuterium density (diamonds and triangles), (g) toroidal rotation (CER).

4.2 Stability Analysis

Equilibria were constructed from data taken ~ 10 ms before the transient events at the start of back transition sequences. The exact timing varied from case to case and the preferred candidates were those with neutral beam blips supplying CER data in close temporal proximity to the start of the events. Use of two CER slices was preferred to ensure accuracy. With a 2.5 ms CER integration time and 5 ms beam blips, this usually meant one blip was needed, but there were occasions where data from two blips were needed. In such cases, the time period from which data were drawn extended to ≈ 20 ms before the start of the back transition. Such a long time period is acceptable given the slow evolution of the discharge preceding the back transition, with ELM-free periods commonly persisting for more than 100 ms between the last type-I ELM and the start of the H-L sequence. In a typical type-I ELM cycle, the edge profiles develop to nearly marginal stability by 80% of the time interval between ELMs. The equilibria were calculated for 257×257 $R - Z$ grids.

To construct a stability map in $p' - J$ space and evaluate how close the plasma is to the stability boundary, the pressure and current profiles which are used to constrain the equilibrium solver are varied and a new equilibrium is calculated at each perturbation point. p and J are soft constraints and it is generally possible to find a self consistent equilibrium solution within the appropriate uncertainties even with perturbations added (there are limits, however. For a large enough perturbation, eventually the solver will fail to converge). Stability calculations are then performed for each new equilibrium reconstruction. The profiles in the core are adjusted to maintain constant total current I_p and β_p. If the initial equilibrium (for experimental data with no variation added) is well constructed, most ($\gtrsim$90%) of the solutions for the variations will typically converge. A set of about 200 perturbation points gives a fairly well resolved view of stability in $p' - J$ space and allows easy identification of outliers, which are then removed. The range of variation in p and J was determined by an initial guess and then expansion as needed to include appreciable areas of stable and unstable space. The range of variation is also limited by the ability of `EFIT` to converge upon

equilibrium solutions for the perturbation points, although this limitation was not an issue for this study. The entire process was controlled using established routines which fit profiles to the experimental temperature and density data and use these to call EFIT with pressure and current constraints, including appropriate sets of variations.[112]

For the purposes of labeling the profiles, p' is evaluated at the location of peak pressure gradient. The current label J is intended to give a sense of the amount of current at the edge of the plasma and is the average of current density at the bootstrap peak and at the "separatrix" (after cutoff) normalized to the average current density throughout the plasma. The full pressure and current profiles output by the equilibrium reconstruction are used by ELITE.

ELITE is used to calculate a growth rate for each point in the $p' - J$ scan for each of a selection of mode numbers. Typically, testing of $n = 5$, 10, 15, 20 and 25 gives a good representation of the overall stability boundary. The majority of runs were carried with a nominal cutoff at 99.5% of ψ_N. The resonance control (see section 3.2.3) was set to $\Delta = m_0 - nq_a = 0.2$, where q_a is the safety factor at the boundary between ideal plasma and ideal vacuum in the model, and m_0 is the poloidal mode number of the resonant surface just outside the plasma, such that $0 \leq \Delta < 1$.

Values for the cutoff location and equilibrium convergence level were chosen for consistency with standard practice, but were tested to ensure adequacy for this study: A more tightly converged equilibrium set was generated for one case and a test with ELITE found insignificant difference in the stability boundary location, demonstrating that the standard convergence level used in the rest of the runs was adequate. A cutoff at 99.7% of ψ_N was tested and found to also have insignificant effect on the stability boundary location.

As further validation that data quality was adequate and the analysis procedure and setup were valid, ELITE was used to analyze conditions not just before back transitions, but also immediately before ELMs (expected to be very close to stability limit) and shortly after the L-H transition (expected to be far from stability limit). The selection of data for these cases was done as follows: Pedestal

pressure drops during an ELM and recovers afterward, until it is high enough to drive the next ELM (see figure 1.9). Data taken after 80% of the inter-ELM time will have a pressure profile which is close to triggering the next ELM. Thus, data which occur between 80 and 99% of the time interval between any two ELMs were collected and used to form a composite profile representing the pedestal shortly before an ELM is triggered. This is a common practice for increasing the number of measurements available and reducing uncertainties. The equilibrium constructed from these data should be very close to the stability boundary. Another equilibrium was constructed from data taken during the ELM-free period after the L-H transition, well before any ELMs occur, and this should be far from the stability boundary. These cases were used to validate the data and procedures being used. Figure 4.4 shows time windows for data selection for the different cases.

Calculations with `ELITE` clearly show the plasma evolving from a condition of P-B stability shortly after the L-H transition, to a condition of P-B instability before each type-I ELM, and back to stability before the H-L transition sequence begins with the transient. Representative stability maps for these three cases are shown in figures 4.5-4.7 with the same plot ranges.[125] Figure 4.4 shows the data selection windows used to produce these stability maps. The normalized pressure gradient α, used as the X axis of these figures, in general magnetic geometry,[126,127] is given by equation 4.1:

$$\alpha = \frac{2\mu_0}{4\pi^2}\frac{dp}{d\psi}\frac{dV}{d\psi}\sqrt{\frac{V}{2\pi^2 R}} \tag{4.1}$$

which in DIII-D may be approximated as:

$$\alpha = \frac{2\mu_0\, q_{95}\, a\, R_{xpt}^2\sqrt{\kappa}\,(2000 p_e/L_{p_e})}{R_0\,|B_t|\,d\psi/dR} \tag{4.2}$$

where L_{p_e} is the electron pressure scale length, V is the plasma volume, and the other variables may be understood from table 4.1 and the coordinate conventions described in chapter 1. In simplified, shifted circle geometry, $\alpha = -Rq^2 d\beta/dr$ (compare to the estimate for critical β before a ballooning mode given by eqn. 3.62: $-d\beta/dr \sim 1/Rq^2$).

It can be seen from figures 4.5 and 4.6 that `ELITE` is correctly predicting stability and instability in the early ELM-free and ELMing validation cases, con-

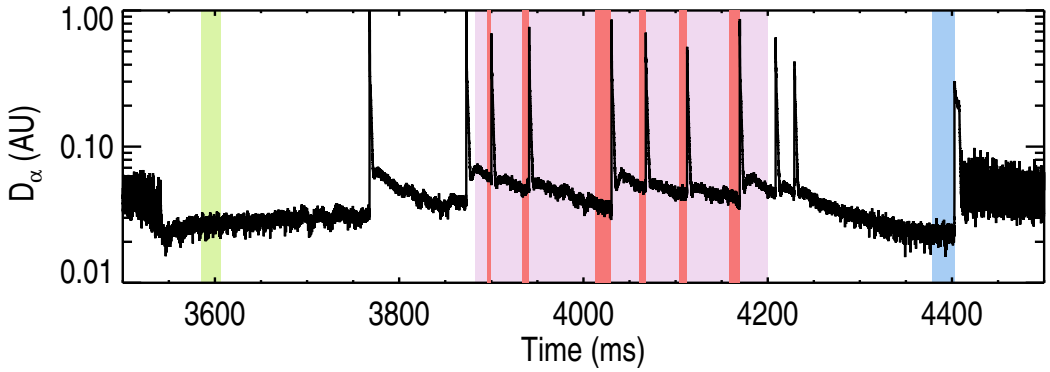

Figure 4.4: Time trace of D_α emission at the outer strike point shaded to show the data selection windows for a set of `ELITE` runs. Shaded in green at the left is an early ELM-free period after the L-H transition. Shaded in pale pink is the overall time window where consideration of ELMs was allowed. The window starts late in an attempt to capture ELMs with consistent properties such as inter-ELM period. The window ends when NBI power is reduced. In red are the windows where the 80-99% criterion was satisfied and data were used. Shaded in blue is the pre-H-L transition time window.

sistent with earlier published results.[14,23] The key results are shown in figure 4.7, which indicates that the plasma is stable before the back transition: the large D_α transient event is not an intermediate-n ideal-peeling ballooning mode and so it is not a type-I ELM.

Figure 4.8 repeats the data shown in figure 4.7 with the grid points marked by their most unstable toroidal mode number, showing that $n = 5$ is common near the peeling boundary and $n = 6-8$ is more common near the "nose", with a trend towards higher n as current decreases along the ballooning boundary at the right.

Figure 4.9 shows the boundaries from figures 4.5-4.7 overlaid. There is a minor difference between the peeling boundary between the ELMing and non-ELMing cases (the top boundary, which is nearly horizontal, and is approached as edge current increases). There is another difference between the H-L back transition and ELMing boundaries at the "nose" of the diagram in the upper right; the ballooning boundary for the ELMing case extends to higher α. However, if the shallow gradient of growth rate in this region (see spacing of dashed lines in fig. 4.8) is interpreted as uncertainty in the ballooning boundary, then the difference in

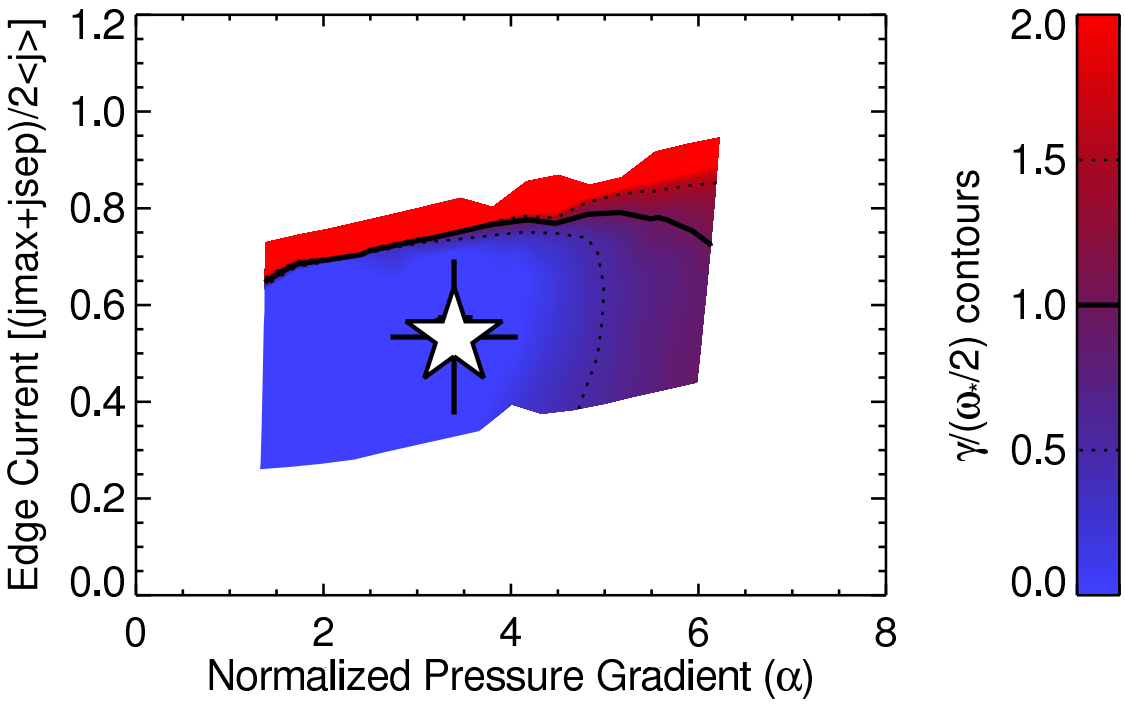

Figure 4.5: Stability diagram for the plasma in ELM-free operation shortly after the completion of the L-H transition sequence. The thick black line shows the boundary between stable and unstable territory in $p' - J$ space, defined by $\gamma = \omega_*/2$, where γ is the ideal MHD growth rate. The operating point, marked by a white star, is well within stable territory.

ELMing and pre-HL boundaries is not very significant. Thus the stability boundary in the ELMing and H-L back transition cases is essentially unchanged.

The relative position of the stability boundary between the ELMing and pre-transition cases (red X vs. blue diamond in fig. 4.9) is important because changes in the boundary are harder to detect from available measurements than are changes in pedestal height. It could be seen from automatic tanh fit series that the electron pressure gradient was not evolving dramatically during the ELM-free period following power reduction, and the gradient was lower throughout ELM-free than it was before the ELMs, having never fully recovered from the last ELM. Although the ion behavior is less obvious, it still could be reasonably expected that the ballooning limit was not being reached by evolution of the pressure gradient. However, the hypothesis that the boundary was contracting to meet the operating point seemed reasonable prior to these calculations. The change in the calculated

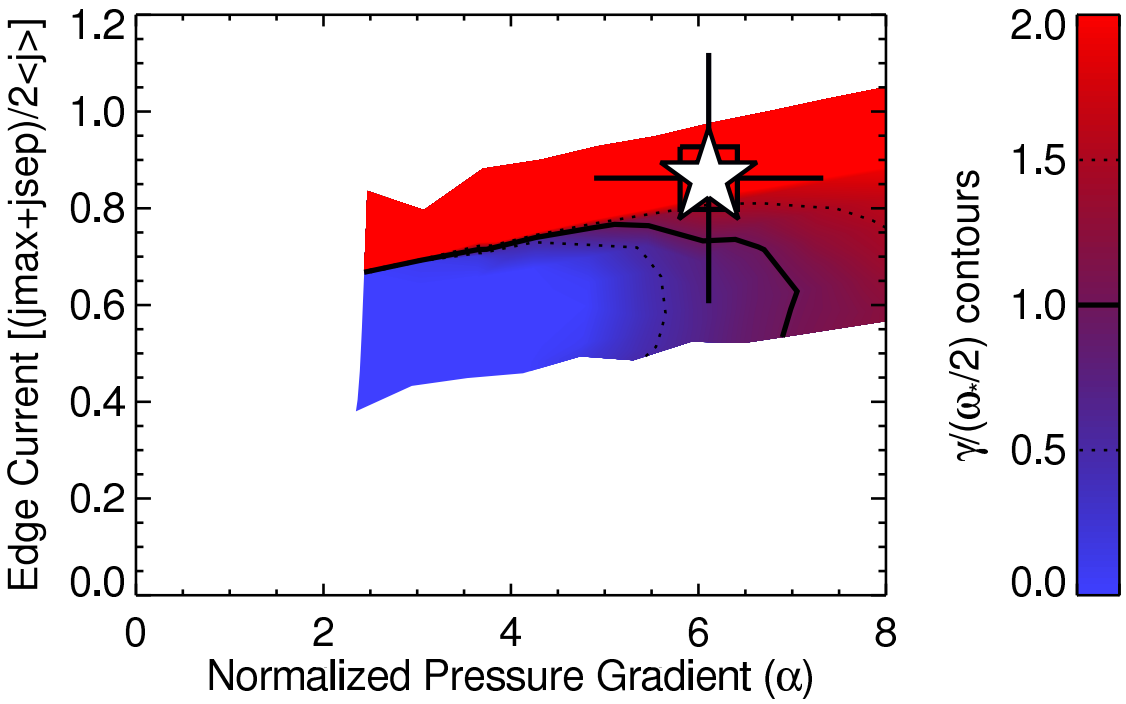

Figure 4.6: Stability diagram for 80-99% of the ELM cycle for the same H-mode as in figure 4.5. The difference between the operating point and the stability boundary is less than the estimated uncertainty, consistent with operation near the onset of peeling-ballooning instability.

ballooning limit is small compared to the difference between either boundary and the operating point, so clearly it is not the case that a ballooning dominated mode is being triggered by a contracting stability boundary at the time of the H-L back transition transient.

Note that it is also possible for a ballooning mode to be triggered by a decrease in current if the pressure gradient is maintained (see fig. 3.6) because edge current has a stabilizing effect on the ballooning mode. It can be seen from the `ELITE` results in figure 4.7 that this triggering mechanism is not responsible for the transient. A ballooning mode triggered by reduction in current might happen with stronger shaping of the plasma boundary because strong shaping tends to produce a ballooning boundary with a shallower positive slope vs. pressure gradient.

The peeling behavior is less obvious. The lowest order expectation from traces of easily diagnosed quantities would be that edge current is decreasing, as electron pressure gradient remains fairly steady while density accumulates, increas-

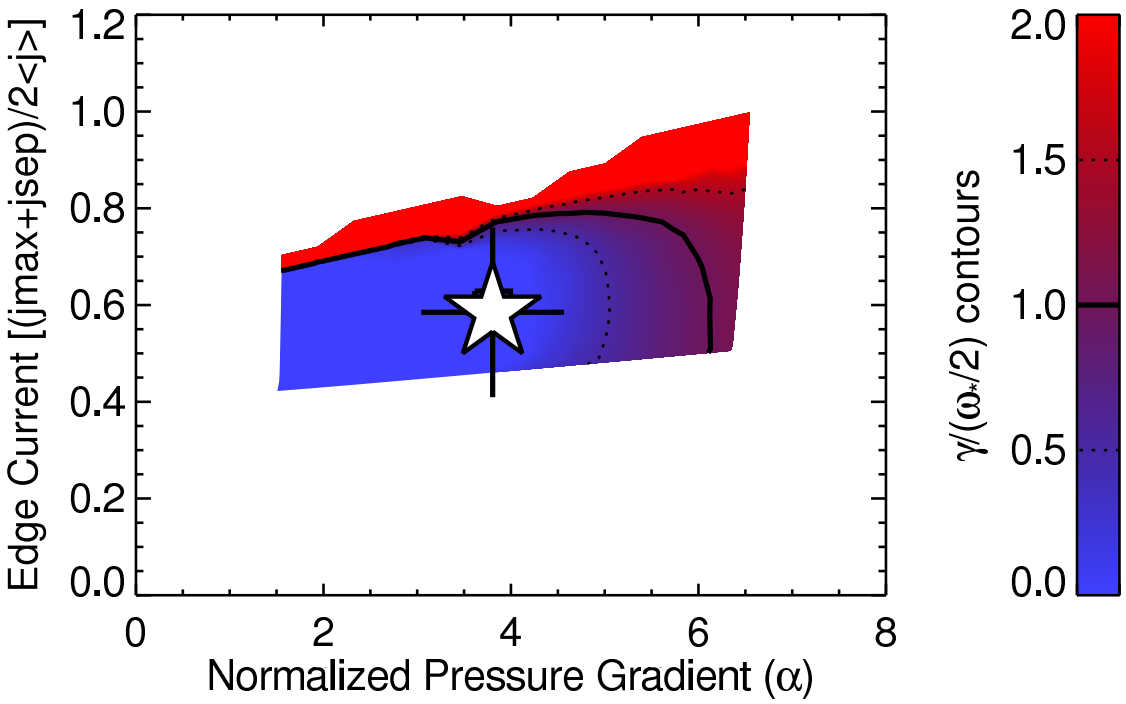

Figure 4.7: Pre-H-L back transition stability diagram. The operating point has returned to stable space. The current error bar nearly reaches the boundary, but falls just short.

ing collisionality and thus damping the bootstrap current. So, in order to trigger a peeling dominated mode, the current limit would have to decrease faster than the edge current. The comparison in figure 4.9 shows that the boundary is not decreasing to meet the operating point; if anything, the current limit is higher before the back transition than it was during the ELMs.

The ELMing and pre-back-transition stability maps were generated for several cases across a range of values of upper triangularity. The results were consistent: the ELMing operating point was always within error bars of the boundary, and the back transition operating point was always in stable territory with error bars not reaching the boundary (figure 4.7 shows the case with the smallest margin between the stability boundary and the maximum expected current, given by measured current + uncertainty). None of the transient events examined were consistent with `ELITE`'s implementation of the ideal peeling-ballooning model for $n = 5$, 10, 15, 20, or 25. All of the ELMing cases were consistent with ideal P-B

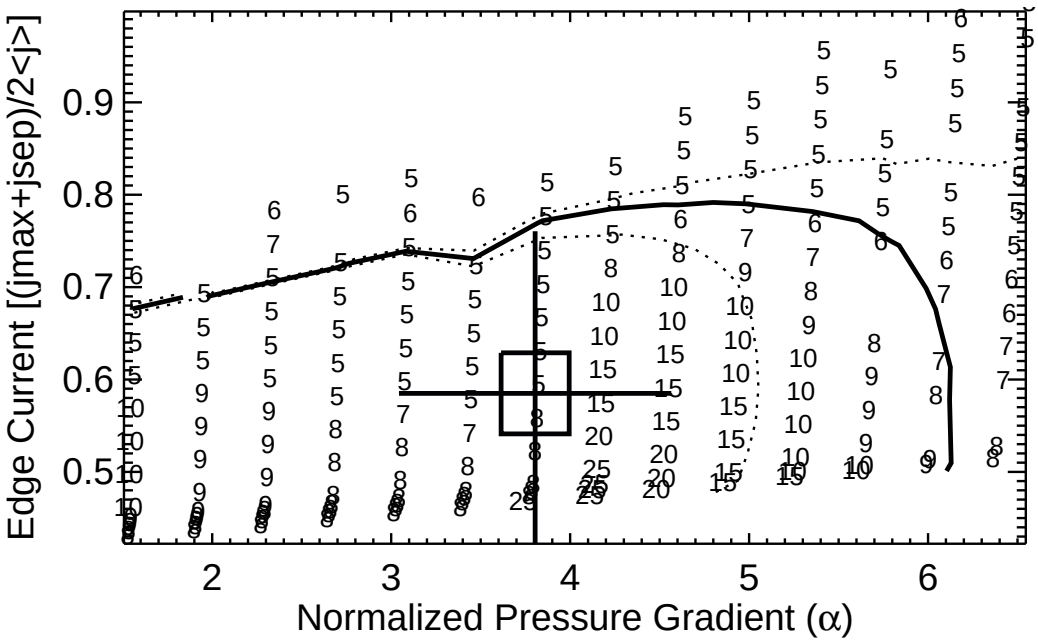

Figure 4.8: Pre-H-L back transition stability diagram, showing the distribution of test points in the $p' - J$ perturbation scan. $\gamma = \omega_*$ is marked by a thick line with thin dashed lines at 0.5 and 1.5 times this value. The numbers on the plot indicate the most unstable mode at each test point. Tested were $n = 5 - 10, 15, 20, 25$.

instability in the same set of mode numbers.

Because the highest growth rate along much of the boundary was for the $n = 5$ mode, followed by $n = 10$, modes $n = 6 - 9$ were tested for one case to ensure that the stability boundary was not exceeded during the H-L transient by one of these intermediate modes. As seen in figure 4.8, $n = 5$ is dominant along the peeling boundary at the top, while n near 7 is more common at the ballooning boundary at the right. Figure 4.10 shows the boundaries for the mode numbers analyzed in figure 4.7. Although $n = 20$ and $n = 25$ were included in the analysis presented in this figure, their stability boundaries are so far from the operating point that the equilibrium set did not capture any point with $n = 25$ instability and only a tiny region of $n = 20$ instability is seen at the very top of the plot.

The peeling boundaries for $n = 5$ and 6 are nearly indistinguishable. The $n = 7 - 10$ boundaries occur at slightly higher current, with the peeling stability boundary moving upward slightly with higher n. It appears that the rate of change

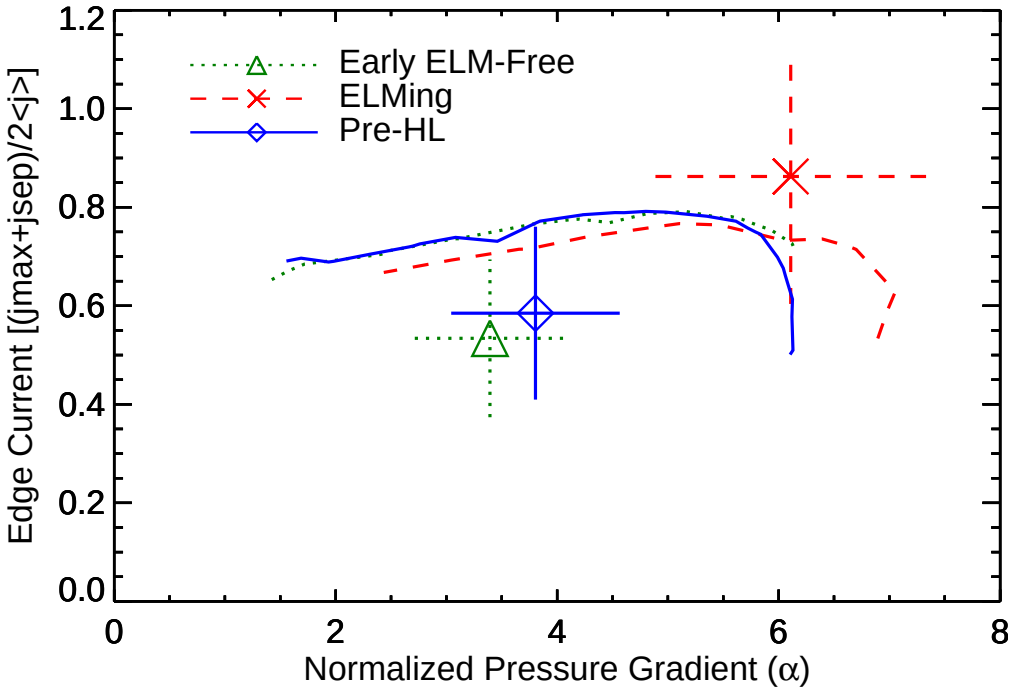

Figure 4.9: Overlay of the boundaries and operating points from figures 4.5-4.7.

of limiting current with n increases at higher n. At the "nose" of the diagram (the coupled peeling-ballooning region at the right), large expansions of the stability boundary are seen as n increases above ≈ 7, although the $n = 5 - 7$ boundaries are nearly co-located. The ballooning limit on the pressure gradient (lower right edge of stability space) contracts with increasing n from $n = 5 - 8$. The boundary expands again for $n \geq 9$, at least within the range of edge current explored in this perturbation scan. Extrapolation of the $n = 9$ and 10 boundaries would suggest that those mode numbers would be most unstable at lower current. So, the stability limit in this shot setup can be defined along much of the boundary from analyzing just the $n = 5$ mode. A good estimate across most of the boundary can be estimated from an analysis of $n = 5$ and $n = 10$ only. The area of $p' - J$ space where $n = 6 - 9$ is limiting is small, it is far from the operating point, and the local uncertainty in boundary location is relatively large. Therefore, the analysis of $n = 5$, 10, 15, 20, and 25 only, which is what was done for all cases except for the example presented here, is sufficient to capture the stability behavior within

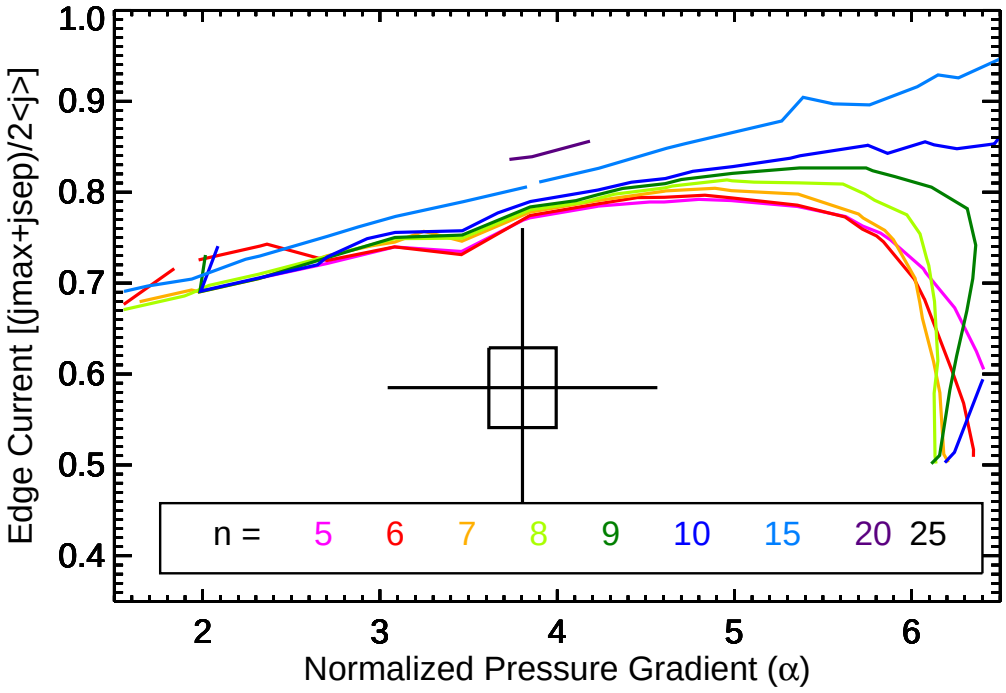

Figure 4.10: Overlay of the boundaries of several mode numbers present in the analysis shown in figure 4.7.

ELITE's range of applicability, and it can be concluded that no $n \geq 5$ ideal peeling-ballooning mode is linearly unstable before any of the back transitions which were analyzed.

4.3 Other Tests

4.3.1 Triangularity Scan

A scan in triangularity was included as a test of parametric dependencies in P-B theory: theory[14] and experiment[17] agree that the limiting pressure gradient before large type-I ELMs should depend on the plasma triangularity opposite to the dominant X-point. Thus if the H-L transients of interest here are large type-I ELMs, they both should then have the same scaling of critical p' with triangularity. The upper triangularity of these lower single null discharges was scanned from 0.11 to 0.39 (fig 4.11) to allow comparison of the pre-back-transition pressure gradient

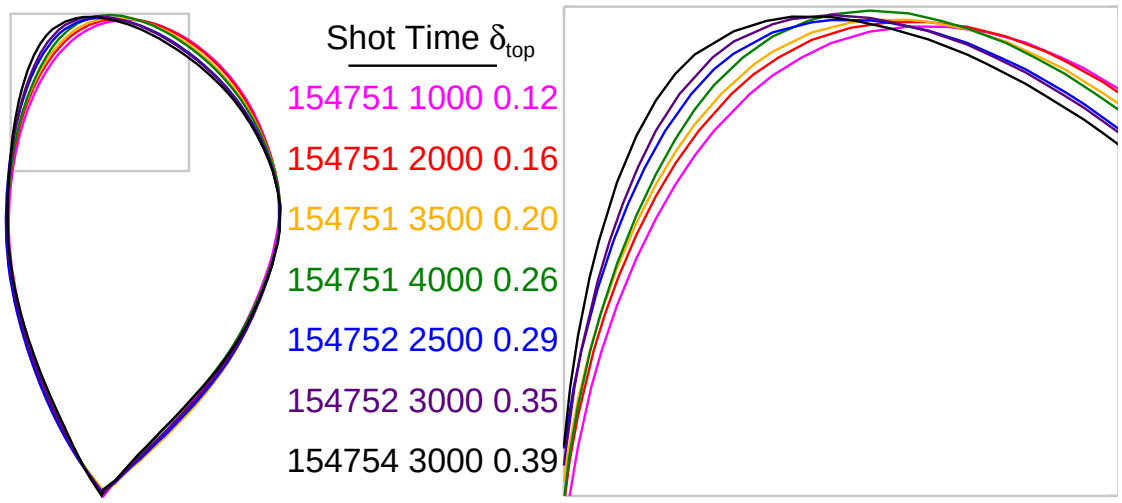

Figure 4.11: Variation of upper triangularity. The plasma boundary is shown at several representative time slices during the triangularity scan. Note the difference in the top left corner of the boundary.

to the pre-ELM pressure gradient to provide a secondary experimental check on the results from ELITE.

To maximize the number of back transitions observed in this scan, primary heating power was cycled on and off, resulting in a series of transitions in and out of H-mode, as seen in figure 4.12. In fact, not all of the transitions proceeded all of the way to L-mode, but rather, H-I-H sequences were common, where I stands for I-phase and represents the dithering part of the transition sequence. The ELM-like transients occur at the H-I transition and thus the H-I-H and H-I-L-I-H sequences provide equally valuable opportunities to evaluate MHD stability.

The first period of H-mode in the example shot is different from some of the others which follow. There was not enough time for the current profile to fully relax. That the core current profile is not fully relaxed is reflected in l_i measured at $\approx 75\%$ of the value seen in the following H-modes. Full current profile relaxation appears to be achieved in the second H-mode. These early H-modes appear to display the same transient at the start of the back transition sequence, tests with ELITE in one of these cases were consistent with tests on the higher l_i cases, and results from the triangularity scan are consistent between high and low l_i H-modes, indicating that the transient is not sensitive to details of the core current profile.

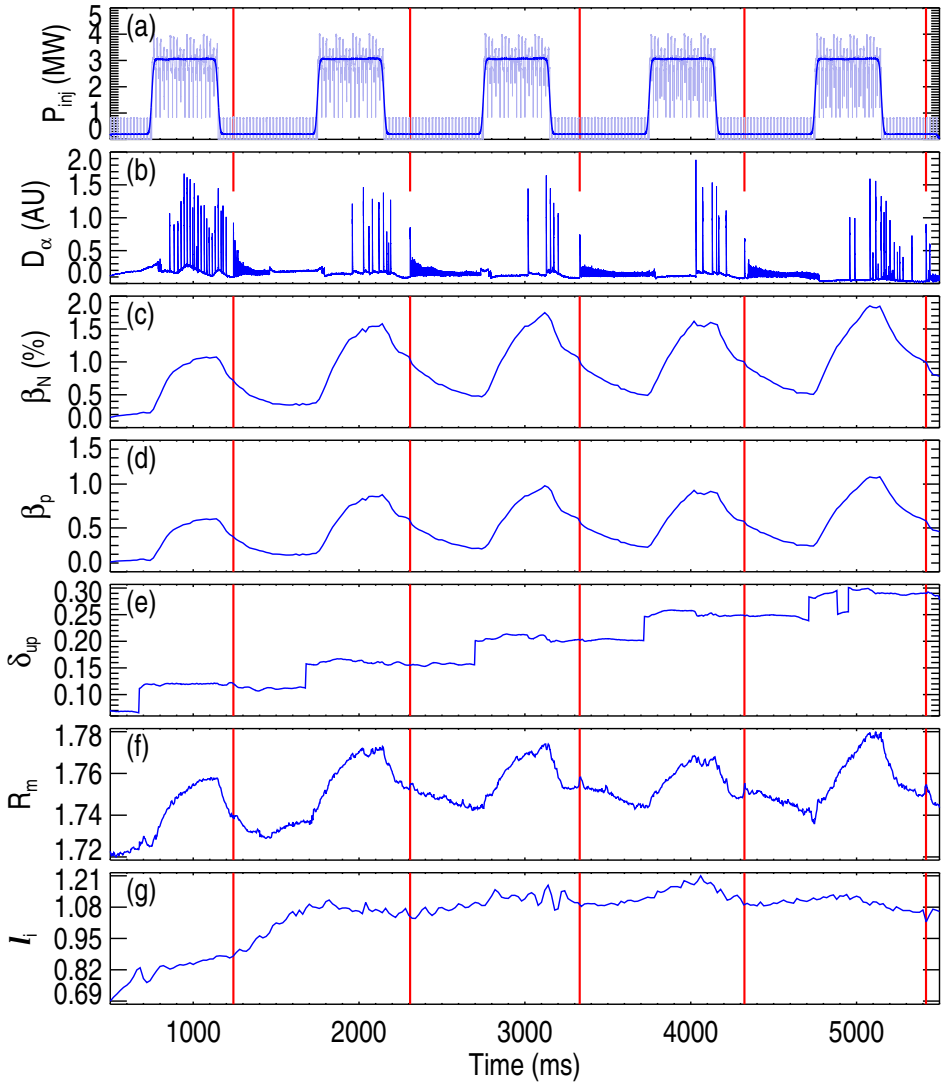

Figure 4.12: Setup of a typical shot including several transitions in and out of H-mode for the upper triangularity scan. Vertical red lines mark the start of five back transition sequences, each beginning with an ELM-like transient. (a) Neutral beam injected power, (b) divertor D_α emission, (c) β_N, (d) β_p poloidal beta, (e) δ_{up}, upper triangularity, (f) R_m, major radius of magnetic axis, (g) l_i, internal inductance, showing that the first H-mode was not fully relaxed. The traces show in figure 4.2 correspond to one of the phases of H-mode in a similarly constructed shot.

Figure 4.13 shows the results of the triangularity scan. Each back transition was preceded by a period of ELMing H-mode. The maximum pressure gradient observed between ELMs is shown in black and the maximum pressure gradient observed between the last ELM and the start of the back transition is shown in red. Here, the pressure gradient is defined by the ratio of height to width of a series of hyperbolic tangent fits to the electron pressure measurements made by Thomson scattering and adjusted to account for flux expansion such that the reported pressure gradient should be equivalent to a measurement made at the outboard midplane. The tanh fit is performed using positions of chords along the vertical laser, shown in figures 2.4 and 4.1. The details of the tanh fit to the pedestal are described in Groebner *et al.*[74] Upper triangularity is calculated from the geometry in the equilibrium reconstruction.[71,127,128]

Linear fits to each group of data show that the maximum pressure gradient before ELMs increases with triangularity with a slope of 1078 ± 91 kPa/m, whereas the maximum pressure gradient before back transitions varied as $\delta_{top} \times 431 \pm 65$ kPa/m. Thus, the pre-ELM critical electron pressure gradient needed for ELM onsent increases 2.5 ± 0.43 times faster than pre-transition gradient when upper triangularity is increased in the range $0.1 < \delta_{top} < 0.4$.

The significantly different dependence on triangularity between the pre-ELM and pre-transition cases shows that the pressure gradient before the transition is not being limited by the same mechanism (ideal P-B instability) that is operative during the type-I ELM events. This is consistent with the conclusion of the `ELITE` tests in section 4.2 that the back transition transient is not a type-I ELM. Note that very large type-I ELMs often occur near the"nose" of the stability diagram (in general[14] and in these experiments, see figure 4.6), where peeling-ballooning coupling is important. The largest type-I ELMs are typically strongly coupled peeling-ballooning modes. Smaller ELMs may be produced by crossing other parts of the P-B boundary. A ballooning dominated ELM, for example, could hypothetically relax its own drive (pressure gradient) and turn itself off fairly quickly.[14] Although the difference in ∇p vs. δ_{top} scaling does not prove that these plasmas are stable to all ideal peeling or ballooning before back transi-

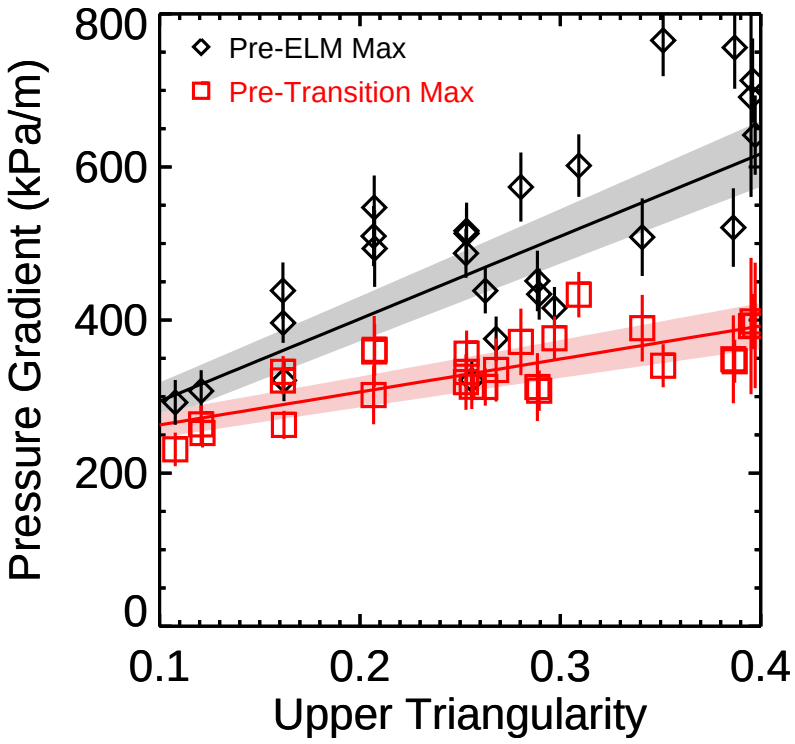

Figure 4.13: Pressure gradients vs. upper triangularity. Black diamonds: maximum gradient measured during ELMs for each H-mode. Red squares: maximum gradient observed during the ELM-free phase before each back transition. The gradient here is calculated from the height and width of a hyperbolic tangent fit to electron pressure. Width is adjusted for flux expansion and geometry to give the gradient at the outboard midplane. The lines are linear fits to the two data sets and the shaded regions represent uncertainty in the fits.

tions, this result does indicate that strongly coupled peeling-ballooning activity is not at work in the H-L transition, again consistent with the conclusion that back transition associated transients are not large type-I ELMs.

4.3.2 Radial Structure of Pedestal Collapse

The normalized temperature loss profile across ELMs $\Delta T_e/T_e = (T_{e,final} - T_{e,initial})/T_{e,initial}$ has been shown to be a good estimator for the mode structure and is consistent with calculated mode amplitude profiles.[14,46] Thus an examination of

this quantity during ELMs and during the H-L transient provides another way to test whether or not peeling-ballooning instability is operative during the H-L back transition. Figure 4.14 compares temperature losses across an example ELM (left) and a back transition transient (right). The top row shows electron temperature profiles measured by Thomson scattering before and after each event, followed by the differences in the before and after profiles on the second row. The timing of the profiles relative to the spikes is shown at the bottom of the figure. Evolution of plasma parameters is typically much faster after a crash than before: in an ELMing H-mode, most of the recovery happens early in the inter-ELM period. So it is critical that the timing between the "after" profiles and the D_α spikes be similar and cases with similar timing were found. The "before" profile is much less sensitive to timing, provided it is not within the short ($\sim 1 - 10\,\mu s$) growth time of the MHD mode that triggers the ELM crash.

Figure 4.14(e) shows the normalized temperature losses from both the ELMing (blue triangle) and back transition (purple square) example cases overlaid. It is seen that the ELM effects penetrate farther than the HL transient, which is more narrowly localized within the edge barrier region. Thus, the transient associated with the back transition has a different radial mode structure than a typical type-I ELM, which suggests that the underlying mechanisms of the two types of transient events are different, consistent with the earlier stability analysis results.

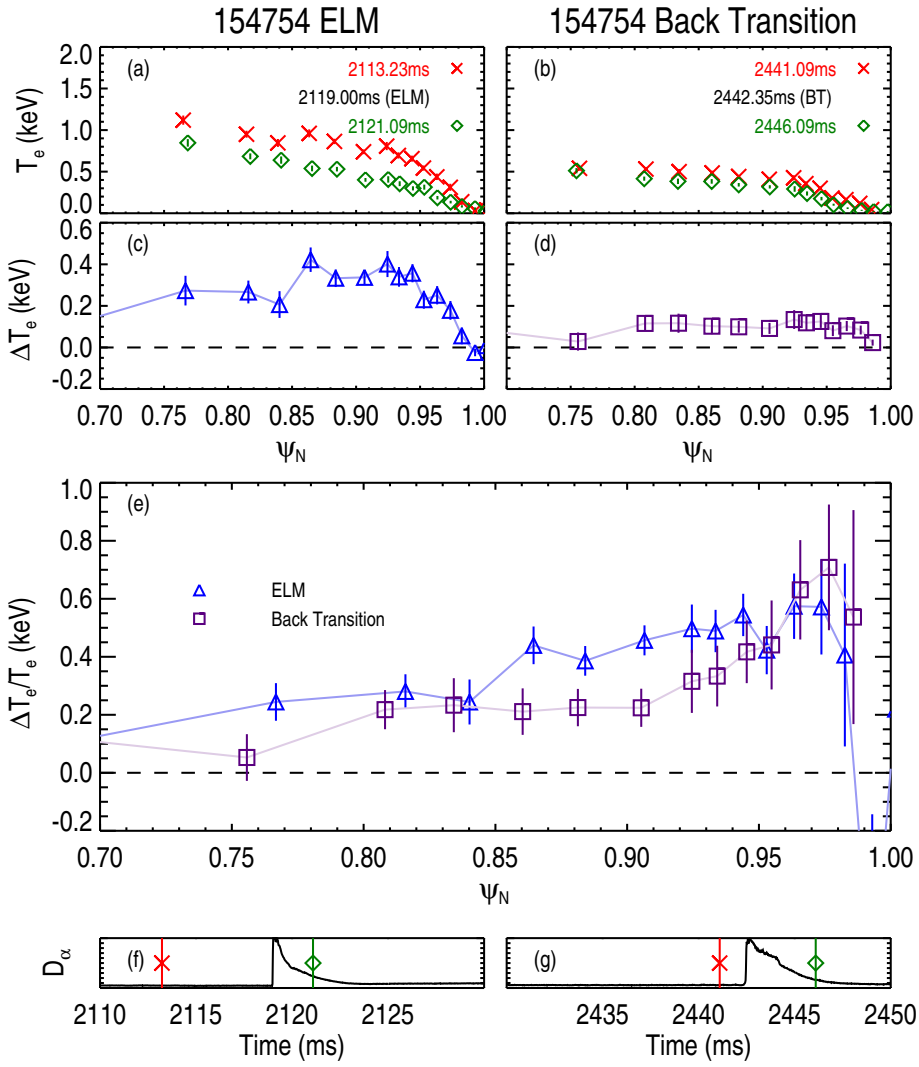

Figure 4.14: Changes in electron temperature profile from Thomson scattering before and after a typical type-I ELM (left) and a back transition transient (right) showing differences in mode structure: (a,b) temperature profiles before (red X) and after (green diamond) the event in question. (c,d) difference between profiles in first row, (e) difference in temperature normalized to local temperature before the ELM (blue triangles) and back transition transient (purple squares), (f,g) time trace of D_α light from the outer strike point. Vertical lines mark the times when profiles were measured.

4.4 Discussion

Experiments were performed to determine if the large transient seen at the start of H-L back transition could be attributed to a P-B instability. In particular, NBI heating power was reduced to the minimum level required for diagnostics (edge CER) while other parameters, such as plasma current and toroidal field, were held steady. This produced discharges where the start of the back transition sequence was separated in time from the typical type-I ELMing period of the discharge. The plasma boundary shape was chosen to produce dithering H-L transitions, as the dithering transition is a candidate for producing a "soft landing" wherein stored energy ramps down smoothly, rather than suffering a sudden drop as in a "hard" back transition. However, even with a setup which produces long, slow, dithering transitions, the H-L sequence still normally begins with the transient: hard back transitions happen even when the rest of the transition sequence is very gradual. This is a barrier to engineering a soft landing, which motivated studies in these particular conditions and this shape.

The results presented here show that the transient event associated with the start of the H-L back transition sequence is not driven by the same physics as the large type-I ELMs it resembles: it is not a linear, ideal peeling-ballooning instability and it is especially not a peeling-ballooning mode triggered near the "nose" of the stability diagram, as is typical of large type-I ELMs. This conclusion is supported by three findings.

First, results drawn from linear MHD stability analysis using `ELITE` clearly show that the triggering mechanism for the transient at the start of these H-L transition sequences is not an $n \geq 5$ ideal peeling-ballooning instability, although resistive, kinetic, and nonlinear effects are not ruled out. In particular, the stability maps in figures 4.5 through 4.10 and the history of pressure gradients in figure 4.2 show that, just prior to the start of the H-L transition sequence, the plasma operating point is well away from the ballooning boundary and is not evolving toward it.

Second, the difference in scaling of the maximum pressure gradient before ELMs and back transitions vs. boundary shape is quite different. If the back

transition transient were due to the same physics as found in type-I ELMs, then the scaling in the two cases should be similar.

A third observation supporting our conclusion is the fact that lower n modes typically penetrate deeper into the plasma,[46] yet the H-L perturbation shown in figure 4.14 shows shallower penetration depth than the type-I ELMs, indicating that the transient has a higher n than do the type-I ELMs, which are consistent with $n = 5 - 10$ P-B instability. Thus, the back transition transient is likely not due to $n < 5$ P-B instabililty. This is consistent with prelimiary `GATO`[116] results, which so far do not indicate any $n < 5$ unstable modes, but a detailed discussion of low-n stability is deferred to future work.

It is true that the error bars on the operating point on the stability maps are large in the vertical direction and nearly reach the stability boundary (fig. 4.7). However, during the ELM-free period prior to the back transition, density is increasing and temperature is decreasing at the edge (see fig. 4.2), which means that collisionality $\nu_* \sim n/T^2$ is increasing and bootstrap current should thus decrease.[12] Electron collisionality $\nu_{e*} \lesssim 1$ during ELMs and $\gtrsim 1$ during ELM-free prior to back transition. This implies that the plasma operating point is moving down in the stability plot (e.g. fig. 4.7)- away from the peeling boundary. As a result, it seems quite implausible that instability could be triggered by the operating point reaching the peeling stability boundary. Figure 4.9 shows that the stability boundary positions are fairly consistent at different times in the shot, indicating that instability is not triggered by the boundary evolving toward a stationary operating point.

Figure 4.10 shows that the limiting current value at fixed pressure decreases with n, suggesting that a lower peeling limit would be present at lower n. However, the effect of a conducting wall, which is not accounted for in `ELITE`, becomes increasingly important at low n: the perturbation to the vacuum field decreases with increasing poloidal mode number m[93,129] and given that $m > nq_a$ for an external kink, it is clear that higher n requires higher m. A perfectly conducting wall should have a significant stabilizing effect on low n external kink modes, and a resistive wall should act like a perfectly conducting wall for modes rotating with

$\omega_{rot}\tau_W \gg 1$ where τ_W is the wall penetration time.[130,131] The typical edge toroidal rotation speed was 40-50 km/s at 2.2-2.3 m for these discharges and the wall penetration time in DIII-D is a few milliseconds for low n,[130,132] so $\omega_{rot}\tau_W \gg 1$ is satisfied and the vacuum vessel acts like an ideal wall. Low n should be expected to be more stable to kinking than would be suggested by an extrapolation of the `ELITE` results to $n < 5$. In the results shown in figure 4.10, it appears that $n = 5$ and $n = 6$ have essentially identical peeling limits, with $n = 7 - 10$ only slightly higher. This trend suggests an $n = 1$ boundary very close to the $n = 5$ boundary in the no-wall limit, with an even higher limiting current after wall stabilization is accounted for. Therefore, low $n < 5$ external kinks should not be expected to be unstable in these cases.

Competing models for the bootstrap current were examined. Koh *et al.*[133] recently proposed a modification to the model by Sauter *et al.*[12] based on studies with the `XGC0`[134] code. The prediction by the modified model, KCK12, is roughly 5% less than the value from the Sauter model at the bootstrap current peak in the shots examined, with a more severe under-prediction at larger major radius (near the foot of the pedestal). However, studies with the code `NEO` indicate that Sauter is more accurate.[135] So, Sauter's model was used to calculate the bootstrap current used to constrain equilibrium reconstructions before stability analysis. However, calculations from both models were compared and the difference was less than the uncertainty in edge current. When DIII-D had a functional lithium beam diagnostic, spatially resolved measurements of the edge current profile indicated that Sauter's model was valid.[136]

When the P-B coupling is reduced by strong shaping, the stabilizing effect of edge current on ballooning modes dominates the slope of the ballooning boundary (see fig. 3.6) and it should be possible to trigger a ballooning dominated mode by decreasing edge current while holding pressure gradient constant. This is qualitatively consistent with what is observed: the pressure gradient doesn't change much during the pre-HL ELM-free period [figure 4.2(f)], but temperature [figure 4.2(e)] decreases while density [figure 4.2(d)] increases, implying decay of the bootstrap current. However, the nose of the calculated stability diagrams does

not appear to be prominent enough to support this as a mechanism for the H-L back transition initiator event, nor is the pressure gradient prior to the transition high enough (the operating point doesn't start in the nose, so it can't exit it by moving to lower current). Furthermore, the lowest values in the triangularity scan had no sign of the "overhang" in the stability boundary (formed by positive slope of the ballooning boundary as seen in figure 3.6) which would allow this phenomenon: the stabilizing effect of edge current on the ballooning mode was negated by coupling between peeling and ballooning, and the ballooning limited pressure gradient decreased with more current. The transients were still observed in these low triangularity cases. This rules out the last possible path across the boundary and eliminates ideal peeling-ballooning as an explanation for the observed transient.

Having eliminated type-I ELM like events as the trigger for the prompt H-L back transition, we are then left searching for an alternate explanation. We note that during the ELM-free period before the start of the back transition sequence, the electron pressure gradient was not found to decay significantly in these experiments. Pedestal density rises significantly while temperature falls, resulting in increasing resistivity in the pedestal. These conditions could be driving a resistive instability. High density type-III ELMs, thought to be associated with resistive instabilities, are an example of ELM-like phenomena which occur below the zero resistivity peeling-ballooning boundary;[14] thus it is possible that the D_α burst associated with the start of the back transition sequence is related to this type of resistive MHD phenomena. A more detailed analysis of this possibility requires further work.

Other explanations related to E×B shear and fluctuations in the pedestal are explored in the following chapters.

4.5 Acknowledgements

Chapter 4 contains material from Physics of Plasmas vol. 22. Eldon, David; Boivin, Réjean L.; Groebner, Richard J.; Osborne, Thomas H.; Snyder, Philip B.; Turnbull, Alan D.; Tynan, George R.; Boedo, Jose A.; Burrell, Keith H.; Kolemen,

Egemen; Schmitz, Lothar; Wilson, Howard R., American Institute of Physics, 2015. The disseration author was the primary investigator and author of this paper.

5 Evolution of E×B Shear and Coherent Fluctuations Prior to H-L Transitions in DIII-D and Contol Strategies for H-L Transitions

5.1 Introduction

As discussed in previous chapters, high confinement mode (H-mode) is an attractive regime for tokamak reactor operation as it allows higher temperature, density, and confinement time than L-mode or Ohmic operation.[9,10] However, the H-L back transition is often led by a transient spike in D_α emission and rapid relaxation of the edge pressure profile which is superficially similar to a large type-I ELM. This occurs even in shots which are specifically constructed to produce a long dithering phase between ELM-free H-mode and L-mode; that is, even slow transition sequences are observed to include sudden drops in stored energy in addition to an otherwise gradual decay of energy. This is a problem because rapid pedestal relaxations are expected to cause severe heat loads on plasma facing components in ITER.[17–20] Limited tolerance for transient energy release in future devices requires understanding and control of the H-L back transition. Although the D_α spike and pedestal reduction at the start of many H-L sequences are similar to the results of

a large type-I ELM, it was shown in chapter 4 that the triggering mechanism is different: type-I ELMs result from ideal peeling-ballooning instability,[14,49] whereas these H-L back transition transients do not.[137] This means that attempts to predict heat loads for these transients cannot take advantage of work that has been done to develop scaling relations for ELM power deposition, nor are ELM suppression techniques likely to be effective. Thus, we seek understanding of the physical nature of the transient and a means to limit the amount of energy it releases. This chapter tracks the evolution of the $E \times B$ shearing rate $\omega_{E\times B}$ in comparison to the decorrelation rate of turbulence ω_T to show that activity associated with the H-L transiton, including the transient, begins when the shear suppression mechanism is still strong.

Turbulence suppression by radially sheared $E \times B$ flows has been identified as the mechanism for sustaining the H-mode transport barrier.[10,26,28–32] So logically, a reduction in flow shear could weaken the transport barrier. Should the shearing rate $\omega_{E\times B}$ (due to radial variation of the $E \times B$ drift) decay to the point that turbulent transport began to increase, then the gradients in the pedestal would be reduced. Reduction in the diamagnetic contribution to the radial electric field from the pedestal pressure gradient would further weaken the shear suppression mechanism, allowing turbulent transport to increase even more. If this process fed back on itself quickly enough, the edge pressure could be very quickly reduced to L-mode levels, and the resulting outflow of material would rapidly refill the SOL region of the plasma. The plasma in the SOL would then quickly flow along the field and cause a flash of D_α light at the strike point, consistent with the observed transient at the beginning of the H-L transition sequence, which is shown, along with the experimental setup, in section 5.2. The critical test is whether the shearing rate $\omega_{E\times B}$ decays before the transition sequence begins and becomes comparable to the turbulence decorrelation rate ω_T when the transient occurs. It will be shown in section 5.3 that decay of $\omega_{E\times B}$ is quite small and that the transient occurs when $\omega_{E\times B} > \omega_T$, so the transient is not triggered by a rapid turbulence recovery resulting from the collapse of the shear suppression mechanism.

Having ruled out P-B instability previously in chapter 4 and now $E \times B$

shear suppression failure in section 5.3 as triggers for the transient at the beginning of the H-L transition sequence, we search for other clues which might help explain the hard H-L transition. Of particular interest is the MPM, a coherent density fluctuation which exhibits modulations in amplitude and propagation velocity that are synchronous with the transient and other events in the H-L sequence. The MPM is characterized in detail in section 5.4. In section 5.5, we document conditions where back transitions occur without the large initial transient and compare them to similar cases which do experience the transient. We find that toroidal rotation of the edge of the plasma, which is varied through use of neutral beams injecting torque in opposite directions, is most clearly correlated with the occurrence of a "hard" vs. "soft" H-L back transition (with and without a sudden pedestal relaxation at the start of the H-L sequence), with hard transitions occurring when rotation is faster in the co-current direction.

5.2 Experiment

The DIII-D[1,7] shots examined here share the setup discussed in chapter 4. They were run with toroidal field $B_t = -2.15$ T, plasma current $I_p = 1.0$ MA, safety factor at the $95\%\psi_N$ flux surface $q_{95} = 4.6 - 4.9$, elongation $\kappa = 1.75$, triangularity $\delta = 0.3$, and more parameters are listed in table 4.1. The separatrix shape (Fig. 1.7) of these discharges was chosen for its compatibility with the production of long dithering L-H and H-L transition sequences; a long sequence is a more likely candidate for the soft landing being sought and is more easily diagnosed. Although the shots examined here are from the same series as the ones used in chapter 4, this subset ignores the triangularity scan and instead includes cases where a low powered neutral beam was used to provide BES data during the H-mode termination phase, and cases where torque applied by the neutral beams is varied by using combinations of co and counter (to the direction of plasma current) injecting beams. The beam program is shown in figure 5.1 and a plan view of DIII-D's beams is shown in figure 2.25.

The evolution of a typical H-mode is shown in Fig. 5.2 (a reproduction

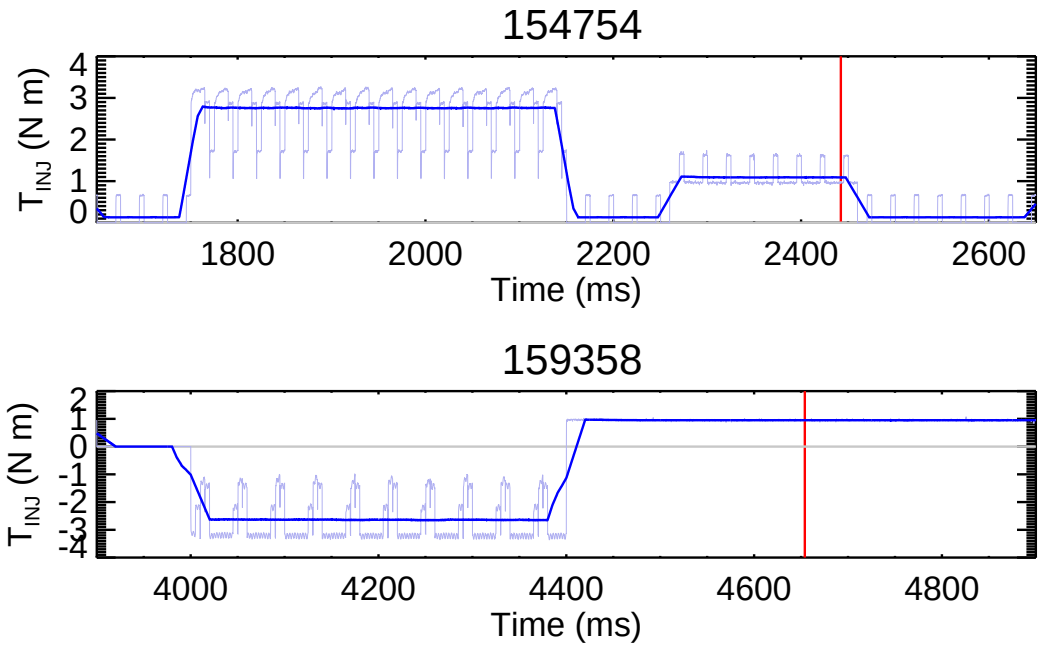

Figure 5.1: Neutral beam injected torque vs. time for producing two classes of back transitions. Dark blue: smoothed. Faint blue: unsmoothed (most beams are modulated for diagnostic purposes). Red line marks propagation velocity drop (start of H-L transition activity) discussed in subsection 5.4.2. Top: primary heating is from co-injected beams. After primary heating, a low power beam turns on at 2260 ms to enable BES. Bottom: primary heating is from counter beam. The BES beam turns on when primary heating power is cut at 4400 ms. Locations of co and counter beams can be seen in figure 2.25.

of Fig. 4.2). A forward L-H transition completes at 3540 ms, and the plasma is in ELM-free H-mode until the type-I ELMs begin at 3770 ms. The primary heating phase lasts until 4200 ms, after which neutral beam injection (NBI) is only used for diagnostic purposes. The last type-I ELM occurs at 4230 ms. During the following ELM-free period, pedestal density accumulates while the pedestal electron temperature decays, resulting in a pedestal pressure that remains fairly steady. At 4402 ms, a rapid ($\sim$ 1 ms) event reduces the pedestal density by $\approx$ 50%, relaxes the pedestal pressure gradient, and releases $\sim$ 10% of the total plasma stored energy, which is typically $300 - 400$ kJ total before the reduction in these cases. As shown in chapter 4, this event is distinct from a type-I ELM as the plasma is stable to ideal P-B modes before it is triggered. The rest of the

dithering transition sequence follows. In some shots, a de-rated neutral beam (reduced accelerating voltage and perveance to produce lower power) was run continuously during the H-mode termination phase to allow measurements with Beam Emission Spectroscopy (BES),[85] while modulated beams for CER[25] were used alone in others (as seen in Fig. 5.2). The total beam power was assumed to be below the H-L transition threshold in both beam setups and both cases experienced similar transition sequences, as seen by comparing figures 5.2 and 5.3.

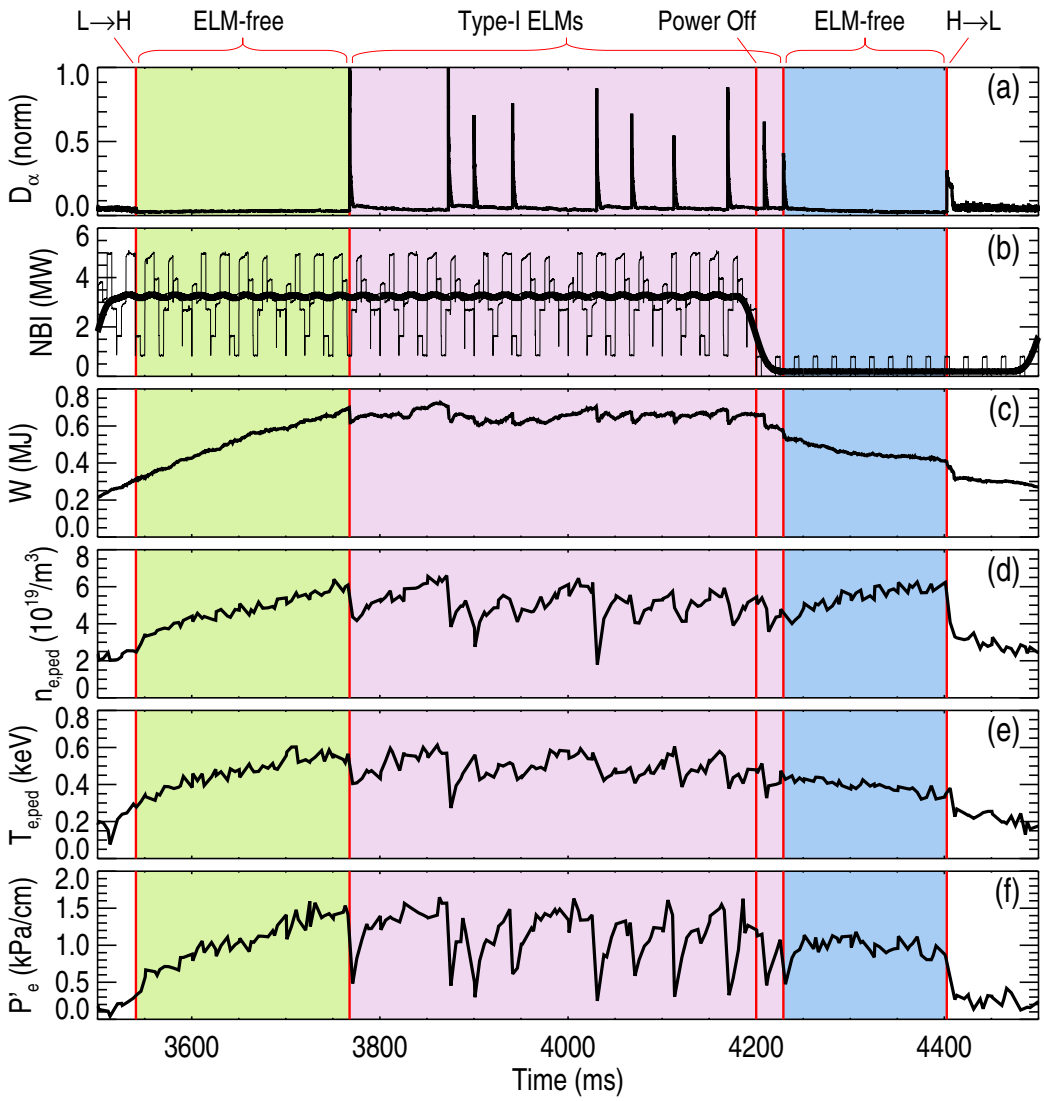

Figure 5.2: History of H-mode from the conclusion of the L-H transition sequence until the beginning of the H-L sequence. (a) D_α emission from the outer strike point (b) neutral beam injected power; thick line shows average power (c) plasma stored energy (d) electron density pedestal height (e) electron temperature pedestal height (f) pedestal electron pressure gradient. Electron quantities determined from tanh fits[74] to Thomson scattering data.[51] Shot 154749.

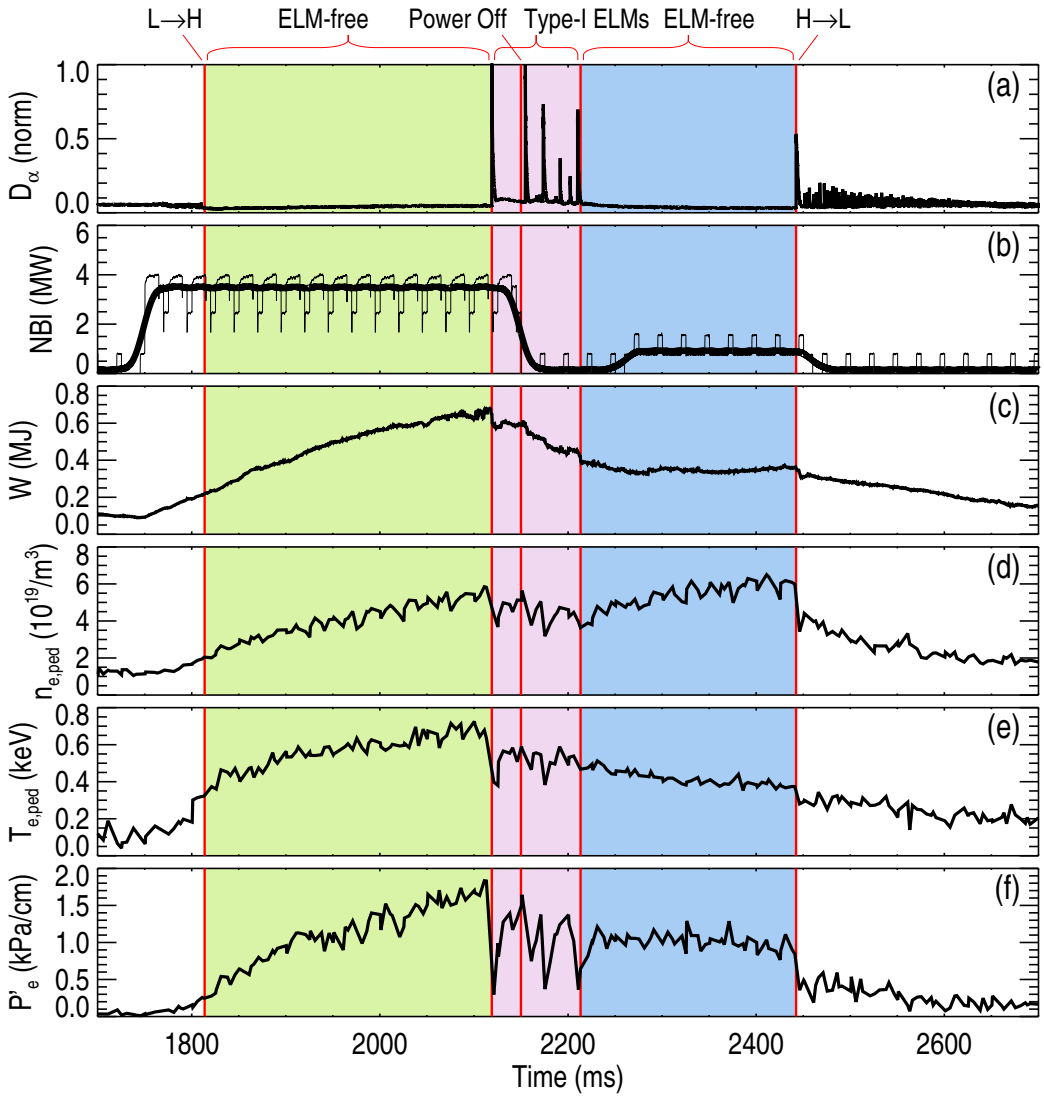

Figure 5.3: History of H-mode for a shot with low-power steady NBI providing BES measurements. The essential similarity of the H-mode termination phases and H-L transition sequences between the CER only and BES setups can be seen by comparing (a), (d), and (f) with the same plots in Fig. 5.2: an ELM-free period ends with a large D_α spike, density accumulates during the ELM-free period, and the pedestal pressure gradient remains fairly constant. Extra power from the beam used for BES tends to extend the time between the last ELM and the H-L transition. Therefore, the duration of type-I ELMs was reduced to maintain the same number of H-modes per shot. Shot 154754.

5.3 Evolution of E×B Shear Prior to H-L Sequence

In order to test the hypothesis that the hard back transition is initated by a collapse in the $E \times B$ shearing rate associated with the H-mode pedestal, we used the CER diagnostic to study the evolution of $\omega_{E\times B}$ prior to the start of H-L sequence. The radial electric field was calculated from force balance using Eq. 5.1, which is valid if pressure p, density n, and flow velocity v are measured for the same species (fully stripped carbon in this case; $Z = +6$).[26]

$$E_r = \frac{\partial p/\partial r}{Zen} - v_\theta B_\phi + v_\phi B_\theta \tag{5.1}$$

The $E \times B$ drift is primarily in the poloidal direction and may be approximated as

$$v_{E\times B} \approx v_{E\times B,\theta} \approx \frac{E_r}{B_\phi} \tag{5.2}$$

The shearing rate for flute-like (correlation length along the field $\Delta\eta$ is long compared to the circumference, in contrast to ballooning-like, where $\Delta\eta$ is on the order of the circumference) turbulence as a result of shear in the $v_{E\times B}$ drift[26] is given by Eq. 5.3:

$$\omega_{E\times B} = \frac{\Delta r_0}{\Delta\phi}\frac{\partial}{\partial r}\left(\frac{q\, v_{E\times B}}{r}\right) \tag{5.3}$$

where Δr_0 or L_r is the correlation length of turbulence in the radial direction and $\Delta\phi$ is the correlation angle in the toroidal direction. $v_{E\times B,\theta}/r$ is the poloidal rotation frequency due to $v_{E\times B}$. The magnetic field pitch $q = rB_\phi/RB_\theta$ accounts for magnetic shear.[29] Because the fluctuations have been assumed to be flute like with long correlation length parallel to the field, only $E \times B$ flow shear is important and shearing of parallel flows has been neglected.[30] Given $\Delta\psi_0 = RB_\theta\Delta r_0$,[26] equation 5.3 can be written:

$$\omega_{E\times B} = \frac{\Delta\psi_0}{\Delta\phi}\frac{\partial}{\partial\psi}\left(\frac{E_r}{RB_\theta}\right) \tag{5.4}$$

The perpendicular correlation length within a flux surface is $L_\perp = RB_\theta\Delta\phi/B$ and the assumption $L_\perp = L_r$ has been shown to be reasonable by numerical simualtions

and experiment,[26] so $\Delta\psi_0/\Delta\phi = (RB_\theta)^2/B$ and

$$\omega_{E\times B} = \frac{(RB_\theta)^2}{B}\frac{\partial}{\partial\psi}\left(\frac{E_r}{RB_\theta}\right) \tag{5.5}$$

Equation 5.5 is the Hahm-Burrell form for the $E\times B$ shearing rate in toroidal geometry with the assumption that turbulence is flute-like. This is the quantity which should be compared to the turbulence decorrelation rate ω_T.[30] Note that the derivative is with respect to ψ and not ψ_N. Also, $1/\tau_c$ is interpreted as an angular frequency because of its appearance in an exponential: if ω_T were imaginary (as in $e^{i|\omega_T|t}$), periodic behavior would result and ω_T would be the angular frequency. $\omega_{E\times B}$ is clearly an angular frequency as well, as seen in the v/r factor in equation 5.3.

The analysis of E_r is performed as follows. Closely spaced pairs of vertical and tangential chords are used to determine v_θ and v_ϕ. Because of the significant height of the neutral beam ($\sim$ 20 cm), density measurements from the vertical chords are averaged over a larger extent in ψ space than are measurements from tangential chords, so density is determined using tangential chords alone. This effect is less of a problem for temperature measurements, as ion temperature tends to vary more slowly than density, but temperatures are still taken from the tangential chords only. v_ϕ is strongly dominated by measurements from the tangential chords, but the vertical chords pick up components of both v_θ and v_ϕ, so both tangential and vertical chords are required to determine v_θ. Further corrections account for atomic physics effects, such as gyro-motion of ions during the finite lifetime of the excited states and dependence of charge exchange cross section on relative velocity between neutral and ion, which affect the measured velocities with respect to the true velocities.[84,138] Hyperbolic tangent fits to density and pressure are used to allow better determination of the diamagnetic term in E_r, which is sensitive to gradients. The resulting E_r value is used in the subsequent analysis.

The $E \times B$ rotation frequency $\omega_E = E_r/RB_\theta$ is fit to the form developed

by Burrell[139] and given by Eq. 5.6.

$$\begin{aligned}\omega_E = B &+ A_{in}\frac{(1+\alpha_{in}x_{in})e^{x_{in}} - e^{-x_{in}}}{e^{x_{in}} - e^{-x_{in}}} \\ &- A_{out}\frac{e^{x_{out}} - (1+\alpha_{out}x_{out})e^{-x_{out}}}{e^{x_{out}} - e^{-x_{out}}} \\ x_{in} = (\psi_{in} - \psi_N)/w_{in}, &\quad x_{out} = (\psi_{out} - \psi_N)/w_{out}\end{aligned} \tag{5.6}$$

Example profiles of E_r, ω_E, and $\omega_{E\times B}$ are shown in figure 5.4. The fit to equation 5.6 is plotted along with a cubic spline fit for comparison. The two curves agree well and measure similar peak shearing rates. The fit to equation 5.6 is used in calculations. Beam blips in this experiment were 10 ms long and CER was set to average signal over 2.5 ms windows, producing four time-slices per blip. Data were thus supplied to the fitter in groups of four slices. The sign of $\omega_{E\times B}$ is not important, so figure 5.4 displays its magnitude. Notice that there are two peaks on the inner and outer sides of the E_r well.

For comparison, the turbulence decorrelation rate ω_T is computed using data from vertically separated BES chords as follows (the procedure is a standard part of BES analysis). The time delayed cross correlation $C(t_{delay})$ is calculated for a pair of chords, producing the red curve labeled "Correlation" shown in Fig. 5.5(a). The Hilbert envelope $\sqrt{y^2 + H(y)^2}$, where $H(y)$ is the Hilbert transform, of $C(t_{delay})$ is calculated (black curve above the red one) and the coordinates of the peak are recorded. The coordinates from the peak correlations of several chord pairs with different vertical separations are fit to $C(t_{delay}) = C_{max}\exp(-|t_{delay}\omega_T|)$, as seen in Fig. 5.5(b). This procedure measures the plasma frame decorrelation rate. Using the autocorrelation time [as could be calculated from the width of the envelope in Fig. 5.5(a)] gives the rate in the lab frame which is unsuitable because it includes spatial decorrelation as eddies are advected past the BES chords by $E \times B$ drifts.[27] The BES data are bandpass filtered to $150 \leq f \leq 450$ kHz before calculating ω_T ($f > 450$ kHz is noise). This is necessary to avoid contributions from the MPM.

If the entire frequency range were included, the calculated decorrelation rate would be so low (about two orders of magnitude lower, as an upper bound) that $\omega_{E\times B}$ would be much larger than ω_T at all times. However, the theory behind

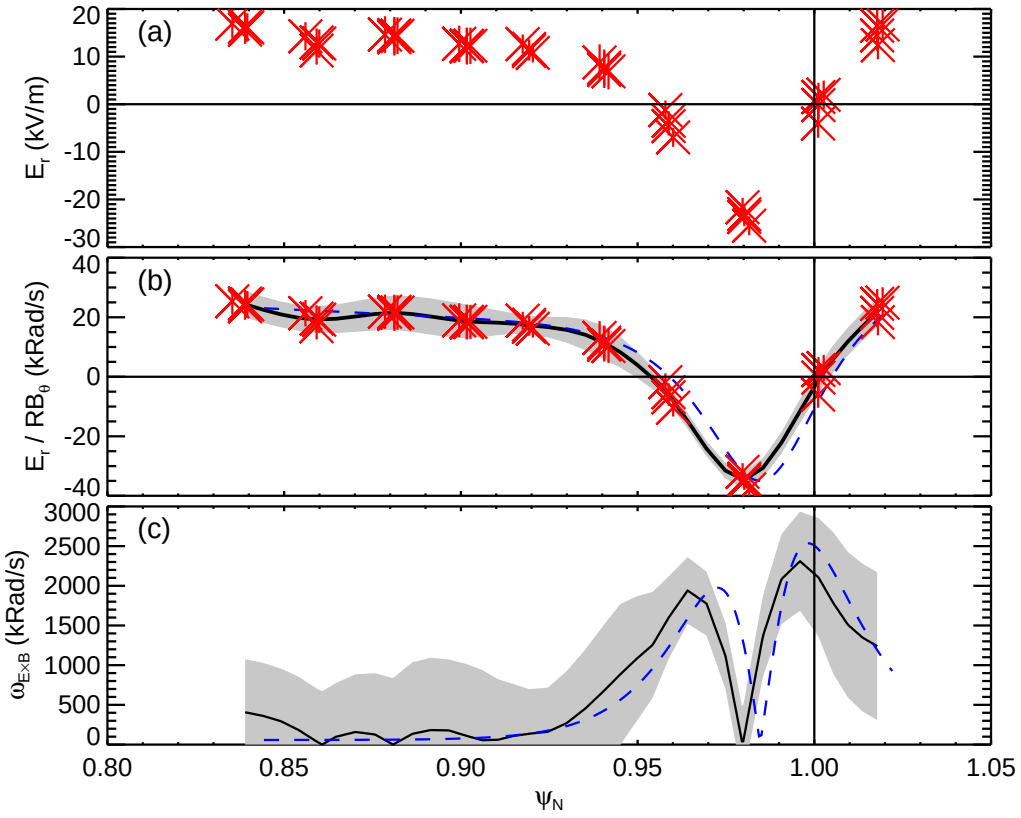

Figure 5.4: E_r and shear profiles. (a) Example profile of E_r calculated from equation 5.1 and using the four 2.5 ms averaging windows from one 10 ms beam blip. (b) $E \times B$ rotation frequency times magnetic pitch $q\, v_{E\times B}/r = E_r/RB_\theta$. B_θ is from a JT EFIT. The black line is a cubic spline interpolation between the red points, and the shaded gray area is the standard deviation of the black curve. The dashed blue line is a fit to equation 5.6. (c) magnitude of ω_{SE} calculated by equation 5.5,[26] using the derivative of the black and blue lines above.

this calculation of $\omega_{E\times B}$ assumes that the fluctuations are broadband incoherent fluctuations, which is reasonable for the modes which are commonly thought to drive turbulence in tokamaks. It is not appropriate to include the coherent and as yet unidentified MPM in this analysis, especially since the MPM appears to be ballooning-like instead of flute-like (see localization in section 5.4.4). This is supported by the observation that $\omega_{E\times B} \gg \omega_T$ when the frequency band with the MPM is included, yet the MPM exists at high amplitude. So, $E \times B$ shear would seem to be ineffective at suppressing the MPM: the shear suppression model does not apply to the MPM and it must be filtered out.

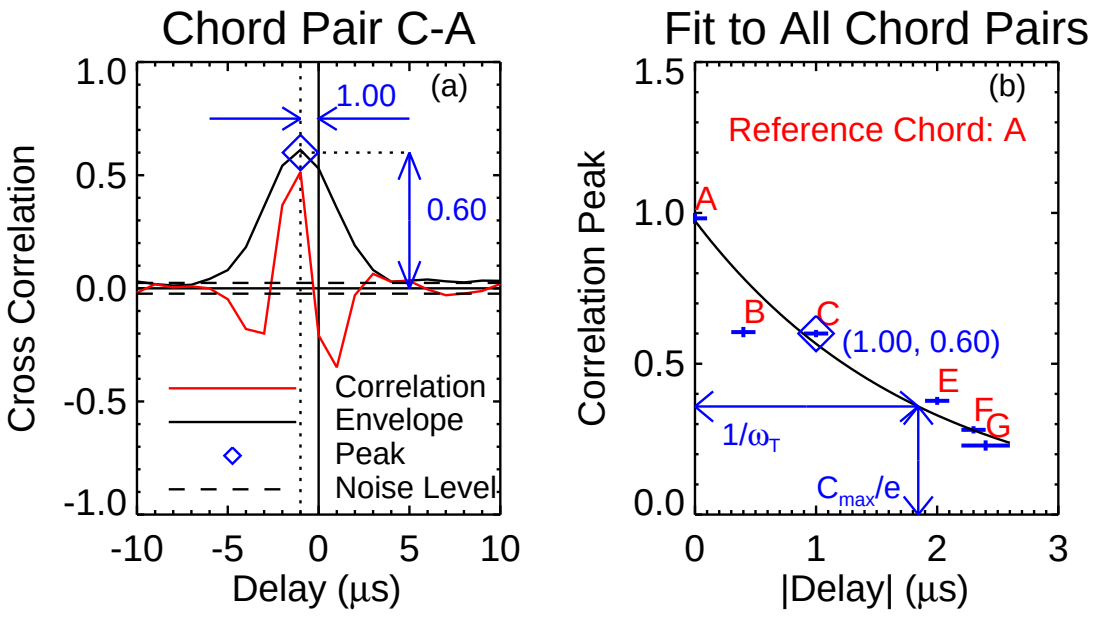

Figure 5.5: Method of calculating decorrelation rate ω_T from BES data. (a) time delayed cross correlation function (red) between two vertically separated chord pairs with Hilbert envelope overlaid in black. The envelope peak is marked with a blue diamond and the peak envelope value and delay at this peak are measured by blue with arrows. (b) the peak from the left plot is plotted here along with similar measurements from other chord pairs; blue symbols with red labels (see Fig. 2.27 for chord positions). The size of the blue symbols shows uncertainty in the measurements in both dimensions. The point calculated from the left plot is marked with a diamond and coordinate label. The data are fit to $C(t_{delay}) = C_{max}\exp(-|t_{delay}\,\omega_T|)$ (black curve) and ω_T is recorded.

The results are shown in Figs. 5.6 and 5.7 for example back transitions with and without the initial transient, respectively (means of avoiding the transient are documented in section 5.5). Additionally, Fig. 5.8 shows ∇p_e and E_r evolution across the hard back transition in Fig. 5.6. Reduction in turbulent transport by $E\times B$ flow shear should be expected when $\omega_{E\times B} \gg \omega_T$ (H-mode), with $\omega_{E\times B} \approx \omega_T$ resulting in a weaker suppression effect (not H-mode).[30]

These results show that $\omega_{E\times B}$ remains well above ω_T until after the back transition sequence begins in both cases. Thus the initiation of the back transition sequence does not appear to be associated with a collapse in $\omega_{E\times B}$ during the period before the start of the sequence.

Interestingly, the decorrelation rate in both cases is tending toward about 500 kRad/s before the back transition. $\omega_{E\times B}$ decays to become comparable to this level at around the time the character of D_α bursts changes from type-III ELMs to LCOs and then evolves no further. These data are consistent with the expectation that the LCO should take over turbulence regulation as the slowly evolving shear layer (generated by the equilibrium pressure gradient) collapses, which is expected when $\omega_{E\times B} \approx \omega_T$. However, the extrapolation of decorrelation rates into the transition sequence (as required because noise associated with D_α bursts pollutes the spectrum here) is not ideal.

One of the vertical CER chords in the outer half of the E_r well was unavailable during this experiment, so one point is missing in the poloidal flow v_θ profile. However, toroidal flow v_ϕ, temperature T, and density are still available, and v_θ is very small and is not experiencing strong radial variation. Thus the $v_\theta B_\phi$ term in Eq. 5.1 is about 10% of the $v_\phi B_\theta$ term across most of the profile and roughly 10% as large as the peak in the diamagnetic term (p'/Zen). Furthermore, radial variation in v_θ is comparable to the uncertainty in the measurements. Rather than discard important and valid information about the other profiles, the missing point in v_θ is interpolated from its nearest neighbors and assigned double uncertainty (compared to interpolating from its neighbors' uncertainty). However, the term in question is so small that the extra uncertainty is difficult to discern when propagated into the final product.

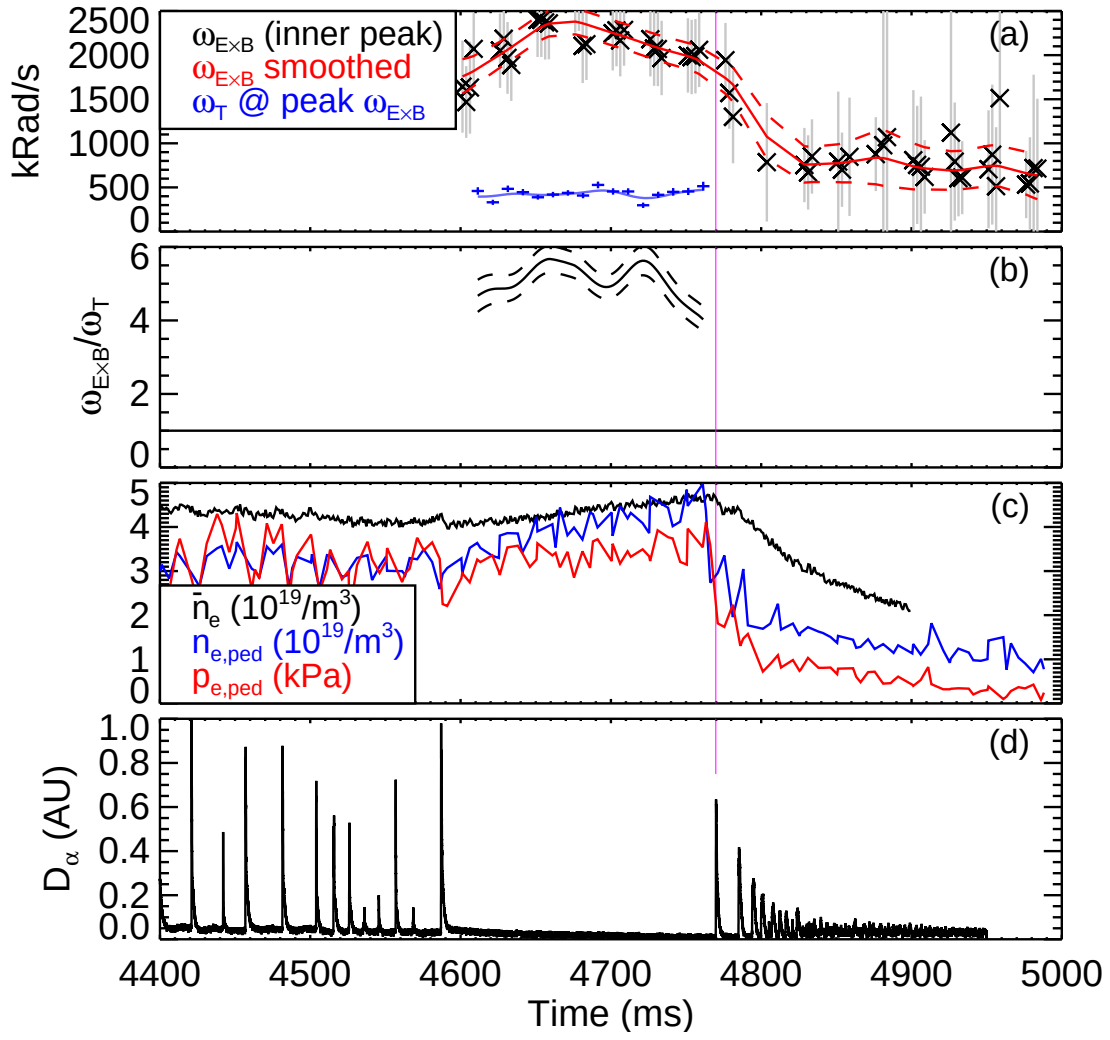

Figure 5.6: $\omega_{E\times B}$ and ω_T comparison for the termination phase of an H-mode with a hard H-L transition. (a) value of $\omega_{E\times B}$ at the peak at the inside of the E_r well (black X w/ gray error bar) and smoothed curve to peak $\omega_{E\times B}$ values (red) with propagated uncertainties (dashes); ω_T (blue) calculated during the ELM-free period prior to the beginning of the transition sequence. (b) $\omega_{E\times B}/\omega_T$. (c) line average density (black), pedestal e^- density (blue), and pedestal e^- pressure (red). (d) D_α emission at the outer strike point. NBI was reduced to diagnostic levels at 4505 ms. Most quantities from shot 159355, with beams setup for best CER data quality. Decorrelation rate calculated from matched shot 154754, which used beams for BES. The time sequences are aligned at the transient.

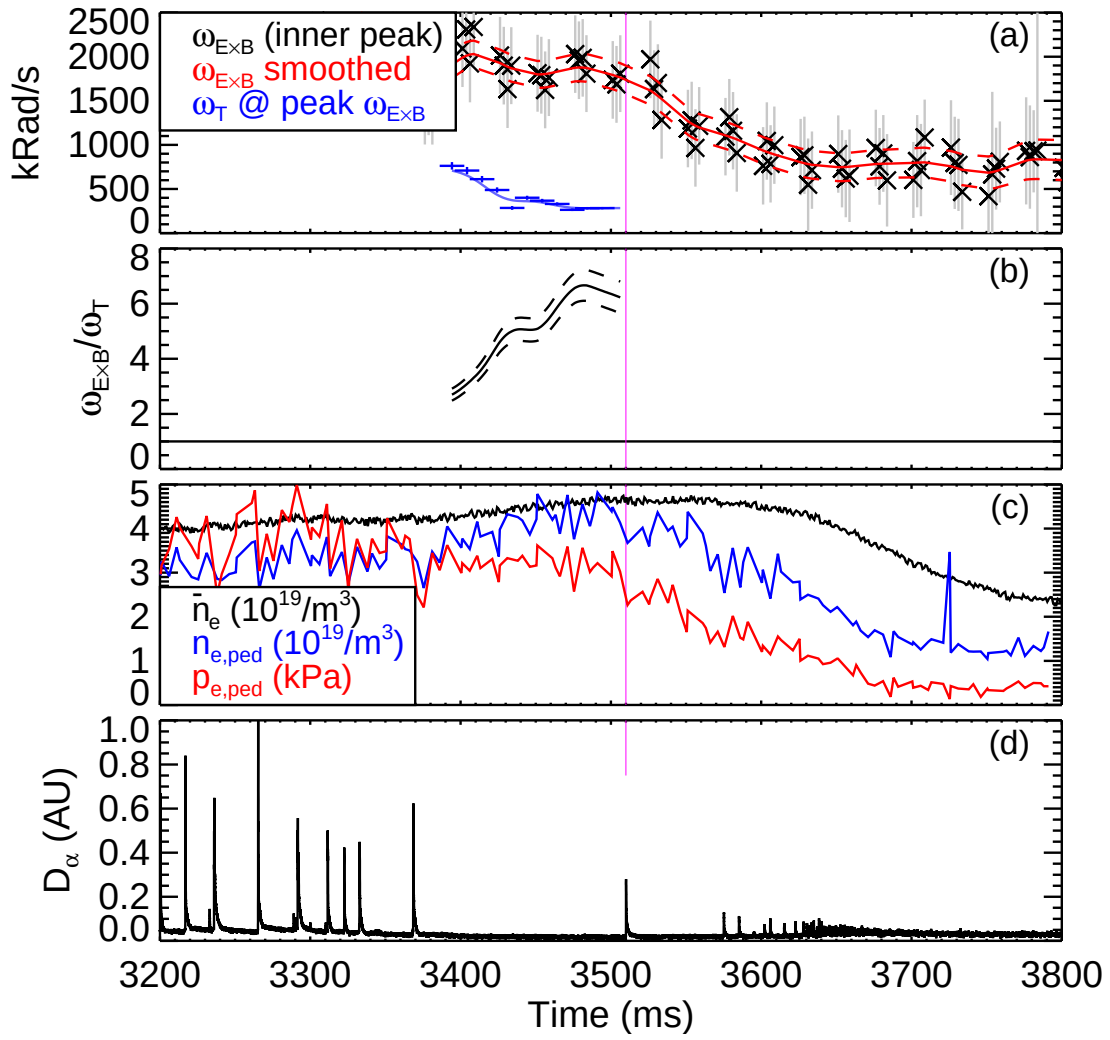

Figure 5.7: $\omega_{E\times B}$ and ω_T comparison for the termination phase of an H-mode with a soft H-L transition. Compare with Fig. 5.6. NBI was reduced to diagnostic levels at 3300 ms. Most quantities from shot 159354. Decorrelation rate calculated from matched shot 159358.

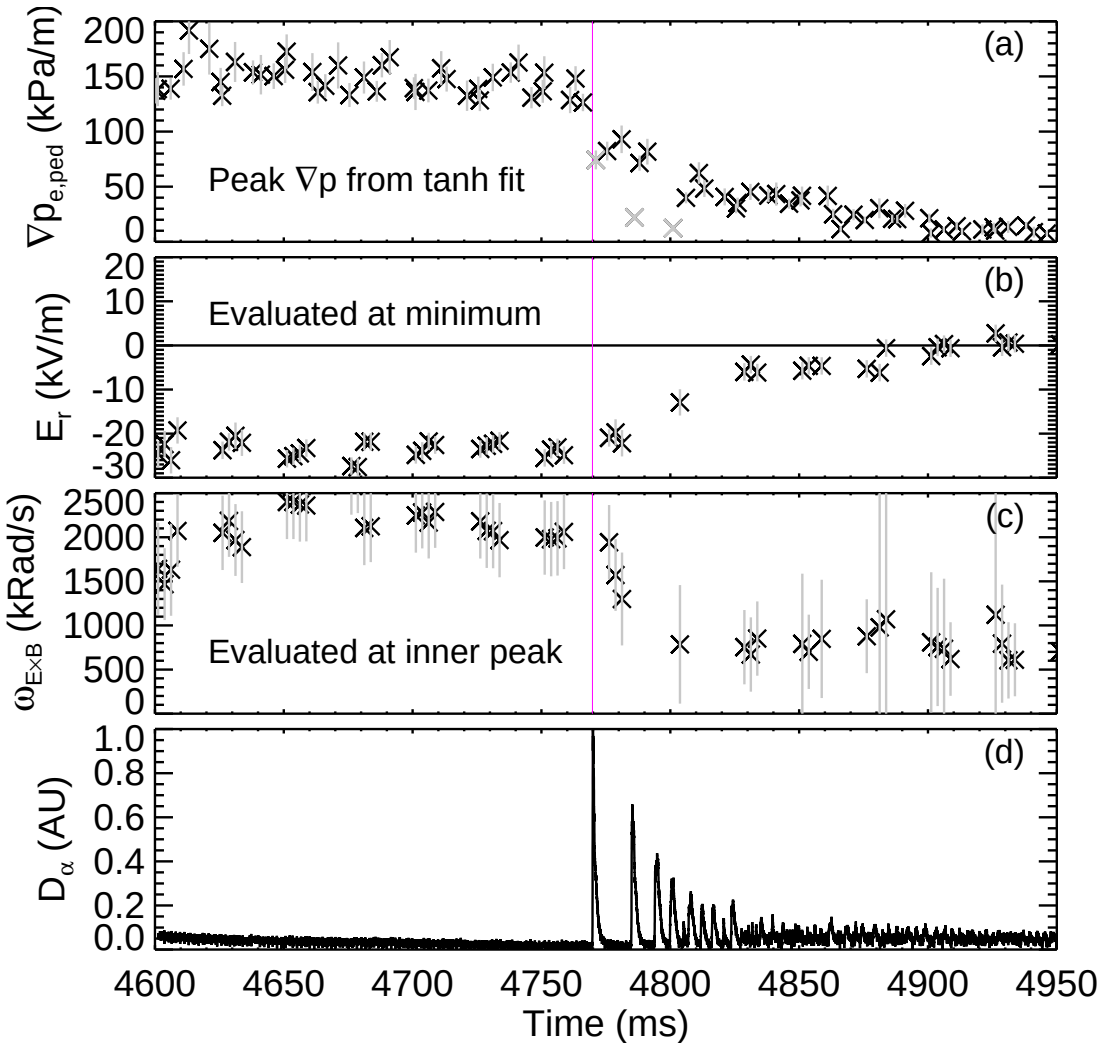

Figure 5.8: (a) Electron pressure gradient, (b) radial electric field, and (c) $E \times B$ shear evolution up to and during H-L transition sequence. Quantities are evaluated at their peaks in the pedestal. (d) shows D_α emission from the outer strike point for reference. This is the same case as shown in figure 5.6. It is seen that both ∇p_e and E_r (which is dominated by ∇p_i) are fairly steady before the start of the sequence and are reduced after the transient, reaching low levels by about 4825 ms. The two outliers in ∇p_e at 4786 and 4801 ms, and the point at 4771 ms (on the magenta line), occur during D_α spikes when pressure is temporarily reduced and are plotted with gray symbols instead of black.

5.4 Characterization of the Modulating Pedestal Mode

Since the hard H-L back transition transient is not a P-B type-I ELM[137] and is not due to collapse of $E \times B$ shear suppression, we now seek to understand the start of the H-L sequence by examining the properties of fluctuations in the pedestal prior to the start of the sequence.

During the ELM-free period, starting shortly after primary heating power is cut and before the start of back transition activity, a powerful coherent fluctuation is seen in all fast density measurements: BES,[85] Doppler BackScattering (DBS),[140] and the CO_2 interferometer.[141]

This so-called modulating pedestal mode (MPM) is observed before the start of both hard and soft H-L transition sequences and also reappears between the type-III ELMs at the start of the dithering H-L sequence.

The layout of BES chords is shown in Fig. 2.27. If column 1 is the farthest into the plasma (smallest minor radius), then column 5 is at the top of the pedestal, column 6 is at the upper knee, column 7 is at the lower knee, and column 8 is in the scrape off layer. Data from BES column 6 will be used unless otherwise specified.

5.4.1 Fluctuation Spectra Evolution Prior to the H-L Back Transition

Spectrograms of density fluctuations measured with BES during the termination phases of example H-modes with hard and soft back transitions are shown in Fig. 5.9. In the hard (soft) case, primary power was cut at 2150 ms (4400 ms), type-I ELMs stopped at 2210 ms (4424 ms), and the beam used for BES measurements was turned on at 2260 ms (4400 ms). It can be seen that the fluctuation power peaks between 40 and 80 kHz and grows in amplitude until the event at 2442 ms (4653 ms), which is associated with a bright burst of D_α emission from the divertor strike point in the case of the hard H-L transition sequence. During the growth of the MPM amplitude, pedestal density is accumulating while pedestal pressure remains roughly steady, as seen in figures 5.2 and 5.3. For the type of

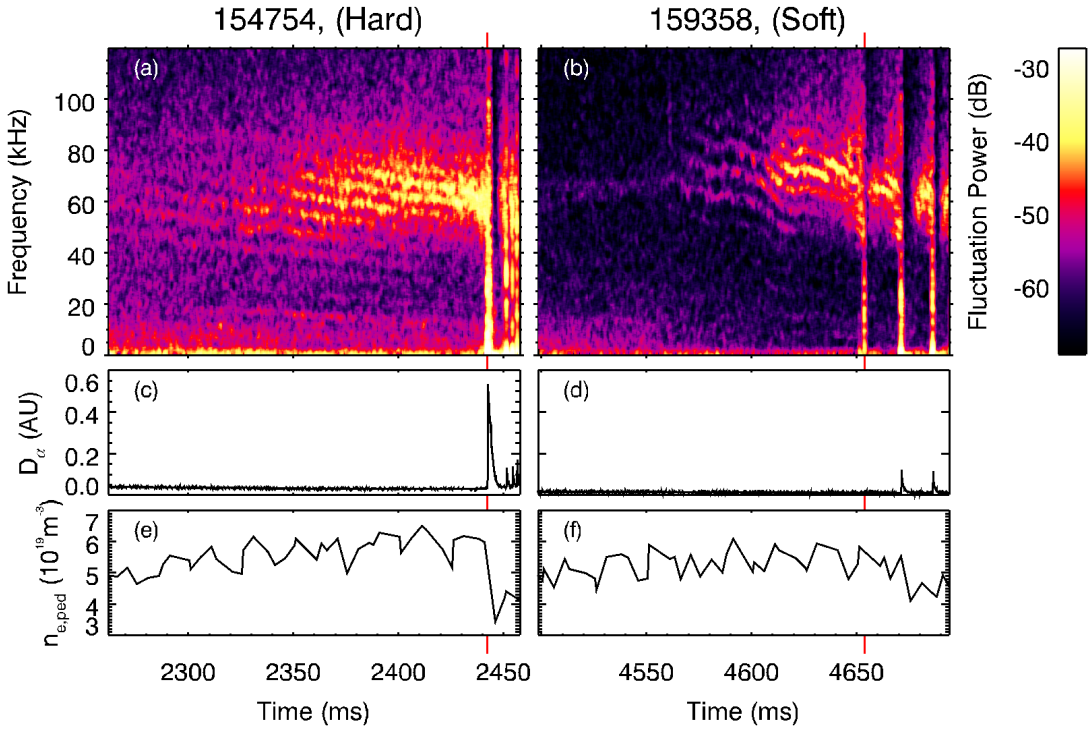

Figure 5.9: Spectrograms of a BES chord aimed at the steep gradient region, measuring fast density fluctuations before the start of a hard H-L transition sequence (a) and a soft transition (b). Corresponding time histories of D_α emissions from the outer strike point (c,d) and pedestal density (e,f) are plotted below the spectrograms. The FFT windows are 4096 samples (4.096 ms) each with 95% overlap. The D_α traces are normalized to the large type-I ELMs which occurred earlier in the shot, before the start of the display time window. In the case of the hard transition, the large transient at 2442.37 ms, easily identified by the D_α spike in (c) is associated with a vertical stripe in the spectrogram (a). Similar fluctuation behavior before the soft transition [at 4653.76 ms, see (b)] does not always result in any spike in D_α emission, such as in this example.

event at 2442 ms (4653 ms) in the figure, which is discussed in more detail later, the associated D_α spike can be large, small (a type-III ELM), or absent [as in the example shown in Fig. 5.9(d)] and the size or absence of the D_α spike is qualitatively consistent across all filterscope chords in the upper and lower divertors and tangent to the edge of the plasma at the outboard midplane. It can also be seen that the MPM has some spectral sidebands. The bands are roughly 5 kHz apart at 2400 ms (4630 ms), but they can be seen to contract together over time.

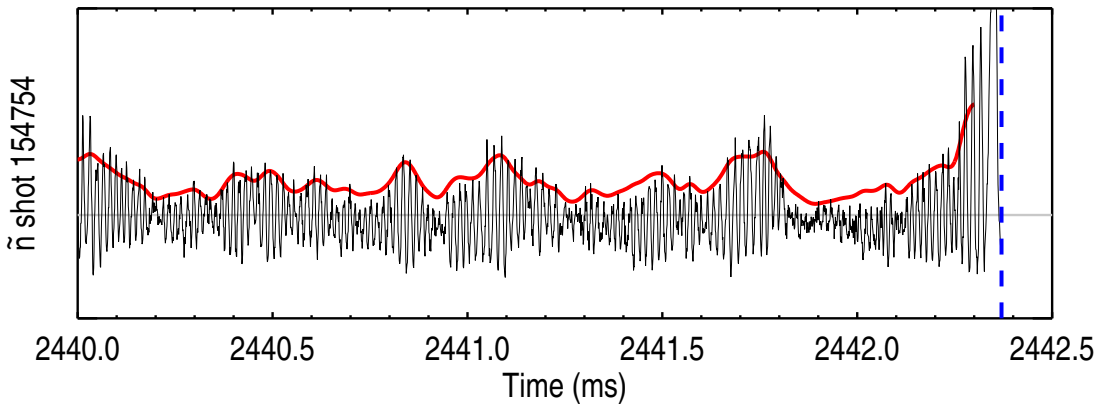

Figure 5.10: 1 MS/s, AC coupled BES signal measuring short timescale density fluctuations from the same chord as was used in Fig. 5.9(a). The thick red line behind the raw signal is a smoothed Hilbert envelope: $A = |y + iH(y)|$, where $i = \sqrt{-1}$ and H() is the Hilbert transform. The dashed blue vertical line marks the time when the D_α spike begins.

The MPM can be even more clearly connected to the back transition by examining its propagation velocity, amplitude and associated transport - topics that we take up in the next sections. Despite dramatic differences in the *results* of the first "event" of the sequence (which is a rapid slowdonw of the MPM's propagation velocity, as shown below), there is no obvious differece in the MPM betwen cases with hard and soft H-L transitions. Thus, the following characterization of the MPM applies to both cases.

5.4.2 Amplitude and Propagation Velocity Modulations Prior to the H-L Back Transition

The amplitude of these fluctuations is modulated at $\approx$ 2 kHz in the last few milliseconds before the transition sequence begins, as seen in Fig. 5.10. The modulation frequency is initially higher, but decreases over time. This can be seen in the spacing of the sidebands in Fig. 5.9(a,b).

Poloidal propagation of this mode can be seen in the delay between signals on vertically separated chords with the same radial position. The BES diagnostic

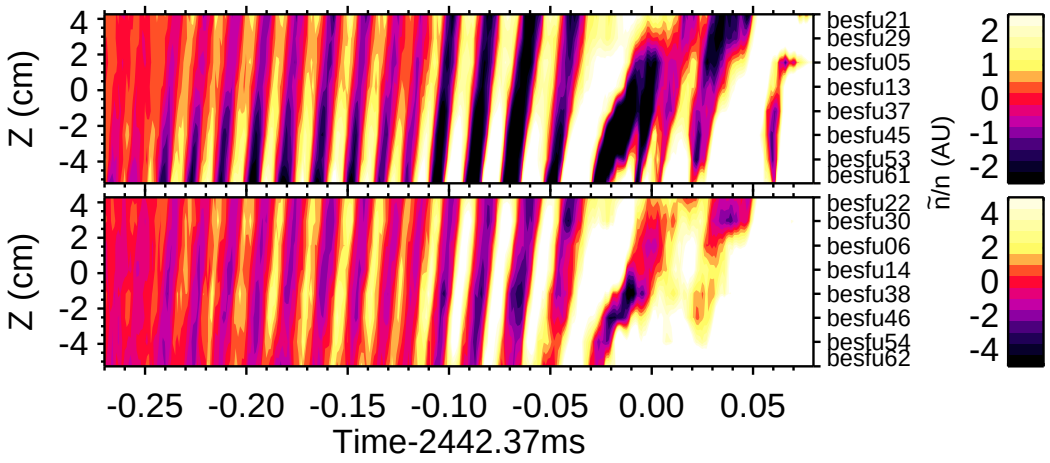

Figure 5.11: Contours of BES $\tilde{I}/I \propto \tilde{n}/n$,[85] for shot 154754 with a back transition starting near the end of the time window. Each of the two plots shows BES data from a different column of chords at the same radius. The two columns are 5 and 6 ($R = 225.5$ and 226.6 cm) and had the strongest reading of the MPM. The time is given relative to the large spike in D_α emission, which begins at 2442.37 ms. The second row includes the chord used for Fig. 5.9(a).

produces two types of measurements: there is a fast signal which is AC coupled and digitized at 1 MS/s for detecting high frequency fluctuations, and a slow signal which is DC coupled and digitized at 10 kS/s. The ratio of fast/slow BES intensity $\tilde{I}/I$ is proportional to $\tilde{n}/n$.[85] Figure 5.11 shows contours of $\tilde{I}/I \propto \tilde{n}/n$. The tilt of these contours is due to the poloidal propagation velocity, with faster moving features producing more vertically oriented stripes and slowly propagating features producing more horizontally oriented stripes. It can be seen that as the MPM amplitude grows (stripes become "brighter"), the propagation velocity slows down (the stripes tilt over to the right more). By 2442.37 ms (0 on the plot axis), the perturbation slows and eventually stops at the time when the hard back transition occurs. The propagation velocity prior to the slowdown, when evolution of v_p is slow compared to CER time resolution, is consistent with the local $E \times B$ drift velocity, although there is uncertainty in the relative positions of CER and BES chords. The slowdown happens too fast for CER measurements to resolve and thus it cannot be determined whether $v_{E\times B}$ experiences a temporary reduction during the D_α spike or v_p departs from $v_{E\times B}$.

The dominant frequency and wavenumber of the MPM are found using the method described in appendix A.1. From these, the lab frame propagation velocity v_p and amplitude of the dominant frequency component are found as well. The results are plotted in figure 5.12, along with D_α for reference. It can be seen in Fig. 5.12 that all of the quantities of interest are experiencing modulation. The modulations in dominant frequency and wavenumber are phased to produce minimal change in v_p for most of the time window, but changes in propagation velocity become more significant in the last ≈ 2 ms before the event at 2442.37 ms. During the penultimate peak in amplitude, just before 2442 ms, the propagation velocity drops noticeably [marked by a blue arrow in Fig. 5.12(d)]. There is another drop in v_p just before the D_α spike begins; this time v_p drops to ≈ 0 in a behavior which, for convenience, will be referred to as "locking."

It can be seen in figure 5.12 that modulations in both amplitude and propagation velocity appear to be related, but are not in phase. The phase difference is measured in figure 5.13: the time delayed cross correlation function is computed between $\tilde{n}$ and v_p over a 4 ms time window ending before the D_α transient. The phase difference is taken from a sinusoidal fit to the cross correlation function and it is found that v_p lags $\tilde{n}$ by $140\,^\circ$. Or since the critical behavior involves a peak in amplitude corresponding to a drop in v_p, it may be better to say that $-v_p$ lags $\tilde{n}$ by $40\,^\circ$.

5.4.3 Evolution of Dispersion Relation Leading up to the H-L Back Transition

While section 5.4.2 showed f and k for the dominant frequency component, it is also useful to view the dispersion relation of the entire spectrum. This is accomplished by the local wavenumber analysis technique descrbed in appendix A.2 with results shown in figure 5.14 for several time windows during the ELM-free period prior to the beginning of a back transition sequence. The shot and general time range correspond to figure 5.9(a). In most of the panels of Fig. 5.14, including (i) for example, it can be seen that all of the frequency components of the MPM lie along a straight line intersecting $k = 0$, $f = 0$: the fundamental and

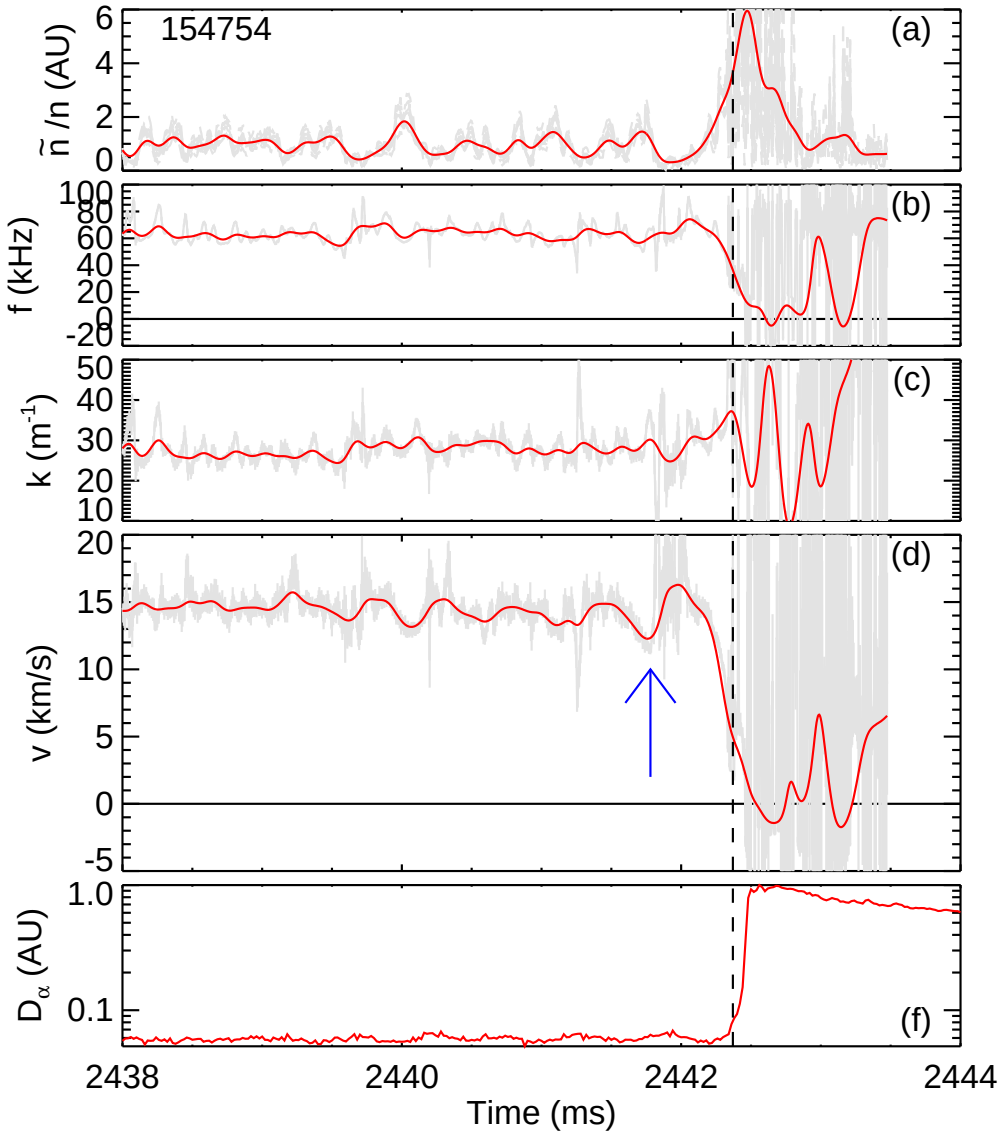

Figure 5.12: Time histories of (a) amplitude ($\tilde{n}/n$), (b) frequency, (c) wavenumber, (d) propagation velocity, and (e) D_α from a photodiode aimed at the outer strike point. f and k are calculated by the fit to Eq. A.1. A back transition begins at 2442.37 ms, marked by a vertical black dashed line. The smoothed results are plotted in red with the un-smoothed results in light gray to give a sense of the scatter produced by this method. Positive velocity indicates propagation vertically upward at the outboard midplane. BES data from column 6.

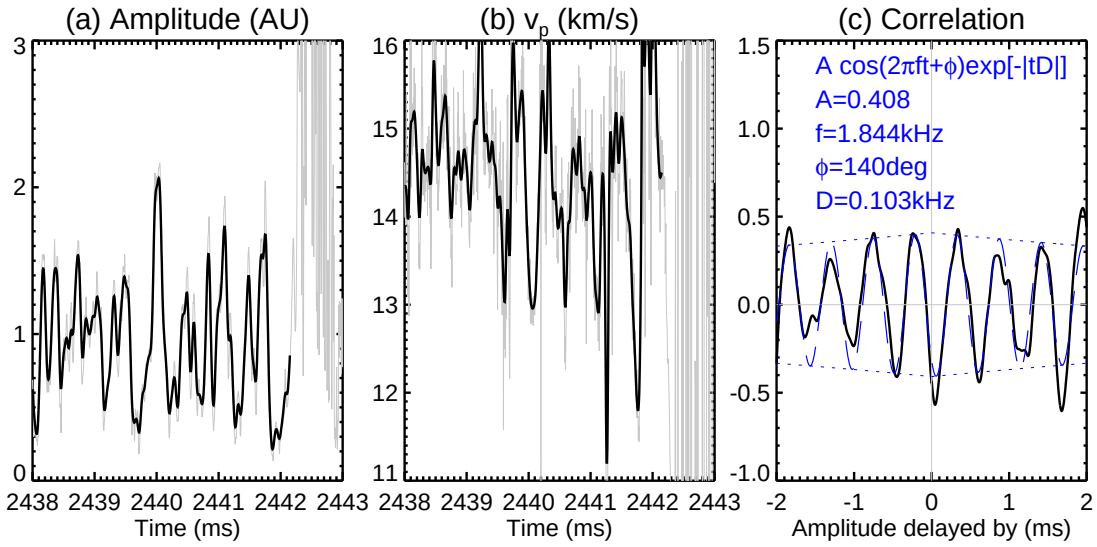

Figure 5.13: Phase relationship between (a) MPM amplitude and (b) propagation velocity. (c) The time delayed cross correlation function is computed for the smoothed data (black) in (a) and (b) and fit to $A\cos(2\pi ft+\phi)\times\exp\left[-|tD|\right]$ to obtain the phase difference ϕ.

the sidebands propagate at the same propagation velocity v_p. This means that the amplitude modulation is propagating with the mode. A purely time dependent modulation would produce sidebands at constant k, but different v_p. The series in Fig. 5.14 shows the overall coherence of the spectrum increasing as the mode grows in amplitude, and a decrease in propagation velocity over time in the period leading up to the H-L back transition.

5.4.4 Spatial Localization of the MPM Leading up to the H-L Back Transition

The MPM radial position is highly localized. The banded structure seen in the spectrograms of Fig. 5.9(a,b) emerges very clearly from the background on chords from three columns in the BES array (cols. 5, 6, and 7; see Fig. 2.27). The signature is fainter or undetectable on chords located farther out or deeper into the plasma. Figure 5.15(a) shows the spatially and temporally resolved, frequency averaged amplitude of fluctuations between 40 and 80 kHz during the ELM-free

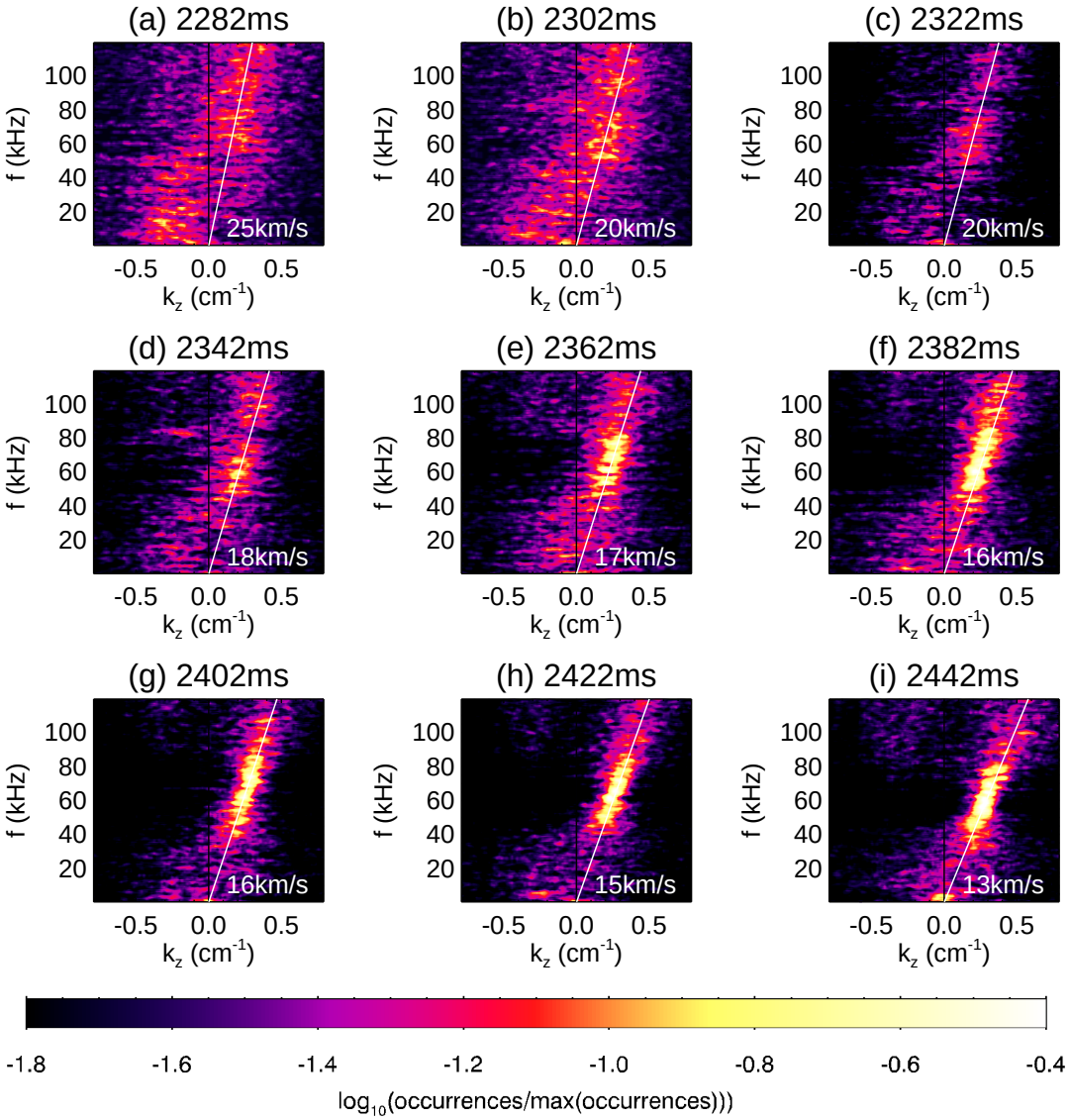

Figure 5.14: Dispersion plot: histograms of k, f for 3072 μs windows of BES data calculated from one column (column 6, see Fig. 2.27) of chords in the steep gradient region. Plots are labeled with the end of the time window. A hard back transition sequence begins at 2442.37 ms. k is calculated from the crossphase between chord pairs (see Eq. A.2). Data are aggregated from all chord pairs in the column. For each plot, propagation velocity is estimated by drawing a white line through the most densely populated region of $f - k$ space.

period prior to the start of the back transition sequence. From this plot, it is clear that this mode is localized to a width of a few $\times 10^{-2}\psi_N$. Figure 5.15 also shows that the MPM is located near the peak in ∇p (specific diagnostic alignment and position uncertainty issues and corrections are discussed in appendix B.1).

The mode is further localized to the low field side by using a CO_2 interferometer[141] that measures line integrated density along three vertical chords at the V1, V2, and V3 ports at $R = 1.48$, 1.94, and 2.10 m (compare to $R_m = 1.75$ m and $R_m + a = 2.28$ m) and one horizontal chord at the R0 port (midplane). The sampling rate is 3.33 MS/s, allowing detection of high frequency fluctuations, provided they are not lost in the spatial averaging. Although the chords sample primarily through the core, the MPM is strong enough that it still stands out against the background of other fluctuations picked up along the length of the interferometer chord. That is, density fluctuations with the same temporal and frequency evolution as shown in the BES data [Fig. 5.9(a,b)], including the spectral sidebands, are present in spectrograms from the interferometer, as seen in figure 5.16. The characteristic banded structure of the MPM is seen clearly in the spectrogram of the outermost vertical chord [chord V3 in Fig. 5.16(d)], is barely detected on the high-field side chord [chord V1 in Fig. 5.16(b)], and is seen but at lower intensity on the horizontal chord which samples both high-field and low-field sides [chord R0 in Fig. 5.16(a)].

Figure 5.17 shows the distribution of power in the relevant frequency band on different interferometer chords. The average measured fluctuation power in the relevant frequency band, normalized to the length of the interferometer chords in the region $0.92 < \psi_N < 0.97$, reveals that these fluctuations have at least $\approx 10\times$ more power on the low-field side V3 chord than on the V1 chord which samples more towards the high-field side. A significant increase in power is also seen from V2 to V3, which are 16 cm apart and both on the low-field side. Of course, not all power in the chosen frequency band has to come from the mode, so this technique underestimates the degree of localization. Thus it is concluded that the MPM is radially localized to the pedestal and poloidally localized to the low-field side.

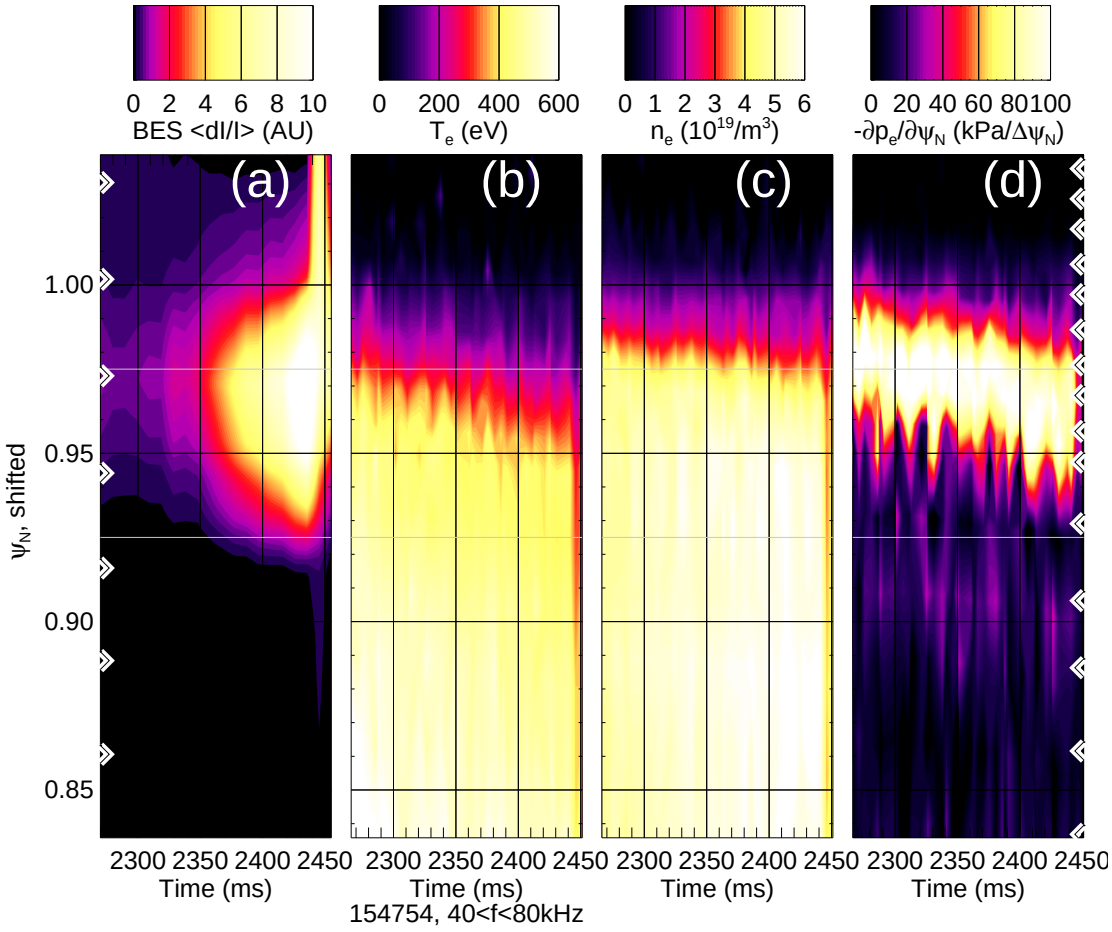

Figure 5.15: Comparison of spatial localization of (a) density fluctuations with $40 \leq f \leq 80$ kHz measured by BES to (b) electron temperature, (c) density, and (d) pressure gradient measured by Thomson scattering (TS). Primary heating power was cut at 2150 ms and a hard back transition sequence begins at 2442 ms. (a) BES intensity fluctuation power normalized to average intensity (ratio of fast to slow signals, proportional to $\tilde{n}/n$). All 64 BES chords in a square array (see fig. 2.27) at the outboard midplane are mapped to ψ_N. FFT windows are 10 ms long and power is averaged over the selected frequency band. A JT EFIT is used for mapping with shifts to correct the alignment of the profiles (see appendix B.1). Triangles at the edges of the plots indicate the spatial resolution of (a) BES and (d) TS. The limited resolution of the BES compared to TS explains why movement of the peak ∇p in (d) is not reflected by BES measurements in (a).

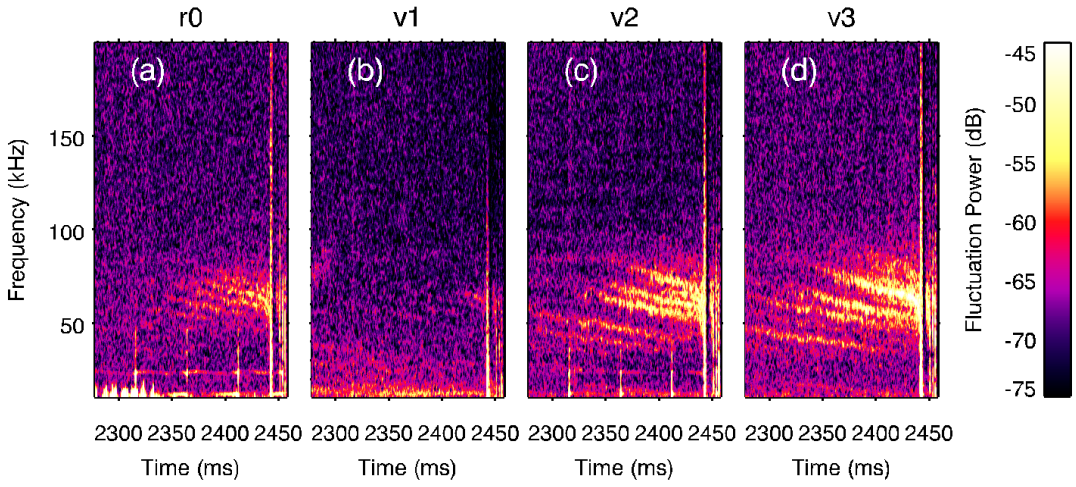

Figure 5.16: Spectrograms of line averaged density measurements by the CO_2 interferometer. (a) is a horizontal chord, (b) is vertical on the high field side, (c) and (d) are vertical on the low field side (see Fig. 5.17(a) for chord locations). Compare to figure 5.9(a), which shows corresponding BES measurements from the same shot and time with a hard back transition starting at 2442.37 ms.

5.4.5 Transport Effects of the MPM

Emission of light at the D_α line from a viewchord aimed near the point where the outer leg of the separatrix intersects the divertor target surface (outer strike point) can serve as a proxy for particle transport across the separatrix. Upon closer inspection, it is seen that there is a modulation in D_α at the same frequency as the modulation of the mode amplitude and phase velocity, implying that the mode has an effect on transport (aside from the D_α spikes which follow v_p locking events). Figure 5.18 shows an example using the column of BES chords with the highest average amplitude.

From figure 5.18, it can be seen that D_α has a $\approx 200\,\mu$s delay with respect to the mode amplitude modulation, consistent with the transit time for escaping material from the midplane (starting one gyroradius outside the separatrix) to reach the divertor if it propagated through the scrape off layer at 30% of the ion sound speed c_s as evaluated at the starting position (calculated as $222\,\mu$s). However, the D_α traces from filterscope chords aimed at the inner and outer strike points on the divertor shelf correlate with essentially no phase lag, indicating that

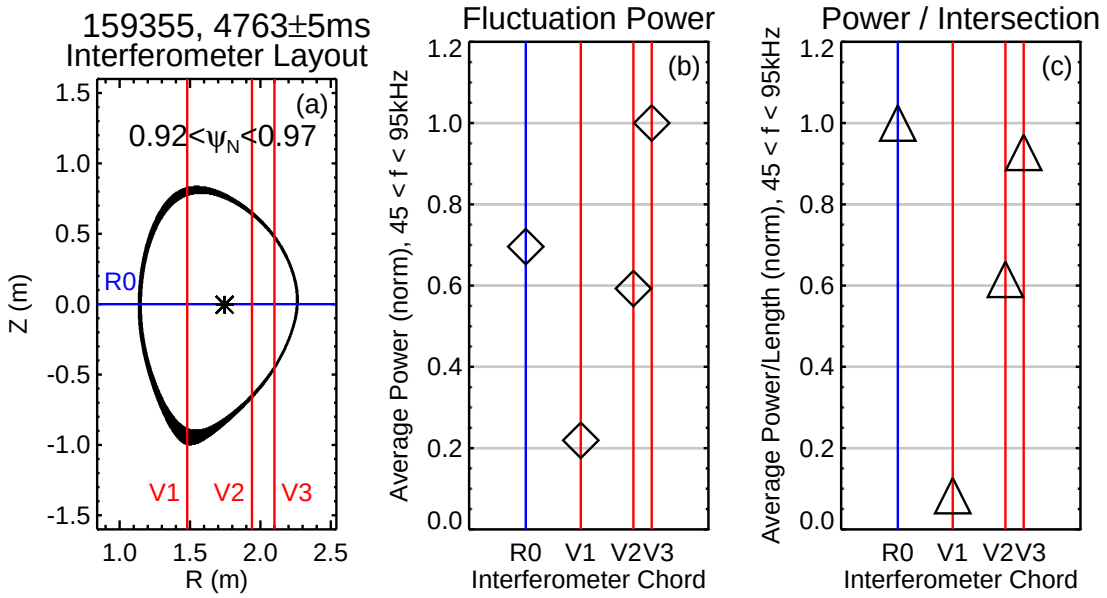

Figure 5.17: Localization to the low field side by using the interferometer. (a) Physical positions of the interferometer chords (blue and red lines) compared to the pedestal region of the plasma (black). A black asterisk marks the magnetic axis. (b) Average fluctuation power for $45 < f < 95$ kHz. (c) Fluctuation power from (b) divided by the lengths of the intersections of the chords with the pedestal region. The start of back transition activity starts shortly (< 1 ms) after the end of the time window from which data were taken. The horizontal spacing between the points for the vertical chords in (b) and (c) is proportional to the physical locations of the chords; R0 has been placed arbitrarily for ease of viewing.

the particle source is not localized strongly to the outboard midplane, so the delay between fluctuation activity at the midplane and D_α isn't due to parallel propagation time in the SOL. Furthermore, the localization from the interferometer in figure 5.17 is not so tight as to justify a source exactly at the midplane, as was assumed in the $\approx 200\,\mu$s result. On the other hand, the localization results from the interferometer are inconsistent with there being no lag in D_α emissions from the outer and inner strike points. Maybe the modulation in D_α is not coming from the strike point, but is being picked up at some other point along the viewchord. If the source were the outer edge of the plasma, there would be almost no lag as the chords viewing the two strike points cross the outboard separatrix in close proximity to each other.

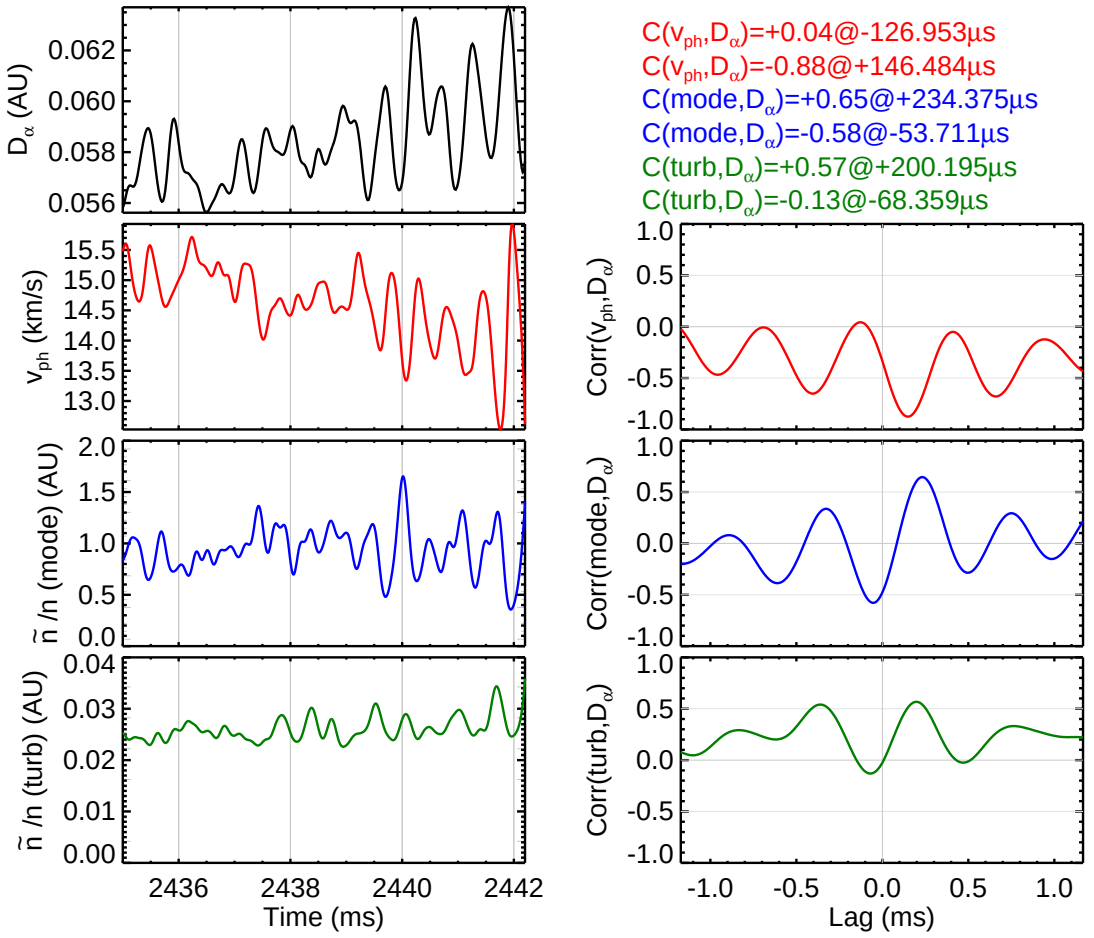

Figure 5.18: Effect of the MPM on transport. Left column: Strike point D_α, v_p, $\tilde{n}/n$ at the frequency of the coherent mode, average $\tilde{n}/n$ for $200 < f < 425$ kHz, representing the turbulence. The D_α trace excludes the start of the back transition and any ELM-like activity: these are small amplitude modulations in ELM-free H-mode. Right column: table of peaks in cross correlation functions, correlation of the waveforms on the left with D_α. $\tilde{n}/n$ and v_p are taken from figure 5.12. BES data are from column 6.

To see if delay between mode activity and D_α may be due to radial propagation instead, the analysis in figure 5.18 is repeated for a column closer to the separatrix, as shown in figure 5.19. The difference in position is roughly from the top of the pedestal to the bottom of the pedestal. Interestingly, the mode amplitude at this radius peaks at the same time as before, but the phase velocity is shifted in time, as is the power in the higher frequency fluctuations. The results

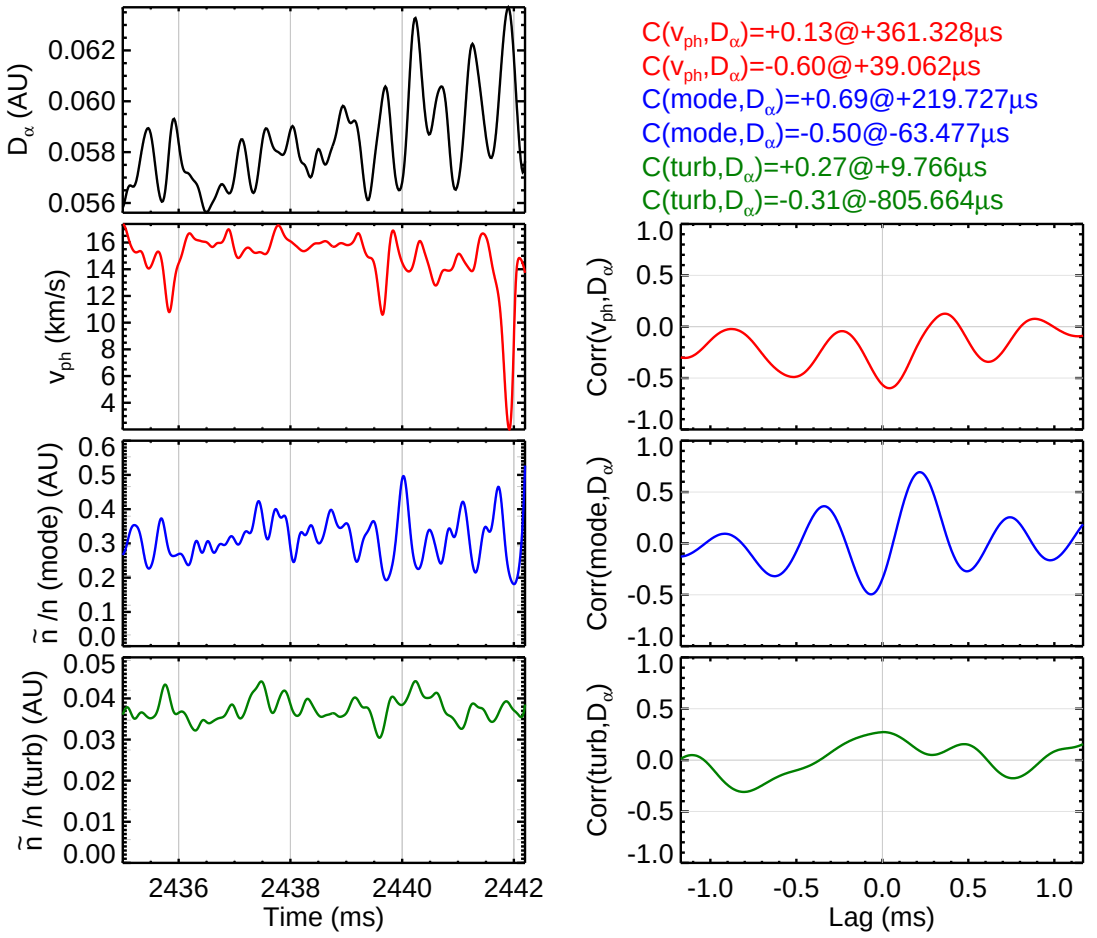

Figure 5.19: Analysis shown in figure 5.18 repeated for a column of chords closer to the separatrix. The drops in velocity and peaks in high frequency incoherent fluctuation amplitude now correlate well with D_α with very little phase lag. BES data are from column 7.

suggest that D_α modulations are out of phase with v_p modulations, consistent with a picture in which a drop in v_p is accompanied by an increase in D_α emissions.

The radial propagation of velocity modulations away from the location of peak mode amplitude is illustrated in figure 5.20, which shows analysis of four BES columns ending with one just inside the separatrix and using the sinusoidal fit to time delayed cross correlations described in figure 5.13. Excluded are one column of BES chords in the scrape off layer and the three columns deeper into the plasma (see Fig. 2.27). Measurements on the excluded channels did not support the fit described in the discussion of figure A.1 as the coherent mode was not

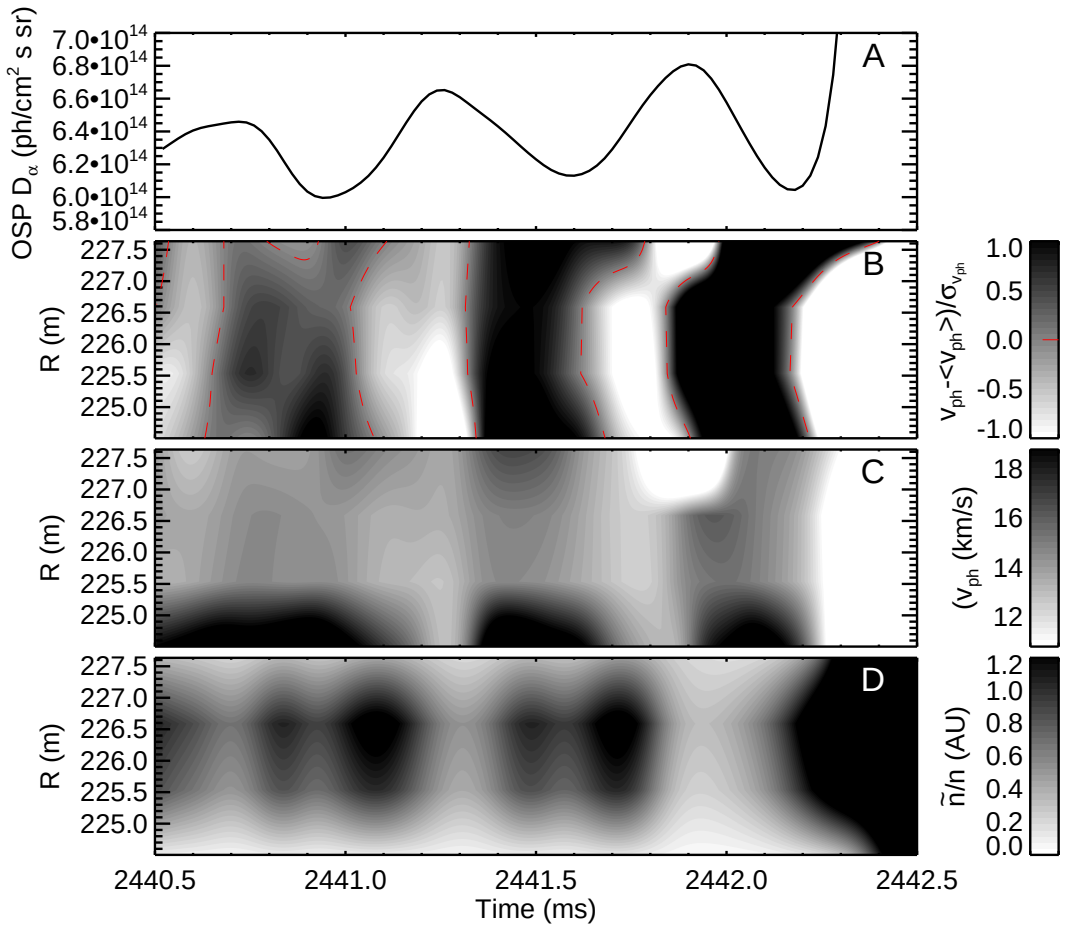

Figure 5.20: Demonstration that the lag in propagation velocity on outboard chords relative to the location of peak amplitude is consistent with the delay in D_α emission. A: D_α emission from the outer strike point. B: v_p with local moving average subtracted and then normalized to local standard deviation. C: Unmodified v_p, D: Mode amplitude. The crash is at the right edge of the plot range. BES data are from columns 4-7

expressed strongly enough. As seen in 5.20B, changes in phase velocity appear to begin near the center of the plot range, where the mode amplitude (5.20D) is highest. Note the crescent shape of the contours in 5.20B. The amplitude is found by interpolating the power spectrum to the frequency calculated with the fit to the correlation functions (that is, it is the amplitude of the dominant frequency component). 5.20C shows unmodified v_p, whereas 5.20B shows the normalized deviation of v_p from the local moving average (also excluding the crash) for each

chord (normalization is to the standard deviation for a few milliseconds before the crash). Notice in 5.20C that the penultimate dip in v_p appears to be severe at the bottom of the pedestal (top of the contour range). Indeed, figure 5.19 indicates that the phase velocity comes close to zero at this location (for the penultimate dip; the dip associated with the actual crash is excluded from the plot range). Thus, the dips in phase velocity are correlated with small, transient increases in particle flux across the separatrix as indicated by D_α emission from the divertor. The final plunge of v_p to ≈ 0 is associated with the large spike in D_α and a roughly $2\times$ reduction in pedestal height. These results thus provide further evidence that links the MPM modulation to cross-field transport and thus, ultimately, to the rapid collapse of the pedestal in the hard H-L back transition.

5.5 Conditions for Soft H-L Transitions

Soft H-L transitions (without the large transients at the start of the sequences) were observed in four cases: after very short H-modes, after H-modes powered by ECH, in connection with a sudden shape change executed in anticipation of the transient, and after H-modes which received primary heating from NBI counter to the plasma current.

The short H-modes terminate before triggering any type-I ELMs and have durations of ≈ 100 ms or less, which is comparable to or shorter than the length of the termination phases of the H-modes studied in earlier sections (see Fig. 5.9). These cases probably do not have enough time to evolve to a state which can drive the hard back transition. Regardless of the reason for the soft transitions out of short H-modes, they are of little interest. Strategies for producing soft H-L transitions should be distinguished from the short H-mode case by comparison between H-modes of similar length with soft and hard H-L transitions or by the presence of type-I ELMs at some point in the H-mode. Presumably, an ELMing plasma has had enough time to evolve to the point where hard back transitions can be triggered.

The ECH H-modes were compared to NBI H-modes of similar length; the

H-L sequences following ECH were soft whereas the post-NBI cases were hard, as seen in Fig. 5.21. Specifically, Fig. 5.21(c) shows stored energy decrease steadily at the end of the ECH H-mode (the first heating period) and drop suddenly after the NBI H-mode. Use of ECH instead of NBI heating tends to help produce a soft H-L transition sequence. Although several examples similar to Fig. 5.21 exist, none of the ECH phases lasted long enough to produce ELMs. It is not clear whether substituting ECH for NBI would allow a soft transition out of a type-I ELMing plasma and more testing would be needed to determine this.

The sudden shape change involved an increase in upper triangularity designed to modify the coupling strength between peeling and ballooning modes and move the P-B stability boundary in $p' - J$ space. This scheme was conceived of before the transient was shown to be P-B stable.[137] The limiting pressure gradient for a large type-I ELM (strongly coupled ideal P-B) depends heavily on upper triangularity[14,17] and thus a rapid enough shape change should be able to temporarily outrun increases in pressure gradient, providing an opportunity for some other process to take over and initiate the H-L sequence. Since the common initiator is not a strongly coupled ideal P-B mode[137] and p' is not increasing before the transition starts, this technique should not work as expected. Despite these arguments, the technique appears to be successful in removing the transient. Figure 5.22 shows the results of a sudden triangularity increase in anticipation of the H-L transition, where the second H-L sequence is initiated by a much smaller D_α spike than in Fig. 5.21 and pressure, density, and stored energy decrease smoothly, rather than falling suddenly in one step [compare panels (a), (c), (d), and (e) between Figs. 5.21 and 5.22 for the second H-L transition at $\approx$ 3000 ms]. Figure 5.23 shows the change in boundary shape. When the triangularity excursion was not timed correctly or was absent, the transient occurred (Fig. 5.21 shows an example of identical setup but with no triangularity change). It is clear that the quick change is important: in the example shown in Fig. 5.22, triangularity increases from 0.2 to 0.4. Simply running the discharge at triangularity of 0.4 does not prevent the transient from occurring; instead, triangularity must be at a lower value and then be increased quickly at the correct time. The transient resulted if

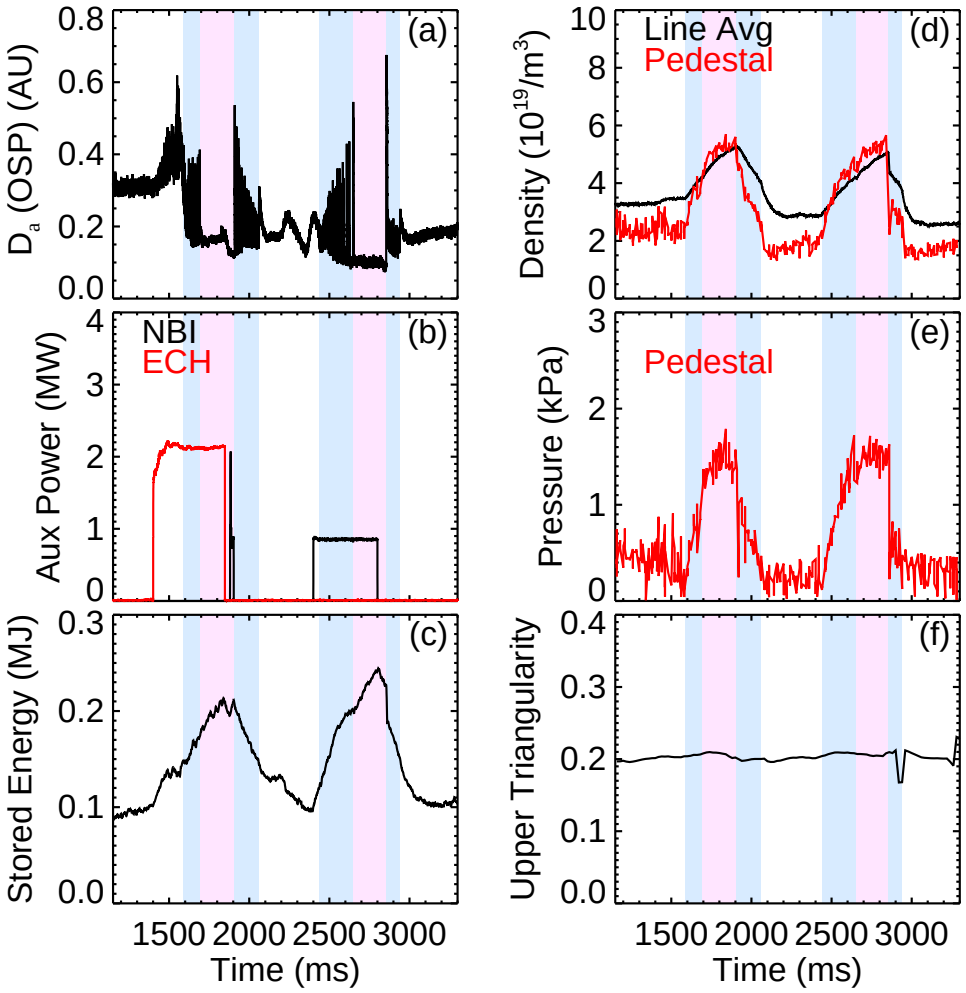

Figure 5.21: Comparison of H-L back transitions out of ECH and NBI powered H-modes. (a) D_α emission (b) heating power from ECH (red) and NBI (black) (c) stored energy (d) density, pedestal value from Thomson scattering (red) and line averaged value from the interferometer (black)[141] (e) pedestal pressure from Thomson scattering (f) upper triangularity. Periods of ELM-free H-mode operation are shaded pale pink, and periods of dithering are shaded blue. Although pedestal density and pressure are essentially equal prior to the transition, the H-L sequence following the NBI case begins with a large D_α spike and sharp decrease in pedestal height at 2854 ms, whereas the pedestal relaxes more gradually (starting at 1909 ms) following ECH heating.

the shape change occurred too soon such that the sequence began late in the flat top of the triangularity excursion. It would be useful to conduct further testing to determine whether this technique would work in the termination phase of an H-mode that had been heated for long enough to produce type-I ELMs.

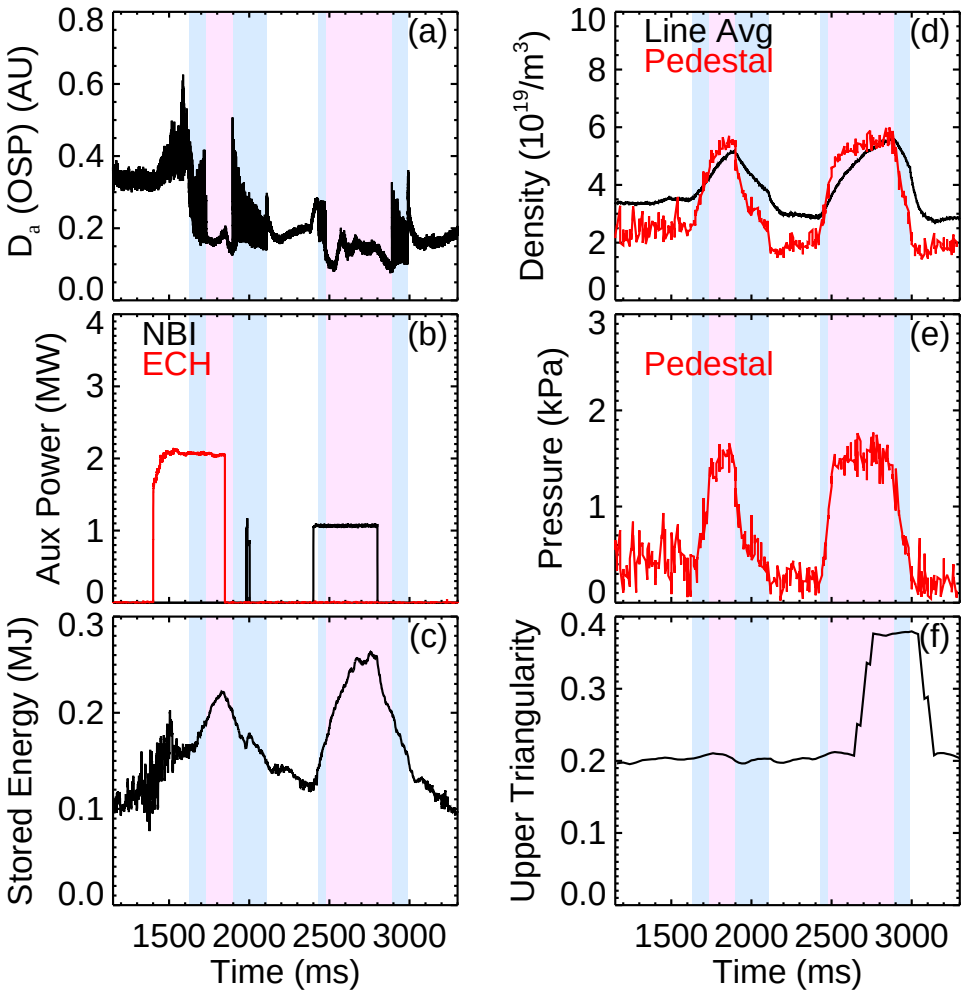

Figure 5.22: H-L Back transition sequences following NBI powered H-modes were "soft" if a correctly timed increase in upper triangularity was added : δ_{top} ramped from 0.2 to 0.38 in 20 ms and the H-L sequence began 130 ms later. Compare to figure 5.21, which is identical other than the triangularity excursion. Back transitions start at 1896.16 and 2890.46 ms. ELM free H-mode is shaded pale pink, dithering during transition sequences is shaded blue.

The most robust method for producing soft H-L transition sequences is through application of counter-torque during the primary heating phase. Figure

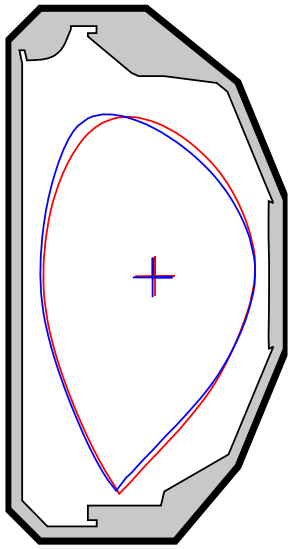

Figure 5.23: Change in boundary from 2500 ms (red) to 2900 ms (blue) in shot 153622 as a result of the triangularity jog shown in figure 5.22. The top left corner of the plasma has moved closer to the upper divertor.

5.24 shows an example of this behavior. It can be seen from the figure that although the rotation imparted by the beams decays quickly, a significant difference remains at the start of the H-L transition sequence. The start of the sequence is being defined by the locking behavior of the MPM (see section 5.4), marked by vertical lines. The beams used for diagnostics introduce a small amount of co-torque during the termination phase: blips for CER add an average of +0.2 to +0.3 Nm co-torque and continuous beam usage for BES adds about +1.0 Nm. For comparison, torque injected during the heating phase is -3.3 to -2.6 Nm or +2.7 Nm to +3.9 Nm for counter and co setups.

Many counter-torque H-modes were produced and they reliably underwent soft back transitions. The counter-torque shots were interleaved with co-torque shots, which continued to produce hard back transitions. A pair of co-torque shots with hard transitions was surrounded by counter and balanced torque tests which experienced soft transitions, and the counter torque shots were surrounded by co-torque shots with hard transitions. So, the difference does not appear to result from wall loading or other evolving conditions inside the machine. Because of the interleaving of co and counter torque shots, it was easy to find hard counterparts

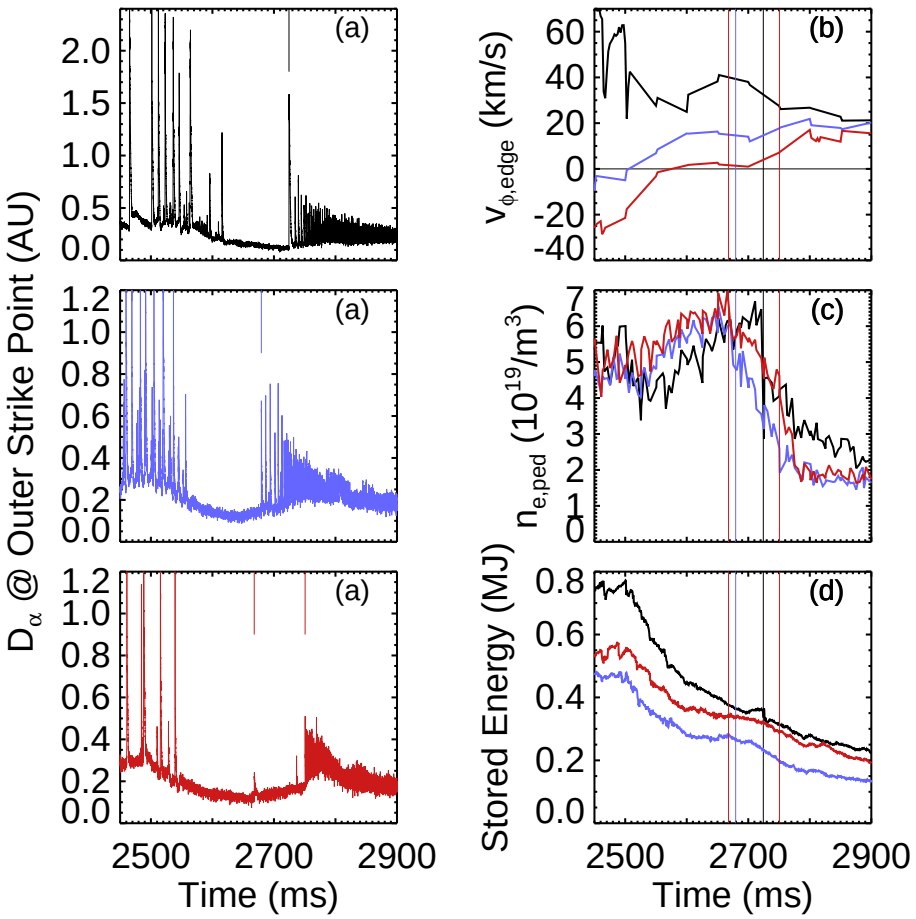

Figure 5.24: Control of the transient associated with H-L transition sequences by varying torque injection τ_{INJ}. (a-c) D_α emission from three cases, (a) co ($\tau_{INJ} = +3.9$ Nm black), (b) balanced ($\tau_{INJ} = -0.9$ Nm light blue), and (c) counter ($\tau_{INJ} = -3.3$ Nm red) primary NBI. Primary NBI heating is terminated at 2500 ms, followed by co-NBI blips for diagnostic purposes producing $\tau_{INJ} = +0.2$ Nm on average. In (d) through (f), quantities from the three cases are overlaid with colors matching (a) - (c). (d) toroidal rotation from a CER chord aimed near the edge of the plasma ($R = 2.267$ m vs. $R_{LCFS} \approx 2.28$ m) (e) electron pedestal density (f) stored energy. Vertical lines mark the v_p locking behavior discussed in Sec. 5.4. Note that only the co-torque case experiences a sharp drop in stored energy at the onset of the H-L sequence.

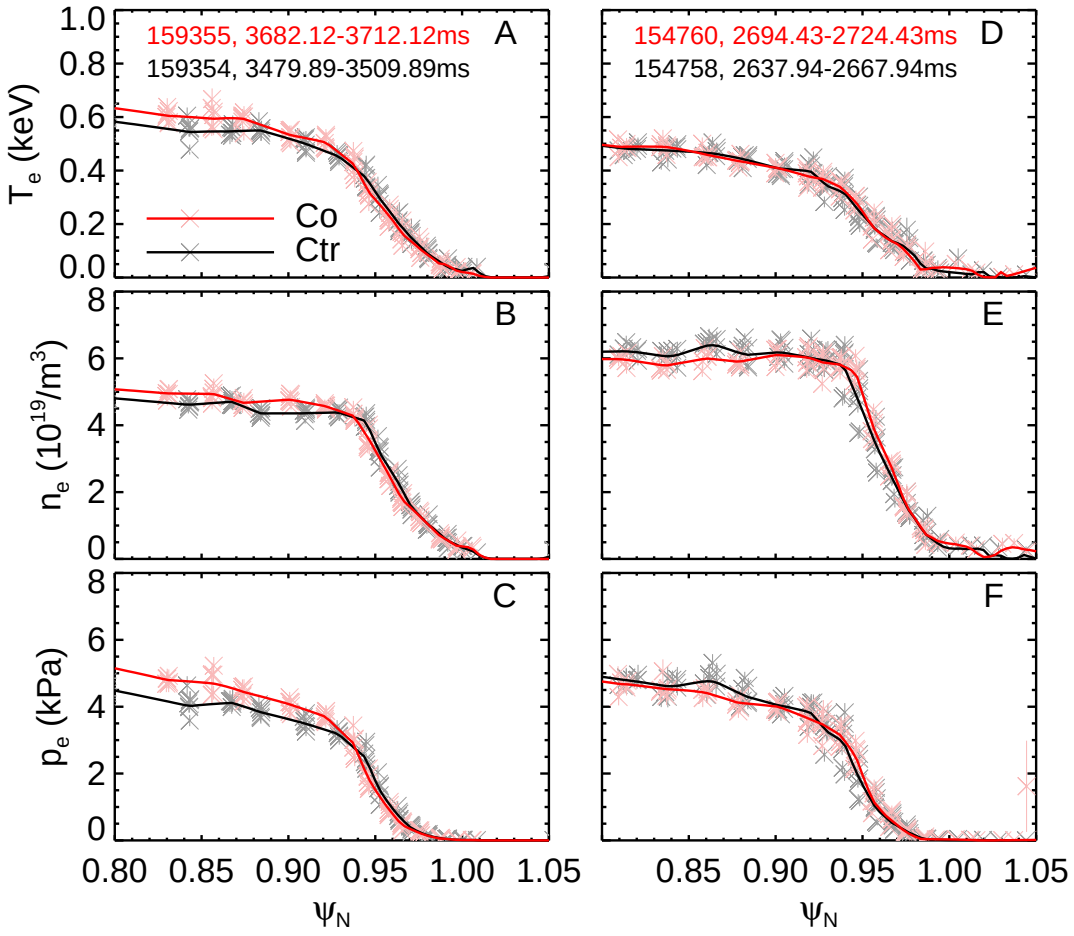

Figure 5.25: Electron profiles from Thomson scattering before the first v_p locking events in co (red) and counter (black) torque cases. Two examples are shown. A: Temperature, B: Density, C: Pressure, D-F: repeats of A-C for a different pair of shots from a different run day. The source data are shown with Xs. The thick line through them is obtained from the WAIC method (see section 2.6.2). The profiles in both example co-ctr pairs are nearly identical, so the difference in hard vs. soft H-L transitions is not explained by electron temperature and density.

for soft transitions. It was found that for most co/ctr pairs of transitions, the only significant difference in the basic measurements was in the toroidal rotation. As demonstrated by representative examples in Fig. 5.25, electron profiles were essentially identical in most cases: the difference between hard and soft H-L transitions is not determined by electron temperature or density.

Figure 5.26 shows profiles of flow speeds of carbon ions in the toroidal and

poloidal directions, the $E \times B$ drift velocity, and $\tilde{n}/n$ for reference. It is clear that the main difference between the co and counter cases is in v_{tor}. Although there are differences in $v_{E\times B}$, the values at the bottom of the well are very similar.

Figure 5.26 also shows that the MPM amplitude peaks near the bottom of the E_r well. Relative error in profile alignment between BES and CER is about 5 mm,[82] and delays in beam emission ($\approx$ 3 ns at this temperature, density, and beam energy[87,142]) coupled with the inward velocity of the beam (2.2 mm/ns) result in an inward shift of 6.6 mm for this case. The positions of BES chords have been corrected by this amount (6.6 mm) and the 5 mm relative uncertainty between BES and CER is shown in the figure. In addition, the propagation velocity of the MPM (see Fig. 5.12) is consistent with $v_{E\times B}$ at the bottom of the well.

Finally, we notice that although the initial v_p locking event of H-L sequences after balanced torque injection releases much less energy than the transients of hard back transition sequences (co-torque), such that these cases have been categorized as "soft", the drop in energy and density across the initial D_α spike is now measurable above the noise. The prompt energy loss across the first v_p lock of soft H-L sequences (counter-torque) is typically small enough that it is obscured by scatter in the data. Figure 5.27 shows changes in energy and density vs. edge toroidal rotation for a set of shots where beam power, timing and other conditions were well matched (data in figure 5.24 are drawn from the same set). Cases where the prompt energy loss was indiscernible are reported as a drop of 0 with uncertainty estimated from scatter in the data or experimental uncertainty before the D_α spike, the interval between the last pre-D_α datum and the spike, and the slope of a linear fit to pre-D_α data. D_α itself is used as more than merely a landmark in this case: Fig. 5.27(d) shows that the peak magnitude of the initial D_α spike of the H-L sequence above the background D_α level increases with $\omega_{tor,edge}$, and is easily measured as > 0 even for the counter-torque cases in this dataset.

The results in figure 5.27 show that for intermediate torque and rotation, energy release is intermediate between the hard and soft back transitions (although it is closer to being "soft" than "hard"). This suggests that there is a continuum of possible transient/type-III ELM sizes which can result from the first v_p locking

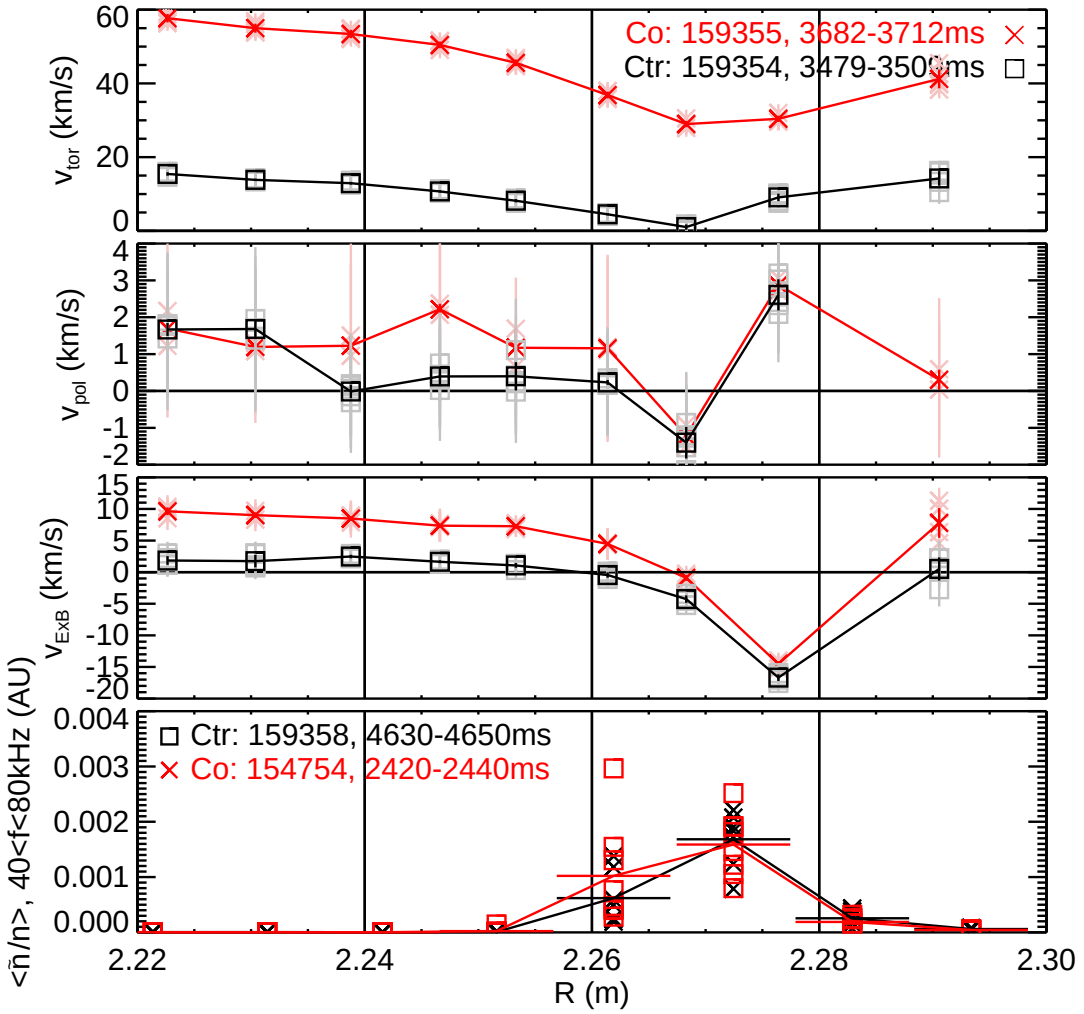

Figure 5.26: Carbon ion rotation profiles from CER with BES fluctuation power for reference . From top to bottom: toroidal rotation profile, poloidal rotation, $E \times B$ drift velocity, and $\tilde{n}/n$ from BES. Red Xs follow co-torque application. Black squares: counter torque. Horizontal error bars on BES data show relative error between the BES and CER arrays. BES positions have been shifted outward by 6.6 mm to account for finite lifetime and time of flight delays.

event. A cotinuum of transient/type-III ELM sizes in turn implies that small type-III ELMs and large transients are two limits of the same physical phenomenon, which is consistent with the identical behavior of the MPM observed before each. If this is true, we have found a scenario where normally benign type-III ELMs can grow large enough to collapse the pedestal.

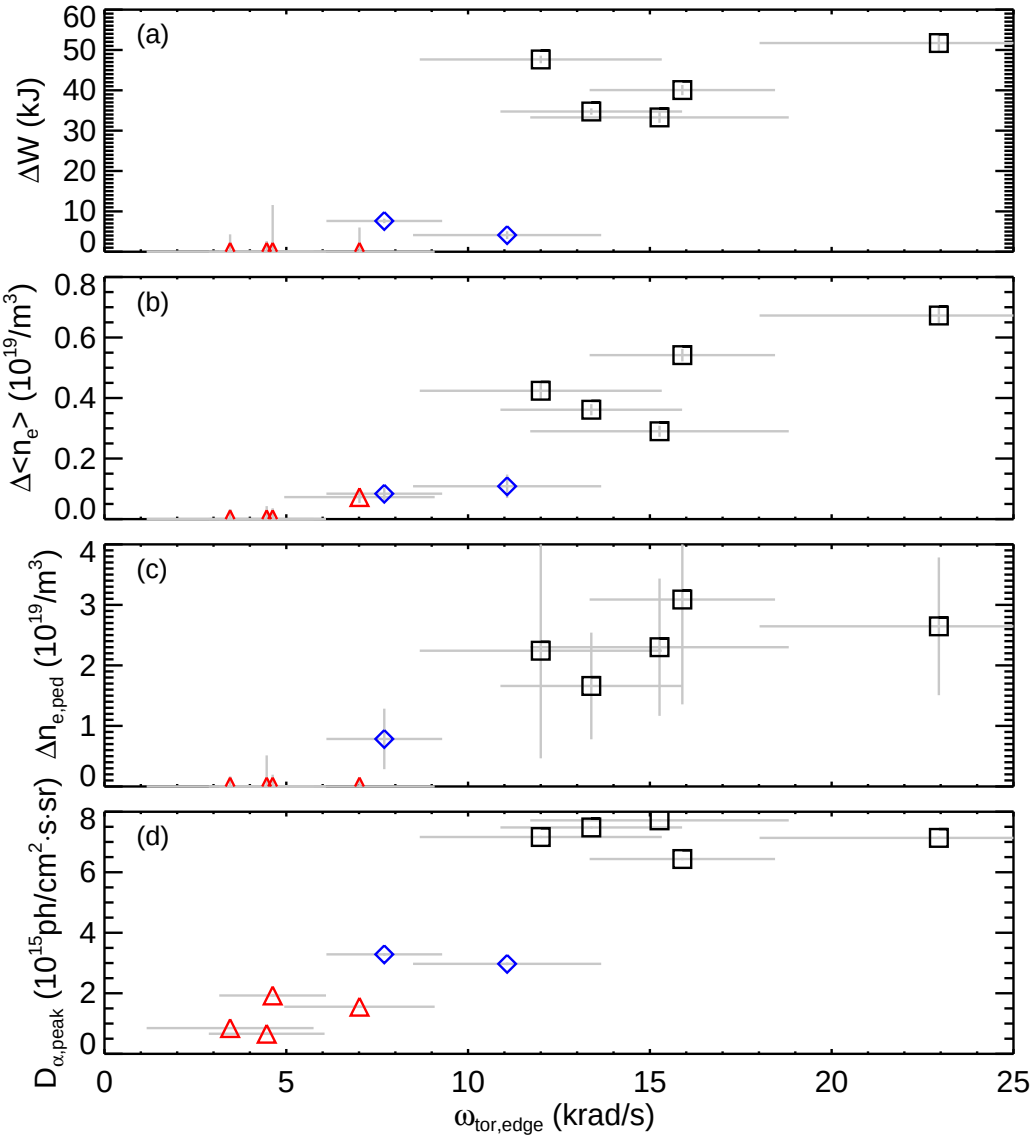

Figure 5.27: Effects of the intial event of H-L sequences vs. edge toroidal rotation. Cases which received co-, balanced, and counter-torque during the primary heating phase are marked with red triangles, blue diamonds, and black squares, respectively. (a) change in stored energy, (b) change in line averaged density (interferometry), (c) change in pedestal density (tanh fit to Thomson scattering), (d) peak in D_α emission. $\omega_{tor,edge}$ is obtained from the CER chord in the bottom of the E_r well (see Fig. 5.26).

5.6 Discussion

We find that dithering H-L transition sequences in DIII-D can begin when $E \times B$ shear should be strongly suppressing turbulence ($\omega_{E\times B} > \omega_T$, see Sec. 5.3), indicating that the low-power ELM-free H-mode preceding the transition sequence in our scenario is promoting the growth of some instability which reduces the pedestal height and thus weakens the diamagnetic contribution to E_r, ultimately collapsing the shear layer and terminating H-mode. This is true in "hard" back transitions where a large transient quickly relaxes most of the pedestal pressure gradient in ~ 1 ms and in "soft" back transitions where the pedestal is gradually relaxed over ~ 100 ms by a series of small type-III ELMs. In both cases, we find a coherent density fluctuation which appears in the pedestal and grows in amplitude until the start of the back transition. This so-called modulating pedestal mode (MPM) is implicated as a conspirator in the death of the transport barrier by the synchronization of its propagation velocity "locking" events with the transients and type-III ELMs of both types of H-L sequence.

The localization of the MPM is consistent with an instability of ballooning character. Only the ideal, intermediate to high n linear peeling-ballooning mode was eliminated by the stability analysis of chapter 4; a resistive, kinetic, or nonlinear variant of ballooning or peeling-ballooning is not ruled out. As seen in figure 5.28, temperature decreases during the ELM-free period before the H-L transition, so resistivity ($\eta \sim T_e^{-1.5}$) increases. Decreases in temperature are balanced by increases in density (see Fig. 5.2) to maintain a nearly steady pressure gradient. Trends in resistive ballooning mode drive are estimated by $\eta \nabla p$, which is increasing.[143] The lifetime of the MPM (> 100 ms) is far longer than linear growth timescales for common ideal or resistive instabilities. For comparison, typical linear growth timescales for ideal instabilities are on the order of the Alfvén time $\tau_A \sim 1\ \mu$s,[14,119,131,144] whereas the linear growth of resistive wall modes (which are among the slowest growing linear instabilities) is determined largely by the timescale for flux to diffuse through the wall of the vacuum vessel $\tau_w \sim 1 - 10$ ms in DIII-D.[130–132] Nonlinear instabilities such as tearing modes[a],

[a] Tearing modes are kinks with resonant surfaces inside the plasma; finite resistivity makes it

however, can evolve on timescales of $\gtrsim 100$ ms.[146] This suggests that the nonlinear dynamics of the mode are important. If, for example, the mode were nonlinearly saturated, then amplitude would increase with drive. If the drive were proportional to resistivity, then the mode amplitude should slowly evolve during the ELM free period before the back transition. Figure 5.28(d) shows that the MPM's amplitude grows and correlates with increasing resistivity. So, these observations are consistent with a linearly unstable, nonlinearly saturated, resistive ballooning or peeling-ballooning mode. Modeling results suggest that resistivity should be destabilizing to peeling-ballooning modes.[147] Resistive interchange or ballooning instability has been proposed as the trigger for type-III ELMs.[45] Future work could test these back transitions against resistive instabilities using a code such as `BOUT++`.[114,119,147]

We note that a similar phenomenon to the MPM, labeled the Bursty Chirping Mode (BCM), has been observed in DIII-D H-modes in connection to experiments with lithium, although lithium does not appear to be strictly required.[148,149] The BCM appears in ELM-free periods when density is accumulating, similar to our observations of MPM. The lifetimes, frequencies, and bursty behaviors of both modes are similar. However, the ELM-free windows with the BCM are observed between ELMing periods in plasmas which receive significant auxiliary heating power, and temperature increases with time during BCM activity. This is in contrast with the falling temperatures observed during the ELM-free periods wherein the MPM appears. It is not yet clear whether the BCM and MPM are related, but the BCM would seem to be incompatible with our speculative hypothesis that the MPM is resistive in nature.

Use of mixtures of co-injected and counter-injected neutral beams and ECH have produced H-mode terminations with a variety of edge toroidal rotation profiles. There is a clear link between fast co-rotation and back transitions which begin with a large sudden pedestal relaxation. However, between the high co-torque, hard back transition and full counter torque, soft back transition cases, we find some intermediate results: at the first v_p lock, cases with balanced torque

possible for these to be unstable,[93] but only if an initial seed displacement is provided.[145]

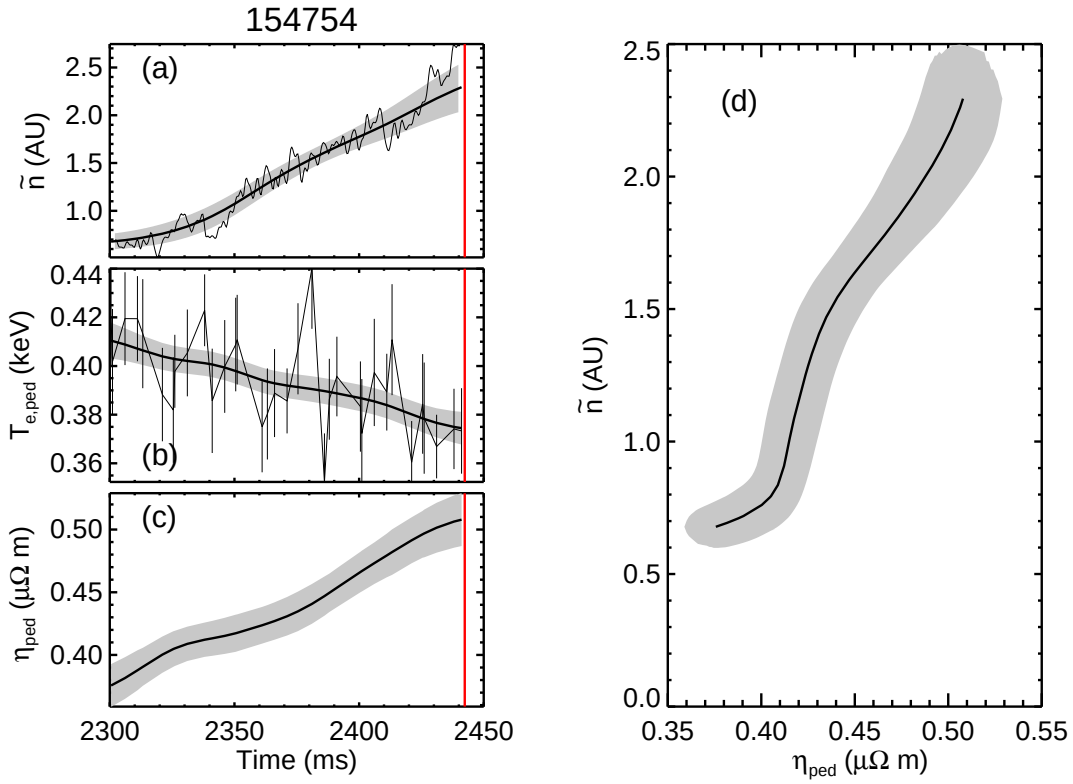

Figure 5.28: Evolution of density fluctuation amplitude and resistivity prior to the start of an H-L transition. Time histories of (a) average fluctuation power for $40 < f < 90$ kHz, which is strongly dominated by the MPM; (b) Pedestal electron temperature from tanh fit to Thomson scattering data; and (c) Spitzer transverse resistivity[92] at the top of the pedestal. Fluctuation amplitude vs. Resistivity is plotted in (d), showing a strong positive correlation between mode amplitude and resistivity. Gray area shows uncertainty: (a) local standard deviation, (b) experimental uncertainties propagated through the smoothing kernel, (c) standard deviation of 200 Monte-Carlo trials using experimental uncertainties in T_e, n_e and assuming 10% error in Z_{eff}.

injection experienced small but finite prompt energy and density losses, whereas prompt energy and density losses from fully counter-injected cases were typically lost in the noise. The D_α spike was also larger in the balanced torque (-0.9 Nm) case than in the counter torque case (-3.3 Nm). There were some cases which received counter-torque from the primary heating beams but were diagnosed with BES using a steady co-beam and which produced sudden drops in pedestal height characteristic of hard back transitions, although with a smaller amount of energy

lost compared to cases with all co-torque NBI (these are exlcued from figure 5.27, which compares only shots from the same day of a carefully controlled torque scan). This suggests a continuous range of energy release which depends on toroidal rotation. It would be helpful to have more data to confirm this.

Identical MPM v_p locking events occur before the large transients in hard back transition sequences and before the type-III ELMs, including the first type-III ELMs in a soft transition sequence. This suggests that these events may be triggered by the same physics, consistent with the existence of a continuum of energy release amounts associated with the initial D_α spike in the dithering H-L sequence. If this is indeed the case, then the large initial transients are the high toroidal rotation limit of the type-III ELMs.

However, rotation effects in and of themselves are not sufficient to explain the different types of back transitions. In particular, v_p locking events which greatly reduce the pedestal height, as in hard back transitions, do not reduce the rotation speed enough to match the soft back transition scenario. If rotation alone controlled the back transition, then subsequent v_p locks should also cause large transients, but they commonly result in small type-III ELMs. The principal changes following a locking event with a large transient are in pedestal density and edge pressure gradient. One of these must be important for production of the large transients, or else several transients would normally be produced in succession until the rotation was sufficiently reduced. If a resistive ballooning mode were involved, as suggested in previous discussion, the pressure gradient would be important to the drive, so reduction of the pedestal pressure gradient by the transients in the hard transition sequences would tend to prevent double transients.

The long lifetime (often > 100 ms) of the MPM in these cases means that, given real time detection of this mode and a suitable actuator, a plasma control system may have a realistic chance of using MPM to help avoid unintentional H-L transitions. Density measurements by the interferometer should be suitable for mode detection. Applying full counter-NBI should provide a sufficient reduction in v_ϕ in ~ 100 ms while also raising temperature (lowering resistivity), and the triangularity change also takes about 100 ms. ECH could help lower resistivity

without adding co-torque, which would help buy time for one of the other methods to take effect even if electron heating alone were insufficient to prevent the onset of the H-L sequence. However, it is not yet clear exactly what conditions are required for production of MPM or if it will appear in future, large tokamaks such as ITER.

These experiments were not carried out using DIII-D's ITER similar shape or any of the typical high performance scenarios, but instead were executed in a shape which was developed for examining fluctuations and flows in the boundary and pedestal during L-H transitions. However, the findings in this shape should not be dismissed as high performance or ITER simulation experiments in DIII-D concentrate on conditions in the core plasma and make little to no effort to produce reactor relevant boundary plasmas (core-edge integration is an area of active research). As the H-mode transport barrier, MPM, and back transition transients occur at the edge of the plasma, conditions in the pedestal and perhaps even the SOL are much more important for this study than core performance. The boundary shape (Fig. 1.7) used in these experiments placed the X-point and separatrix legs on the divertor shelf, away from the duct to the cryopump (which is under the shelf in the lower divertor). This placement of the X-point appears to be the key feature which allows these plasmas to produce long periods of LCOs during transitions. While the cause for this is uncertain, it is possible that increased neutral density in the SOL due to lower pumping efficiency is a factor (no measurements of neutral density near the plasma are available). That would make this scenario more reactor relevant, as divertor detachment (a condition where pressure is not conserved along the open field lines),[150,151] which comes with high neutral density in the divertor and SOL,[150] is commonly accepted as a requirement for tokamak reactor operation.[151–153] However, it is not immediately clear what operation space will experience similar back transition phenomenology as was observed in these experiments.

5.7 Conclusion

Activity associated with the dithering H-L transition sequence begins when $\omega_{E\times B} > \omega_T$ in the experiments examined, showing that the large initial transients and at least some of the first few type-III ELMs take place when the shear suppression mechanism is still strong. Therefore, the large transients and type-III ELMs probably are not directly related to L-H/H-L transition physics, but rather, are responsible for relaxing the pedestal, which reduces the diamagnetic contribution to $v_{E\times B}$ and weakens the shear suppression mechanism, leading to the H-L transition proper. The transient observed in most H-L back transition sequences is probably driven by the same mechanism as the smaller type-III ELMs in the early part of the dithering transition, as both are synchronous with identical v_p locking behavior of the MPM and a continuum of transient/type-III ELM sizes appears to exist. The amplitude is very sensitive to edge toroidal rotation, which in turn may be controlled by adjusting torque inputs to the plasma. The MPM is a potential indicator of an impending H-L transition in a low powered H-mode, at least for this class of plasma discharge, and its lifetime is often long enough ($\gtrsim$ 100 ms in these DIII-D shots) that a control system might have a realistic chance of acting to avoid an unintentional back transition.

5.8 Acknowledgments

Chapter 5 contains material which has been submitted for publication in Physics of Plasmas. Eldon, David; Boivin, Réjean L.; Chrystal, Colin ; Groebner, Richard J.; McKee, George R. ; Schmitz, Lothar; Tynan, George R. ; Yan, Zheng ; Boedo, Jose A.; Burrell, Keith H.; King, Josh D. ; Kolemen, Egemen; Muscatello, Chris ; Osborne, Thomas H. ; Snyder, Philip B., American Institute of Physics, 2015. The disseration author was the primary investigator and author of this paper.

6 Conclusion

6.1 High Resolution Thomson Scattering Upgrade

Thomson scattering is a critical tokamak diagnostic. The utility of the Thomson scattering system on DIII-D has been greatly improved by the high spatial resolution upgrade, concurrent electronics and laser upgrades, and subsequent dramatic improvements to the calibration and maintenance procedures, as described in chapter 2. Virtually all DIII-D experiments use Thomson scattering data to some extent, making it vitally important that this diagnostic delivers accurate results. This is now the case.

Spatial resolution around the pedestal was increased by $\approx 2\times$ and preexisting systematic errors in temperature measurements, as large as $\approx 30\%$, were identified and then corrected. Routine monitoring of data quality, facilitated by new control room and analysis software, ensures continued accuracy. The physics analysis in this work has benefited greatly from the new and improved Thomson data, with the stability analysis of chapter 4 being especially dependent on profiles returned by the diagnostic.

6.2 Ideal MHD Stability Analysis

The linear ideal MHD code ELITE has been used to test for peeling-ballooning instability just prior to ELM-like events which are commonly observed at the start of back transition sequences. As detailed in chapter 4, this stability

analysis indicates that the plasma is stable to all linear ideal peeling, ballooning, and coupled peeling-ballooning modes of toroidal mode number $n \geq 5$ and that lower n instability is unlikely. This conclusion is supported by differences in penetration depth and scaling with shape of the back transition ELM-candidates and the confirmed type-I ELMs typical of H-mode. These result falsifies the hypothesis that the event common to the start of the H-L back transition sequence is an ideal peeling-ballooning triggered type-I ELM.

6.3 Evolution of E×B Shear and Comparison to Turbulence Decorrelation Rate

Section 5.3 tested the hypothesis that transition sequences start when the peak $E \times B$ shearing rate $\omega_{E\times B}$ drops below the turbulence decorrelation rate ω_T, representing the failure of shear suppression of turbulence in the edge transport barrier. It was found that $\omega_{E\times B}$ regularly remains nearly constant during the ELM-free period prior to the H-L transition sequence and only changes appreciably after the D_α bursts begin. Thus it is inferred that the transient and type-III ELMs are not an intrinsic part of L-H/H-L transition physics but are the result of some instability which is excited by conditions in the pedestal prior to the transition sequence. Relaxation of the pedestal caused by the transients and type-III ELMs leads to reductions in the shearing rate, ultimately terminating H-mode.

6.4 Investigation of the Modulating Pedestal Mode

The Modulating Pedestal Mode (MPM) is a long-lived coherent oscillation that was detected in the pedestal during these experiments. Typical frequency is $\approx 60 - 70$ kHz and wavenumber $k \approx 0.3 - 0.4$ cm^{-1}. A detailed characterization is given in section 5.4. The type-III ELMs and transients associated with the H-L sequences are synchronous with the modulations of the MPM. The mode grows

in amplitude as pedestal temperature decreases and density increases during the ELM-free period between input power reduction and the start of H-L activity. The localization of this mode and its relationship with temperature indicates a resistive instability with ballooning character is at work. The long lifetime (often > 100 ms) of the MPM makes it a candidate for early warning of back transitions in low powered discharges, although it is not yet known what operational space will experience the MPM prior to back transitions beyond the scenario examined in this work.

6.5 Conditions for a "Soft Landing"

Section 5.5 identified a strong relationship between large H-L transients and fast toroidal rotation in the co-current direction at the edge of the plasma: controlling torque inputs to the plasma appears to be a reliable means of suppressing this type of transient. Other potential methods of controlling the transient were explored. Of interest was a sudden increase in the triangularity of the plasma boundary in anticipation of the transient. This technique was designed to reduce peeling-ballooning coupling strength and stabilize the plasma to P-B modes long enough for some other process to initiate the H-L sequence. While ideal P-B instability has been eliminated as a trigger for the transient, the effectiveness of this technique suggests that a resistive cousin of the coupled P-B mode may be involved.

The experiments with rotation control produced not only large transients and small type-III ELMs as the first D_α burst of the transition sequence, but also events of intermediate size. This implies that these phenomena have the same triggering mechanism (consistent with identical MPM behavior before each of them) and that transients are simply the high toroidal rotation limit of the type-III ELMs.

6.6 Summary

Experiments were performed to test for specific triggering mechanisms at the start of the dithering H-L transition sequence. It was found that ideal P-B instability is not the trigger from this class of H-L transition, but that the sequence of events which terminates H-mode does begin when the $E \times B$ shear suppression mechanism is still strong, implying that some instability is triggering the transition by relaxing the pressure pedestal. The relaxation can be abrupt or can occur over the first $\sim 10 - 100$ ms of the dithering H-L transition sequence. The D_α bursts during this early phase of dithering are probably driven by the same instability as the large initial transient, but are smaller because the transient reduces the drive for the instability. The presence of a large, rapid pedestal pressure relaxation at the start of the H-L sequence is observed when edge toroidal rotation in the co-current direction is relatively fast, but may be suppressed by lowering rotation by applying torque counter to the plasma current.

A Notes on Calculations and Programming

A.1 Method of Determining Dominant MPM Parameters: k, f, and v_p

In order to measure the frequency f, wavenumber k, and lab-frame propagation velocity v_p of the mode in question, $\tilde{I}/I \propto \tilde{n}/n$ was computed for each chord in a column. Time delay cross correlation functions (the built in IDL function required correction; see appendix A.3) were calculated for each unique chord pair, excluding correlations of chords with themselves. The result, $C(t_{delay}, \Delta Z)$, where t_{delay} is the variable lag time and ΔZ is the spatial separation of the chords, was fit to

$$\begin{aligned} C(t_{delay}, \Delta Z) =& C_{max} \cos\left(2\pi f t_{delay} - k\Delta Z\right) \\ & \times \exp\left[-|t_{delay}/\tau_c|\right] \exp\left[-|\Delta Z/\lambda_c|\right] \end{aligned} \tag{A.1}$$

where C_{max} is the peak cross correlation, τ_c is the correlation time and λ_c is the correlation length. The IDL MPFIT[154] implementation of the Levenberg-Marquardt algorithm for least squares minimization[69] was used. An example of this analysis is shown in figure A.1.

C_{max} may differ from 1 as random noise will prevent two separate chords from agreeing perfectly, even at arbitrarily close spacing. The value of τ_c obtained from the fit includes effects of decorrelation of the entire spectrum, not just the MPM, as no frequency filtering was performed in this analysis. The correlation length λ_c is much longer than the physical array of BES chords and is probably

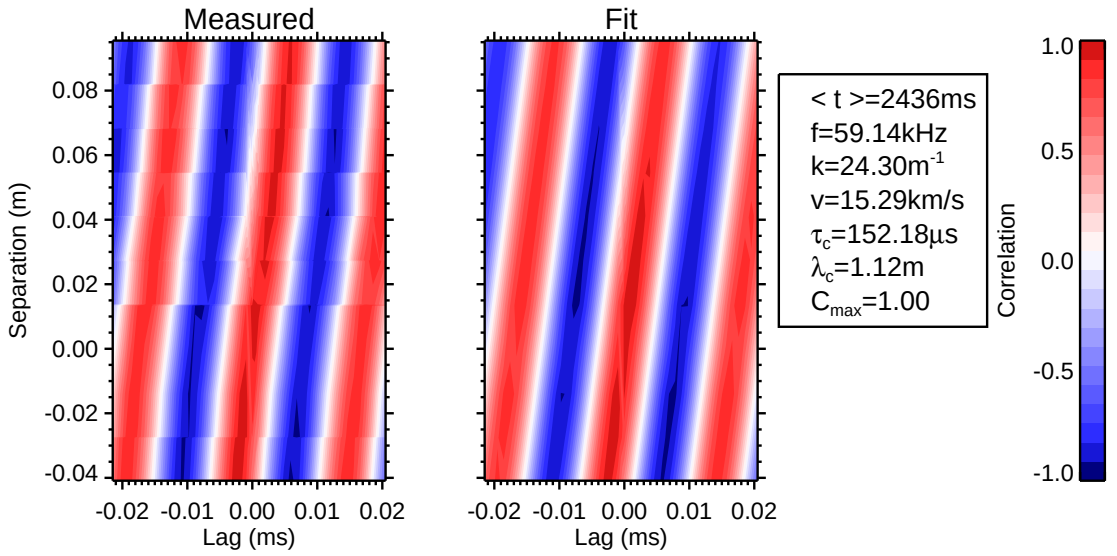

Figure A.1: Time delayed cross correlation functions from column 6 BES data (left) from an example time window centered around 2436ms in shot 154754 are shown with a fit to $C_{max}\cos\left(2\pi f t_{lag} - k\Delta Z\right)\exp\left[-|t_{lag}/\tau_c|\right]\exp\left[-|\Delta Z/\lambda_c|\right]$ (right).

not measured accurately beyond the statement that $\lambda_c \gg \max(\Delta Z) = 9.6\,\text{cm}$. Similarly, τ_c is often much longer than the time window chosen. This analysis was repeated for many sequential overlapping time windows to build a time history of $v_p = 2\pi f/k$ and other quantities. The data were not frequency filtered before this analysis because the MPM strongly dominates the fit in Eq. A.1 and the frequency changes during the slowdown and the MPM could escape the filtering window. A windowed Fourier transform was calculated and from this the MPM amplitude at f was found at each time-slice. The result is qualitatively the same as averaging amplitude over a frequency range containing the MPM and its sidebands, such as taking the average amplitude in $40 < f < 80\,\text{kHz}$ for each slice. The resulting histories are shown in Fig. 5.12 for a short time window just before the start of transition activity.

Some of the BES chords experience clipping or saturation during the hard back transition transients, but as the purpose of this analysis is to track the motion of "blobs", this should not be a serious problem as the photodiodes used by BES[88] do not appear to suffer long lasting systematic changes to their behavior after a saturation/clipping event. In this case, it is clear from Fig. 5.11 and videos of BES

fast intensity vs. R-Z that the v_p lock is not an artifact of clipping. Locking also occurs before the first small D_α spike in soft H-L sequences and in these cases, clipping is uncommon (because the change in density is not as great), and still the behavior is the same.

A.2 Local Wavenumber Anaysis to Determine the Dispersion Relation of the MPM

Local wavenumber k_{ij} may be calculated using the two point technique:[155]

$$\begin{aligned} G_{ij}(f) &= F_i^* F_j \\ \phi_{ij}(f) &= \text{atan}\left(\frac{Im(G_{ij})}{Re(G_{ij})}\right) \\ k_{ij}(f) &= \frac{\phi_{ij}(f)}{Z_i - Z_j} \end{aligned} \tag{A.2}$$

where F_i^* is the complex conjugate of the Fourier transform of the normalized $(\tilde{n}/n)$ signal from chord i and $-\pi < \phi < \pi$, G_{ij} is the cross-power spectrum between chords i and j, ϕ_{ij} is the corresponding phase delay between the two chords, and then the local wavenumber k_{ij} is as given. This operation is repeated on all of the unique chord pairs in a column, excluding $i = j$. A dispersion diagram can be made from the histogram of k and f values. In general, BES is not equally sensitive to all wavenumbers and a spatial transfer function can be used to correct the k spectrum. However, the transfer function is essentially flat[87] for $k_z < 1\ \text{cm}^{-1}$, so no correction is needed when studying the MPM.

Figure 5.14 shows the results of the local wavenumber analysis.

A.3 Correction to `IDL`'s Native Time Delayed Cross Correlation Function

The built in function `C_CORRELATE` in IDL Version 8.1 is not properly normalized and a corrected version was developed and used. `C_CORRELATE` calculates

the correlation between two input arrays A and B and adds relative time lag by shifting one array relative to the other as follows:

$$P_{AB}(L) = \frac{\sum_{k=0}^{N-L-1} \left(A_k - \bar{A}\right)\left(B_{k+L} - \bar{B}\right)}{\sqrt{\left[\sum_{k=0}^{N-1} \left(A_k - \bar{A}\right)^2\right]\left[\sum_{k=0}^{N-1} \left(B_k - \bar{B}\right)^2\right]}} \tag{A.3}$$

where L is the number of array elements to shift by and the form given is valid for $L \geq 0$. For $L < 0$, the subscript of A instead of B in the numerator is modified using L. It can be seen that the number of array elements used to calculate the numerator is not the same as the number of elements used to calculate the denominator unless $L = 0$. This means that the time delayed correlation between two perfect sinusoids will have an envelope peaking at $L = 0$ and decaying approximately linearly such that the correlation will approach 0 as $L \to N$. Of course, $L \approx N$ is not advisable for this calculation (number of samples decreases to 0 as L approaches N), but the error is apparent for reasonable choices of L/N.

To perform the calculations needed for this work, `C_CORRELATE` was modified such that the sums in the denominator are over the same range of array elements as the numerator. Thus, the corrected time delayed cross correlation function for two sinusoids with the same frequency is another sinusoid with constant amplitude, rather than approximately linearly decreasing amplitude away from 0 delay. The flaw in `C_CORRELATE` as well as the correction are demonstrated in figure A.2.

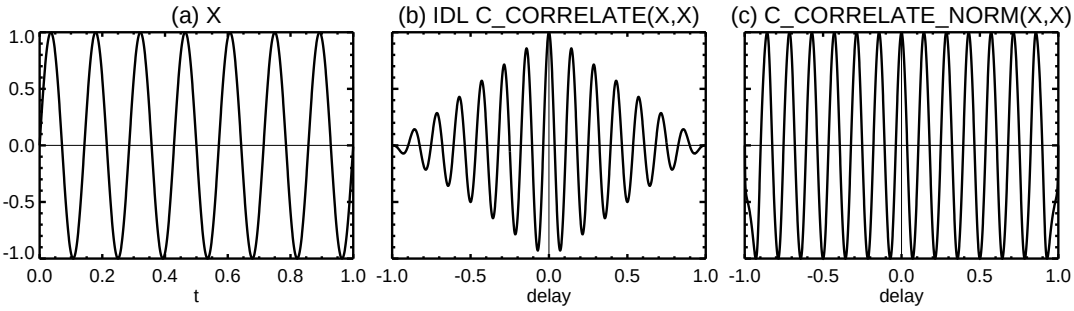

Figure A.2: Correction of the time delay cross correlation function. (a) A test signal $X = \sin(\omega t)$, (b) time delayed cross correlation function of X with itself using the built in IDL function and (c) the cross correlation of X with itself using the corrected version. $-(N-2) < L < (N-2)$ and $N = 1001$. There should be no decorrelation with time of a two pure tones, so (b) is obviously wrong and the correction in (c) is required unless $L \ll N$.

A.4 Modification to IDL's 2D Histogram to Better Handle Floating Point Numbers

The HIST_2D function provided with IDL works with floating point numbers, but appears to be designed with integers in mind. This function defines histogram bins such that the last bin starts at the maximum value in the input array. For a set of integers like [0,1,2,3], this is okay. For floats, this behavior typically results in a mostly empty bin at the end. This breaks the natural symmetry of the dispersion plot (although only the positive frequency half is shown in the figures in this work, the full plot is symmetric) and puts awkward stripes at the edges. HIST_2D also has the limitation that it does not return any information about the bins it has chosen, which can be confusing given its choices about binning.

To overcome these issues, a wrapper for HIST_2D was created and used to generate dispersion plots in section 5.4.3. PLOT_HIST2D_B accepts user requests for histogram binning then calls HIST_2D with settings such that there are extra bins outside of the desired range. The extra bins are sacrificial and will be the ones which are mostly empty. The output is cropped by copying counts from the nearly empty bins at the edges into their neighbors and removing the edge bins. If the combination of input data and bin request produce bins which are completely

empty, HIST_2D will suppress these and return a smaller array. PLOT_HIST2D_B has logic to inflate undersized arrays to the expected dimensions. PLOT_HIST2D_B returns the histogram and bin definitions, produces a dispersion plot, and provides optional secondary plots and analysis features.

A.5 Using the Distribution of χ^2 Values to Detect Calibration Errors

As a test of calibration quality of the Thomson scattering diagnostic, the following statistical test is integrated into the Thomson Scattering Data Viewer (TSDV) program, which is described in section 2.3.3.

For any least squares fit, the distribution of reduced χ^2 values will follow a predictable trend if the model used in the fit is a good representation of the reality being measured. That is: if the calibration is valid, a histogram of reduced χ^2 values will follow a curve given by:

$$prob(\chi^2, K) = \frac{(\chi^2)^{K/2-1}}{2^{K/2}\Gamma(K/2)} e^{-\chi^2/2} \tag{A.4}$$

provided that the number of degrees of freedom K is known. K = the number of samples N - the number of fit parameters P if the model is linear and all of the basis functions are linearly independent. If the model is nonlinear or the basis functions are not linearly indpendent, K can be anywhere from $N - P$ to $N - 1$. The fit parameters in use are temperature and density and the data are the signals from a set of detectors.

The expected signal is defined by equations 2.1, 2.2, 2.3, 2.6 and 2.5 found in sections 2.2.1 and 2.2.2, but the basic dependencies on temperature T_e and density n_e can be understood by

$$signal \sim n_e \times \frac{\mathrm{Exp}\,(-const/T_e)}{\mathrm{K}_2(const/T_e)} \tag{A.5}$$

As seen in equation A.5 for scattered signal, the model is not a linear combination of separate basis functions for temperature and density, so $K \neq N - P$.[156] However, histograms of reduced χ^2 were compared to the probability function

given in equation A.4 (with modification to be vs. reduced χ^2) anyway and found to agree extremely well for chords which appeared to be well behaved, and very poorly for chords which were experiencing obvious calibration problems or hardware malfunctions. From this it is inferred that the Thomson scattering model can be linearized around minima in χ^2 in temperature and density well enough that one may approximate $K \approx N - P$ and use this statistical test to help detect problems.

TSDV's built in χ^2 histogram quickly performs this test for all of the view-chords simultaneously, using an arbitrarily selectable subset of time-slices within the shot up to and including the entire data set. Specific chords may be flagged and these are then marked on the histogram output and on the other plots, allowing the user to easily understand the correlation between systematic errors in the profiles and bad χ^2 statistics. As this test is not perfect due to the nonlinearity of the TS signal equation, only relatively severe errors are detected. As of 2014, calibration quality has improved to the point where some of the worst systematic errors are too subtle to be detected by this test, and are best characterized by inspection of time averaged profiles from steady plasmas or from the look up table comparison plot. It is still useful as a means of checking for new problems, such as hardware failures. Newly failed hardware shows up prominently on this test. Tools like this which provide detailed quantification of system performance have provided significant motivation for improving the calibration quality as well as guidance as to what improvements are needed.

B Corrections to Account for Diagnostic Alignment Errors

B.1 Alignment Issues When Comparing Thomson scattering to BES

Data from BES and TS are mapped to ψ_N using a simple equilibrium reconstruction (JT EFIT).[71] However, this mapping suffers from uncertainties in the positions of diagnostic chords, errors in the reconstruction due to 3D error fields, and finite lifetime of the excitation state of injected neutral atoms. The data in Fig. 5.15 have been corrected for these alignment issues as follows: The foot of the T_e pedestal, as determined by a tanh fit, is assumed to be at the separatrix and the Thomson profiles [Fig. 5.15(b-c)] are shifted outward by about $2\%\psi_N$ to enforce this. The BES data [Fig. 5.15(a)] are shifted outward as well on the basis that excited beam ions have a finite lifetime and the delay between excitation and emission translates to an inward shift in position. The magnitude of this shift is expected to be about 0.66 cm ($\approx$ 3 ns lifetime $\times$ 2.2 mm/ns for 50 kV beam accelerating voltage),[87] which translates to about 2% in ψ_N. Absolute error in the measurements of the BES array's position[82] could be ≈ 5 mm (because of the way the chords are secured in a common mounting bracket,[157] uncertainty in the relative positions between chords should be negligible). The corrected alignment is consistent with the mode amplitude peaking at $\psi_N \approx 0.96 - 0.97$, which is located in the steep gradient region or just at the top of the pedestal.

Bibliography

[1] J. L. Luxon, "A design retrospective of the DIII-D tokamak", Nucl. Fusion **42**, 614 (2002), DOI:10.1088/0029-5515/42/5/513.

[2] J. Wesson, *Tokamaks* (Oxford University Press, New York, 1987), pp. 4, 60-65, 94-95, 137-145, 154-157.

[3] L. A. Artsimovich, "Tokamak devices", Nucl. Fusion **12**, 215 (1972), DOI:10.1088/0029-5515/12/2/012.

[4] R. F. Post, T. K. Fowler, J. Killeen, and A. A. Mirin, "Concept for a high-power-density mirror fusion reactor", Phys. Rev. Lett. **31**, 280 (1973), DOI:10.1103/PhysRevLett.31.280.

[5] L. Spitzer, "The stellarator concept", Phys. Fluids **1**, 253 (1958), DOI:10.1063/1.1705883.

[6] A. Y. Aydemir, "Pfirsch-Schlüter current-driven edge electric fields and their effect on the L-H transition power threshold", Nucl. Fusion **52**, 063026 (2012), DOI:10.1088/0029-5515/52/6/063026.

[7] D. N. Hill and the DIII-D Team, "DIII-D research towards resolving key issues for ITER and steady-state tokamaks", Nucl. Fusion **53**, 104001 (2013), DOI:10.1088/0029-5515/53/10/104001.

[8] E. J. Strait, "Magnetic diagnostic system of the DIII-D tokamak", Rev. Sci. Instrum. **77**, 023502 (2006), DOI:10.1063/1.1266493.

[9] F. Wagner, G. Becker, K. Behringer, D. Campbell, A. Eberhagen, W. Engelhardt, G. Fussmann, O. Gehre, J. Gernhardt, G. v. Gierke, G. Haas, M. Huang, F. Karger, M. Keilhacker, O. Klüber, M. Kornherr, K. Lackner, G. Lisitano, G. G. Lister, H. M. Mayer, D. Meisel, E. R. Müller, H. Murmann, H. Niedermeyer, W. Poschenrieder, H. Rapp, H. Röhr, F. Schneider, G. Siller, E. Speth, A. Stäbler, K. H. Steuer, G. Venus, O. Vollmer, and Z. Yü, "Regime of improved confinement and high beta in neutral-beam-heated-divertor discharges of the ASDEX tokamak", Phys. Rev. Lett. **49**, 1408 (1982), DOI:10.1103/PhysRevLett.49.1408.

[10] K. H. Burrell, "Summary of experimental progress and suggestions for future work (H mode confinement)", Plasma Phys. Control. Fusion **36**, A291 (1994), DOI:10.1088/0741-3335/36/7A/043.

[11] E. A. Frieman, J. M. Greene, J. L. Johnson, and K. E. Weimer, "Toroidal effects on magnetohydrodynamic modes in tokamaks", Phys. Fluids **16**, 1108 (1973), DOI:10.1063/1.1694474.

[12] O. Sauter, C. Angioni, and Y. R. Lin-Liu, "Neoclassical conductivity and bootstrap current formulas for general axisymmetric equilibria and arbitrary collisionality regime", Phys. Plasmas **6**, 2834 (1999), ***See Sauter et al.[13] for erratum***, DOI:10.1063/1.873240.

[13] O. Sauter, C. Angioni, and Y. R. Lin-Liu, "Erratum: 'neoclassical conductivity and bootstrap current formulas for general axisymmetric equilibria and arbitrary collisionality regime' [phys. plasmas 6, 2834 (1999)]", Phys. Plasmas **9**, 5140 (2002), ***Erratum for Sauter et al.[12]***, DOI:10.1063/1.1517052.

[14] P. B. Snyder, H. R. Wilson, J. R. Ferron, L. L. Lao, A. W. Leonard, T. H. Osborne, A. D. Turnbull, D. Mossessian, M. Murakami, and X. Q. Xu, "Edge localized modes and the pedestal: A model based on coupled peeling-ballooning modes", Phys. Plasmas **9**, 2037 (2002), DOI:10.1063/1.1449463.

[15] H. R. Wilson, J. W. Connor, A. R. Field, S. J. Fielding, R. L. Miller, L. L. Lao, J. R. Ferron, and A. D. Turnbull, "Ideal magnetohydrodynamic stability of the tokamak high-confinement-mode edge region", Phys. Plasmas **6**, 1925 (1999), DOI:10.1063/1.873492.

[16] J. Reader, "Reference wavelengths for strong lines of atomic hydrogen and deuterium", Applied Spectroscopy **58**, 1469 (2004).

[17] T. H. Osborne, J. R. Ferron, R. J. Groebner, L. L. Lao, A. W. Leonard, M. A. Mahdavi, R. Maingi, R. L. Miller, A. D. Turnbull, M. Wade, and J. Watkins, "The effect of plasma shape on H-mode pedestal characteristics on DIII-D", Plasma Phys. Control. Fusion **42**, A175 (2000), DOI:10.1088/0741-3335/42/5A/319.

[18] G. Federici, P. Andrew, P. Barabaschi, J. Brooks, R. Doerner, A. Geier, A. Herrmann, G. Janeschitz, K. Krieger, A. Kukushkin, A. Loarte, R. Neu, G. Saibene, M. Shimada, G. Strohmayer, and M. Sugihara, "Key ITER plasma edge and plasma-material interaction issues", J. Nucl. Materials **313**, 11 (2003), DOI:10.1016/S0022-3115(02)01327-2.

[19] A. Loarte, M. Sugihara, M. Shimada, A. Kukushkin, D. Campbell, M. Pick, C. Lowry, M. Merola, R. A. Pitts, V. Riccardo, G. Arnoux, W. Fundamenski, G. F. Matthews, S. Pinches, A. Kirk, E. Nardon, T. Eich, A. Herrmann,

G. Pautasso, A. Kallenbach, G. Saibene, G. Federici, R. Sartori, G. Counsell, A. Portone, M. Cavinato, M. Lehnen, A. Huber, V. Philipps, D. Reiter, V. Kotov, R. Koslowski, G. Maddaluno, B. Lipschultz, D. Whyte, B. LaBombard, R. Granetz, A. W. Leonard, M. Fenstermacher, E. Hollman, P. C. Stangeby, M. Kobayashi, R. Albanese, G. Ambrosino, M. Ariola, G. de Tommasi, J. Gunn, M. Becoulet, L. Colas, M. Goniche, E. Faudot, and D. Milanesio, "Power and particle fluxes at the plasma edge of ITER: Specifications and physics basis", Proceedings of the 22nd IAEA Fusion Energy Conference in Genevea (2008).

[20] A. Loarte, G. Huijsmans, S. Futatani, L. R. Baylor, T. E. Evans, D. M. Orlov, O. Schmitz, M. Becoulet, P. Cahyna, Y. Gribov, A. Kavin, A. S. Naik, D. J. Campbell, T. Casper, E. Daly, H. Frerichs, A. Kischner, R. Laengner, S. Lisgo, R. A. Pitts, G. Saibene, and A. Wingen, "Progress on the application of ELM control schemes to ITER scenarios from the non-active phase to DT operation", Nucl. Fusion **54**, 033007 (2014), DOI:10.1088/0029-5515/54/3/033007.

[21] F. Wagner, "A quarter-century of H-mode studies", Plasma Phys. Control. Fusion **49**, B1 (2007), DOI:10.1088/0741-3335/49/12B/S01.

[22] R. Hawryluk, D. Campbell, G. Janeschitz, P. Thomas, R. Albanese, R. Ambrosino, C. Bachmann, L. Baylor, M. Becoulet, I. Benfatto, J. Bialek, A. Boozer, A. Brooks, R. Budny, T. Casper, M. Cavinato, J.-J. Cordier, V. Chuyanov, E. Doyle, T. Evans, G. Federici, M. Fenstermacher, H. Fujieda, K. G'al, A. Garofalo, L. Garzotti, D. Gates, Y. Gribov, P. Heitzenroeder, T. Hender, N. Holtkamp, D. Humphreys, I. Hutchinson, K. Ioki, J. Johner, G. Johnson, Y. Kamada, A. Kavin, C. Kessel, R. Khayrutdinov, G. Kramer, A. Kukushkin, K. Lackner, I. Landman, P. Lang, Y. Liang, J. Linke, B. Lipschultz, A. Loarte, G. Loesser, C. Lowry, T. Luce, V. Lukash, S. Maruyama, M. Mattei, J. Menard, M. Merola, A. Mineev, N. Mitchell, E. Nardon, R. Nazikian, B. Nelson, C. Neumeyer, J.-K. Park, R. Pearce, R. Pitts, A. Polevoi, A. Portone, M. Okabayashi, P. Rebut, V. Riccardo, J. Roth, S. Sabbagh, G. Saibene, G. Sannazzaro, M. Schaffer, M. Shimada, A. Sen, A. Sips, C. Skinner, P. Snyder, R. Stambaugh, E. Strait, M. Sugihara, E. Tsitrone, J. Urano, M. Valovic, M. Wade, J. Wesley, R. White, D. Whyte, S. Wu, M. Wykes, and L. Zakharov, "Principal physics developments evaluated in the ITER design review", Nucl. Fusion **49**, 065012 (2009), DOI:10.1088/0029-5515/49/6/065012.

[23] P. Snyder, N. Aiba, M. Beurskens, R. Groebner, L. Horton, A. Hubbard, J. Hughes, G. Huysmans, Y. Kamada, A. Kirk, C. Konz, A. Leonard, J. Lnnroth, C. Maggi, R. Maingi, T. Osborne, N. Oyama, A. Pankin, S. Saarelma, G. Saibene, J. Terry, H. Urano, and H. Wilson, "Pedestal stability comparison and ITER pedestal prediction", Nucl. Fusion **49**, 085035 (2009), DOI:10.1088/0029-5515/49/8/085035.

[24] G. R. Tynan, A. Fujisawa, and G. McKee, "A review of experimental drift turbulence studies", Plasma Phys. Control. Fusion **51**, 113001 (2009), DOI:10.1088/0741-3335/51/11/113001.

[25] K. H. Burrell, P. Gohil, R. J. Groebner, D. H. Kaplan, J. I. Robinson, and W. M. Solomon, "Improved charge-coupled device detectors for high-speed, charge exchange spectrscopy studies on the DIII-D tokamak", Rev. Sci. Instrum. **75**, 3455 (2004), DOI:10.1063/1.1787949.

[26] K. H. Burrell, "Effects of E×B velocity shear and magnetic shear on turbulence and transport in magnetic confinement devices", Phys. Plasmas **4**, 1499 (1997), DOI:10.1063/1.872367.

[27] G. R. McKee, R. J. Fonk, D. K. Gupta, D. J. Schlossberg, M. W. Shafer, R. L. Boivin, and W. Solomon, "Plasma turbulence imaging via beam emission spectroscopy in the core of the DIII-D tokamak", Plasma and Fusion Research **2**, S1025 (2007), DOI:10.1585/pfr.2.S1025.

[28] H. Biglari, P. H. Diamond, and P. W. Terry, "Influence of sheared poloidal rotation on edge turbulence", Phys. Fluids. B **2**, 1 (1990), DOI:10.1063/1.859529.

[29] T. S. Hahm, "Rotation shear induced fluctuation decorrelation in a toroidal plasma", Phys. Plasmas **1**, 2940 (1994), DOI:10.1063/1.870534.

[30] T. S. Hahm and K. H. Burrell, "Flow shear induced fluctuation sppression in finite aspect ratio shaped tokamak plasma", Phys. Plasmas **2**, 1648 (1995), DOI:10.1063/1.871313.

[31] T. S. Hahm and K. H. Burrell, "ExB flow shear effects on radial correlation length of turbulence and gyroradius scaling of confinement", Phys. Plasmas **3**, 427 (1996), DOI:10.1063/1.871814.

[32] O. D. Gürcan, "Effect of sheared flow on the growth rate and turbulence decorrelation", Phys. Rev. Lett. **109**, 155006 (2012), DOI:10.1103/PhysRevLett.109.155006.

[33] G. R. Tynan, M. Xu, P. H. Diamond, J. A. Boedo, I. Cziegler, N. Fedorczak, P. Manz, K. Miki, S. Thakur, L. Schmitz, L. Zeng, E. Doyle, G. M. McKee, Z. Yan, G. S. Xu, B. N. Wan, H. Q. Wang, H. Y. Guo, J. Dong, K. Zhao, J. Cheng, W. Y. Hong, and L. W. Yan, "Turbulent-driven low-frequency sheared E×B flows as the trigger for the H-mode transition", Nucl. Fusion **53**, 073053 (2013), DOI:10.1088/0029-5515/53/7/073053.

[34] I. Cziegler, G. R. Tynan, P. H. Diamond, A. E. Hubbard, J. W. Hughes, J. Irby, and J. L. Terry, "Zonal flow production in the L-H transition in Alcator C-Mod", Plasma Phys. Control. Fusion **56**, 075013 (2014), DOI:10.1088/0741-3335/56/7/075013.

[35] E.-J. Kim and P. H. Diamond, "Mean shear flows, zonal flows, and generalized kelvin-helmholtz modes in drift wave turbulence: A minimal model for L→H transition", Phys. Plasmas **10**, 1698 (2003), DOI:10.1063/1.1559006.

[36] E.-J. Kim and P. H. Diamond, "Zonal flows and transient dynamics of the L-H transition", Phys. Rev. Lett. **90**, 185006 (2003), DOI:10.1103/PhysRevLett.90.185006.

[37] K. Miki, P. H. Diamond, Ö. D. Gürcan, G. R. Tynan, T. Estrada, L. Schmitz, and G. S. Xu, "Spatio-temporal evolution of the L-I-H transition", Phys. Plasmas **20**, 062304 (2012), DOI:10.1063/1.4753931.

[38] K. Miki, P. H. Diamond, L. Schmitz, D. C. McDonald, T. Estrada, Ö. D. Gürcan, and G. R. Tynan, "Spatio-temporal evolution of the H-L back transition", Phys. Plasmas **20**, 062304 (2013), DOI:10.1063/1.4812555.

[39] S. B. Korsholm, P. K. Michelsen, V. Naulin, J. Juul Rasussen, L. Garcia, B. A. Carrerass, and V. E. Lynch, "Reynolds stress and shear flow generation", Plasma Phys. Control. Fusion **43**, 1377 (2001), DOI:10.1088/0741-3335/43/10/308.

[40] P. H. Diamond and Y. B. Kim, "Theory of mean poloidal flow generation by turbulence", Phys. Fluids B **3**, 1626 (1991), DOI:10.1063/1.859681.

[41] L. Schmitz, L. Zeng, T. L. Rhodes, J. C. Hillesheim, E. J. Doyle, R. J. Groebner, W. A. Peebles, K. H. Burrell, and G. Wang, "Role of zonal flow predator-prey oscillations in triggering the transition to H-Mode confinement", Phys. Rev. Lett. **108**, 155002 (2012), DOI:10.1103/PhysRevLett.108.155002.

[42] L. Schmitz, L. Zeng, T. L. Rhodes, J. C. Hillesheim, W. A. Peebles, R. J. Groebner, K. H. Burrell, G. R. McKee, Z. Yan, G. R. Tynan, P. H. Diamond, J. A. Boedo, E. J. Doyle, B. A. Grierson, C. Chrystal, M. E. Austin, W. M. Solomon, and G. Wang, "The role of zonal flows and predator-prey oscillations in triggering the formation of edge and core transport barriers", Nucl. Fusion **54**, 073012 (2014), DOI:10.1088/0029-5515/54/7/073012.

[43] Z. Yan, G. R. McKee, R. Fonck, P. Gohil, R. J. Groebner, and T. H. Osborne, "Observation of the L-H confinement bifurcation triggered by a turbulence-driven shear flow in a tokamak plasma", Phys. Rev. Lett. **112**, 125002 (2014), DOI:10.1103/PhysRevLett.112.125002.

[44] A. Loarte, F. Koechl, M. J. Leyland, A. Polevoi, M. Beurskens, V. Parail, I. Nunes, G. R. Saibene, R. I. A. Satori, and JET EFDA contributors, "Evolution of plasma parameters in the termination phase of high confinement H-modes at JET and implications for ITER", Nucl. Fusion **54**, 123014 (2014), DOI:10.1088/0029-5515/54/12/123014.

[45] R. Sartori, G. Saibene, L. D. Horton, M. Becoulet, R. Budny, D. Borba, A. Chankin, G. D. Conway, G. Cordey, D. McDonald, K. Guenther, M. G. von Hellermann, Y. Igithkanov, A. Loarte, P. J. Lomas, O. Pogutse, and J. Rapp, "Study of type III ELMs in JET", Plasma Phys. Control. Fusion **46**, 723 (2004), DOI:10.1088/0741-3335/46/5/002.

[46] A. D. Turnbull, L. L. Lao, T. H. Osborne, O. Sauter, E. J. Strait, T. S. Taylor, M. S. Chu, J. R. Ferron, C. M. Greenfield, A. W. Leonard, R. L. Miller, P. B. Snyder, H. R. Wilson, and H. Zohm, "Edge localized modes in DIII-D high performance discharges", Plasma Phys. Control. Fusion **45**, 1845 (2003), DOI:10.1088/0741-3335/45/10/002.

[47] H. Zohm, F. Wagner, M. Endler, J. Gernhardt, E. Holzhauer, W. Kerner, and V. Mertens, "Studies of edge localized modes on ASDEX", Nucl. Fusion **32**, 489 (1992), DOI:10.1088/0029-5515/32/3/I11.

[48] G. S. Xu, H. Q. Wang, M. Xu, B. N. Wan, H. Y. Guo, P. H. Diamond, G. R. Tynan, R. Chen, N. Yan, D. F. Kong, H. L. Zhao, A. D. Liu, T. Lan, V. Naulin, A. H. Nielsen, J. J. Rasmussen, K. Miki, P. Manz, W. Zhang, L. Wang, L. M. Shao, S. C. Liu, L. Chen, S. Y. Ding, N. Zhao, Y. L. Li, Y. L. Liu, G. H. Hu, X. Q. Wu, and X. Z. Gong, "Dynamics of L-H transition and I-phase in EAST", Nucl. Fusion **54**, 103002 (2014), DOI:10.1088/0029-5515/54/10/103002.

[49] H. R. Wilson, P. B. Snyder, G. T. A. Huysmans, and R. L. Miller, "Numerical studies of edge localized instabilities in tokamaks", Phys. Plasmas **9**, 1277 (2002), DOI:10.1063/1.1459058.

[50] P. B. Snyder, T. H. Osborne, K. H. Burrell, R. J. Groebner, A. W. Leonard, R. Nazikian, D. M. Orlov, O. Schmitz, M. R. Wade, and H. R. Wilson, "The EPED pedestal mode and edge localized mode-suppressed regimes: studies of quiescent H-mode and development of a model for edge localized mode suppression via resonant magnetic perturbations", Phys. of Plasmas **19**, 056115 (2012), DOI:10.1063/1.3699623.

[51] D. Eldon, B. D. Bray, T. M. Deterly, C. Liu, M. Watkins, R. J. Groebner, A. W. Leonard, T. H. Osborne, P. B. Snyder, R. L. Boivin, and G. R. Tynan, "Initial results of the high resolution edge Thomson scattering upgrade at DIII-D", Rev. Sci. Instrum. **83**, 10E343 (2012), DOI:10.1063/1.4738656.

[52] D. Eldon, B. D. Bray, D. M. Ponce, A. J. Chavez, T. M. Deterly, R. J. Groebner, C. Liu, T. H. Osborne, and P. B. Snyder. "High resolution pedestal Thomson scattering system at DIII-D", Poster presented at the 52nd meeting of the APS DPP in Chicago, IL (2010).

[53] D. Eldon, B. D. Bray, T. M. Deterly, C. Liu, D. M. P. M. Watkins, R. J. Groebner, A. W. Leonard, T. H. Osborne, P. B. Snyder, R. L. Boivin, and

G. R. Tynan. "Initial results of the high resolution edge Thomson scattering upgrade at DIII-D", Poster presented at the 13th H-mode Workshop in Oxford, United Kingdom (2011).

[54] D. Eldon, B. D. Bray, T. M. Deterly, C. Liu, M. Watkins, R. J. Groebner, A. W. Leonard, T. H. Osborne, P. B. Snyder, R. L. Boivin, and G. R. Tynan. "Initial results of the high resolution edge Thomson scattering upgrade at DIII-D", Poster presented at the 19th topical conference on High-Temperature Plasma Diagnostics in Montery, CA (2012).

[55] D. Eldon, G. R. Tynan, R. J. Groebern, T. H. Osborne, B. D. Bray, R. L. Boivin, and R. Nazikian. "Evaluating pedestal gradients and scale lengths without functional fits in order to test for non-diffusive transport processes", Poster presented at the 54th meeting of the APS DPP in Providence, RI (2012).

[56] D. Eldon, A. G. McLean, T. N. Carlstrom, C. Liu, M. Watkins, B. D. Bray, E. Kolemen, R. J. Groebner, T. H. Osborne, P. B. Snyder, R. L. Boivin, and G. R. Tynan. "Maintaining, upgrading, and expanding the role of Thomson scattering at DIII-D", Invited talk presented at the 16th international symposium on Laser-Aided Plasma Diagnostics in Madison, WI (2013).

[57] T. M. Deterly, B. D. Bray, C. L. Hsieh, J. A. Kulchar, C. Liu, and D. M. Ponce, "The design, implementation, and preliminary results of a new photodetector for the DIII-D Thomson scattering diagnostic", Plasma Science, IEEE Transactions **38**, 1699 (2010), DOI:10.1109/TPS.2010.2049587.

[58] D. M. Ponce-Marquez, B. D. Bray, T. M. Deterly, C. Liu, and D. Eldon, "Thomson scattering diagnostic upgraded on DIII-D", Rev. Sci. Instrum. **81**, 10D525 (2010), DOI:10.1063/1.3495759.

[59] R. E. Stockdale, T. N. Carlstrom, C. L. Hsieh, and C. C. Makariou, "Progress on the multipulse Thomson scattering diagnostic on DIII-D", Rev. Sci. Instrum. **66**, 490 (1995), DOI:10.1063/10.1063/1.1146326.

[60] P. K. Trost, T. N. Carlstrom, J. C. DeBoo, C. M. Greenfield, C. L. Hsieh, and R. T. Snider, "A multilaser system for a fast sampling Thomson scattering diagnostic", Rev. Sci. Instrum. **61**, 2864 (1990), DOI:10.1063/1.1141808.

[61] V. A. Zhuravlev and G. D. Petrov, "Scattering of radiation by finite volumes of relativistic plasma streams", Sov. J. Plasma Phys. **5**, 3 (1979).

[62] O. Naito, H. Yoshida, and T. Matoba, "Analytic formula for fully relativistic Thomson scattering spectrum", Phys. Fluids B **5**, 4256 (1993), DOI:10.1063/1.860593.

[63] A. C. Selden, "Simple analytic form of the relativistic Thomson scattering spectrum", Physics Letters A **79**, 405 (1980), DOI:10.1016/0375-9601(80)90276-5.

[64] J. Sheffield, "The incoherent scattering of radiation from a high temperature plasma", Plasma Physics **14**, 783 (1972), DOI:10.1088/0032-1028/14/8/003.

[65] T. N. Carlstrom, G. L. Campbell, J. C. DeBoo, R. Evanko, J. Evans, C. M. Greenfield, J. Haskovec, C. L. Hsieh, E. McKee, R. T. Snider, R. Stockdale, P. K. Trost, and M. P. Thomas, "Design and operation of the multipulse Thomson scattering diagnostic on DIII-D (invited)", Rev. Sci. Instrum. **63**, 4901 (1992), DOI:10.1063/1.1143545.

[66] J. E. Geusic, H. M. Marcos, and L. G. Van Uitert, "Laser oscillations in Nd-doped yttrium aluminum, yttrium gallium and gadolinium garnets", Appl. Phys. Lett. **4**, 182 (1964), DOI:10.1063/1.1753928.

[67] T. N. Carlstrom, J. C. DeBoo, R. Evanko, C. M. Greenfield, C. L. Hsieh, R. T. Snider, and P. Trost, "A compact, low cost, seven channel polychromator for Thomson scattering measurements", Rev. Sci. Instrum. **61**, 2858 (1990), DOI:10.1063/1.1141806.

[68] C. L. Hsieh, J. Haskovec, T. N. Carlstrom, J. C. DeBoo, C. M. Greenfield, R. T. Snider, and P. Trost, "Silicon avalanche photodiode detector circuit for Nd:YAG laser scattering", Rev. Sci. Instrum. **61**, 2855 (1990), DOI:10.1063/1.1141805.

[69] D. W. Marquardt, "An algorithm for least-squares estimation of nonlinear parameters", J. Soc. Ind. Appl. Math. **11**, 431 (1963).

[70] M. A. Van Zeeland, J. H. Yu, M. S. Chu, K. H. Burrell, R. J. La Haye, T. C. Luce, R. Nazikian, W. M. Solomon, and W. P. West, "Tearing mode structure in the DIII-D tokamak through spectrall filtered fast visible bremsstrahlung imaging", Nucl. Fusion **48**, 092002 (2008), DOI:10.1088/0029-5515/48/9/092002.

[71] L. L. Lao, H. S. John, R. D. Stambauh, A. G. Kellman, and W. Pfeiffer, "Reconstruction of current profile parameters and plasma shapes in tokamaks", Nucl. Fusion **25**, 1611 (1985), DOI:10.1088/0029-5515/25/11/007.

[72] D. Shiraki, N. Commaux, L. R. Baylor, N. W. Eidietis, E. Hollmann, V. A. Izzo, R. A. Moyer, and C. Paz-Soldan, "Characterization of MHD activity and its influence on radiation asymmetries during massive gas injection in DIII-D", Nucl. Fusion **55**, 073029 (2015), DOI:10.1088/0029-5515/55/7/073029.

[73] H. M. Smith, T. Fehér, T. Fülöp, K. Gál, and E. Verwichte, "Runaway electron generation in tokamak disruptions", Plasma Phys. Control. Fusion **51**, 124008 (2009), DOI:10.1088/0741-3335/51/12/124008.

[74] R. J. Groebner, D. R. Baker, K. H. Burrell, T. N. Carlstrom, J. R. Ferron, P. Gohil, L. L. Lao, T. H. Osborne, D. M. Thomas, W. P. West, J. A. Boedo, R. A. Moyer, G. R. McKee, R. D. Deranian, E. J. Doyle, C. L. Rettig, T. L.

Rhodes, and J. C. Rost, "Progress in quantifying the edge physics of the H mode regime in DIII-D", Nucl. Fusion **41**, 1789 (2001), DOI:10.1088/0029-5515/41/12/306.

[75] R. J. Groebner, C. S. Chang, J. W. Hughes, R. Maingi, P. B. Snyder, X. Q. Xu, J. A. Boedo, D. P. Boyle, J. D. Callen, J. M. Canik, I. Cziegler, E. M. Davis, A. Diallo, P. H. Diamond, J. D. Elder, D. P. Eldon, D. R. Ernst, D. P. Fulton, M. Landerman, A. W. Leonard, J. D. Lore, T. H. Osborne, A. Y. Pankin, S. E. Parker, T. L. Rhodes, S. P. Smith, A. C. Sontag, W. M. Stacey, J. Walk, W. Wan, E. H.-J. Wang, J. G. Watkins, A. E. White, D. G. Whyte, Z. Yan, E. A. Belli, B. D. Bray, J. Candy, R. M. Churchill, T. M. Deterly, E. J. Doyle, M. E. Fenstermacher, N. M. Ferraro, A. E. Hubbard, I. Joseph, J. E. Kinsey, B. LaBombard, C. J. Lasnier, Z. Lin, B. L. Lipshultz, C. Liu, Y. Ma, G. R. McKee, D. M. Ponce, J. C. Rost, L. Schmitz, G. M. Staebler, L. E. Sugiyama, J. L. Terry, M. V. Umansky, R. E. Waltz, S. M. Wolfe, L. Zeng, and S. J. Zweben, "Improved understanding of physics process in pedestal structure, leading to improved predictive capability for ITER", Nucl. Fusion **53**, 093024 (2013), DOI:10.1088/0029-5515/53/9/093024.

[76] M. A. Makowski, C. J. Lasnier, A. W. Leonard, D. Elder, T. H. Osborne, and P. C. Stangeby, "The scaling of the heat flux width in DIII-D", Journal of Nuclear Materials **438**, S208 (2013), DOI:10.1016/j.jnucmat.2013.01.028.

[77] M. A. Makowski, C. J. Lasnier, A. W. Leonard, T. H. Osborne, M. Umansky, J. D. Elder, J. H. Nichols, P. C. Stangeby, D. A. Baver, and J. R. Myra, "Models of SOL transport and their relation to scaling of the divertor heat flux width in DIII-D", Journal of Nuclear Materials **463**, 55 (2014), DOI:10.1016/j.jnucmat.2014.09.065.

[78] T. E. Evans, R. A. Moyer, J. G. Watkins, T. H. Osborne, P. R. Thomas, M. Becoulet, J. A. Boedo, E. J. Doyle, M. E. Fenstermacher, K. H. Finken, R. J. Groebner, M. Groth, J. H. Harris, G. L. Jackson, R. J. L. Haye, C. J. Lasnier, S. Masuzaki, N. Ohyabu, D. G. Pretty, H. Reimerdes, T. L. Rhodes, D. L. Rudakov, M. J. Schaffer, M. R. Wade, G. Wang, W. P. West, and L. Zeng, "Suppression of large edge localized modes with edge resonant magnetic fields in high confinement DIII-D plasmas", Nucl. Fusion **45**, 595 (2005), DOI:10.1088/0029-5515/45/7/007.

[79] R. Nazikian, C. Paz-Soldan, J. deGrassie, D. Eldon, T. E. Evans, N. M. Ferraro, B. A. Grierson, R. J. Groebner, S. Haskey, J. D. King, N. Logan, G. R. McKee, R. A. Moyer, M. Okabayashi, D. M. Orlov, T. H. Osborne, J.-K. Park, T. L. Rhodes, M. W. Shaefer, S. P. Smith, P. B. Snyder, E. J. Strait, and M. R. Wade, "Pedestal bifurcations and resonant field penetration near the threshold of ELM suppression in the DIII-D tokamak", Phys. Rev. Lett. **114**, 105002 (2015), DOI:10.1103/PhysRevLett.114.105002.

[80] J. D. King, E. J. Strait, R. Nazikian, C. Paz-Soldan, M. E. Fenstermacher, N. Ferraro, J. M. Hanson, S. Haskey, R. J. La Haye, M. J. Lanctot, S. A. Lazerson, N. C. Logan, Y. Liu, M. Okabayashi, J.-K. Park, D. Shiraki, and A. D. Turnbull, "Three-dimensional equilibria and island energy transport due to RMP ELM suppression on DIII-D", Phys. Plasmas **submitted** (2015).

[81] D. M. Orlov, R. A. Moyer, T. E. Evans, A. Wingen, R. J. Buttery, N. M. Ferraro, B. A. Grierson, D. Eldon, J. G. Watkins, and R. Nazikian, "Comparison of the numerical modelling and experimental measurements of DIII-D separatrix displacements during H-modes with resomant magnetic perturbations", Nucl. Fusion **54**, 093008 (2014), DOI:10.1088/0029-5515/54/9/093008.

[82] W. M. Solomon, K. H. Burrell, P. Gohil, R. Groebner, and D. Kaplan, "Cross-calibrating spatial positions of light-viewing diagnostics using plasma edge sweeps in DIII-D", Rev. Sci. Instrum. **74**, 5084 (2003), DOI:10.1063/1.1623622.

[83] R. P. Seraydarian and K. H. Burrell, "Multichordal charge exchange recombination spectroscopy on the DIII-D tokamak", Rev. Sci. Instrum. **57**, 2012 (1986), DOI:10.1063/1.1138774.

[84] C. Chrystal. "Experimental tests of the theory of poloidal rotation in the DIII-D tokamak", Ph.D. Dissertation (2014).

[85] G. McKee, R. Ashley, R. Durst, R. Fonk, M. Jakubowski, K. Tritz, K. Burrell, C. Greenfield, and J. Robinson, "The beam emission spectroscopy diagnostic on the DIII-D tokamak", Rev. Sci. Instrum. **70**, 913 (1999), DOI:10.1063/1.1149416.

[86] D. K. Gupta, R. J. Fonk, G. R. McKee, D. J. Schlossberg, and M. W. Shafer, "Enhanced sensitivity beam emission spectroscopy system for non-linear turbulence measurements", Rev. Sci. Instrum. **75**, 3493 (2004), DOI:10.1063/1.1787951.

[87] M. W. Shafer, R. J. Fonk, G. R. Mckee, and D. J. Schlossberg, "Spatial transfer function for the beam emission spectroscopy diagnostic on DIII-D", Rev. Sci. Instrum. **77**, 10F110 (2006), DOI:10.1063/1.2221908.

[88] G. R. McKee, R. J. Fonck, D. K. Gupta, D. J. Schlossberg, M. W. Shafer, and R. L. Boivin, "High sensitivity beam emission spectroscopy for core plasma turbulence imaging", Rev. Sci. Instrum. **77**, 10F104 (2006), DOI:10.1063/1.2219429.

[89] J. D. King, E. J. Strait, R. L. Boivin, D. Taussig, M. G. Watkins, J. M. Hanson, N. C. Logan, C. Paz-Soldan, D. C. Pace, D. Shiraki, M. J. Lanctot, R. J. La Haye, L. L. Lao, D. J. Battaglia, A. C. Sontag, S. R. Haskey, and J. G. Bak, "An upgrade of the magnetic diagnostic system of the DIII-D tokamak

for non-axisymmetric measurements", Rev. Sci. Instrum. **85**, 083503 (2014), DOI:10.1063/1.4891817.

[90] F. F. Chen, *Plasma Physics and Controlled Fusion* (Plenum Press, New York, 1984), pp. 53-68, 184-186, 199-218.

[91] R. M. Kulsrud, *Plasma Physics for Astrophysics* (Princeton University Press, Princeton, 2005), pp. 12, 40-45, 151-171.

[92] J. D. Huba, *NRL Plasma Formulary* (Naval Research Laboratory, Washington, D.C., 2009), pp. 19, 28-29.

[93] J. A. Wesson, "Hydromagnetic stability of tokamaks", Nucl. Fusion **18**, 87 (1978), DOI:10.1088/0029-5515/18/1/010.

[94] L. Spitzer, *Physics of Fully Ionized Gases* (Dover Publications, Inc., Mineola, N.Y., 2006), pp. 95-99.

[95] K. Miyamoto, *Plasma Physics for Nuclear Fusion* (The MIT Press, Cambridge, MA, 1989), pp. 228-247, 371-372.

[96] H. Alfvén, "Existence of electromagnetic-hydrodynamic waves", Nature **150**, 405 (1942), DOI:10.1038/150405d0.

[97] P. M. Bellan, "Why current-carrying magnetic flux tubes gobble up plasma and become thin as a result", Phys. Plasmas **10**, 1999 (2003), DOI:10.1063/1.1558275.

[98] I. B. Bernstein, E. A. Frieman, M. D. Kruskal, and R. M. Kulsrud, "An energy principle for hydromagnetic stability problems", Proc. Roy. Soc. A **244**, 17 (1958), DOI:10.1585/pfr.2.010.

[99] R. J. Goldston and P. H. Rutherford, *Introduction to Plasma Physics* (Institute of Physics Publishing, London, 1995), pp. 323,326.

[100] K. V. Roberts and J. B. Taylor, "Magnetohydrodynamic equations for finite larmor radius", Phys. Rev. Lett. **8**, 197 (1962), DOI:10.1103/PhysRevLett.8.197.

[101] J. W. Connor, R. J. Hastie, H. R. Wilson, and R. L. Miller, "Magnetohydrodynamic stability of tokamak edge plasmas", Phys. Plasmas **5**, 2687 (1998), DOI:10.1063/1.872956.

[102] C. C. Hegna, J. W. Connor, R. J. Hastie, and H. R. Wilson, "Toroidal coupling of ideal magnetohydrodynmaic instabililties in tokamak plasmas", Phys. Plasmas **3**, 584 (1996), DOI:10.1063/1.871886.

[103] F. L. Hinton and R. D. Hazeltine, "Theory of plasma transport in toroidal confinement systems", Review of Modern Physics **48**, 239 (1976), DOI:10.1103/RevModPhys.48.239.

[104] R. J. Bickerton, J. W. Connor, and J. B. Taylor, "Diffusion driven plasma currents and bootstrap tokamak", Nature Physical Science **229**, 110 (1971), DOI:10.1038/physci229110a0.

[105] C. E. Kessel, "Bootstrap current in a tokamak", Nucl. Fusion **34**, 1221 (1994), DOI:10.1088/0029-5515/34/9/I04.

[106] D. M. Thomas, G. R. Mckee, K. H. Burrell, F. Levinton, E. L. Foley, and R. K. Fisher, "Active spectroscopy", Fusion Sci. Technol. **53**, 487 (2008).

[107] T. H. Osborne, P. B. Snyder, K. H. Burrell, T. E. Evans, M. E. Fenstermacher, A. W. Leonard, R. A. Moyer, M. J. Schaffer, and W. P. West, "Edge stability of stationary ELM-suppressed regimes on DIII-D", Journal of Physics: Conference Series **123**, 012014 (2008), DOI:10.1088/1742-6596/123/1/012014.

[108] H. St. John, T. S. Taylor, Y. R. Lin-Liu, and A. D. Turnbull, "Transport simulation of negative magnetic shear discharges", Proc. 15th Int. Conf. on Plasma Physics and Controlled Nuclear Fusion Research in Seville **IAEA-CN-60/D-P22**, 603 (1994).

[109] H. Grad and H. Rubin, "Hydromagnetic equilibria and force-free fields", Proceedings of the 2nd UN Conf. on the Peaceful Uses of Atomic Energy **31**, 190 (1958).

[110] V. D. Shafranov, "Determination of the parameters β_i and l_i in a tokamak for arbitrary shape of plasma pinch cross-section", Plasma Physics **13**, 757 (1971), DOI:10.1088/0032-1028/13/9/006.

[111] C. T. Holcomb, M. A. Makowski, S. L. Allen, W. H. Meyer, and M. A. Van Zeeland, "Overview of equilibrium reconstruction on DIII-D using new measurements from an expanded motional Stark effect diagnostic", Rev. Sci. Instrum. **79**, 10F518 (2008), DOI:10.1063/1.2955711.

[112] T. H. Osborne. "Private communication", (2013).

[113] P. B. Snyder, K. H. Burrell, H. R. Wilson, M. S. Chu, M. E. Fenstermacher, A. W. Leonard, R. A. Moyer, T. H. Osborne, M. Umansky, W. P. West, and X. Q. Xu, "Stability and dynamics of the edge pedestal in the low collisionality regime: physics mechanisms for steady-state ELM-free operation", Nucl. Fusion **47**, 961 (2007), DOI:10.1088/0029-5515/47/8/030.

[114] B. D. Dudson, M. V. Umansky, X. Q. Xu, P. B. Snyder, and H. R. Wilson, "BOUT++: a framework for parallel plasma fluid simulations", Comp. Phys. Comm. **9**, 1467 (2009), DOI:10.1016/j.cpc.2009.03.008.

[115] P. B. Snyder, G. J. Groebner, J. W. Hughes, T. H. Osborne, M. Beurskens, A. W. Leonard, H. R. Wilson, and X. Q. Xu, "A first-principles predictive model of the pedestal height and width: development, testing and ITER optimization with the EPED model", Nucl. Fusion **51**, 103016 (2011), DOI:10.1088/0029-5515/51/10/103016.

[116] L. C. Bernard, F. J. Helton, and R. W. Moore, "GATO: an MHD stability code for axisymmetric plasmas with internal separatricies", Comp. Phys. Comm. **24**, 377 (1981), DOI:10.1016/0010-4655(81)90160-0.

[117] A. B. Mikhailovskii, G. T. A. Huysmans, S. E. Sharapov, and W. Kerner, "Optimization of computational MHD normal-mode analysis for tokamaks", Plasma Phys. Rep. **23**, 844 (1997).

[118] N. Aiba, S. Tokuda, T. Fujita, T. Ozeki, M. S. Chu, P. B. Snyder, and H. R. Wilson, "Numerical method for the stability analysis of ideal MHD modes with a wide range of toroidal mode numbers in tokamaks", Plasma and Fusion Research **2**, 010 (2007), DOI:10.1585/pfr.2.010.

[119] N. M. Ferraro, S. C. Jardin, and P. B. Snyder, "Ideal and resistive edge stability calculations with M3D-C^1", Phys. Plasmas **17**, 102508 (2010), DOI:10.1063/1.3492727.

[120] B. J. Burke, S. E. Kruger, C. C. Hegna, P. Zhu, P. B. Snyder, C. R. Sovinec, and E. C. Howell, "Edge localized linear ideal magnetohydrodynamic instability studies in an extended-magnetohydrodynamic code", Phys. Plasmas **17**, 032103 (2010), DOI:10.1063/1.3309732.

[121] G. Q. Li, X. Q. Xu, P. B. Snyder, A. D. Turnbull, T. Y. Xia, C. H. Ma, and P. W. Xi, "Linear calculations of edge current driven kink modes with BOUT++ code", Phys. Plasmas **21**, 102511 (2014), DOI:10.1063/1.4898673.

[122] G. T. A. Huysmans, "External kink (peeling) modes in X-point geometry", Plasma Phys. Control. Fusion **47**, 2107 (2005).

[123] P. B. Snyder, H. R. Wilson, T. H. Osborne, and A. W. Leonard, "Characterization of peeling-ballooning stability limits on the pedestal", Plasma Phys. Control. Fusion **46**, A131 (2004), DOI:10.1088/0741-3335/46/5A/014.

[124] P. B. Snyder, H. R. Wilson, and X. Q. Xu, "Progress in the peeling-ballooning model of edge localized modes: numerical studies of nonlinear dynamics", Phys. Plasmas **12**, 056115 (2005), DOI:10.1063/1.1873792.

[125] D. Eldon, P. H. Diamond, G. R. Tynan, L. Schmitz, R. J. Groeber, P. B. Snyder, T. H. Osborne, T. E. Evans, J. D. King, and R. L. Boivin. "Linear ideal MHD stability anaysis preceding H-L back transitions using ELITE", Poster presented at the 55th meeting of the APS DPP in Denver, CO (2013).

[126] T. N. Carlstrom, K. H. Burrell, R. J. Groebner, A. W. Leonard, T. H. Osborne, and D. M. Thomas, "Comparison of L-H transition measurements with physics models", Nuclear Fusion **39**, 1941 (1999), DOI:10.1088/0029-5515/39/11Y/338.

[127] R. L. Miller, M. S. Chu, J. M. Greene, Y. R. Lin-Liu, and R. E. Waltz, "Non-circular, finite aspect ratio, local equilibrium model", Phys. Plasmas **5**, 973 (1998), DOI:10.1063/1.872666.

[128] W. M. Stacey and C. Bae, "Representation of the plasma fluid equations in 'Miller equilibrium' analytical flux surface geometry", Phys. Plasmas **16**, 082501 (2009), DOI:10.1063/1.3177613.

[129] X.-Z. Li, J. Kesner, and B. Lane, "Conducting-wall and pressure profile effect on MHD stabilization of axisymmetric mirror", Nucl. Fusion **25**, 907 (1985), DOI:10.1088/0029-5515/25/8/004.

[130] E. J. Strait, T. S. Taylor, A. D. Turnbull, J. R. Ferron, L. L. Lao, B. Rice, O. Sauter, S. J. Thomson, and D. Wróblewski, "Wall stabilization of high beta tokamak discharges in DIII-D", Phys. Rev. Lett. **74**, 2483 (1995), DOI:10.1103/PhysRevLett.74.2483.

[131] M. S. Chu and M. Okabayashi, "Stabilization of the external kink and the resistive wall mode", Plasma Phys. Control. Fusion **52**, 123001 (2010), DOI:10.1088/0741-3335/52/12/123001.

[132] M. Okabayashi, J. Bialek, A. Bondeson, M. S. Chance, M. S. Chu, A. M. Garofalo, R. Hatcher, Y. In, G. L. Jackson, R. J. Jayakumar, T. H. Jensen, O. Katsuro-Hopkins, R. J. La Haye, Y. Q. Liu, G. A. Navratil, H. Reimerdes, J. T. Scoville, E. J. Strait, M. Takechi, A. D. Turnbull, P. Gohil, J. S. Kim, M. A. Makowski, J. Manickam, and J. Menard, "Control of the resistive wall mode with internal coils in the DIII-D tokamak", Nucl. Fusion **45**, 1715 (2005), DOI:10.1088/0029-5515/45/12/028.

[133] S. Koh, C. S. Chang, S. Ku, J. E. Menard, H. Weitzner, and W. Choe, "Bootstrap current for the edge pedestal plasma in a diverted tokamak geometry", Phys Plasmas **19**, 072505 (2012), DOI:10.1063/1.4736953.

[134] C. S. Chang, S. Ku, and H. Weitzner, "Numerical study of neoclassical plasma pedestal in a tokamak geometry", Phys. Plasmas **11**, 2649 (2004), DOI:10.1063/1.1707024.

[135] E. A. Belli, J. Candy, O. Meneghini, and T. H. Osborne, "Limitations of bootstrap current models", Plasma Phys. Control. Fusion **56**, 045006 (2014), DOI:10.1088/0741-3335/56/4/045006.

[136] D. M. Thomas, A. W. Leonard, R. J. Groebner, T. H. Osborne, T. A. Casper, P. B. Snyder, and L. L. Lao, "Measurement of edge currents in DIII-D and their implication for pedestal analysis", Phys. Plasmas **12**, 056123 (2005), DOI:10.1063/1.1879992.

[137] D. Eldon, R. L. Boivin, R. J. Groebner, T. H. Osborne, P. B. Snyder, A. D. Turnbull, J. A. Boedo, K. H. Burrell, E. Kolemen, L. Schmitz, G. R. Tynan, and H. R. Wilson, "Investigation of peeling-ballooning stability prior to transient outbursts accompanying transitions out of H-mode in DIII-D", Phys. Plasmas **22**, 052109 (2015), DOI:10.1063/1.4919942.

[138] J. M. Muñoz Burgos, K. H. Burrell, W. M. Solomon, B. A. Grierson, S. D. Loch, and C. Chrystal, "Kinetic theory and atomic physics corrections for determination of ion velocities from charge-exchange spectroscopy", Nucl. Fusion **53**, 093012 (2013), DOI:10.1088/0029-5515/53/9/093012.

[139] K. H. Burrell. "Fitting function for characterization of the edge E_r well in H-mode plasmas", manuscript in preparation (2015).

[140] J. C. Hillesheim, W. A. Peebles, T. L. Rhodes, L. Schmitz, A. E. White, and T. A. Carter, "New plasma measurements with a multichannel millimeter-wave fluctuation diagnostic system in the DIII-D tokamak", Rev. Sci. Instrum. **81**, 10D907 (2010), DOI:10.1063/1.3466900.

[141] M. A. Van Zeeland, R. L. Boivin, T. N. Carlstrom, T. Deterly, and D. K. Finkenthal, "Fiber optic two-color vibration compensated interferometer for plasma density measurements", Rev. Sci. Instrum. **77**, 10F325 (2006), DOI:10.1063/1.2336437.

[142] I. H. Hutchinson, "Excited-state populations in neutral beam emission", Plasma Phys. Control. Fusion **44**, 71 (2002), DOI:10.1088/0741-3335/44/1/307.

[143] G. Bateman and D. B. Nelson, "Resistive-ballooning-mode equation", Phys. Rev. Lett. **41**, 1804 (1978), DOI:10.1103/PhysRevLett.41.1804.

[144] B. I. Cohen, M. V. Umansky, W. M. Nevins, M. A. Makowski, J. A. Boedo, D. L. Rudakov, G. R. McKee, Z. Yan, and R. J. Groebner, "Simulations of drift resistive ballooning L-mode turbulence in the edge plasma of the DIII-D tokamak", Phys. Plasmas **20**, 055906 (2013), DOI:10.1063/1.4804638.

[145] R. J. La Haye, R. J. Buttery, S. Guenter, G. T. A. Huysmans, M. Maraschek, and H. R. Wilson, "Dimensionless scaling of the critical beta for onset of a neoclassical tearing mode", Phys. Plasmas **7**, 3349 (2000), DOI:10.1063/1.874199.

[146] D. A. Humphreys, J. R. Ferron, R. J. La Haye, T. C. Luce, C. C. Petty, R. Prater, and A. S. Welander, "Active control for stabilization of neoclassical tearing modes", Phys. Plasmas **13**, 056113 (2006), DOI:10.1063/1.2173606.

[147] X. Q. Xu, B. D. Dudson, P. B. Snyder, M. V. Umansky, H. R. Wilson, and T. Casper, "Nonlinear ELM simulations based on a nonideal peeling-ballooning model using the BOUT++ code", Nucl. Fusion **51**, 103040 (2011), DOI:10.1088/0029-5515/51/10/103040.

[148] T. H. Osborne, G. Jackson, Z. Yan, R. Maingi, D. Mansfield, B. Grierson, C. Chrobak, A. McLean, S. Allen, D. Battaglia, A. Briesemeister, M. Fenstermacher, G. McKee, and P. Snyder, "Enhanced H-mode pedestals with lithium injection in DIII-D", Nucl. Fusion **55**, 063018 (2015), DOI:10.1088/0029-5515/55/6/063018.

[149] Z. Yan, G. McKee, R. Maingi, D. K. Mansfield, D. J. Battaglia, B. A. Grierson, R. Nazikian, A. L. Roquemore, G. L. Jackson, T. H. Osborne, C. P. Chrobak, J. S. deGrassie, R. J. Groebner, P. B. Snyder, and A. G. McLean. "Onset of a "broadband bursty" with lithium aerosol injection in DIII-D", Poster presented at the 56th annual meeting of the APS DPP in New Orleans (2014).

[150] ITER Physics Expert Group on Divertor, ITER Physics Expert Group on Divertor Modelling and Database, ITER Physics Basis Editors, and ITER EDA, "Chapter 4: Power and particle control", Nucl. Fusion **39**, 2391 (1999), DOI:10.1088/0029-5515/39/12/304.

[151] A. W. Leonard, M. A. Mahdavi, C. J. Lasnier, T. W. Petrie, and P. C. Stangeby, "Scaling radiative divertor solutions to high power in DIII-D", Nucl. Fusion **52**, 063015 (2012), DOI:10.1088/0029-5515/52/6/063015.

[152] T. Eich, B. Sieglin, A. Scarabosio, A. Herrmann, A. Kallenbach, G. F. Matthews, S. Jachmich, S. Brezinsek, M. Rack, and R. J. Goldston, "Empirical scaling of inter-ELM power widths in ASDEX upgrade and JET", J. Nucl. Mater. **438**, S72 (2013), DOI:10.1016/j.jnucmat.2013.01.011.

[153] E. Kolemen, S. L. Allen, B. D. Bray, M. E. Fenstermacher, D. A. Humphreys, A. W. Hyatt, C. J. Lasnier, A. W. Leonard, M. A. Makowski, A. G. McLean, R. Maingi, R. Nazikian, T. W. Petrie, V. A. Soukhanovskii, and E. A. Unterberg, "Heat flux management via advanced divertor configurations and divertor detachment", J. Nucl. Mater. **463**, 1186 (2014), DOI:10.1016/j.jnucmat.2014.11.099.

[154] C. B. Markwardt, "Non-linear least squares fitting in IDL with MPFIT", Astronomical Data Analysis Software and Systems XVIII **ASP Conf. Ser. 411**, 251 (2009).

[155] J. M. Beall, Y. C. Kim, and E. J. Powers, "Estimation of wavenumber and frequency spectra using fixed probe pairs", J. Appl. Phys. **53**, 3933 (1982), DOI:10.1063/1.331279.

[156] R. Andrae, T. Schulze-Hartung, and P. Melchior, "Dos and don'ts of reduced chi-squared", (2010) `ArXiv:1012.3754v1`.

[157] G. McKee, R. Ashley, R. Durst, R. Fonck, M. Jakubowski, K. Tritz, K. H. Burrell, C. M. Greenfield, and J. Robinson. "Beam emission spectroscopy diagnostic on the DIII-D tokamak", presented at the 12th High Temperature Plasma Diagnostics Conference in Princeton, NJ (1998).